Development and application of extreme ultraviolet light sources – harnessing novel geometries of high-harmonic generation and using photoelectron spectroscopy to study nanoparticle dynamics

by

Jennifer L. Ellis

B.S., University of Texas at Austin, 2012

M.S., University of Colorado Boulder, 2015

A thesis submitted to the

Faculty of the Graduate School of the

University of Colorado in partial fulfillment

of the requirements for the degree of

Doctor of Philosophy

Department of Physics

2018

This thesis entitled:
Development and application of extreme ultraviolet light sources – harnessing novel geometries of high-harmonic generation and using photoelectron spectroscopy to study nanoparticle dynamics
written by Jennifer L. Ellis
has been approved for the Department of Physics

_____

Prof. Margaret M. Murnane

_____

Prof. Henry C. Kapteyn

Date _____

The final copy of this thesis has been examined by the signatories, and we find that both the content and the form meet acceptable presentation standards of scholarly work in the above mentioned discipline.

Ellis, Jennifer L. (Ph.D., Physics)

Development and application of extreme ultraviolet light sources – harnessing novel geometries of high-harmonic generation and using photoelectron spectroscopy to study nanoparticle dynamics

Thesis directed by Professors Margaret M. Murnane and Henry C. Kapteyn

High-harmonic generation (HHG) is an extreme nonlinear optical process, in which visible femtosecond laser light is coherently upconverted to produce ultrashort pulses of extreme ultraviolet (EUV) or soft x-ray radiation. In this thesis, I describe both the development of new HHG sources and the application of HHG to study nanoparticle structure and dynamics. In the first section of this thesis, I discuss the development of novel geometries of HHG that enable the production of EUV light with controllable polarization. In these geometries, either two driving lasers or two high-harmonic sources are combined to give greater control over the HHG process and the resulting HHG beams. In addition to control over the polarization state, the specific geometry can have significant ramifications on the macroscopic physics or phase matching of HHG and therefore substantially modify the experimental conditions at which HHG is optimized as compared to traditional single-beam HHG. In the second section of this thesis, I will discuss using photoelectron spectroscopy to study the electronic structure and dynamics of nanoparticles. Using a nanoparticle aerosol source we were able to introduce nanoparticles of varying compositions into a photoelectron spectrometer. I will describe several experiments studying first the electronic structure and coupling of excitons in quantum dots (semiconductor nanocrystals) and then the properties and dynamics of hot electrons in nanoparticles with a wide array of compositions - ranging from ionic crystals to nanodroplets of organic liquids. The findings presented in this thesis will guide future efforts to extend the capabilities of EUV sources, develop nanoparticle-based devices, and understand how highly excited electrons behave in unconventional and previously inaccessible materials.

Dedication

To my parents, who raised me to believe I could do anything, and my husband, who was there for me whenever that belief faltered.

Acknowledgements

The work presented here would not have been possible without the assistance of many wonderful people. My sincere thanks goes out to:

- Margaret and Henry for being the best advisors on the planet and providing me with so many opportunities and with their invaluable guidance and expertise.

- My mentors in the Kapteyn-Murnane Group, especially Daniel Hickstein, Franklin Dollar, and Wei Xiong, who have taught me almost everything I know about working in a lab and constantly inspire me with their talent and passion for science.

- My labmates over the years, who have all been a joy to work with, including Kevin Dorney, Ellen Keister, Chris Mancuso, Nathan Brooks, Quynh Nguyen, Drew Morrill, Tingting Fan, and Chengyuan Ding. I would especially like to thank Kevin for being a fantastic partner in crime during the past few years of muddling through without a post doc.

- The members of the magnetics team in the Kapteyn-Murnane Group, especially Christian Gentry, Dmitriy Zusin, and Patrick Grychtol, who put up with all my dumb questions about magnets.

- The other members of the Kapteyn-Murnane Group, past and present, including Craig Hogle, Tory Carr, Kathy Hoogeboom-Pot, Dan Adams, Tenio Popmintchev, Zhensheng Tao, Bill Peters, David Couch, Cong Chen, Nico Hernandez-Charpak, Ben Galloway, Liz Shanblatt, Phoebe Tengdin, Adam Blonsky, Maithreyi Gopalakrishnan, Giulia Mancini,

and many many more, who taught me a lot and graciously let me steal/borrow their equipment sometimes if I asked nicely.

- My talented collaborators, including Chip Durfee, Carlos Hernandez-Garcia, Kyle Schnitzenbaumer, Molly Wilker, Gordana Dukovic, Brett Palm, Jose-Luis Jimenez, Justin Shaw, and Stefan Witte, who made this work possible.

- Daisy Raymondson, Mike Walls, Michael Gerrity, and Amelie Auger, who taught me how to fix the laser.

- The JILA Instrument Shop, including Hans Green, David Alchenburger, Todd Asnicar, Blaine Horner, Kyle Thatcher, and Kels Detra, who have thankfully been able to solve every technical problem I've thrown at them.

- The JILA Computing Team, including J. R. Raith and Corey Keasling, who somehow keep all the lab computers happy.

- Julie Phillips, who taught me how to write.

- Professors Markus Raschke, Ralph Jimenez, and Gordana Dukovic for serving on my thesis committee and lending me their advice and expertise.

- My previous research mentors, Don Winget and Mike Montgomery (UT Austin), who introduced me to the thrill of research and inspired me to pursue a PhD.

- The friends I've made throughout grad school, who reminded me to get out of the basement and hit the trails sometimes.

- My family, who has always supported me.

Contents

Chapter

Figures

Figure

List of Abbreviations

HHG	high-harmonic generation
EUV	extreme ultraviolet
QD	quantum dot
PES	photoelectron spectroscopy
RCP	right circularly polarized
LCP	left circulalry polarized
BBO	barium borate (BaB_2O_4)
CCD	charge-coupled device
XMCD	x-ray magnetic circular dichroism
MCD	magnetic circular dichroism
VMI	velocity map imaging
SMI	spatial map imaging
BASEX	basis set expansion
TEM	transmission electron microscopy
SMPS	scanning mobility particle sizer
UV	ultraviolet
NIR	near infrared
2PPE	two-photon photoemission
NCP-HHG	noncollinear circularly polarized HHG
HOSFG	high-order-sum-frequency generation

HODFG	high-order-difference-frequency generation
SVE-HHG	high harmonics with spatially varying ellipticity
FT	Fourier transform
TA	transient absorption
MV	methyl viologen
LUMO	lowest unoccupied molecular orbital
IRF	instrument response function
MFP	mean free path
IR	infrared
CXRO	center for x-ray optics

Outline

This thesis describes four main studies, which were the subject of five publications:

- A publication in *Nature Photonics* titled "Non-collinear generation of angularly isolated circularly polarized high harmonics," in which we presented a new technique to produce circularly polarized high harmonics using two crossed beams.

- A publication in *Optics Express* titled "Phase matching of noncollinear sum and difference frequency high harmonic generation above and below the critical ionization level." In this work, we further explored the capabilities and limitations of noncollinear high-harmonic generation, specifically focusing on the role of phase matching.

- A forthcoming publication titled "High harmonics with spatially varying ellipticity," in which we present another new technique for producing high harmonics with circular polarization. In this case, we combine two harmonic sources to create a far-field harmonic beam with spatially varying ellipticity.

- A publication in *The Journal of the American Chemical Society* titled "Solvents effects on charge transfer from quantum dots." In this work, we study electron transfer between quantum dots and attached dye molecules in both solvated and solution free environments, thereby isolating the role of solvent molecules in the charge transfer process.

- A publication in *The Journal of Physical Chemistry Letters* titled "Materials properties and solvated electron dynamics of isolated nanoparticles and nanodroplets probed with

ultrafast extreme ultraviolet beams," in which we investigate the interaction of extreme ultraviolet light with nanomaterials.

I was the lead researcher on four of these five publications. My colleague, Daniel Hickstein, led the first investigations into noncollinear high harmonic generation, which resulted in the *Nature Photonics* publication. I either led or was an integral part of the construction and implementation of all of the equipment and experimental apparatuses in this thesis, except for the velocity-map-imaging photoelectron spectrometer, which was constructed before I joined the group. However, I was involved in coupling the nanoparticle aerosol source to the photoelectron spectrometer, which had previously employed a conventional gas jet.

First, the introduction to this thesis (Chapter 1) provides a motivation for extreme ultraviolet and photoelectron spectroscopies and their application to studying nanomaterials. This chapter also provides an overview of some of the relevant physics of high-harmonic generation as an extreme ultraviolet light source. Next, I present a thorough description of the methods and apparatuses used throughout this work (Chapter 2). The following four chapters then describe the four previously mentioned experimental studies, in which we investigated noncollinear high-harmonic generation (Chapter 3), the production of high harmonics with spatially varying ellipticity (Chapter 4), solvent effects in charge transfer from quantum dots (Chapter 5), and extreme ultraviolet photoelectron spectroscopy as a probe of nanomaterials (Chapter 6). I then conclude with some discussion of where this work is headed and future experiments that I hope will be successfully implemented (Chapter 7).

Chapter 1

Introduction

1.1 Motivation and Background

1.1.1 Perceiving the Imperceptible

Broadly stated, science is the process of developing an understanding of the world around us. While it is fun to imagine ancient astronomers gazing up at the night sky or Galileo dropping balls off of towers to learn about gravity, science quickly progressed beyond the realms of human perception. Consequently, pushing the frontiers of science has become inexorably linked with developing new technologies or new ways to "perceive the imperceptible" in order to further our understanding. Indeed, it was the aforementioned Galileo who pointed the first telescope at the night sky. In doing so, he used a new technology to observe moons orbiting Jupiter, the rings of Saturn, and other astronomical features that had never been seen before.

In addition to astronomical objects requiring Galileo's telescope, there are many other ways that processes and phenomena can be imperceptible to us. For example objects can be too small to see, like the nanostructures responsible for iridescence in butterfly wings (Fig. 1.1). Alternatively, processes can occur on timescales that are vastly different from our own (Fig. 1.2). On one extreme, galaxy formation occurs over many billions of years, and on the other extreme, electron motions can occur in one millionth of one billionth of a second. This thesis is based on the study of both ultrafast time scales ($\sim$ fs) and ultrashort length scales ($\sim$ nm).

Ultrafast science has blossomed over the last several decades with the development of short-

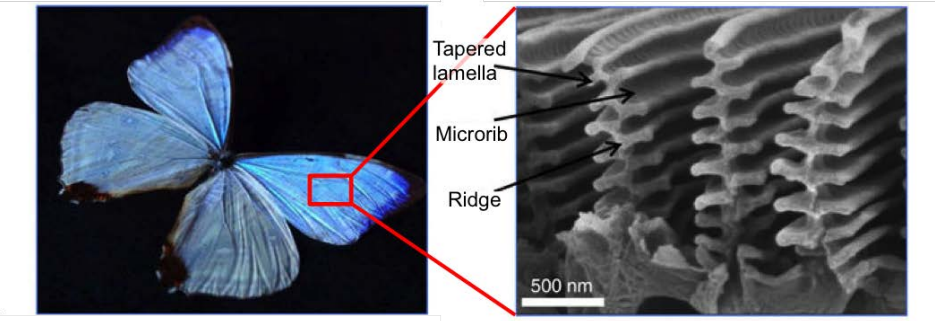

Figure 1.1: **Example of nanostructures in nature.** *Morpho* butterfly and scanning electron microscope image of nanostructures in the wings that cause blue iridescence. Adapted from [1].

pulse lasers that enable researchers to make "movies" with femtosecond (10^{-15} sec) timing resolution. These movies are typically captured through pump-probe techniques, in which an initial laser pulse (the pump) interacts with the system and initiates some dynamics. The changing state of the system is read-out at some later time when it interacts with a second laser pulse (the probe). Scanning the time delay between the pump and the probe therefore maps out the evolution of the system, in effect making a movie of the associated ultrafast dynamics. The timing resolution achievable is limited by the duration of the pump and probe pulses, so developing shorter laser pulses enables you to make movies with higher "frame rates" and thereby resolve faster processes.

In addition to resolving ultrafast dynamics, short-pulse lasers are remarkable because they achieve very strong electric fields that can drive nonlinear interactions or even suppress the Coulomb potential of atoms. This is because a pulsed laser is "off" most of the time, so that all of the light is compressed into very short bursts. Therefore, femtosecond lasers with very modest average powers have exceedingly high peak powers. For example, the laser used in this thesis operates at 10 watts of average power, which is comparable to a dim incandescent light bulb. However, it emits a burst of light that's only about 50 fs in duration once every millisecond, thereby reaching peak powers of 0.2 terawatts (10^{12} W). One of the many ways that these high peak powers are useful is to generate an even more exotic ultrafast light source via high-harmonic generation.

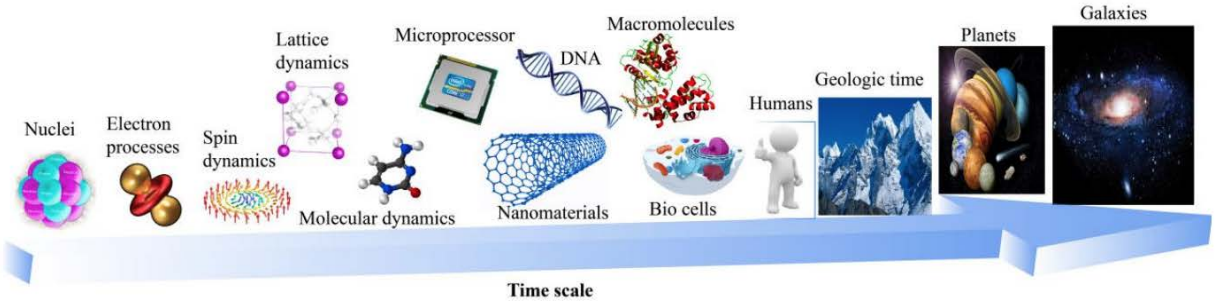

Figure 1.2: **Different processes occur on different time scales, which vary by many orders of magnitude in duration.** Figure from [2].

1.1.2 High-Harmonic Generation as an Enabling Light Source

High-harmonic generation (HHG) is an extreme nonlinear optical process in which a sufficiently strong visible laser is coherently upconverted to extreme ultraviolet (EUV) or soft x-ray wavelengths [3–5]. The HHG process is both spatially and temporally coherent [6], so the light that is produced is "laser like." The availability of a tabletop x-ray laser has many exciting applications in both imaging and spectroscopy. Due to the well-known diffraction limit, conventional visible light sources cannot be used to image nanostructured materials.[1] However, with wavelengths ranging from a few to tens of nanometers, HHG sources are well suited to imaging the nanoworld [7–10]. The wavelengths accessible with current HHG sources are also advantageous because there are many elemental absorption edges in the EUV and soft x-ray regions of the spectrum (Fig. 1.3) [11–16]. The ability to spectrally access specific atomic absorption edges enables measurements with chemical specificity. Furthermore, HHG has been used to produce the shortest pulses known to date, with the current record being 43 attoseconds [17]. Therefore, HHG based sources are well suited to studying the fastest known dynamics. While somewhat heroic experimental efforts must currently be undertaken to produce truly isolated attosecond pulses [18–23], amazingly, attosecond temporal dynamics can sometimes still be accessed with more common HHG sources [24–28].

[1] Unless nanoscale tips are used to cleverly beat the diffraction limit, which is an active and exciting area of research.

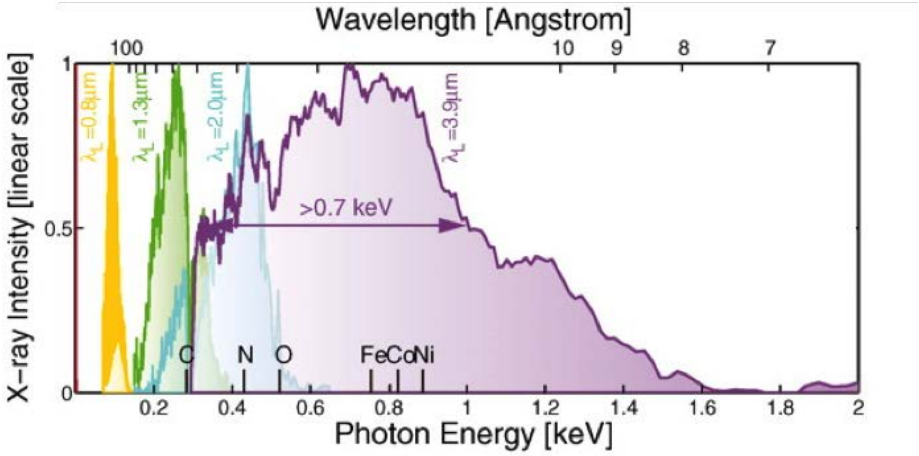

Figure 1.3: **Example high-harmonic generation (HHG) spectra, which cover several relevant atomic absorption edges.** Adapted from [14].

These sources have more moderate pulse durations of ∼10s of femtoseconds but possess underlying attosecond scale temporal structure, which has been used to make the fastest time-domain measurements of final-state lifetimes to date. For example, the lifetime of the Λ_1^B band in nickel was recently measured to be ∼200 attoseconds [29].

There are of course other methods to produce ultrashort pulses of x-ray light with good spatial and temporal coherence. However, these tend to be facility-scale experiments, such as free-electron lasers [30] or synchrotrons [31], which cost many billions of dollars, can be the size of several football fields, and require a full-time staff to keep them up and running. HHG, on the other hand, can be done on a tabletop and run by one or two graduate students. The facility-scale sources are brighter and reach higher photon energies than HHG but time is a very limited resource. Therefore, HHG and facility-scale x-ray experiments are very complimentary techniques. For example, higher risk studies can first be explored on relatively inexpensive HHG beamlines before moving to the big facilities. Additionally, many experiments simply do not need the higher flux levels and are perfectly tractable for investigation with HHG beamlines, so that the big facilities can be reserved for experiments that best exploit their capabilities.

HHG was first observed about 30 years ago [3, 4], and has since become a well-developed technology that is rapidly approaching turn-key operation. An understanding of both the single-

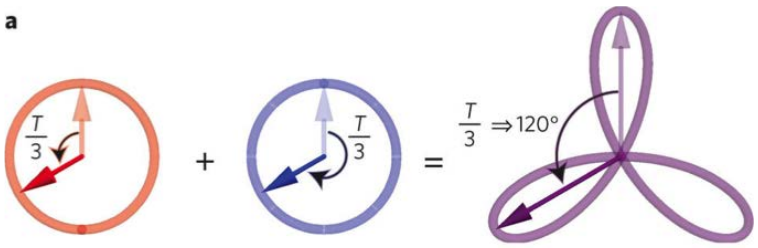

Figure 1.4: **Bichromatic laser field to drive circularly polarized HHG.** The collinear combination of a circularly polarized field with a counter-rotating field at twice the frequency creates a trefoil shaped field that can efficiently drive the HHG process. Adapted from [43].

atom physics [32–35] and important macroscopic effects [5, 36–38] in HHG was soon developed, enabling optimization of the flux that can be produced. Additionally, the scaling laws to push HHG sources to higher photon energies are well understood [14] and it is now largely a matter of developing the required driving laser technologies to extend the energy range over which HHG sources operate. Furthermore, the pulse durations achievable with HHG are also consistently improving [17, 19, 20, 23, 39]. The main characteristic of light that HHG could not access (until recently) was the polarization – for many years bright HHG emission was restricted to linear polarization [34, 40, 41]. However, many systems, such as magnetic materials or chiral molecules, exhibit circular dichroism, meaning that they interact differently with different helicities of light. Therefore, a circularly polarized HHG source was desired to probe these chiral phenomena. Fortunately, there has been recent rapid progress in the development of bright HHG sources with circular polarization [42–49]. These breakthrough techniques use the combination of several driving lasers to sculpt the driving light field and gain greater control over the HHG process (see Fig. 1.4 for an example of these synthesized light fields). Furthermore, the geometry of how these driving lasers are combined is another parameter that provides even greater control [50–52].

Chapters 3 and 4 in this thesis describe two such geometries that either combine two driving lasers or two high-harmonic sources to produce EUV light with controllable polarization. In addition to control over the polarization state, the specific geometry employed can have significant ramifications on the macroscopic physics (i.e. phase matching) of HHG and therefore substantially

modify the experimental conditions at which HHG is optimized as compared to traditional single-beam HHG. These phase matching effects will be discussed in Chapter 3 for the specific case of noncollinear HHG. While HHG is swiftly becoming a mature and reliable light source, continual source development is still necessary to extend the applicability of HHG as a versatile probe of the ultrafast dynamics of nanoscale phenomena.

1.1.3 Nanoparticles: Smaller is Different

In addition to exploring ultrafast time scales, another exciting area of current research is concerned with ultrashort length scales.[2] While techniques to create and probe either bulk materials or individual atoms and molecules are reasonably well established, the intermediate regime between those two extremes was relatively inaccessible until recently. Therefore, there is a wide array of new and exciting physics to be explored at the nanometer length scale. Typically, nanoparticles have properties that are both somewhat atom-like and somewhat bulk-like. Additionally, nanoparticles can even possess entirely new and unexpected characteristics. For example, we are all familiar with the color and appearance of bulk gold, however gold nanoparticles don't look "gold" at all. Instead, gold nanoparticles (∼10 nm diameter) are a deep red color, as seen in the Lycurgus Cup (Fig. 1.5a). This red coloring arises because of collective electron motions within the nanoparticle known as plasmon resonances. These plasmon resonances cause gold nanoparticles to preferentially absorb green light, thereby transmitting predominantly red light and appearing red. The exact location in wavelength of the plasmon resonance depends on the size of the nanoparticle and the electron density, therefore these plasmon resonances can be tuned by changing the size and composition of metallic nanoparticles.

Nanoparticles made out of semiconducting material can be even more visually striking than metallic nanoparticles (Fig. 1.5b). Semiconductor nanocrystals, which are often referred to as quantum dots (QDs), also have absorption and emission features that depend on the size of the

[2] Interestingly, the study of ultrafast time scales and ultrashort length scales tend to be inexorably linked because dynamics occurring on ultrashort length scales are often inherently ultrafast, and vice versa.

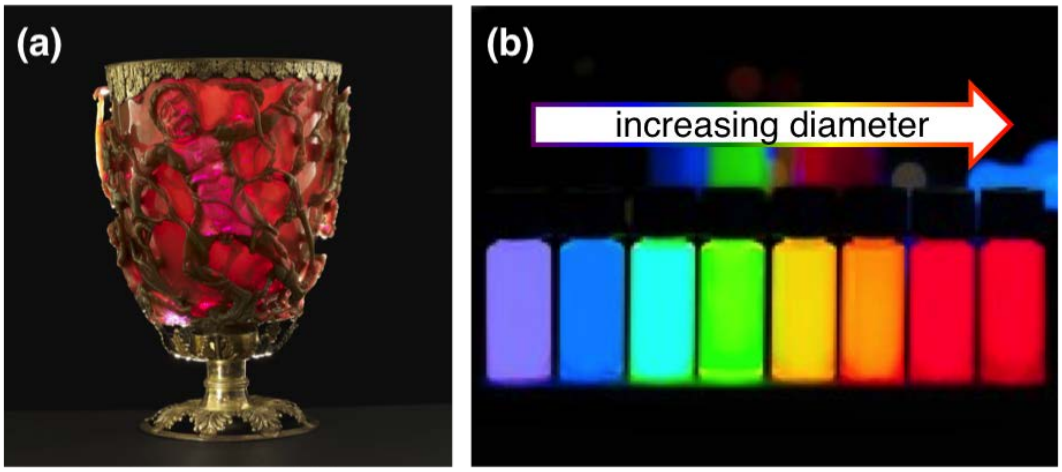

Figure 1.5: **Nanoparticles can have new and interesting properties.** (a) Even though we don't think of gold as being red, the gold nanoparticles present in the glass in the Lycurgus Cup makes the cup a dramatic red color when light is transmitted through it. Figure from the British Museum, ©Trustees of the British Museum. (b) Quantum dots (QDs, i.e. semiconductor nanocrystals) fluoresce all across the visible spectrum. The color at which the QDs emit depends on their diameter, with smaller QDs emitting bluer light and larger QDs emitting redder light. Figure adapted from PlasmaChem.

nanoparticle. In this case, the energies of electrons and holes excited within the semiconductor are increased due to quantum confinement effects from trying to trap an excited particle in too small of a space. In fact, this phenomena is reasonably well described by the standard "particle in a box" problem from introductory quantum mechanics, where the nanoparticle diameter is analogous to the size of the box. These confinement effects arise when the diameter of the nanoparticle is of order a few nanometers, and cause the band-gap fluorescence of the QDs to become bluer as the diameter of the QD gets smaller.

Because of their interesting features and vast tunablility, nanoparticles provide for the exciting possibility of developing nano-engineered devices.[3] Ideally, we would be able to tailor-make a given nanoparticle with the desired characteristics to function in a specific way in some device. To achieve this goal, we first need to develop a firm and fully predictive understanding of how the controllable physical characteristics of the nanoparticle (size, shape, composition, etc.) determine

[3] It is already possible to purchase QD-based televisions, so there is at least one nano-egineered device currently on the market!

the resulting functionality (electronic structure and coupling, catalytic activity, etc.) [53]. Gaining additional insight into precisely this question is what motivated us to develop an apparatus to conduct photoelectron spectroscopy measurements on "gas-phase" nanoparticles (this apparatus is used in Chapters 5 and 6 in this thesis).

Investigating completely isolated or gas-phase nanoparticles is advantageous for several reasons. First, it completely decouples the nanoparticle system from any environmental effects. Typically, nanoparticles are studied either while suspended in solution [54–57], embedded in some bulk material [58–61], or deposited on surfaces [62–64]. These different environments can perturb the nanoparticle properties [55], particularly if the nanoparticle is strongly coupled to said environment. Since any eventual device is necessarily going to involve some sort of complex environment [65–69], studying isolated nanoparticles may seem artificial. However, isolated nanoparticles are simpler and more theoretically approachable, allowing us to build up our theoretical understanding of the nanoparticles themselves before moving on to nanoparticles in complex environments. Indeed, in Chapter 5 we investigate this question of what role the environment might play by studying charge transfer dynamics in both solvated and solution-free QDs. Additionally, these gas-phase nanoparticles are experimentally advantageous because they are delivered via a constantly flowing aerosol source. This flowing source refreshes the nanoparticles for each laser shot, so that we automatically avoid any problems from damage or charging effects that can plague other experiments [64, 70–73]. Finally, the main advantage and motivation for studying isolated nanoparticles is that it enables us to apply photoemission techniques, which must be conducted in ultra-high vacuum environments. The large majority of nanoparticle characterization and research is done with absorption based measurements, however photoemission is a very powerful and complementary technique that can give additional information. Several pioneering studies have previously demonstrated that photoemission can be successfully used to measure the electronic structure, coupling, and dynamics of QDs on surfaces [62–64, 74]. Therefore, we simply had to extend this technique to the gas phase.

1.1.4 Photoemission

Photoemission, or photoelectron and photoion spectroscopy, is a technique in which a system is probed by detecting electrons or ions that are ejected from it after interaction with light. There are a number of different ways that light can cause the emission of electrons or ions. Perhaps the simplest to consider is illuminating a system with high-energy photons. In that case, when a photon is absorbed it can impart it's energy to an electron in the system. If the energy of the photon is greater than the energy binding the electron, then the electron can escape and be detected. Since energy is conserved, and typically the photon energy is known, measuring the kinetic energy of the emitted electron tells you how tightly that electron was bound in the first place. Therefore, photoelectron spectroscopy can give information about the electronic structure of a system.

Photoelectron spectroscopy (PES) is therefore a very complementary technique to absorption or emission spectroscopy because they both give slightly different information about electronic structure. In the case of absorption spectroscopy, you are measuring transitions between an initial and final state in the absorbing medium. Therefore, the properties of both the initial and the final state, and the coupling (a.k.a matrix element) between them effect the transition. On the other hand, in PES, the final state is always a free electron (i.e., an electron plane-wave state) in the vacuum. Therefore, PES isolates an individual state, instead of convolving initial and final states in a transition. Furthermore, PES measures the absolute binding energy of electronic states, whereas absorption spectroscopy measures energy differences between two states. Taken together, these two techniques can provide a more complete picture of the system.

Photoemission is routinely used to study both atoms or molecules and bulk materials. While the basic principles are the same, there are slightly different considerations for the two cases. One of these considerations is that when an electron is excited in an atom or molecule that electron is essentially immediately free to escape the system and travel to the detector. Therefore, ionization from atoms and molecules is basically a one-step process that consists of a Fermi's Golden Rule type transition and immediate ionization.[4] Conversely, in ionization from a bulk material, once an

[4] This is of course somewhat of an over simplification. The presence of the nuclei and additional electrons in an

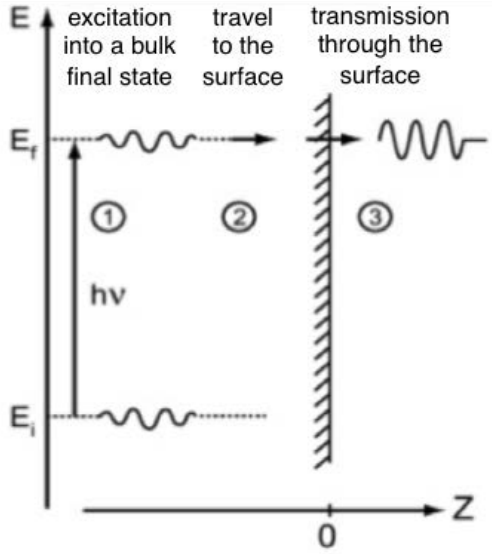

Figure 1.6: **Three-step model of photoemission from bulk materials.** Figure from [78].

electron is excited it is still physically located inside of a material and must escape to be detected. Photoemission from bulk materials is therefore often described in terms of a three-step model [78] (Fig. 1.6). The first step is the absorption of a photon, which promotes the electron to some highly excited final state in the bulk, where it now has enough energy to escape the system. The second step is for that electron to travel to the surface of the material. While it is traveling through the material the electron has some probability to scatter off of phonons or other electrons; this probability is quantified by the electron mean free path. The third and final step is for the electron to transmit through the surface. Once it does so the electron is considered ionized and is free to travel on its way to be detected. However, there is some probability for the electron to instead reflect off of the interface and therefore fail to escape the material.[5] In this thesis, we apply photoemission to study nanoparticles and therefore must consider both extremes (atoms versus bulk) and how these processes manifest in our nanosystems [79].

The second step in the three-step model of photoemission is particularly relevant when com-

atomic or molecular system can in fact effect an electron as it is ionizing and exiting the system. One example of this is a "photoionization time delay," where electrons emitted from different states can take slightly different amounts of time to ionize [24, 75–77].

[5] This is similar to the total-internal reflection of light.

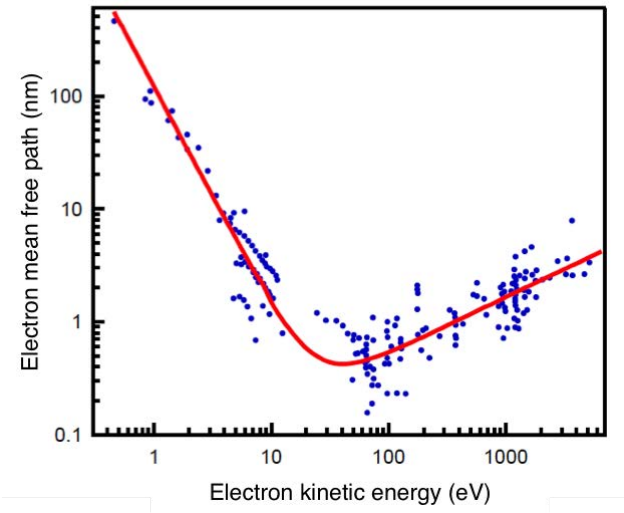

Figure 1.7: **Electron mean free paths as a function of kinetic energy.** This is the so-called universal curve, since most materials tend to follow this behavior. The universal curve has strong ramifications for EUV PES because it indicates that electrons that are excited by EUV light have short escape depths, making EUV PES a surface sensitive technique. Figure from [80].

bining PES techniques with HHG-based light sources. This is because electron mean free paths are energy dependent (Fig. 1.7), and it just so happens that the photon energies associated with EUV light (∼10 – 100 eV) tend to produce electrons with very short mean free paths (∼1 nm) [78, 80, 81]. This means that EUV photoemission tends to be very surface sensitive because electrons that are excited deep inside the material simply cannot make it to the surface without scattering. On the other hand, this also makes EUV photoemission a sensitive technique to probe electron scattering and the behavior of hot (i.e. highly excited) electrons in materials.

In Chapter 6 we use our flowing nanoparticle aerosol source to investigate the behavior of hot electrons in a series of unconventional materials, such as ionic crystals and liquid nanodroplets. These materials are generally inaccessible with traditional bulk PES systems because they are either difficult to get into the vacuum chamber (in the case of liquids)[6] or they suffer from charging issues (in the case of insulating materials). However, our flowing nanoparticle source mitigates these problems and enables us to conduct EUV photoemission investigations in a wide array of

[6] Excitingly, PES studies of liquid samples have recently become more accessible due to advances in the use of liquid microjets to introduce liquid samples into high-vacuum environments [82–85].

nanoparticle compositions.

1.2 Physical Principles of High-Harmonic Generation

In this section I will quickly introduce some of the basic and relevant physical principles of HHG in gases.[7] This is by no means intended to be a complete description of HHG but will hopefully provide a reasonable overview. I will first discuss the single-atom picture of HHG and the associated spectral and temporal characteristics of the emitted harmonics. Then, I will introduce macroscopic effects in HHG and the constraints they impose. Finally, I will describe some of the ideas behind polarization control in HHG.

Several more detailed reviews of the basics of HHG can be found in previous theses from the Kapteyn-Murnane group, including those of Tenio Popmintchev [91] and Ben Galloway [92], also the thesis of Tingting Fan for a complete discussion of circularly polarized HHG with collinear bichromatic drivers [93].

1.2.1 Single-Atom Picture

In HHG, lower-energy driving-laser photons are converted into higher-energy high-harmonic photons. To some extent, one can simply imagine adding photons together, so that N driving laser photons, each with energy $\hbar\omega$, combine to form one higher energy photon, with a corresponding energy of $N\hbar\omega$. This conversion is enabled by nonlinear interactions between an atom and a strong (and typically linearly polarized) laser field, which occur when the laser electric field becomes comparable to the internal electric field of the atom. A surprisingly large number of the important features of HHG are captured by describing these interactions through a simple three-step model [33, 34]:

(1) An electron is ionized by a strong laser field. In HHG this ionization occurs primarily via tunnel ionization, where the electric field of the laser suppresses the Coulomb field of

[7] It is also possible to produce HHG through interactions with solid targets, either relativistically [86, 87] or nonrelativistically [88–90]. However, in these cases HHG occurs through different mechanisms than in the gas phase situation that is relevant to this thesis. Therefore, only gas phase HHG will be discussed here.

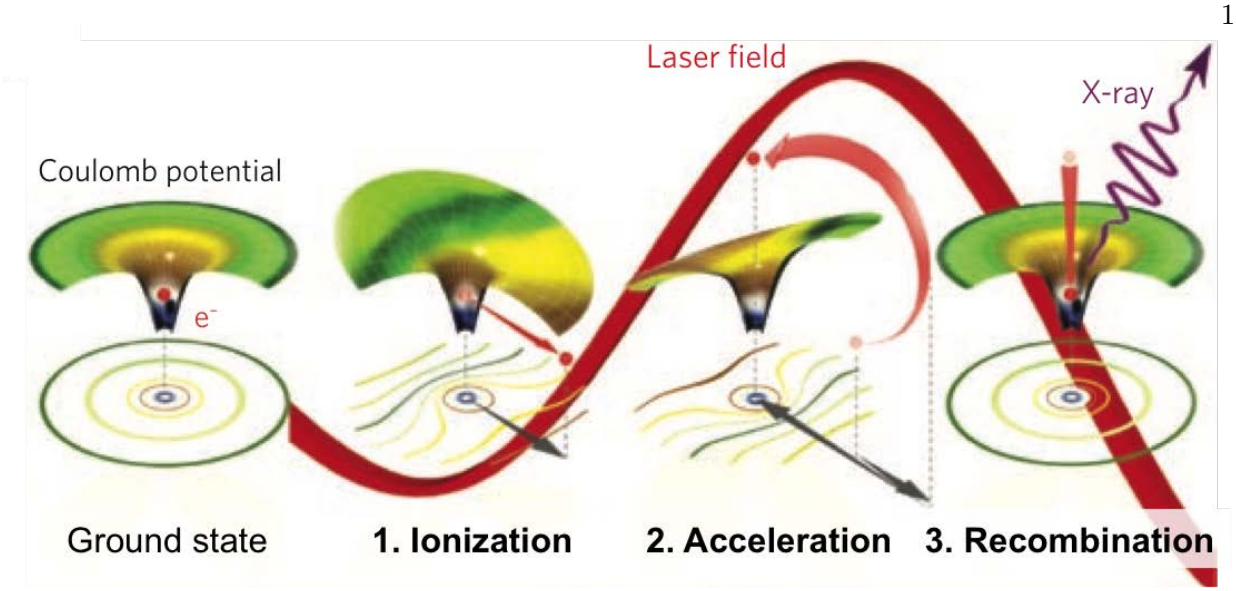

Figure 1.8: **The three-step model of HHG.** First an electron is ionized by a strong laser field. That electron is then accelerated by that strong laser field. Finally, the electron is driven back to its parent ion where it recombines and releases its excess energy as a high-energy photon. Adapted from [96].

the atom enough to allow a fraction of the electron wavefunction to tunnel out into the continuum [94, 95].

(2) The liberated electron is accelerated by the laser field and gains energy.

(3) The electron is then driven back towards the parent ion and recombines, releasing the energy gained from the laser field as a high-energy photon.

One feature that is well captured by the three-step model is the maximum photon energy produced through HHG (Fig. 1.9, bottom) and how that cutoff energy scales. The cutoff energy can be described by starting from basic kinematic equations of a free-electron oscillating in a laser field. Depending on when in the laser cycle the electron is "born," the electron will have some amount of kinetic energy when it re-encounters the ion (i.e. when it returns to the position that it started at). Considering all of the different possible "start-times" shows that the maximum kinetic energy that the electron can possibly have at recombination is $E_{kin} = 3.17U_p$, where U_p is the ponderomotive energy (i.e. the cycle-averaged "wiggle" energy) of the electron oscillating in the laser field. The

ponderomotive energy is given by $U_p = (q_e^2 E^2)/(4 m_e w_1^2)$, where q_e is the electron charge, E is the electric field strength of the laser, m_e is the mass of the electron, and w_1 is the driving laser frequency. Therefore, the maximum photon energy that can be produced is this maximum electron kinetic energy plus the ionization potential of the atom. The ionization potential (IP) contributes because upon recombination the electron goes from being a free electron in the continuum to being bound in the atom and therefore that binding energy also goes into the final photon energy. Putting the ponderomotive energy into more experimentally relevant parameters we find that

$$E_{cutoff} = 3.17 U_p + IP \approx I \lambda_1^2, \tag{1.1}$$

where I is the driving laser intensity and λ_1 is the driving laser wavelength. Therefore, extending the cutoff to higher photon energies requires scaling the driving laser to either higher intensities or longer wavelengths.

The spectral and temporal structure of HHG can also be understood through this model. In the time domain, harmonics are emitted every time the oscillating driving-laser electric field is sufficiently strong to suppress the Coulomb field of the atom and initiate the processes in the three-step model. This means that a burst of harmonics are emitted every half cycle of the driving laser (Fig. 1.9, top), thereby producing a train of harmonic pulses that are separated in time by half the laser period (1.3 fs for 800 nm driving fields). These harmonic pulse trains are often called "attosecond pulse trains" since the individual pulses within the train have sub-femtosecond pulse durations. This temporal structure also gives us insight into the spectral structure produced through HHG, because time and frequency are conjugate variables and therefore related by a Fourier transform. Interestingly, a train of periodic pulses in the time domain also corresponds to a train of periodic peaks in the frequency domain (Fig. 1.9, bottom). Since the high-harmonic pulses are separated by half the driving laser optical period in time the resulting spectral peaks are separated by twice the driving laser photon energy. Therefore, HHG produces a spectral comb of high-harmonic orders.[8]

[8] The astute reader may notice the similarity to optical frequency combs [97, 98].

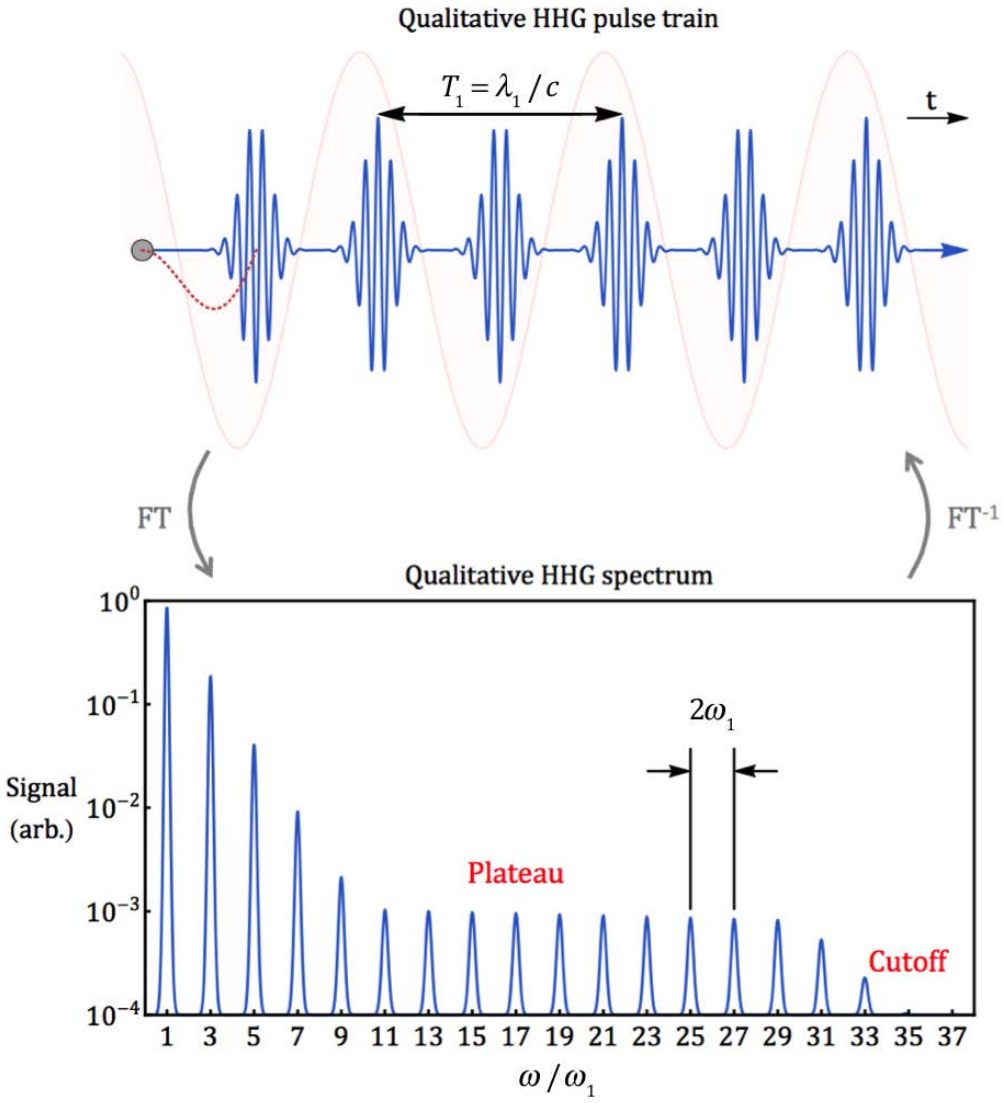

Figure 1.9: **Temporal and spectral structure of HHG.** A burst of high harmonics is emitted every half cycle of the driving laser field in the time domain. Adjacent bursts have a π phase shift due to the oscillating sign of the driving laser field. The Fourier transform of this temporal structure reveals the spectral structure of HHG – harmonics are found at odd integer multiples of the driving laser photon energy resulting in a high-harmonic comb with a spacing of $2\omega_1$. This harmonic comb extends up to the cutoff photon energy. Figure from [92].

Technically, all that we have discovered so far is that the harmonic peaks are separated by twice the driving laser photon energy in the frequency domain. We have not yet established that these peaks are located at *integer multiples* of the driving laser frequency (i.e. we know the separation of the comb teeth but not their absolute position). The simplest way to establish the

absolute position of the harmonic comb is to recognize that $N = 1$ has to be a comb tooth, because physically the case where driving laser photons go in, nothing happens, and driving laser photons come out has be allowed. Therefore, the high harmonics appear at odd integer multiples of the driving laser photon energy. More rigorously, the Fourier relationship between time and frequency also allows us to determine the position of the harmonic comb teeth. To do so, we must note that there is a π phase shift between adjacent attosecond pulses in the time domain. This π phase shift arises because the driving laser has an opposite sign during adjacent half cycles. It is this π phase shift that restricts the harmonics to odd integer multiples of the driving laser photon energy in frequency space.

Additionally, we can squeeze a little bit more physics out of this model if we push on the idea that the comb-like structure of harmonics in the frequency domain is a direct consequence of the attosecond pulse train in the time domain. On the one hand, this means that using longer pulse driving lasers, so that there are more pulses in the attosecond pulse train, gives spectrally narrower harmonics. On the other hand, this means that if you no longer have an attosecond pulse train, and instead have just one isolated attosecond pulse, you consequently no longer have well-resolved harmonic orders in the frequency domain. Indeed, the transition from a high-harmonic comb to a harmonic supercontinuum is the first and most experimentally accessible indication that isolated attosecond pulses are being produced [14, 22, 39, 99–101].

Finally, the remaining important single-atom feature of HHG that I will discuss here requires that we consider the quantum nature of the electron [35]. This feature is the so-called wave packet spreading that occurs during the acceleration/propagation step. Since the electron is a quantum mechanical particle it is described by a wave packet, which spreads out as a function of time (i.e. the electron becomes more delocalized the more time it spends not bound to the atom). This spreading is more pronounced for longer wavelength driving lasers because the time that the electron spends in the continuum depends on the period of the driving laser. The increased wave packet spreading for longer wavelength driving lasers means that there is less electron density at the position of the ion when the electron returns and therefore there is a decreased probability to recombine. This

means that the single-atom yield decreases as the driving laser wavelength increases. Inversely, driving the HHG process with shorter wavelength drivers tends to increase the achievable harmonic flux.[9]

1.2.2 Macroscopic Effects

While the single-atom physics of HHG captures many of the experimentally observed features, there are also macroscopic effects that must be considered. Macroscopic effects are relevant because bright HHG emission requires more than just a single atom. Indeed, producing bright HHG beams requires the emission from many atoms to add together constructively [5, 36, 37, 91, 102–105]. Therefore, the harmonics that are emitted at one spatial location must add in phase with harmonics that are emitted at some later spatial location (Fig. 1.10). This is accomplished by ensuring that the phase velocity of the driving laser matches that of the emitted high harmonics, so that they do not walk off of each other and begin to destructively interfere.

A convenient way to represent the differences in the phase velocities of the driving laser and high harmonics is through a wave vector mismatch: $\Delta k = qk_1 - k_q$, where q is the harmonic order, k_1 is the driving laser wave vector, and k_q is the wave vector of the harmonics.[10] Ideally, we would like this phase mismatch to be zero for optimal HHG emission. When simply considering the vacuum wave vectors ($k_{vac} = 2\pi/\lambda$), this condition is automatically satisfied. However, in a real experiment there are two main factors that effect the relative phase velocities of the driving laser and the emitted harmonics – the index of refraction of the HHG medium and the specific experimental geometry chosen. Practically speaking, the HHG geometry is often fixed by other considerations so that, in the lab, the index of refraction of the generating medium is tuned to compensate those geometric contributions to achieve phase matching. Each of these contributing

[9] This decrease in the single-atom yield is offset somewhat by the fact that longer wavelength driving lasers require increased phase-matching pressures. However, even with an increase in the number of emitters contributing to the HHG process, HHG sources with longer wavelength driving lasers tend to be quite a bit dimmer than those with shorter wavelength driving lasers. Therefore, there is often a trade off between higher harmonic flux (optimized with shorter wavelength driving lasers) and higher photon energies (optimized with longer wavelength driving lasers).

[10] This condition ensures that the phase velocities are the same because $v_p = \omega/k$ (where v_p is the phase velocity) and $\omega_q = q\omega_1$.

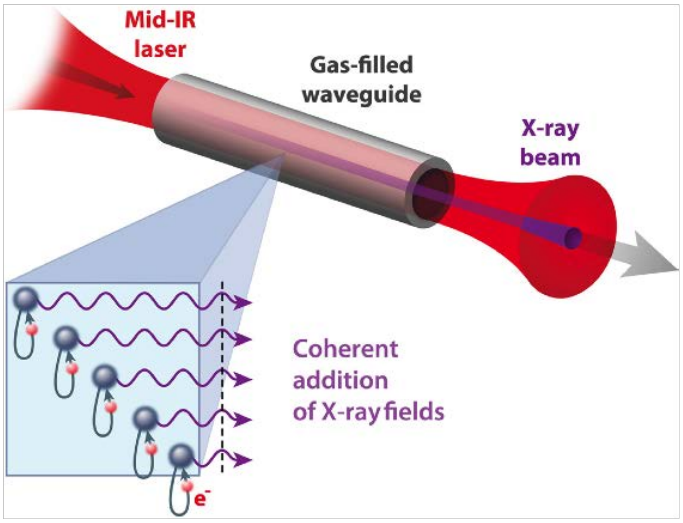

Figure 1.10: **Producing bright HHG beams requires phase matching the HHG process.** Phase matching is achieved by ensuring that the phase velocity of the driving laser is the same as the phase velocity of the emitted high harmonics. If the phase velocities are matched then harmonics that are emitted at one spatial location add consutructively with harmonics that are emitted farther down the line. Figure from [104]

effects can be considered individually, so that $k = k_{vac} + k_{medium} + k_{geom} + ...$

The generating medium plays a large role in phase matching because it significantly affects the phase velocity of the driving laser. However, to a good approximation, the index of refraction at the high-harmonic wavelengths is one, so that the harmonics themselves are essentially unaffected, which leads to a phase mismatch. The driving laser wave vector is adjusted by the generating medium in two opposing ways. First, the phase velocity is *decreased* by the neutral atoms in the gas. However, the phase velocity is also *increased* due to the presence of free electrons, some amount of which are inevitably generated because HHG requires a strong laser field. Mathematically, these two effects are given by

$$\begin{aligned} k_{1,\,neutral} &= \frac{2\pi}{\lambda_1}(n-1)(1-\eta)P \\ k_{1,\,plasma} &= -r_e N_{atm} \lambda_1 \eta P, \end{aligned} \tag{1.2}$$

where n is the index of refraction of the gas at the driving laser wavelength, η is the ionization fraction, P is the pressure in atmospheres, r_e is the classical electron radius, and N_{atm} is the number

density of atoms in an atmosphere of gas at standard temperature and pressure. For a given gas and driving laser wavelength, the tunable parameters here are the pressure and the ionization fraction. The neutral and plasma terms have opposite signs, their relative contributions are determined by the ionization fraction, and the magnitude of the net effect scales linearly with pressure.

An important ramification of phase matching can already be seen here if you consider the case of very high ionization fractions. If the ionization fraction is large enough that the plasma term is greater than the neutral term then the net effect of the index of refraction of the generating medium is to decrease the driving laser wave vector. This increases the phase velocity of the driving laser to greater than the speed of light, which is greater than the phase velocity achievable by the high harmonics. Therefore, at high enough ionization fractions phase matching cannot occur.[11] The ionization fraction at which this happens is known as critical ionization [5, 36]. The critical ionization level sets a de facto upper limit on the intensities that can be used to drive the HHG process since higher intensities lead to more ionization. Therefore, if we recall the scaling of the cutoff photon energies in Eq. 1.1, we unfortunately cannot scale the photon energies indefinitely by simply increasing the intensity. Practically speaking, for a given driving laser wavelength, there is a maximum intensity allowed to remain under the critical ionization level, which results in a phase-matched cutoff energy (Fig. 1.11). Therefore, scaling HHG to higher photon energies requires developing longer wavelength driving lasers. The actual value of the critical ionization level is given by

$$\eta_c = \frac{1}{1 - \frac{r_e N_{atm} \lambda_1^2}{2\pi(n-1)}}, \tag{1.3}$$

which can be found by setting $k_{1,plasma} = k_{1,neutral}$ and solving for η. Plugging some numbers in we find that $\eta_c \approx 0.5\%$ for 800 nm driving lasers using helium as the HHG medium. The critical ionization level decreases for increasing driving laser wavelengths, which means that the phase

[11] Technically, we haven't said anything about the geometric contributions to the phase mismatch yet. However, generally the geometric terms serve to speed up the phase velocity of the driving laser, so that the neutral atoms need to "win" slightly and slow the phase velocity of the driving laser back down to achieve phase matching. Therefore, the discussion of critical ionization in this paragraph is completely valid. Interestingly, if there was a way to speed of the phase velocity of the harmonics with respect to the driving laser, then ionization levels above critical ionization would be allowed (necessary even!), as is discussed in Chapter 3.

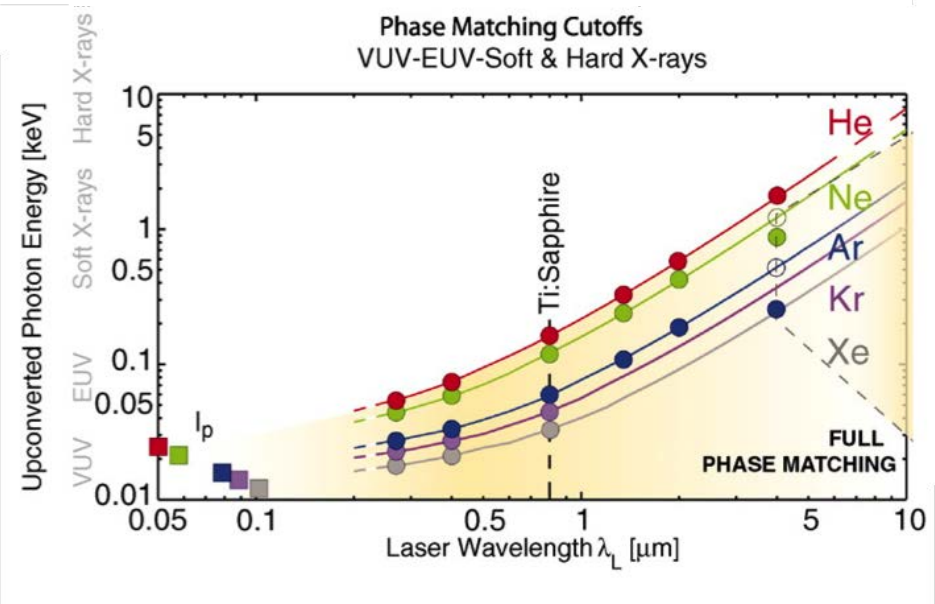

Figure 1.11: **Phase matching cutoff for HHG.** For a given driving laser wavelength, there is a maximum intensity that can be used to efficiently drive the HHG process and therefore a maximum photon energy that can be achieved. This intensity is limited by the critical ionization level. Figure from [14].

matched cutoff energy scales slightly more slowly than the λ_1^2 found in Eq. 1.1.

The remaining contributions to phase matching in HHG are the so-called geometric terms. How exactly these effects come into play depends on the precise focusing geometry employed. For example, in a free-focusing geometry such as a gas jet, the relevant contributions are from the Gouy phase and atomic dipole terms. Alternatively, for HHG in a gas-filled capillary those terms don't matter and instead there is a waveguide term that must be considered.[12] In general, these geometric effects consist of phase shifts in the light field as a function of position along the direction of propagation, which will affect the relative phase of harmonics emitted at one spatial location versus another.

In a free-focusing geometry there is a phase shift in the driving laser field as a function of position through the focus known as the Gouy phase [107, 108]. This Gouy phase shift typically

[12] I found the thesis of Tenio Popmintchev [91] and Ba Khuong Dinh [106] helpful for understanding these different situations.

only affects the wave vector of the driving laser and is given by

$$k_{Gouy} = \frac{d\Phi_{Gouy}}{dz} = \frac{-1}{z_r + z^2/z_r}, \tag{1.4}$$

where z is the position through the focus (the focus is at $z = 0$) and z_r is the Rayleigh length. The Rayleigh length is the distance over which the laser is reasonably tightly focused and is given by $z_r = 4\lambda_1/\pi(F/D)^2$ where F is the focal length and D is the diameter of the initial collimated beam. Note that the phase mismatch induced by the Gouy phase is always negative. Additionally, there is a phase shift due to the propagation or acceleration step in the three-step model. This is an intensity dependent phase that the electron picks up while traveling in the continuum before recombining to emit a harmonic photon [35], as such it is a phase that applies to the harmonics and not the driving laser. This effect is included through the atomic dipole term:

$$k_{AD} = \boldsymbol{\nabla}\alpha_q I(z) = \frac{8z\alpha_q I_0}{z_r^2(1 + (2z/z_r)^2)^2}, \tag{1.5}$$

where α_q is a parameter that depends on the trajectory of the electron and I is the intensity of the driving laser (I_0 is the intensity at the focus). Unlike the Gouy phase term, which is always negative, the sign of this atomic dipole term switches as a function of position on either side of the focus.

Alternatively, in the gas-filled capillary or waveguide geometry, there is no focus so there is no Gouy phase shift. Additionally, the intensity is approximately constant as a function of propagation direction along the waveguide, so there is also no atomic dipole term. However, there is dispersion due to the waveguide, which speeds up the phase velocity of guided modes, i.e. of the driving laser. The waveguide term is given by

$$k_{WG} = -\frac{u^2\lambda_1}{4\pi a^2}, \tag{1.6}$$

where u is a constant that depends on the waveguide mode the light is coupled in to [102, 109] and a is the radius of the waveguide. Note that, just like the Gouy phase term, the waveguide term is always negative and therefore acts in the same way as plasma.

This was just a brief introduction to phase matching in HHG, which primarily discusses the concepts that are relevant to the rest of this thesis. There are of course additional effects that were

not discussed here, for example the possibility of a nonlinear index of refraction [91] or the presence of charged ions in the generating medium [110].

The final macroscopic effect that is relevant for HHG is absorption [37]. Sadly, the gaseous medium that is necessary to do HHG can also absorb your harmonic photons. The main ramification of absorption is that it decreases the flux that you can produce. However, a side effect of the presence of absorption is to relax the phase matching conditions so there's often no need to actually achieve perfect phase matching (i.e. $\Delta k = 0$). If there is a small, but non-zero, phase mismatch then there is some length over which the HHG process can be considered effectively phase matched, because it takes some amount of propagation distance for the harmonic and driving laser fields to walk off of each other and begin to destructively interfere. This distance is known as the coherence length, $L_{coh} = \pi/\Delta k$. Once the coherence length is sufficiently longer than the absorption length (L_{abs}),[13] you actually don't gain much by phase matching "better." For example, a coherence length that's only ten times longer than the absorption length already gets you about 75% of the flux that a coherence length of infinity achieves (Fig. 1.12). This is because a steady state is reached, where any new harmonic photons that are created are just replacing old harmonic photons that got absorbed. This situation is known as being absorption limited. The other relevant distance is the medium length over which HHG is occurring (L_{med}), the requirements for which are also relaxed due to the presence of absorption. A good general guideline is to shoot for $L_{med} > 3L_{abs}$ and $L_{coh} > 5L_{abs}$ (Fig. 1.12) [37].

1.2.3 Polarization Control

While we now have a fairly well developed understanding of how to optimize linearly polarized HHG, the production of bright circularly polarized HHG beams is a more recent development that is still being explored. The main difficulty with circularly polarized HHG is that it cannot be done with a single driving laser. This limitation can be understood in the context of the three-step

[13] The absorption length is the length appearing in the Beer's Law absorption expression, or the distance by which the flux drops by a factor of e.

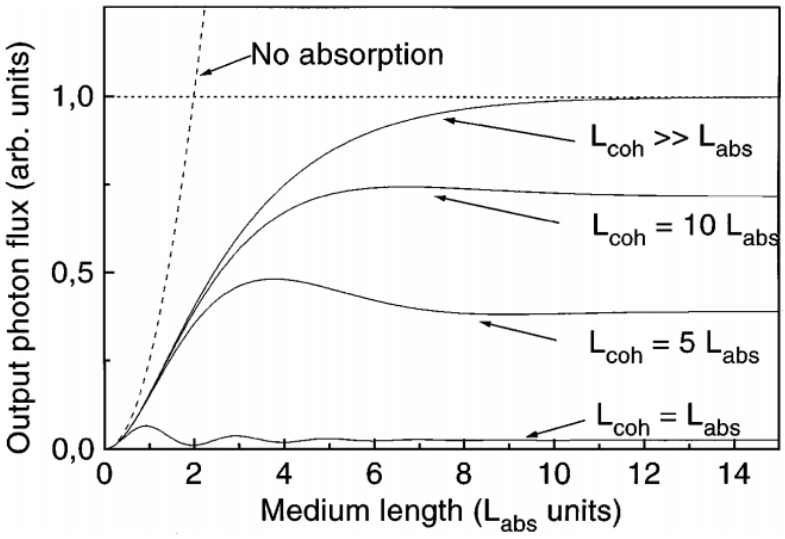

Figure 1.12: **Harmonic flux as a function of medium length for different coherence lengths.** Absorption limits the harmonic flux achievable. Figure from [37].

model of HHG – if the driving laser is circularly, or even elliptically, polarized then the electron gets driven transversely away from the ion and never recombines to emit harmonic photons. Therefore, the HHG flux drops dramatically as any degree of ellipticity is introduced into the driving laser [40].[14] This strong ellipticity dependence of the high-harmonic flux is well known, and is even the basis for the popular "polarization gating" technique to produce shorter HHG pulses [18, 21, 111]. However, this limitation can be overcome by combining several driving laser fields to gain more control over the HHG process. This idea was first explored about 20 years go in a series of theory papers [112–114] and was even experimentally investigated [115]. However, for some reason, this idea failed to gain traction until it was re-discovered in 2014 [42, 43].

The first iteration of circularly polarized HHG was to drive the HHG process with a bichromatic field consisting of a fundamental laser field mixed with its second harmonic, which were counter rotating with respect to one another.[15] For example, an 800 nm beam (ω_1) with right-

[14] It is possible to drive HHG with elliptically polarized driving lasers in atomic or molecular contexts where a resonance can be exploited to allow efficient recombination despite the elliptical polarization of the driver [46]. This technique does produce harmonics with reasonable degrees of ellipticity but is only marginally tunable (since it's energetically tied to a resonance). Excitingly, this technique has been successfully applied to measure photoelectron circular dichroism and is therefore very promising in the right situations.

[15] There has been one subsequent study that produces elliptically polarized harmonics by combining two orthogo-

circular polarization (RCP) combined collinearly with a 400 nm beam (ω_2) with left-circular polarization (LCP). In the photon picture of HHG, there are now two baths of photons to choose from when building a high-harmonic photon. Additionally, when building this high-harmonic photon, energy and spin angular momentum must be conserved. The conservation of spin angular momentum is very restrictive because photons are only allowed to have a spin of ± 1.[16] Therefore, $n_{LCP} = n_{RCP} \pm 1$, where n_{LCP} is the number of LCP photons and n_{RCP} is the number of RCP photons. Since one of the beams consists of purely RCP photons and the other beam is purely LCP photons, conservation of spin restricts the relative number of photons of each color that can contribute, so that $n_1 = n_2 \pm 1$. Therefore, the energy of the final high-harmonic photon is proportional to

$$\begin{aligned} \omega_q &= n_1\omega_1 + n_2\omega_2 \\ &= (n_2 \pm 1)\omega_1 + n_2\omega_2 \\ &= n_2(\omega_1 + \omega_2) \pm \omega_1. \end{aligned} \tag{1.7}$$

So far, this expression is a completely general treatment of HHG with counter-rotating drivers, but we can now restrict it to the previously mentioned example of 800 nm (ω_1) and 400 nm (ω_2) driving fields. In that case, $\omega_2 = 2\omega_1$ so that

$$\omega_q = (3m \pm 1)\omega_1, \tag{1.8}$$

where n_2 has been replaced with m for consistency with the literature. For every integer value of m there are two allowed photon combinations. Here, the $3m+1$ harmonics are circularly polarized with the same handedness as the 800 nm driver (because they include an "extra" 800 nm photon, Fig. 1.13, a). Conversely, the $3m-1$ harmonics are circularly polarized with the same handedness as the 400 nm driver. The $3m$ harmonics are forbidden because there is no way to construct them

nally *linearly* polarized driving laser fields [44]. Interestingly, this approach may provide for a simpler experimental set-up than the counter-rotating driving laser fields discussed here. However, to date, this linear case has not yet been developed as much as the counter-rotating case.

[16] Note that this is another argument for why a single circularly polarized laser field cannot drive the HHG process because the resulting photons would have very large values for their spin angular momentum, which is not allowed.

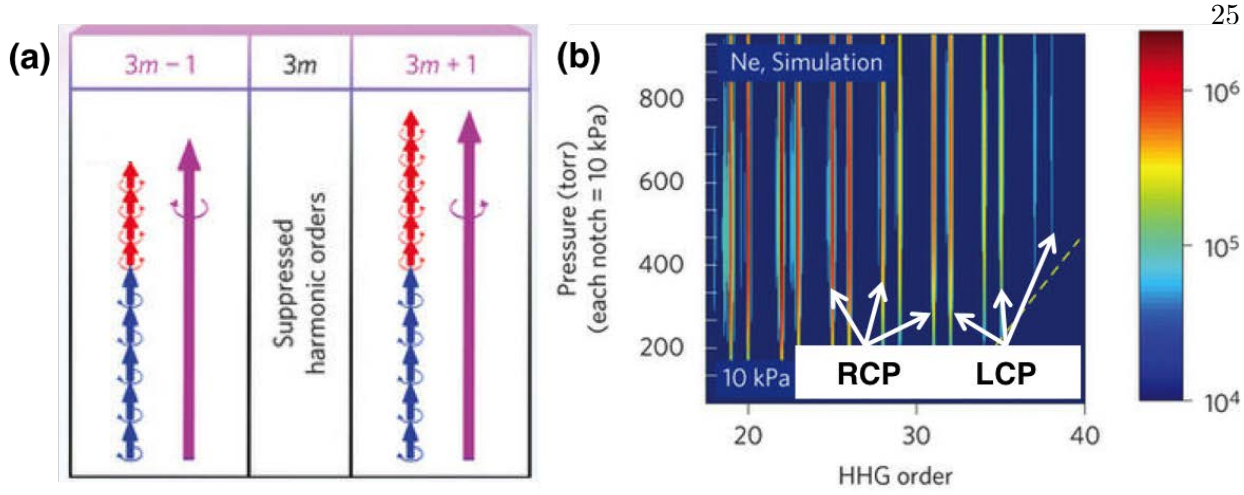

Figure 1.13: **Circularly polarized HHG with counter-rotating bichromatic driving lasers.** (a) Harmonic photons can be constructed out of combinations of red (800 nm) and blue (400 nm) driving laser photons that conserve spin angular momentum. (b) These constraints result in a harmonic spectrum characterized by a series of harmonic pairs, which are separated by a spin-forbidden harmonic order that is suppressed. The harmonic pairs consist of one RCP and one LCP harmonic order. Figure adapted from [43].

while conserving spin angular momentum. Therefore, the resulting spectra consist of a series of pairs of high harmonics (Fig. 1.13, b), where one harmonic in the doublet is RCP and the other is LCP. The harmonic pairs are separated by the suppressed or forbidden harmonic orders.

This process of circularly polarized HHG with counter-rotating bichromatic drivers can also be understood in the time domain by considering the electric fields involved. The combined electric field resulting from counter-rotating 800 nm and 400 nm fields looks like a trefoil (Fig. 1.14a). This trefoil has three-fold symmetry and, if you turn your head and squint, each of the three lobes sort of looks like a linearly polarized field. While turning your head and squinting is by no means rigorous, it turns out that indeed electrons can be ionized, accelerated, and successfully recombined three times per 800 nm optical cycle in this combined field. When the intensities of the 800 nm and 400 nm fields are equal (giving the trefoil shape in Fig. 1.14a), this results in the production of three *linearly polarized* high-harmonic bursts. However, each of these linear bursts rotates by 120°, leading to a high-harmonic pulse train with a net chirality (Fig. 1.14b). This highlights one of the limitations of this method of producing circularly polarized HHG – the circularity is a net

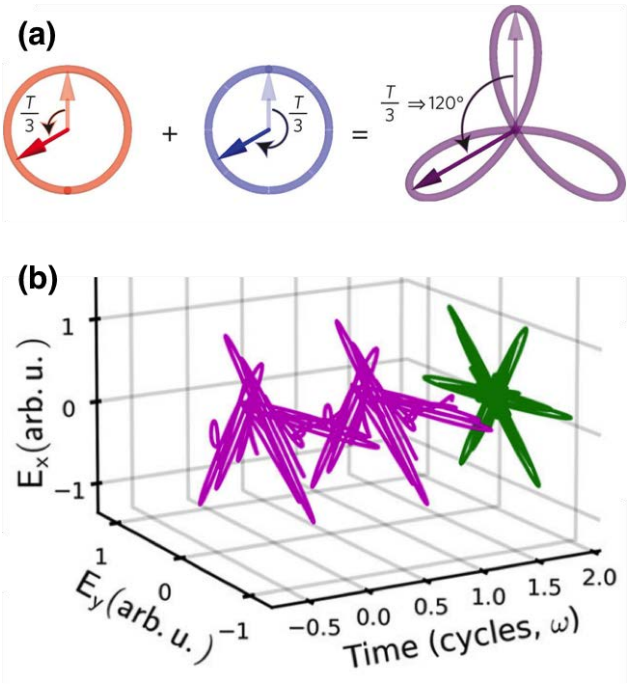

Figure 1.14: **Time domain picture of circularly polarized HHG.** (a) The field resulting from the combination of 800 nm and 400 nm counter-rotating drivers has three-fold symmetry. Harmonics are created once per lobe of the combined trefoil field. Figure from [43]. (b) This leads to the emission of a set of three linearly polarized bursts of high harmonics, where each burst is rotated by 120° leading to a net chirality along the pulse train. Figure from [47].

effect requiring the contribution of several high-harmonic bursts. Therefore, if a single attosecond pulse is isolated it will be linearly polarized and all of the chiral properties will have been lost. This effect therefore limits the pulse durations attainable with this method. Interestingly, it has been shown that adjusting the ratios of the 800 nm and 400 nm driving lasers introduces ellipticity into the individual harmonic bursts, which is a promising technique to produce elliptically polarized isolated attosecond pulses [47].

Additionally, circularly polarized HHG with counter-rotating bichromatic drivers is not limited to 800 nm and 400 nm lasers or even limited to cases where the two fields are commensurate (i.e. harmonics of one another). To date, this method has also been demonstrated with both 800 nm + 1.3 μm fields and 800 nm + 2 μm fields [45]. Returning to the general case of counter-rotating bichromatic mixing (Eq. 1.7) one finds that the general two color counter-rotating HHG spectrum

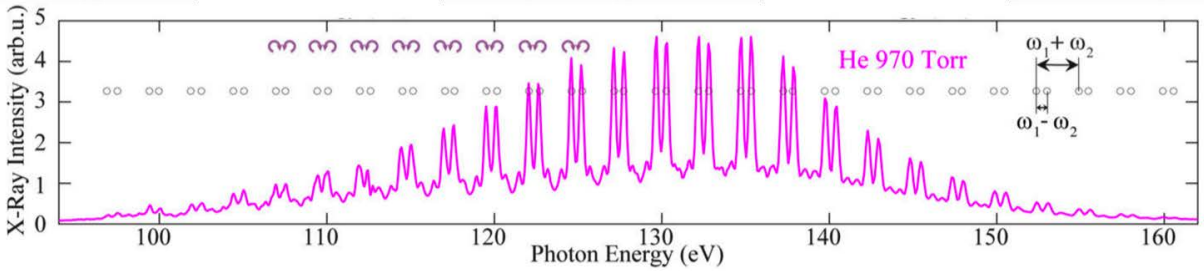

Figure 1.15: **Circularly polarized HHG spectrum generated with counter-rotating 800 nm + 1.3 μm driving laser fields.** The spectrum is characterized by pairs of harmonics, where one peak in the doublet is RCP and the other is LCP. Within a given doublet, the harmonics are separated by $\omega_1 - \omega_2$ and adjacent pairs of peaks are separated by $\omega_1 + \omega_2$. Figure from [45].

consists of pairs of harmonics, where the spectral separation of the harmonics within a doublet is $\omega_1 - \omega_2$ and the spectral separation between adjacent doublets is $\omega_1 + \omega_2$ (Fig. 1.15). As in the 800 nm + 400 nm case, within each doublet, one of the harmonic peaks is RCP and the other is LCP. This presents problems for scaling this method to mid-infrared driving lasers to achieve higher photon energies. These problems arise because if the photon energies of the two driving lasers become too close together then a separation of only $\omega_1 - \omega_2$ can result in significant overlap of the two peaks within the doublet, thereby decreasing the circularity. Unfortunately, it has been shown that circularly polarized HHG with 1.3 μm + 2 μm driving fields produces doublets that are only barely discernible as separate RCP and LCP peaks [93]. As of the time of this writing, this is still an unsolved problem that hinders the scaling of this circularly polarized HHG technique to higher photon energies.

Finally, it is instructive to quickly consider the case where $\omega_1 = \omega_2$. This situation corresponds to combining an RCP and LCP beam of the same color, which simply results in a linearly polarized driving-laser field. Following the rules from Eq. 1.7 gives "doublets" that are separated by $\omega_1 + \omega_1 = 2\omega_1$. However, the separation of the two peaks within this "doublet" is $\omega_1 - \omega_1 = 0$. Therefore, the RCP and LCP peaks overlap in energy, resulting in linearly polarized harmonics separated by twice the photon energy, just as we expect for linearly polarized HHG. This highlights that in the collinear combination of counter-rotating bichromatic driving lasers discussed so far,

the circularly polarized harmonics are separated *spectrally*. Interestingly, if we can find some other way to separate the harmonics with different helicities then we can do circularly polarized HHG with a single wavelength driving laser. For example, in Chapter 3 we separate the helicities of the high harmonics *spatially*, which enables single-color HHG and facilitates scaling circularly polarized HHG to long wavelength driving lasers without sacrificing circularity.

Chapter 2

Apparatus and Methods

2.1 Introduction

This chapter details the main experimental apparatuses used in this thesis. Different subsets of this equipment was used in the various experiments, however everything discussed here was integral in some way at some point in time. I either led or was heavily involved in the construction and implementation of all of the equipment discussed here, except for the laser system, which is commercially available from KM Labs, and the velocity-map-imaging spectrometer, which was built before I joined the group.

2.2 Ti:Sapphire Laser System

The common technology between every experiment presented here is the Ti:Sapphire laser system, which consists of an oscillator and a regenerative amplifier (Wyvern HE, KM Labs). The laser operates at a central wavelength of ∼790 nm, a repetition rate of 1 kHz, a pulse duration of ∼45 fs, and a pulse energy of ∼9 mJ. Remarkably, it works nearly every day with only a small amount of maintenance or down time. However, when we did have laser problems we were very thankful for the assistance of Mike Walls, Daisy Raymondson, Amelie Auger, and Xiaoshi Zhang from KMLabs, Inc.

Ti:Sapphire is an exceedingly common laser in the ultrafast and strong-field communities, because of it's large gain bandwidth and high damage threshold [116, 117]. The system begins with

a Kerr-lens modelocked [118] Ti:Sapphire oscillator,[1] which outputs ∼10 fs pulses at a repetition rate of ∼80 MHz and an average power of ∼500 mW. This corresponds to pulse energies of ∼nJ's per pulse. Unfortunately, these pulse energies are not quite high enough to drive the HHG process, which requires that the electric field strength of the laser be comparable to the Coulomb field binding electrons and nuclei together. Focusing the oscillator to diffraction limited spot sizes gives intensities of $\sim 10^{13}$ W/cm^2 or electric field strengths of $\sim 10^8$ V/cm. However, the field strength between an electron and a proton separated by one Bohr radius (0.5 Å) is $\sim 5 \times 10^9$ V/cm. Since we can't focus any tighter than the diffraction limit, we must therefore increase the pulse energy to reach the required field strengths for HHG.[2] This is the purpose of the amplifier portion of the laser system.

In the amplification step, the nJ pulses from the oscillator are boosted by many orders of magnitude to reach mJ level pulse energies. While the average power does increase by about a factor of 20,[3] most of the approximately six order of magnitude gain in pulse energy comes from dramatically dropping the repetition rate,[4] in essence squeezing a similar amount of average power into fewer pulses. To complicate matters a little more, this amplification cannot be done with femtosecond pulses because the peak powers attained while amplifying are above the damage threshold of the Ti:Sapphire gain medium and other optical components in the amplifier. Therefore, the scheme of chirped-pulse amplification [119] must be used (Fig. 2.1). Here, the pulses are first stretched out in time to be 100s of ps long so that they can be amplified safely. Once the pulses are amplified they are then recompressed to close to their original pulse duration.

Walking through the amplifier (Fig. 2.1), the pulses from the oscillator first encounter the stretcher, where they are chirped-out for amplification. Next a Pockels cell is used to pick out one out of every ∼80000 pulses to be amplified, throwing the rest away. The surviving pulses are let

[1] The oscillator is itself a laser. We typically refer to the entire system as "the laser" and distinguish the constituent parts as the oscillator and the amplifier, which are in themselves both lasers.

[2] There are additional constraints on how tightly lasers can be focused and still efficiently drive the HHG process. These constraints are imposed by macroscopic effects and result in very inefficient HHG if the driving laser is focused to the diffraction limit. Therefore, the driving pulse energies must be increased even more to compensate for the larger focal spot sizes needed.

[3] approximately 0.5 W out of the oscillator vs about 10 W out of the amplifier

[4] 80 MHz out of the oscillator vs 1 kHz out of the amplifier

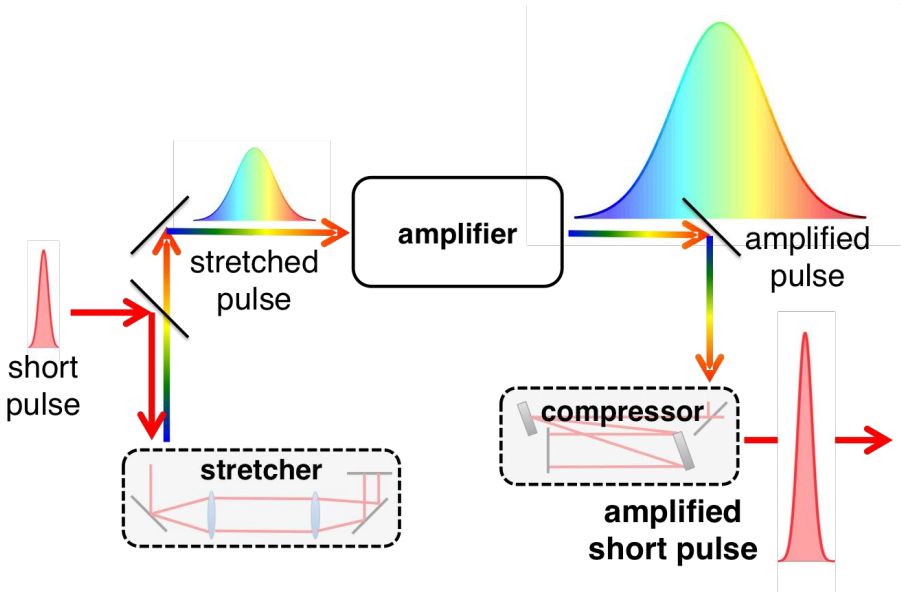

Figure 2.1: **Schematic of a Ti:Sapphire amplifier,** which uses chirped pulse amplification to amplify nJ level pulses to the mJ level. Adapted from [117].

into the amplifier cavity by a second Pockels cell and trapped there for ∼10 round trips. The cavity houses the Ti:Sapphire gain medium, so it is at this time that the pulses are amplified from nJ's to mJ's. After the cavity, the now amplified pulses pass through the compressor, which collapses them back down in time to ∼45 fs. The pulses exiting the amplifier have slightly longer pulse duration than the original pulses from the oscillator because there is gain-narrowing of the spectrum during amplification [117], resulting in longer minimum achievable pulse durations. More details about this laser system can be found in Ding et al. [120] or the thesis of Chengyuan Ding [121].

The gain bandwidth of Ti:Sapphire is centered at 800 nm [116] and therefore that is where most Ti:Sapphire laser systems tend to operate. While it is possible to make Ti:Sapphire oscillators that are somewhat tunable across the broad gain bandwidth (700 nm – 1000 nm), amplifiers are much more difficult to tune. However, oftentimes we would like to use other wavelengths in our experiments. For example, to resonantly pump a specific transition in some system or to control the energies of the harmonics that are produced through HHG. Fortunately, we can use nonlinear optics to transform the 800 nm Ti:Sapphire light into different wavelengths across most of the visible and near-infrared regions of the spectrum. In the experiments presented in this thesis, both the

second and third harmonic of the fundamental Ti:Sapphire light was used. The second harmonic (400 nm) was produced by frequency doubling the fundamental in a β-BBO crystal (200 μm thick, $\theta = 29.2$, $\phi = 90$). The third harmonic (267 nm) was produced through nonlinear mixing (sum frequency generation) of the fundamental and second harmonic, again in a BBO crystal (50 μm thick, $\theta = 44.3$, $\phi = 90$).

2.3 High-Harmonic Beamlines

Many of the experiments presented in this thesis employ HHG in some way, thereby involving EUV and soft x-ray light. There are a number of challenges associated with working in this region of the spectrum, including that these photons cannot propagate any appreciable distance through air and that optics tend to be expensive and lossy. Since typical absorption lengths of EUV light are $\sim$100 μm at atmosphere,[5] much of these experiments must be done in vacuum. The driving laser is therefore coupled into a vacuum chamber and focused down into a gaseous medium (be it a gas-filled capillary, a gas jet, or a semi-infinite gas cell) to drive the HHG process. Then that gas has to be pumped away as soon as possible so that it doesn't absorb too many of the harmonic photons that were just painstakingly created. The harmonics then continue to propagate in vacuum to the rest of the experiment. Two distinct gas-delivery geometries were employed in this thesis – Chapters 3 and 4 were done in a gas jet and Chapter 6 used a gas-filled capillary. These two different geometries employ slightly different beamlines, which are both described in the remainder of this section.

The gas-jet beamline was somewhat of a test bed for exploring novel HHG geometries, which were not immediately compatible with the gas-filled capillary design that is typically employed in the Kapteyn-Murnane group. Therefore, this beamline was designed to have a small footprint and be easily reconfigurable.[6] The beamline consisted of a single vacuum chamber, which contained the gas jet, a grating (Hitachi 001-0266), and an x-ray CCD camera (Andor, D0420-BN). The gas jet

[5] Note that this is somewhat advantageous in that we don't have to worry about any sort of radiation shielding, even though we are working with ionizing radiation.

[6] We affectionately called it "mini-beamline."

consists of a hollow capillary (∼100 μm inner diameter) glued into a Swagelok cap, which we back with typically 10 – 200 psig of noble gas. The grating used in these experiments was curved in one dimension, so that it formed a well resolved spectrum of the harmonics in one direction (thereby trading spatial information for energy information) but left the angular properties of the harmonics unchanged in the orthogonal direction. The fact that this grating maintains angular information in one dimension was important for Chapters 3 and 4 because we were interested in the variation of the emitted harmonics as a function of divergence angle. The grating was designed to be used at an incidence angle of 3° with associated image and object distances of 23 mm. However, small adjustments of the angle of the grating could compensate for slightly different distances necessitated by the experimental set-up. In practice, the grating angle is adjusted while looking at the harmonics to achieve the best spectral focusing.

The gas-filled capillary beamline (Fig. 2.2, used in Chapter 6) was slightly more complicated than the gas-jet beamline for two reasons. First, in this case we wanted to use the harmonics as a probe in a subsequent experiment, instead of simply studying the HHG process itself, so that the harmonic source had to be re-imaged and steered into the experimental chamber. Second, the experiment in question was a photoelectron imaging experiment, which has even more stringent vacuum requirements than HHG. Fortunately, dealing with this situation is one of the strong points of the capillary approach, because it is an ideal geometry for maintaining the required gas pressures in the HHG region (10s – 100s of torr) with minimal conductance of that gas into the rest of the vacuum system. Even so, we employed four to five additional stages of differential pumping to drop the pressure down to the necessary levels for photoelectron imaging ($\sim 10^{-7}$ torr).

To deliver the harmonics into the experimental chamber, we re-image the capillary exit to achieve a loose HHG focus (∼250 μm) in the interaction region. In the EUV region of the spectrum, it is basically impossible to use refractive optics (i.e. lenses) because most materials are far too absorbing and don't have any appreciable refractive index at these wavelengths. Therefore, focusing EUV light is done with either reflective or diffractive optics (mirrors or zone plates respectively). Simple curved mirrors for focusing EUV have to be used at very steep angles (glancing incidence)

to achieve a reasonable degree of reflectivity. For example, for a gold surface the reflectivity is approximately 90% at 2°, 70% at 10°, 10% at 45°, and 5% at normal incidence [11]. However, it is possible to get around this by designing multi-layer structures that can achieve reasonable reflectance (∼30 – 70%) at a specific photon energy and typically normal incidence reflection.

We tried both multilayer mirrors and glancing incidence toroidal mirrors. We found that, specifically for the 400 nm driven HHG employed here, we vastly preferred the glancing incidence optics to focus the harmonics. This preference is primarily because the multilayer mirrors were easily damaged by the 400 nm driving laser, which we sometimes allow to propagate through the system for alignment purposes.[7] One of the advantages of multilayer mirrors is the energy selectivity, which allows you to use the mirrors themselves to isolate a single harmonic order out of the broad harmonic spectrum that is generated. In photoelectron spectroscopy experiments it is typically preferable to use a single energy to ionize so that you can unambiguously correlate a measured photoelectron energy to an initial state binding energy, making multilayers mirrors very attractive. However, in 400 nm driven HHG there are very few harmonic orders generated in the first place [122] and they are much more energetically separated than in the more common 800 nm driven case (6 eV separation vs 3 eV) so that the spectral filtering provided by the multilayer mirrors is less critical. Therefore we used a toroidal mirror (ARW Optical Corporation, R_t = 3220 mm, R_s = 90.5 mm, coated in B_4C) to focus the harmonics. We used the toroid in conjunction with a polished silicon "rejecter mirror" (Gooch & Housego, GO-S200-1), at the same reflection angle as the toroid. This is near Brewster's angle for the driving laser wavelength, so that only a few percent of the fundamental is reflected off of the rejector, while ∼90% of the harmonics are reflected. In addition to rejecting much of the fundamental light, this mirror is advantageous because it maintains a straight beam path (translated by 1" from but parallel to the incoming beam path) and gives you two optics to use to steer the harmonics into the experiment. In this beamline, we used a Hettrick spectrometer and an Andor x-ray CCD camera to monitor the harmonic spectrum and flux.

The remaining necessary components of a high-harmonic beamline are filters to get rid of

[7] We note that we did not encounter these damage problems when using 800 nm to drive the HHG process.

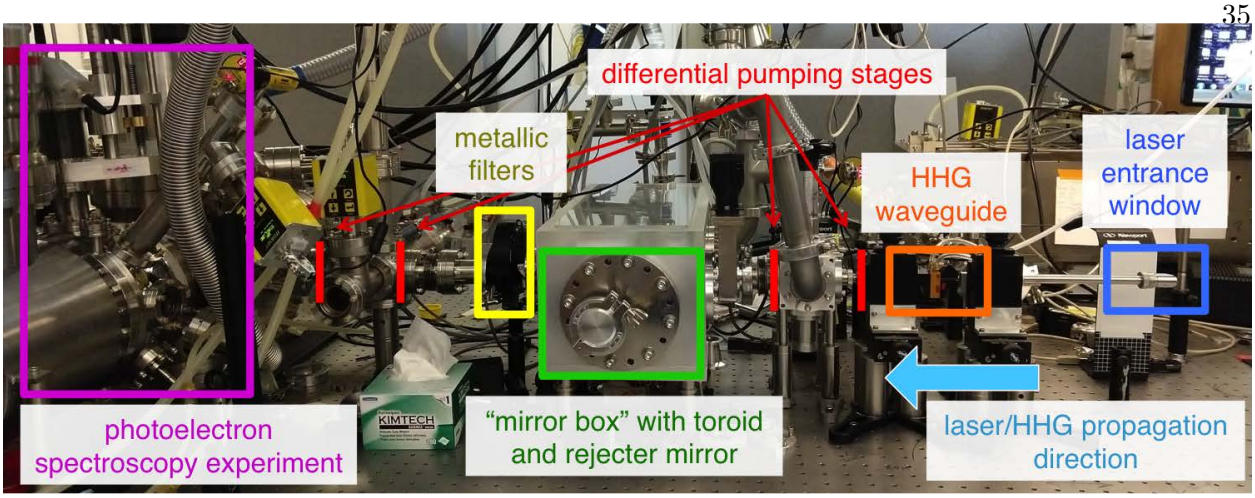

Figure 2.2: **Picture of the HHG beamline used in Chapter 6.** The laser propagates from right to left. It is coupled into the vacuum chamber through a window and focused into a gas-filled capillary (a.k.a waveguide) to drive the HHG process. The residual laser light and generated harmonics continue propagating to the left, encountering a silicon rejecter mirror and focusing toroid before the visible laser light is blocked by metallic filters. The harmonics pass through the metallic filters and continue into the photoelectron spectrometer. There are several stages of differential pumping along the beamline to drop the pressure from ∼10–100 torr in the waveguide to $< 10^{-6}$ torr in the spectrometer.

the residual driving laser light that co-propagates with the emitted harmonics. The driving laser is typically filtered out with thin (100s – 1000s of nm) metal foils placed in the beam path, which reflect or absorb the visible laser light while transmitting a large fraction of the harmonic light. The exact filter choice depends on the photon energies you're working with [11]. Most of the work in this thesis used aluminum filters, which are highly transmissive between about 20 – 70 eV. Zirconium filters were used for photon energies above 70 eV and tin filters were used for calibration of the 400 nm driven harmonic spectrum (because it has a narrow transmission window between 13 – 22 eV).

2.4 Polarization Characterization of High Harmonics

In chapters 3 and 4 we characterize the ellipticity of high harmonics. As with many things in the EUV, this is somewhat more complicated than with visible lasers. One tactic is to use an EUV polarizer constructed out of three mirrors oriented at set angles with respect to each other

[42, 46, 123]. Then, as in the visible, one can monitor the transmitted intensity while rotating the polarizer to determine the circularity. However, these EUV polarizers have very low transmissions and require that you rotate a set of several optics through 360° while under vacuum. Instead, since we were fortunate enough to have a team of experts in studying magnetism with EUV light right down the hall, we found it more convenient to use x-ray magnetic circular dichroism (XMCD) to characterize the circularity of our harmonics.[8] We are very thankful to Dmitriy Zusin, Christian Gentry, Patrick Grychtol and Ronny Knut for helping us implement these XMCD measurements.

XMCD is a phenomenon where the absorption of light by magnetic materials depends on the helicity of that light [124]. For example, a uniformly magnetized material might absorb right-circularly polarized (RCP) light more strongly than left-circularly polarized (LCP) light. The magnitude and sign of the MCD effect depends on the projection of the angular momentum vector of the light onto the magnetization vector of the material. Therefore, in the previous example, flipping the magnetization vector of the material would switch it so that instead LCP light would be absorbed more strongly than RCP light. This effect is typically quantified through the magnetic asymmetry, which is the normalized difference between the transmission for the two opposite orientations, $A = (I_+ - I_-)/(I_+ + I_-)$. The precise value of the measured asymmetry depends on the material and the photon energy you are using: $A = \tanh 2k\Delta\beta L$, where k is the wave vector of the light, $\Delta\beta$ is the energy dependent magneto-optical constant of the material, and L is the path length through the material [125]. This asymmetry could be measured by either flipping the magnetization of the sample or flipping the helicity of the light, but in the EUV it is often more feasible to flip the magnetization.

We can use XMCD to characterize the ellipticity of our EUV light because the magnitude of the MCD effect depends on the degree of circularity of the light [43, 125, 126]. Therefore, we can compare the MCD asymmetry that we measure with the literature values to determine the circularity of the high harmonics. We usually use the common ferromagnets (Fe, Co, Ni) because

[8] Technically, we are doing EUV MCD, since we are using EUV light, but the principles are the same and XMCD is the more common term.

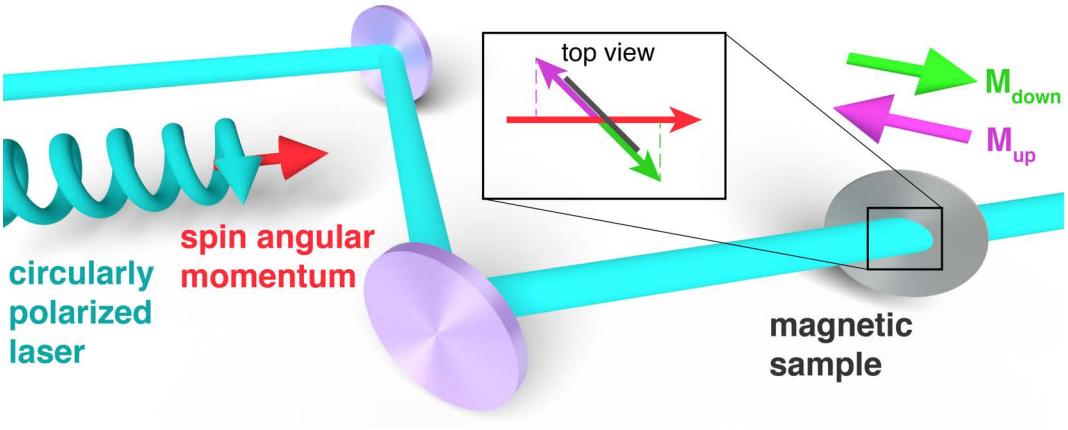

Figure 2.3: **Diagram of the x-ray magnetic circular dichroism experiment.** Circularly polarized laser light is passed through a thin-film ferromagnetic sample. The magnetization vector lies in the plane of the material and is switched between the two opposite magnetization states, M_{up} and M_{down}. The magnetic sample is oriented at 45° with respect to the incoming beam so that a projection of the magnetization vector lies along the spin angular momentum vector of the light. The inset shows the relevant vectors from a "top down" view.

they are well characterized, have relatively large XMCD asymmetries (∼10% near the M-edge for ∼20 nm of material [127]), and their magnetization can be readily and completely switched with a simple electromagnet. These materials magnetize such that the magnetization vector is in the plane of the thin film sample, therefore we do these measurements in transmission with the sample oriented at 45° with respect to the incoming beam (Fig. 2.3). This orientation results in a reasonable projection of the magnetization vector along the angular momentum vector of the light, while still allowing a beam to be transmitted through the sample. The ferromagnets are strongly absorbing at and above their M-edges, which is also energetically where the MCD effect is strongest. Therefore, the samples must be fairly thin (10s of nm) to have any harmonic light transmitted through. For stability, we typically deposit the magnetic thin films on top of a thicker (100s of nm) but more transmissive substrate, such as aluminum or silicon nitride.

2.5 Velocity-Map-Imaging Photoelectron Spectrometer

Photoelectron and photoion imaging techniques use electric fields to guide charged particles to a position sensitive detector. These fields are designed to map some specific property of the

particles to position on the detector. Historically, photoion imaging evolved from time-of-flight spectroscopy. In the case of time of flight, information about the particles is encoded in the amount of time that it takes them to reach the detector, for example with lighter particles arriving earlier than heavier ones. Therefore, time-of-flight spectrometers simply count the number of particles hitting the detector as a function of time. Photoion imaging, on the other hand, was discovered when Chandler and Houston [128] placed a position sensitive detector after a common time-of-flight spectrometer [129]. They used a 266 nm laser to photodissociate CH_3I and found that the resulting CH_3^+ ions hitting the detector formed concentric rings, with the radius of those ring depending on the velocity of the ions. Furthermore, these ring were asymmetric, with more ions being emitted along the laser polarization direction than perpendicular to it, which gives insight into the photodissociation mechanism. Therefore, photoion and photoelectron imaging seemed to be a promising technique that gave additional information not accessible with time of flight.

Photoion imaging really came into its own about 10 years later with the developments made by Eppink and Parker [130, 131]. They replaced the wire-grid electrodes previously employed with an electrostatic lens consisting of three parallel plates with open electrodes (repeller, extractor, and ground, see Figs. 2.9 and 6.2). The electrostatic lens overcame many of the pitfalls of the wire-grid electrodes, removing the blurring and losses associated with charged particles passing through the wire-grid. Furthermore, the electrostatic lens does a much better job of mapping ions with the same velocity to the same position on the detector, regardless of their initial position. This dramatically increases the velocity resolution practically obtained (Fig. 2.4), since experimentally ions are almost always originating from some sort of spatially extended source. Because of this capability Eppink and Parker dubbed their technique "velocity map imaging" (VMI).

The simplest way to understand photoion and photoelectron imaging is to imagine several charged particles that are all emitted some fixed distance away from a 2D detector, with initial velocities all parallel to the plane of that detector but with different speeds. To a first approximation, the electric field of the spectrometer is simply going to push all those charged particles towards the detector. Particles with larger transverse velocities will travel farther in the transverse direction

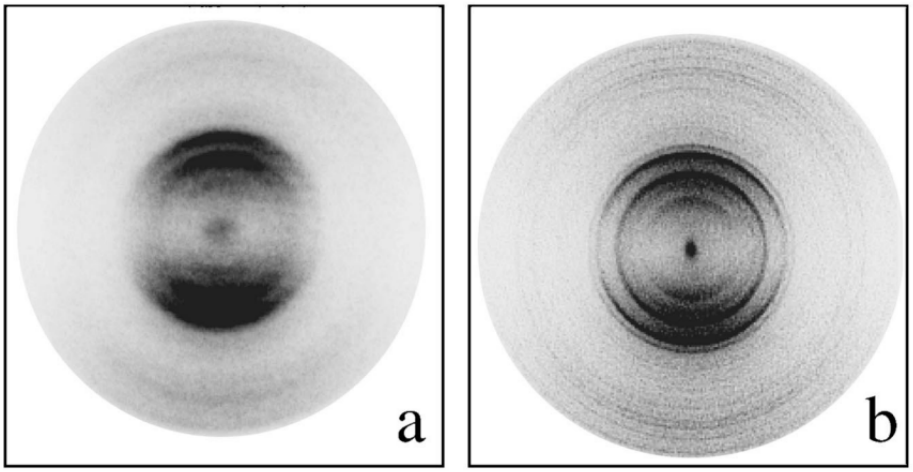

Figure 2.4: **Comparison of velocity map imaging with previous photoion imaging methods.** O^+ ions generated after illuminating O_2 with 255 nm light measured with (a) wire-grid electrodes and (b) an electrostatic lens under similar conditions. In both cases, rings corresponding to different ion velocities are seen, however the electrostatic lens resolves finer details. Figure from [130].

than slower particles in the time it takes to arrive at the detector. Therefore, velocity (v) is mapped to radial position (R). However, as in a time-of-flight spectrometer, the time that it takes those particles to travel to the detector depends on their properties, namely their mass (m) and charge (q). For example, if two ions have the same transverse velocity but different masses, the lighter ion will be accelerated more by the electric field to reach the detector faster and therefore have less time to travel in the radial direction. In general, the radius a particle reaches at the detector is proportional to

$$R \sim \sqrt{\frac{E_k}{q}} \sim \sqrt{\frac{m}{q}} v,$$

where E_k is the kinetic energy. If the mass and charge are held fixed, as is certainly the case in photoelectron imaging since there is only one species being detected, then the radius does increase linearly with increasing velocity. However, we tend to discuss electrons in terms of their energy instead of their velocity, so it is often useful to think if a VMI spectrometer as measuring the square root of the energy.

This simple picture highlights another important aspect of VMI spectroscopy. In the previous

example, we imagined ions being emitted perpendicularly to the detector. However, in reality ions are emitted in all directions. Therefore, instead of expanding in a flat circle to reach some well-defined radius at the detector the ion distribution is actually an expanding sphere (or other similar 3D distribution) that is projected onto the 2D detector. This projection complicates the radial distribution at the detector and must be reversed to extract the actual photoelectron or photoion kinetic energy spectrum. While this is difficult to do in general, the specific case of distributions with cylindrical symmetry has been thoroughly investigated[9] and there are a number of well developed algorithms to recover the full 3D distribution from the 2D projection[10] [132–134].Fortunately, when ionizing with a linearly polarized laser the electron and ion distributions are indeed cylindrically symmetric about the laser polarization axis. Therefore, in most photoelectron and photoion imaging experiments a linearly polarized laser is used, with the polarization oriented in the plane of the detector, so that these reconstructions can be applied. If this cylindrical symmetry is broken in any given experiment then some other method of obtaining the 3D distribution must be employed, if it can be recovered at all. In this thesis, the BASEX algorithm of Dribinski and co-workers was used exclusively [132].

The final aspect of the VMI spectrometer that is important for this thesis is the so-called spatial map imaging (SMI) capability [135, 136]. Similarly to how an optical lens has both an imaging plane and a Fourier plane, the electrostatic lens can be tuned to either image a velocity distribution or a spatial distribution to the detector. The electrostatic lens is tuned between these two modes of operation by adjusting the ratio of the voltages applied to the extractor and repeller electrodes. Note that adjusting the absolute voltages while keeping the extractor and repeller ratio fixed adjusts the magnification and field of view of the spectrometer. The precise ratios needed depend on the geometry and alignment of the spectrometer, in our case $V_E/V_R \sim 0.9$ for VMI and $V_E/V_R \sim 1.3$ for SMI.[11] While the most common mode of operation is of course the VMI

[9] In this case, an Abel transform is applicable

[10] A fabulous python package, PyAbel, was recently developed for doing Abel and inverse Abel transforms that has been optimized for analyzing VMI data. It is currently available on GitHub.

[11] We optimized these ratios by observing the above threshold ionization of noble gases with a strong femtosecond laser field.

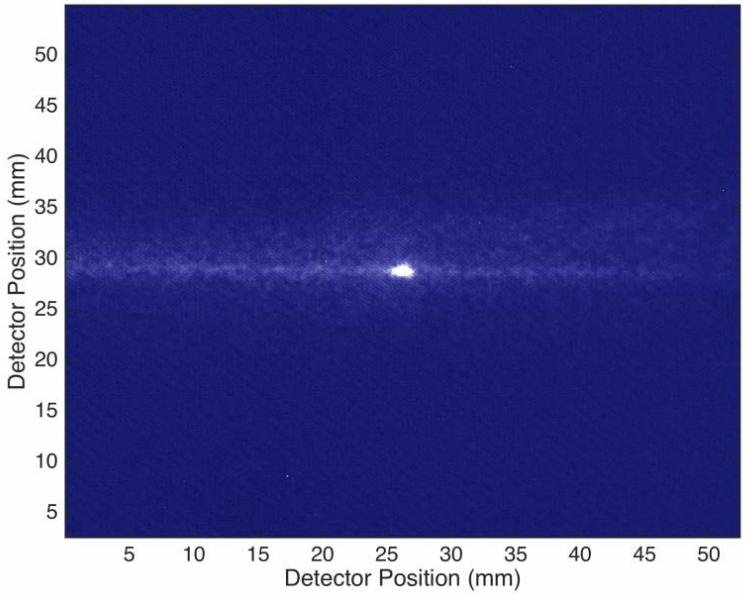

Figure 2.5: **Example of spatial map imaging in the velocity-map-imaging spectrometer.** In this experiment an extreme ultraviolet laser (propagating from left to right) intersects a nanoparticle beam (propagating from bottom to top). The electrons originating from the nanoparticles are therefore confined to the region of overlap, while electrons from the background gas are produced across the length of the chamber. Therefore the signal of interest is easily separated from the background with spatial map imaging. Figure from [138].

mode, SMI is often useful, for example for alignment purposes. In fact, the SMI mode was used for data collection in Chapters 5 and 6 of this thesis to increase the signal-to-noise ratio in those measurements. By using SMI we sacrificed the energy resolution of VMI to instead measure only the photoelectron yield, but with clear separation between the electrons of interest and the electrons originating from the background gas (Fig. 2.5).

The VMI spectrometer used here was built before I joined the group. Details of it's construction and specifications can be found in the thesis of Daniel Hickstein [137].

2.6 Nanoparticle Generation and Characterization

In chapters 5 and 6 we studied isolated "gas-phase" nanoparticles through photoelectron spectroscopy. These particles were produced using a compressed gas atomizer and introduced into the VMI via an aerodynamic lens. This nanoparticle aerosol source was implemented and coupled

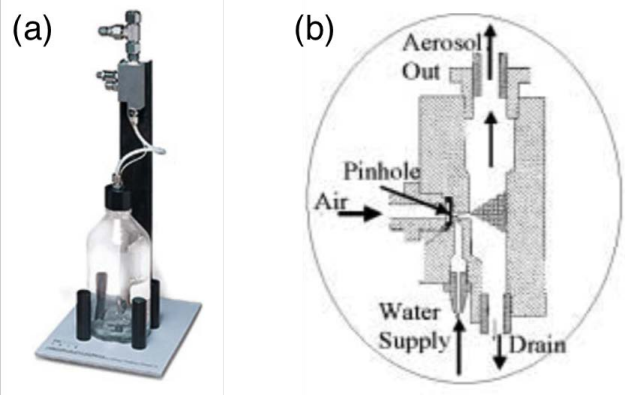

Figure 2.6: **Compressed gas atomizer nanoparticle aerosol source.** (a) Picture of the compressed gas atomizer, courtesy of TSI, Inc. (b) Diagram of operation of the atomizer. Figure from [140].

to the VMI spectrometer with extensive guidance from Prof. Jose-Luis Jimenez and his student Brett Palm in the Chemistry Department at CU Boulder.

2.6.1 Atomizer

We use a Collison-type compressed gas atomizer [139] (TSI, model 3076, Fig. 2.6a) to produce nanoparticles with a wide array of compositions. The atomizer produces an aerosol of droplets from solution, with an average droplet diameter of $\sim$1 μm. It works by flowing gas over a tube that extends down into a liquid reservoir, which causes a pressure drop that wicks liquid from the reservoir up into the tube. When this liquid reaches the top of the tube it is impacted by the flowing gas and droplets are produced. The larger droplets impact onto the walls of the atomizer and return to the reservoir, while smaller droplets are carried along with the gas flow as an aerosol (Fig. 2.6b).

As the droplets travel to the experiment, the solvent in the droplets evaporates leaving behind nanoparticles of the solute. The atomizer is quite versatile in that it can produce nanoparticles with a wide array of compositions depending on the starting solution. For example, if the solute is an ionic compound it will often reform into a nanocrystal once the solvent in the droplet evaporates (Fig. 2.7a) or if the solute consists of chemically synthesized nanoparticles these will clump up

to form a cluster upon evaporation (Fig. 2.7b-d). The size of nanoparticles produced by the atomizer is primarily determined by the concentration of solute in the initial solution because that concentration determines how much solute will be present in the initial droplets that dry to produce the nanoparticle aerosol. There can also be some variation in initial droplet diameter due to changes in solvent viscosity or backing pressure, which in turn effects the final nanoparticle size distribution.

The transmission electron microscopy (TEM) images of different atomizer-produced nanoparticles (Fig. 2.7) highlights one of the main drawbacks of this method of nanoparticle aerosol generation: surface contamination. Any impurities or contaminants in the solvent will likely be left behind as surface contamination on the nanoparticles once the solvent evaporates. Because the initial droplet diameters are large compared to the final nanoparticle diameter ($\sim$1 μm vs $\sim$50 nm) even a small degree of impurities can coat the nanoparticles. This is especially a problem for chemically synthesized particles, where the surface contamination stems from stabilizing agents intentionally added to the solution to keep the nanoparticles suspended (Fig. 2.7c). While this surface contamination did not interfere with photoionization experiments using visible lasers, it was a significant impediment when using EUV lasers to ionize because EUV photoemission is particularly surface sensitive. For this reason we were unable to use chemically synthesized nanoparticles when ionizing with EUV and instead restricted those investigations to solutes that can completely dissolve in solvent without the use of any stabilizing ligands.

2.6.2 Measurement of Particle Size Distributions

We used a scanning mobility particle sizer (SMPS) to characterize the aerosols produced from the compressed gas atomizer. The SMPS system consists of an electrostatic classifier (TSI, model 3080L) and a condensation particle counter (TSI, model 3010). The electrostatic classifier selects a narrow range of nanoparticle diameters out of a broad distribution. It selects nanoparticles based on their mobility diameter[12] by first applying a known charge distribution to the particles in the

[12] For spherical particles, the mobility diameter is equal to the physical diameter. However, in general the mobility diameter is larger than the volume-equivalent diameter, i.e. the diameter resulting from melting the material into a

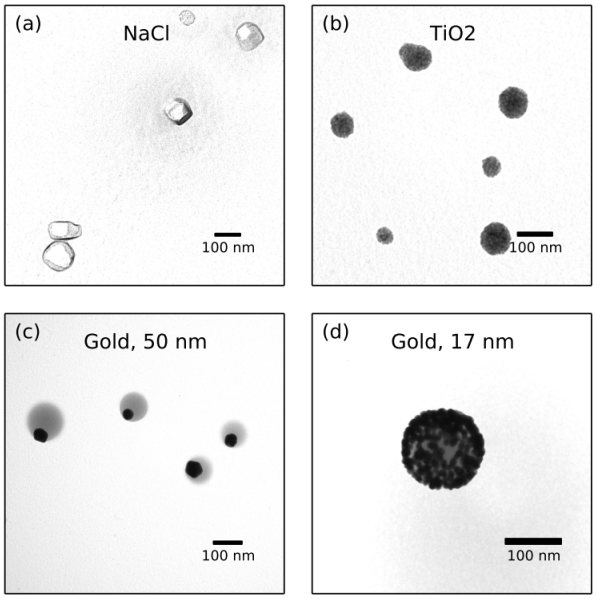

Figure 2.7: **TEM images of various nanoparticles produced with a compressed gas atomizer.** (a) Aqueous NaCl solutions evaporate to form single crystals. (b) Solutions of TiO_2 nanoparticles produce aggregates. (c) Solutions of 40 nm gold nanoparticles produce hybrid nanostructures with single gold nanoparticles housed in spheres of polyvinylpyrrolidone. (d) Similar solutions of 17 nm gold nanoparticles also generate hybrid structures, but these nanostructures contain many gold nanoparticles. Figure from [141].

aerosol and then flowing them through a column with an applied voltage. Due to the voltage, the particles separate along the column by mobility diameter and a small orifice at the bottom of the column selects a certain size. Changing the applied voltage adjusts the mobility diameter that successfully exits the column. The condensation particle counter then determines the number density of nanoparticles at the chosen diameter. It does so by passing the aerosol through a supersaturated gas so that the particles nucleate droplet formation and grow in size to be large enough to be detected and counted by light scattering or other methods. The SMPS therefore scans the voltage on the electrostatic classifier to tune the selected diameter and determines the concentration at that diameter using the condensation particle counter and thereby measures the nanoparticle size distribution in the initial aerosol. Note that the electrostatic classifier can be used on it's own to select a monodisperse aerosol from a polydisperse one, although that was not done

sphere while keeping the same material density [142].

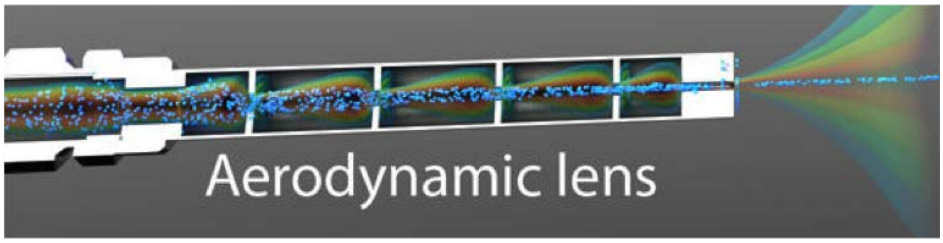

Figure 2.8: **Artist rendering of an aerodynamic lens system.** The nanoparticle aerosol passes through a series of orifices, which focuses the nanoparticles (blue) into a collimated stream while leaving the carrier gas (rainbow) diverging. The upstream flow controlling orifice is not shown. Figure adapted from [79].

in the work presented here.

2.6.3 Aerodynamic Lens

We introduce the nanoparticles into the ultra-high vacuum system via an aerodynamic lens [143, 144], which produces a collimated stream of nanoparticles (∼0.5 mm diameter) while leaving the carrier gas divergent. The aerodynamic lens consists of a series of small orifices inside of a tube (Fig. 2.8) that create converging and diverging flows, which separate the nanoparticles from the carrier gas due to the inertia of the particles. The specific diameters and separations of these orifices are designed to optimize nanoparticle transmission at a given size [145]. Each aerodynamic lens must also be paired with a flow controlling orifice placed upstream, which drops the pressure to that required by the lens. The aerodynamic lens used in this thesis was designed to be used at ∼1.5 torr input pressure and efficiently transmitted and focused nanoparticles with diameters from 70 – 700 nm [146]. Note that it is the aerodynamic diameter that is relevant for particle transmission through an aerodynamic lens system. For a spherical particle, the aerodynamic diameter is different from the physical diameter by a factor of density [142], such that denser particles behave like larger particles when transmitting through the aerodynamic lens. The aerodynamic diameter also depends on particle shape, with nonspherical particles appearing smaller than spherical particles of the same mass [142].

Initially, we used a thin 100 μm pinhole as the flow controlling orifice in our system. However,

this pinhole clogged repeatedly so we replaced it with a longer glass tube that achieved a similar pressure drop with a larger diameter (∼15 cm long, 250 μm diameter), which clogged much less frequently. Similarly, the differential pumping skimmers inside the vacuum chamber were swapped from cone-type molecular beam skimmers (Beam, Dynamics, Inc., 300 μm orifice diameter) to longer cylindrical tube skimmers (1.5 mm inner diameter, 35 mm length). The extra length of these tube skimmers achieved the same conductance as the molecular beam skimmers thereby accomplishing effective differential pumping with a large enough diameter to cleanly pass the entire particle beam.

2.6.4 Light-Scattering Diagnostic for Alignment

To conduct experiments we must intersect the nanoparticle beam with a focused laser in the center of the VMI spectrometer. For simplicity we decoupled the alignment of the nanoparticle beam from that of the tightly focused femtosecond laser by first aligning the nanoparticles to the differential pumping apertures in the vacuum system using a light-scattering based diagnostic.

The aerodynamic lens is mounted on an XYZ-stage (Kurt J. Lesker Company), which controls the position of the nanoparticle beam. For particles to pass into the experimental chamber the nanoparticle beam must be aligned with the differential pumping apertures, which conveniently also ensures alignment to the center of the VMI spectrometer. A very rough alignment is first accomplished by maximizing the pressure in the VMI chamber by adjusting the position of the aerodynamic lens. This gets the aerodynamic lens close to the right position, but is not very precise because the gas exiting the lens is so divergent. Therefore, the more tightly collimated nanoparticle beam may still be clipping on or missing the differential pumping apertures.

To determine if the nanoparticle beam itself is well aligned to the vacuum system we detect the nanoparticles down stream of the experimental chamber with an unfocused green continuous-wave laser (1W, 532 nm, Wicked Lasers). When the nanoparticles pass through the green laser beam they scatter photons out of the beam to produce a visible spot that we record with a CCD camera. Since the green laser beam is unfocused, we can be sure that if the nanoparticles are passing through the differential pumping apertures they will intersect the green laser and be detected. Therefore,

simply adjusting the aerodynamic lens position to maximize the light-scattering signal optimizes the alignment of the nanoparticle beam to the vacuum system and the VMI spectrometer. This simple diagnostic works well for most nanoparticle aerosols investigated here because, in general, the nanoparticles produced by the atomizer are large enough to scatter the laser light efficiently (i.e. the nanoparticle diameter is of order the wavelength of the green light). Smaller particles would not be detectable with this method.

Once we are confident the nanoparticle beam is well aligned to the vacuum system we can align the tightly focused femtosecond laser to the nanoparticles by monitoring the photoelectron signal in the VMI spectrometer.

2.7 Photoelectron Spectroscopy of Semiconductor Nanocrystals

This section is adapted, with permission, from:

- Wei Xiong, Daniel D. Hickstein, Kyle J. Schnitzenbaumer, Jennifer L. Ellis, Brett B. Palm, K. Ellen Keister, Chengyuan Ding, Luis Miaja-Avila, Gordana Dukovic, Jose L. Jimenez, Margaret M. Murnane, and Henry C. Kapteyn. Photoelectron Spectroscopy of CdSe Nanocrystals in the Gas Phase: A Direct Measure of the Evanescent Electron Wave Function of Quantum Dots. *Nano Letters*, **13** (6), 2924–2930 (2013).
  DOI:10.1021/nl401309z.

Putting the previous two sections together, we can conduct photoelectron spectroscopy measurements on quantum dots (QDs, semiconductor nanocrystals) in the gas phase by coupling a nanoparticle aerosol source to a velocity-map-imaging photoelectron spectrometer (Fig. 2.9a). This allows us to study completely isolated QDs, which are usually probed in a liquid solvent [147–153] or while bound to a surface [62, 63]. Additionally, the flowing aerosol ensures that fresh nanoparticles are present for each laser shot, which is advantageous to avoid any effects of charging or long-lived trap states in the QDs [149, 154, 155]. Once the QDs are introduced into the vacuum system, we then use pump-probe photoelectron spectroscopy (a.k.a two-photon photoemission) to study the elec-

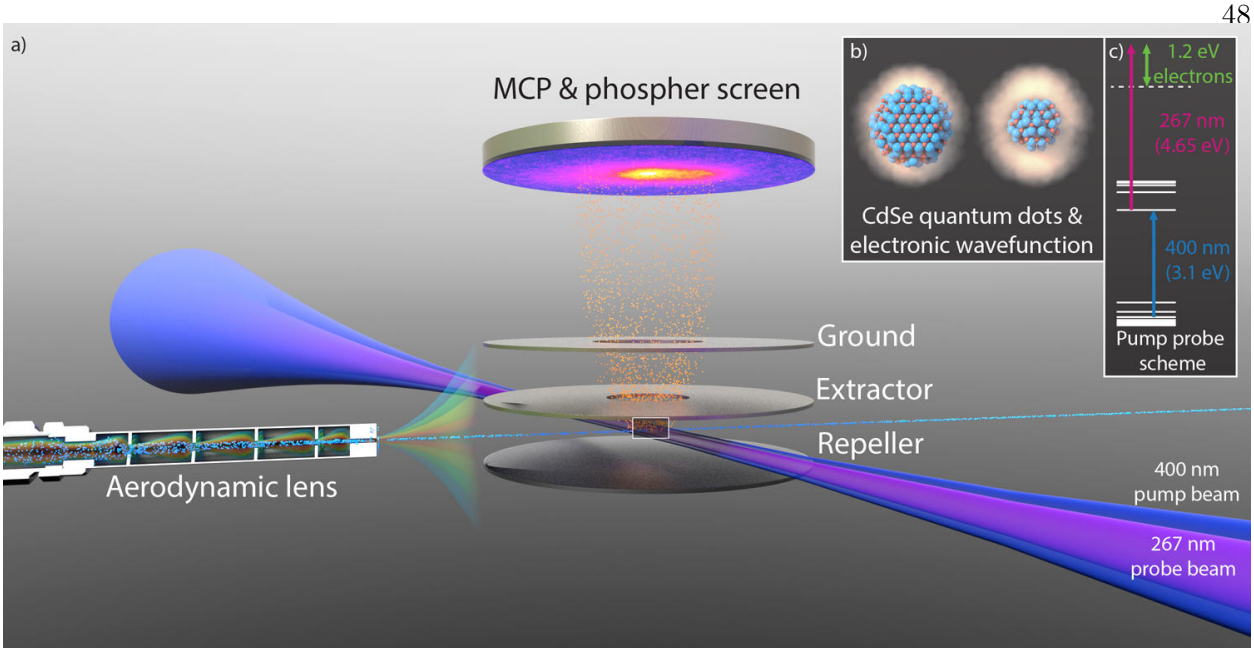

Figure 2.9: **Experimental scheme for photoelectron spectrosocpy (PES) measurements of gas phase quantum dots.** (a) The experimental apparatus consists of a velocity-map-imaging photoelectron spectrometer coupled to a nanoparticle aerosol source. Clusters of quantum dots (QDs) are generated by a compressed gas atomizer (not shown) and then focused into the interaction region by an aerodynamic lens. The QDs are then excited and ionized by two time-delayed 40 fs laser pulses. (b) Visualization of two different diameter CdSe QDs and their associated electron wavefunctions. (c) In the PES experiment, the 400 nm pump pulse excites an electron from the valence band to the conduction band. After a time delay, the 267 nm probe pulse ionizes that electron from the conduction band, leaving it with ∼1.2 eV of kinetic energy. Figure from [79].

tronic structure and dynamics of QDs by first exciting an electron in a QD and then subsequently ionizing and detecting that electron (Fig. 2.9c).

QDs are characterized by discrete energy levels that arise due to the quantum confinement of electrons in the nanocrystal. Since these levels exist because of quantum confinement effects, the precise locations of these energy levels depends on the size of the nanocrystal (Fig. 2.10a). While previous studies have used PES to study dielectric nanoparticles produced with an atomizer [156, 157], no one had studied aerosolized clusters of QDs before. Therefore, it was necessary to first validate that the QDs retained their quantum confined characteristics after aerosolization.

We diluted octadecylamine capped CdSe QDs (NN-Labs, 2.3, 2.5, or 2.8 nm diameter) to 0.01 mg/mL in hexane, and aerosolized that solution with a compressed-gas atomizer using helium

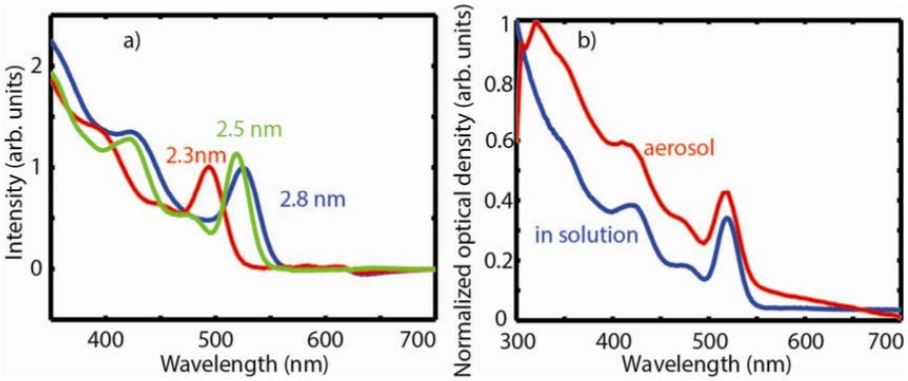

Figure 2.10: **Characterization of QDs with UV-visible absorption measurements.** (a) UV-visible absorption spectra of quantum dots with various diameters, showing the shift in the band gap with QD diameter. (b) Normalized spectra of 2.5 nm CdSe quantum dots in solution (blue) and after passing through the atomizer and aerodynamic lens (red). The absorption is largely unchanged upon aerosolization, indicating that the quantum confined properties of the QDs are preserved. Figure from [79].

as the carrier gas. This formed ∼1 μm diameter droplets, which dried to form clusters of QDs with an average diameter of 50 nm. We verified that the properties of the QDs within these clusters were well preserved after the aerosol system by comparing the UV-visible absorption spectra of the solution phase and aerosolized QDs (Fig. 2.10b). We used a Cary 500 UV-Vis-NIR Spectrophotometer to measure the absorption of the QDs in solution. To measure the absorption spectrum of the QDs after aerosolization, we first collected the QDs by depositing them on a glass slide placed in the path of the collimated nanoparticle stream at the interaction region, which is where they will be intersected by the laser in the PES experiment. The absorption can then be measured using an ellipsometer (JA Woolam VB250). We found that the well-resolved absorption peaks are preserved in the aerosolized QDs collected on the glass slide (Fig. 2.10b). This shows that the QDs retain their quantum-confined characteristics after aerosolization and do not become bulk like. The successful electronic isolation of neighboring QDs in a QD cluster is likely due to the ligand layer surrounding each QD.

Once we had showed that the QDs do remain quantum confined after being aerosolized, we could proceed to investigate their electronic structure with PES. In the PES experiment, we first

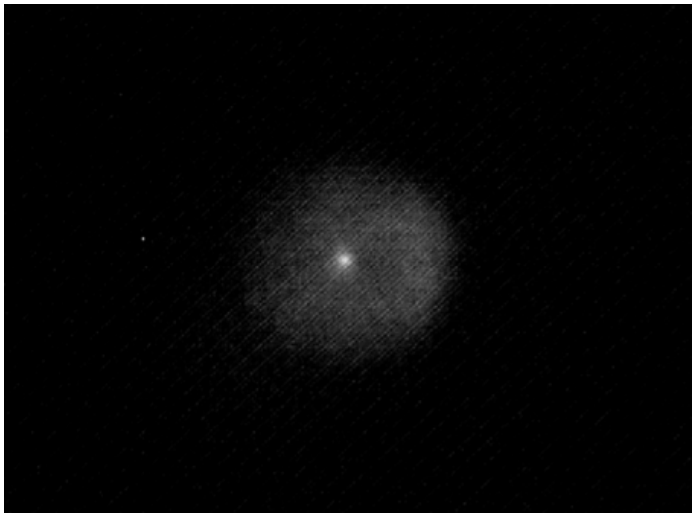

Figure 2.11: **Representative VMI image of the photoelectron momentum distribution from a sample of 2.3 nm diameter CdSe quantum dots taken at t=100 fs.** The center of the image corresponds to zero momentum, with electron energy/momentum increasing radially outward, and the laser polarization is in the vertical direction. The slight left-right asymmetry is due to detector inhomogeneities. This image has been background subtracted to remove contributions due to scattered light and the ionization of the hexane solvent and helium carrier gas. Figure from [79].

excite an electron inside the QDs using a 400 nm pump pulse and then ionize that electron with a subsequent 267 nm probe pulse (both ∼40 fs in duration). The time delay between the pump and the probe pulses is controlled with a Mach-Zehnder interferometer and the powers and polarizations are determined by half-wave plates and polarizers placed in each beam. The polarizations for both beams are fixed parallel to the plane of the detector and the resulting photoelectron momentum distribution exhibits spherical asymmetry (Fig. 2.11). We note that the flux of the 400 nm pump beam is maintained below the single exciton limit [148, 158], so that we expect there to be electrons excited in only ∼10% of QDs, thereby avoiding any multi-electron effects.

An inverse-Abel transform [132] recovers the full 3D photoelectron momentum distribution from the measured 2D projection (Fig. 2.11), which we angularly integrate to obtain a kinetic energy spectrum of the photoelectrons (Fig. 2.12). This kinetic energy spectrum is measured as a function of time delay between the pump and the probe. The time-resolved 2PPE spectra shows a well-resolved peak at positive time delays, where the 400 nm pump pulse interacts with the QDs

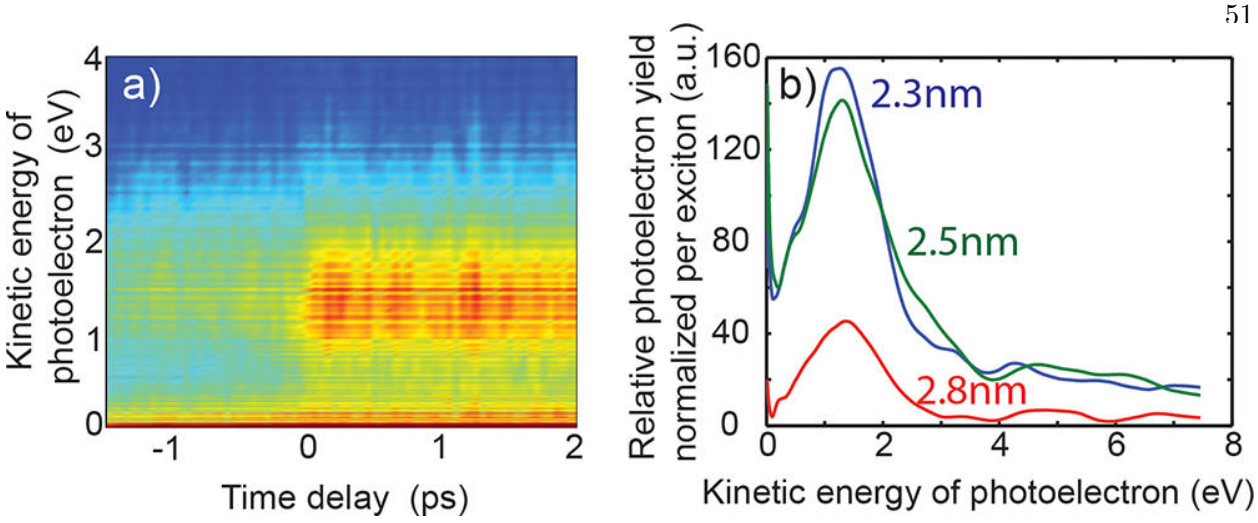

Figure 2.12: **Two-photon photoelectron spectroscopy from exciton states of CdSe QDs.** (a) The temporal evolution of the 2PPE spectra from 2.3 nm diameter CdSe QDs shows a broad peak corresponding to the 1dS electron state. (b) Relative photoelectron yield per exciton for different diameter CdSe QDs, observed with a pump-probe time delay of 50 fs. The time independent signal has been subtracted. The total photoelectron yield per exciton decreases as the QD diameter increases from 2.3 to 2.8 nm. Figure from [79].

before the 267 nm probe pulse, which does not decay on the ∼100 ps time scales measured. To confirm this time dependent PES signal is indeed coming from the QDs, we preformed a control experiment by dissolving only the octadecylamine ligands in hexane and found that the signal from both the ligands and the solvent is negligible (see Supporting Information of Xiong *et al.* [79]).

The peak present in the electron kinetic energy spectrum at positive time delays is centered at 1.2 eV. Our probe photon energy is 4.65 eV, so this corresponds to an exciton state where the electron lies at –3.45 eV below the vacuum (Fig. 2.9). Effective mass calculations [159–161] find that the 1S electron is expected to be bound by –3.4 eV in ∼2.5 nm CdSe. Therefore, we can assign the peak in our photoelectron spectra to the 1S electron. This assignment is further supported by this peak's long lifetime, which is in agreement with previous measurements of the 1S electron in QDs [151]. We note that we do not observe any clear signature of electrons originating from the 1P state, however it has been shown that even when resonantly pumping the 1P state the photoelectron signal from 1P electrons appears only as a small shoulder on the main photoelectron peak [64]. Therefore, since we are not resonantly pumping the 1P state, it is expected that we

should not resolve a distinct peak from the 1P electrons. There is an expected shift of the location of the 1S peak for different QD diameters because of the size dependence of the QD band gap. However, this shift is only expected to be between 0.1 to 0.2 eV and therefore cannot be resolved in these spectra because the 1S peak is broadened to ∼1.5 eV. This broadening of the 1S photoelectron peak could be due to size inhomogeneity of the sample or, more likely, the presence of secondary electrons arising from inelastic electron scattering [162]. In the future, the effects of secondary photoelectrons could be mitigated by using an EUV probe [163].

These validation and characterization measurements show that the quantum-confined characteristics of QDs do indeed persist after aerosolization and that "gas-phase" PES is sensitive to the electronic structure and dynamics of QDs. Therefore, presumably these techniques can be applied to other nanoparticle compositions as well. These characterization measurements were previously presented as part of a study of the size dependence of the evanescent electron wavefunction in QDs, the details of which can be found in Xiong *et al.* [79].

Chapter 3

Noncollinear High-Harmonic Generation

This chapter is adapted, with permission, from:

- Daniel D. Hickstein, Franklin J. Dollar, Patrik Grychtol, Jennifer L. Ellis, Ronny Knut, Carlos Hernandez-Garcia, Dmitriy Zusin, Christian Gentry, Justin M. Shaw, Tingting Fan, Kevin M. Dorney, Andreas Becker, Agnieszka Jaron-Becker, Henry C. Kapteyn, Margaret M. Murnane, and Charles G. Durfee. Non-collinear generation of angularly isolated circularly polarized high harmonics. *Nature Photonics*, **9**, 743–750 (2015).
  DOI:10.1038/nphoton.2015.181.

- Jennifer L. Ellis, Kevin M. Dorney, Charles G. Durfee, Carlos Hernandez-Garcia, Franklin Dollar, Christopher A. Mancuso, Tingting Fan, Dmitriy Zusin, Christian Gentry, Patrik Grychtol, Henry C. Kapteyn, Margaret M. Murnane, and Daniel D. Hickstein. Phase matching of noncollinear sum and difference frequency high harmonic generation above and below the critical ionization level. *Optics Express*, **25**, 10126–10144 (2017).
  DOI:10.1364/OE.25.010126.

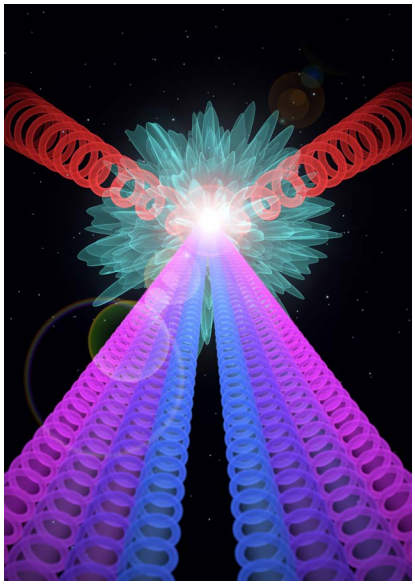

Figure 3.1: **Illustration of noncollinear circularly polarized HHG.** Two driving laser beams are crossed at an angle to drive the HHG process. This produces a fan of angularly separated high harmonic beamlets. Art by Steven Burrows.

3.1 Abstract

We generate angularly isolated beams of circularly polarized extreme ultraviolet light through the first implementation of noncollinear high-harmonic generation (HHG) with circularly polarized driving lasers. This noncollinear technique offers numerous advantages over previous methods, including the generation of higher photon energies, the separation of the harmonics from the pump beam, the production of both left and right circularly polarized harmonics at the same wavelength and the capability of separating the harmonics without using a spectrometer. To confirm the circular polarization of the beams and to demonstrate the practicality of this new light source, we measure the magnetic circular dichroism of a 20 nm iron film. Furthermore, we explain the mechanisms of noncollinear HHG using analytical descriptions in both the photon and wave models. Advanced numerical simulations indicate that this noncollinear mixing enables the generation of isolated attosecond pulses with circular polarization.

We also investigate the macroscopic physics of noncollinear HHG at high pressures. We make the first experimental demonstration of phase matching of noncollinear high-order-difference-

frequency generation at ionization fractions above the critical ionization level, which normally sets an upper limit on the achievable cutoff photon energies. Additionally, we show that noncollinear high-order-sum-frequency generation requires much higher pressures for phase matching than single-beam HHG does, which mitigates the short interaction region in this geometry.

3.2 Introduction

In non-collinear HHG two laser beams are crossed at an angle to drive the HHG process. This geometry is advantageous for a number of reasons, several of which I will discuss in this chapter. First, circularly polarized high harmonics are generated via the noncollinear mixing of counter-rotating circularly polarized driving lasers [48]. Non-collinear circularly polarized HHG (NCP-HHG) offers several key benefits not found in other circularly polarized HHG methods, including generating circularly polarized high harmonics with a single-color driving laser, thereby maximizing the photon energies obtained, and producing angularly isolated circularly polarized beams of left and right helicity at the same wavelength. Additionally, the emitted harmonic orders are naturally angularly separated from both the driving laser beams and from each other [50, 164, 165]. This enables fragile samples to be placed directly into the EUV beams without filtering out the driving lasers and the separation of high harmonic orders without the use of a lossy spectrometer, both of which significantly increase the usable HHG flux. Finally, the angular separation between the driving lasers and the emitted harmonics in non-collinear HHG significantly modifies the macroscopic phase matching as compared to traditional single beam HHG [51, 166], which enables phase matching above the critical ionization barrier [167].

Previous investigations of noncollinear HHG have also exploited this geometry to produce linearly polarized isolated attosecond bursts [52, 168], probe the nonlinear optics of the HHG process [169], and show that this is a promixing geometry for cavity-assisted HHG [170–172]. Other work has used the noncollinear geometry to produce spectrally narrow EUV light [166] and applied a noncollinear probe beam to spatially and temporally characterize attosecond pulses [173]. While it provides new opportunities, a fundamental drawback of noncollinear HHG is that it provides

a limit to the interaction length over which harmonics can be produced, which could result in a reduction in harmonic flux when compared to other geometries.

Non-collinear HHG can be understood through both photon and wave models (Fig. 3.2). In the photon model, each driving laser is considered as a bath of photons and high-harmonic photons are produced by adding up all of the allowed combinations of those driving laser photons. When the two driving lasers are crossed non-collinearly each bath of photons has it's own associated linear momentum, which must be conserved when building a high-harmonic photon. This conservation of linear momentum means that the direction that harmonics are emitted into depends on the number of photons that were absorbed from each driving laser beam. When the driving lasers are linearly polarized there is no restriction on the relative number of photons that can be absorbed from each beam, which results the emission of several high harmonic beamlets corresponding to different permutations of driving laser photons (Fig. 3.2a). For example, the seventh harmonic order can be produced by absorbing four photons from one beam and three from the other or six photons from the first beam and only one from the other. While these two cases result in the same photon energy they are emitted in different directions.

Alternatively, if the driving lasers are circularly polarized then spin-angular momentum (σ) must be conserved as well as linear momentum. This conservation of angular momentum serves to shut down most of the HHG channels because the only allowed angular momentum states for photons are $\sigma = +1$ or $\sigma = -1$. For purely circularly polarized driving lasers beams there are only photons in a single angular momentum state present in each beam, i.e. the left circularly polarized (LCP) driving laser consists of only $\sigma = +1$ photons and the right circularly polarized (RCP) driving laser is made up of only $\sigma = -1$ photons. Therefore, it is only possible to conserve spin-angular momentum if the difference in the number of photons absorbed from each beam is ± 1. This constraint results in the emission of two HHG beamlets, which each have a well defined angular momentum state, where the absorption of an extra photon from the LCP beam results in LCP harmonics and the absorption of an extra photon from the RCP beam results in RCP harmonics (Fig. 3.2c). In both the linearly and circularly polarized cases, the angle of harmonic

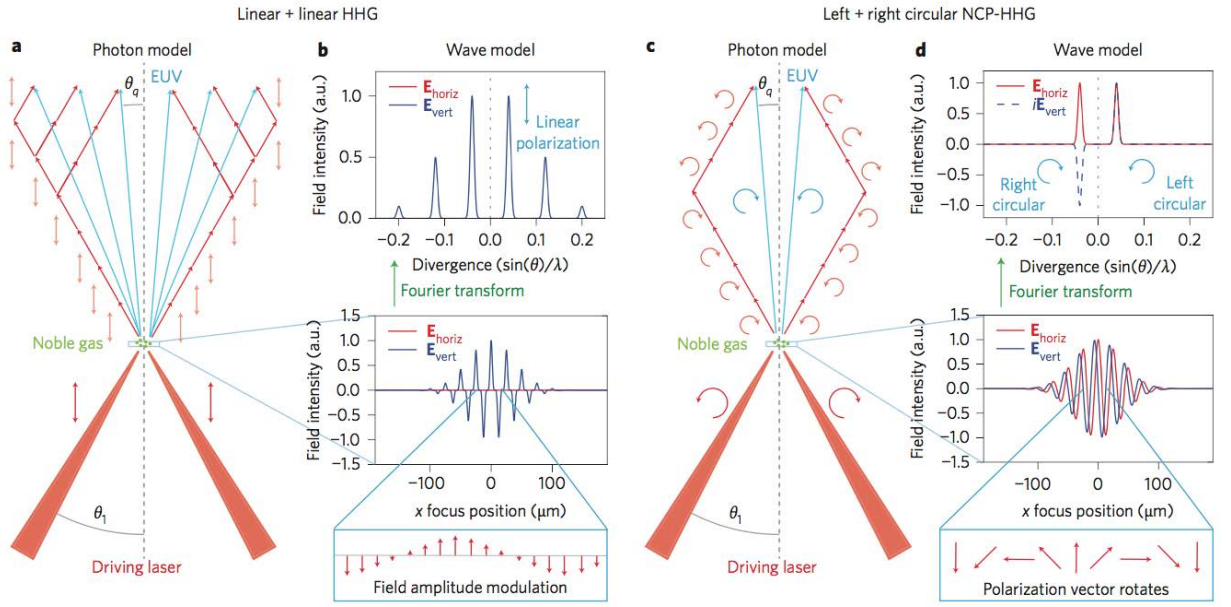

Figure 3.2: **Photon and wave models of noncollinear HHG.** (a) For the mixing of linearly polarized laser beams, the only constraint is that the total number of absorbed photons is odd. This allows many combinations of photons for any given harmonic (7^{th} in this case) and results in high-harmonic beams emerging at many different angles. (b) In the wave model, two-beam mixing produces an amplitude-modulated grating at the focus, which produces multiple peaks in the far field. (c) For counter-rotating circularly polarized beams, conservation of spin angular momentum requires that $n_R = n_L \pm 1$, restricting the output to only two beams for each harmonic order. (d) In the wave picture, the left and right circular mixing produces linear polarization that rotates as a function of the transverse focal position. This rotation is purely sinusoidal and consequently produces just two output beams, one left circularly polarized and one right circularly polarized. Figure from [48].

emission is given by

$$\tan(\theta_q) = \Delta m \tan(\theta_1)/q, \tag{3.1}$$

where $2\theta_1$ is the angular separation between the fundamental driving beams, q is the harmonic order, and Δm is the difference in the number of photons absorbed from each beam.

In the wave model of non-collinear HHG the electric field in the interaction region is considered. In the case of linearly polarized driving lasers, crossing the two beams at an angle results in intensity interference in the combined electric field, which produces a field amplitude grating across the region of overlap (Fig. 3.2b). High harmonics are generated by this amplitude grating, resulting in a high harmonic source function that also looks like a grating and therefore produces

diffracted high harmonic orders in the far field. Because the harmonic yield is highly nonlinear with respect to the driving field there are many diffracted orders in the far field corresponding to the many HHG channels in the photon model.

In the case of circularly polarized counter-rotating driving beams there is no interference pattern at the crossing plane because the polarizations are orthogonal. However, if the amplitudes of the two beams are equal then the combined polarization is everywhere locally linear across the region of overlap. Because the relative phase of the beams varies across the focal spot, the orientation of the linear polarization also varies such that it rotates across the focal spot and thereby forms a rotating polarization grating (Fig. 3.2d). Therefore, in the interaction region atoms emit high harmonic radiation polarized in the direction of the local linear fundamental field, which imprints the rotating polarization grating on the harmonic light. If you consider the horizontally and vertically polarized components individually, the high-harmonic source function varies sinusoidally in space for both with a relative phase shift of $\pi/2$ between them. Consequently, in the far field there are only two diffracted orders $(+1, -1)$, with a relative phase shift of $\pm\pi/2$ between the horizontally and vertically polarized components. This results in the emission of two HHG channels with right- and left-circular polarization, which is again in agreement with the photon model. This locally linear field in the rotating polarization grating in non-collinear HHG is advantageous because everywhere across the focal spot the single-atom HHG process is identical to that of traditional single-beam HHG.

3.3 Circularly Polarized Noncollinear High-Harmonic Generation

To generate circularly polarized high harmonics in a non-collinear geometry, two tightly focused, counter-rotating 45 fs laser pulses were overlapped in a gas jet of noble gas (xenon, argon, or neon), where the HHG process took place. The generated EUV beams propagated in vacuum and passed through an aluminum filter (200-nm-thick, 20 - 72 eV transmission window), which blocked any scattered visible light. The EUV beams were then dispersed by an imaging spectrometer and recorded with an x-ray CCD camera. Harmonics were generated only when the beams were

overlapped both temporally and spatially. Otherwise, the HHG mechanism was suppressed due to the circular polarization of the individual laser beams. Two EUV beams were produced for each odd harmonic order, with one circularly polarized beam propagating to the right of the centerline and the other (with opposite helicity) to the left (Fig. 3.3a).

When two 800-nm driving beams were used to generate harmonics in argon gas, the resulting high harmonic photon energies reached the 29th harmonic order (45 eV). In xenon gas, only 100 μJ in each driving laser beam was sufficient to generate high harmonics, demonstrating that the NCP-HHG method is easily scalable to current multi-kHz laser systems. Numerical simulations confirmed, for the case of perfect alignment, that the harmonics are fully circularly polarized with opposite helicity (Fig. 3.3b,c). Additionally, both experimentally and in the numerical simulations, the output beam directions for harmonic order q follow $\tan\theta_q = \pm\tan\theta_1/q$ as expected (Fig. 3.3d). Significantly, all the harmonics are directed away from the pump beams and, provided the initial crossing angle is sufficiently large and the harmonic divergence sufficiently small, individual harmonics can be separated without using a diffraction grating.

The nature of the harmonic emission can be controlled by changing the wavelength of the driving laser and by mixing driving lasers of two different wavelengths (see Appendix A for details).

3.3.1 EUV MCD Measurements

One of the most powerful uses for ultrashort pulses of circularly polarized EUV and soft x-ray light is the study of femtosecond dynamics of magnetic materials using EUV and x-ray magnetic circular dichroism (MCD) [174]. Because the dichroic absorption scales linearly with the degree of circular polarization, MCD can also provide a rigorous measurement of the ellipticity and helicity of the EUV light. The dichroism can be measured either by comparing the difference in absorption between the left- and right-circularly polarized light or by using a magnetic field to flip the sample magnetization. We performed an EUV MCD measurement by switching the magnetic field (15 mT) applied to a 20-nm-thick iron film and comparing the transmitted EUV intensities (Fig. 3.4a) for opposing magnetization directions, $I_{\pm}$, as expressed by the MCD asymmetry,

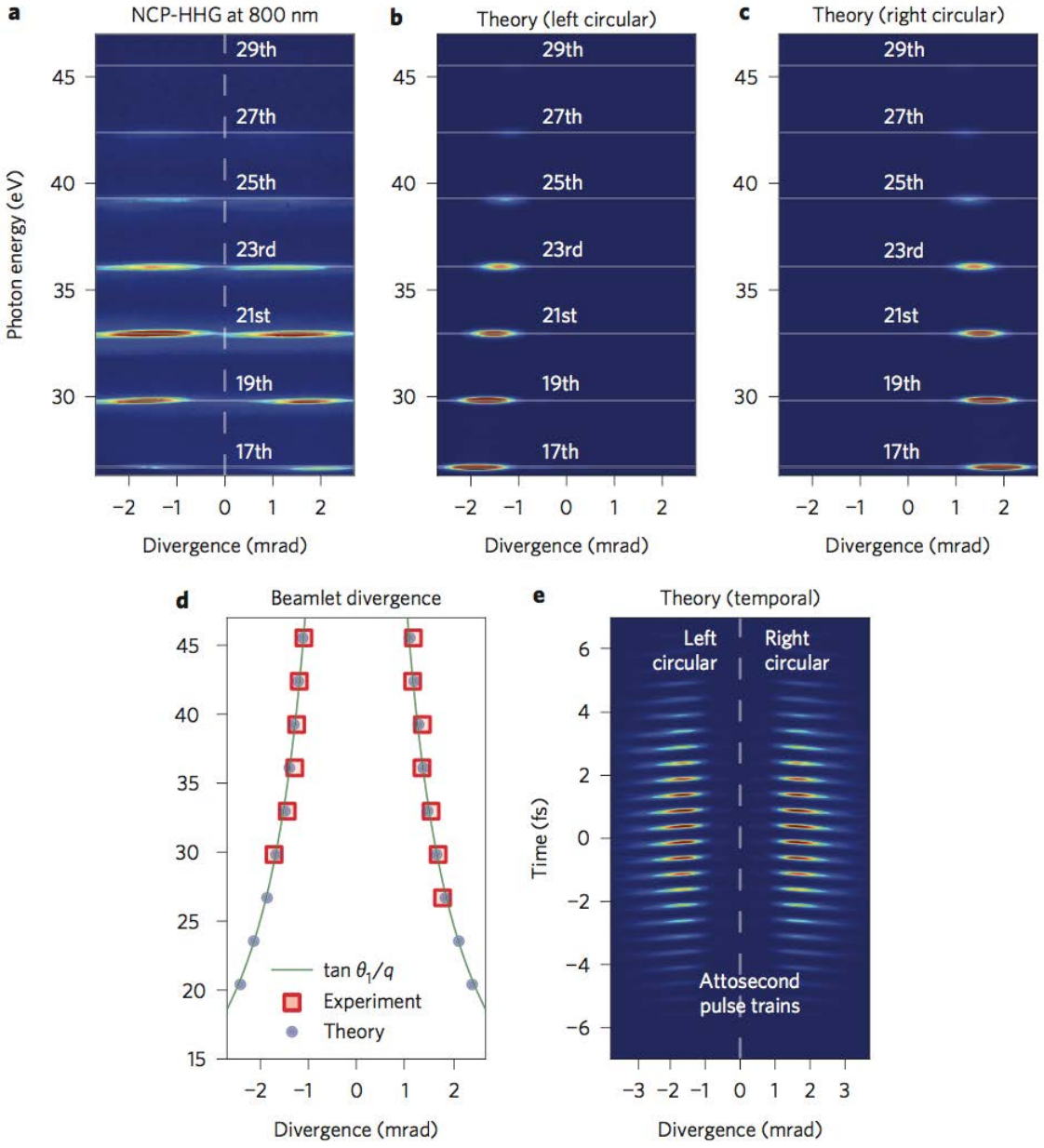

Figure 3.3: **NCP-HHG using two 800 nm pulses.** (a) The EUV output of the NCP-HHG process is recorded after passing through a spectrometer, which disperses the harmonics in the vertical direction. Each harmonic order consists of two beams, one at an angle left of the centerline (LCP) and one to the right of the centerline (RCP). (b,c) Numerical HHG simulations driven by 4.3-cycle 800 nm laser pulses demonstrate that the left beamlets are LCP and the right beamlets are RCP. (d) The divergence of each harmonic order q follows conservation of momentum, which predicts that the angle of harmonic emission, θ_q, is related to the crossing angle of the two laser beams, θ_1, by $\tan\theta_q = \pm\tan\theta_1/q$. (e) The temporal structure of the harmonic emission is a pulse train of many circularly polarized attosecond bursts. Figure from [48].

$A_{MCD} = (I_+ - I_-)/(I_+ + I_-)$.

Experimentally, the MCD asymmetry is readily apparent, even in the two-dimensional image (Fig. 3.4b), and clearly demonstrates that the two beams exhibit opposite helicity. Angular integration (Fig. 3.4c) provides a quantitative estimate of the MCD asymmetry of 1.5% in the range of 29-39 eV. To our knowledge, there is no experimental measurement of the MCD contrast (or magneto-optical constants) of iron in this energy range, but synchrotron data at slightly higher photon energies are available [127, 175]. The trend of the data indicates that the MCD asymmetry in the range of our measurement is less than 2% (Fig. 3.5). Thus, our measurement of 1.5% asymmetry confirms that the EUV light generated by the NCP-HHG process has a high degree of circular polarization. Furthermore, this EUV MCD measurement demonstrates that the NCP-HHG source is a practical tool for measuring ultrafast magnetic dynamics.

3.3.2 Future Capabilities Investigated with Numerical Simulations

Numerical simulations of HHG including propagation provide insight into further capabilities of the NCP-HHG method. First, experimentally the harmonics could only be angularly separated when using 267 nm driving lasers (see Appendix A). However, simulations predict that similar separation can be achieved at longer driving laser wavelengths and higher harmonic photon energies. For example, simulations indicate that 400 + 400 nm-driven NCP-HHG at a 64 mrad crossing angle will produce harmonics that are completely separated angularly (Fig. 3.6a). The situation is similar for longer wavelengths, but the required crossing angle becomes larger. The separation of the harmonics allows for spectroscopic experiments such as x-ray transient absorption spectroscopy and MCD to be completed without a spectrometer to disperse the harmonics, a distinct advantage considering the high expense, low efficiency, and temporal dispersion of gratings in the EUV and soft x-ray regions. In this case, the HHG process itself serves as the dispersive grating. Of course, where separation of the harmonic beams is not desirable, a small crossing angle can be used to achieve good overlap of the harmonic orders, and the NCP-HHG method can still serve as a practical source of circularly polarized high-harmonic light.

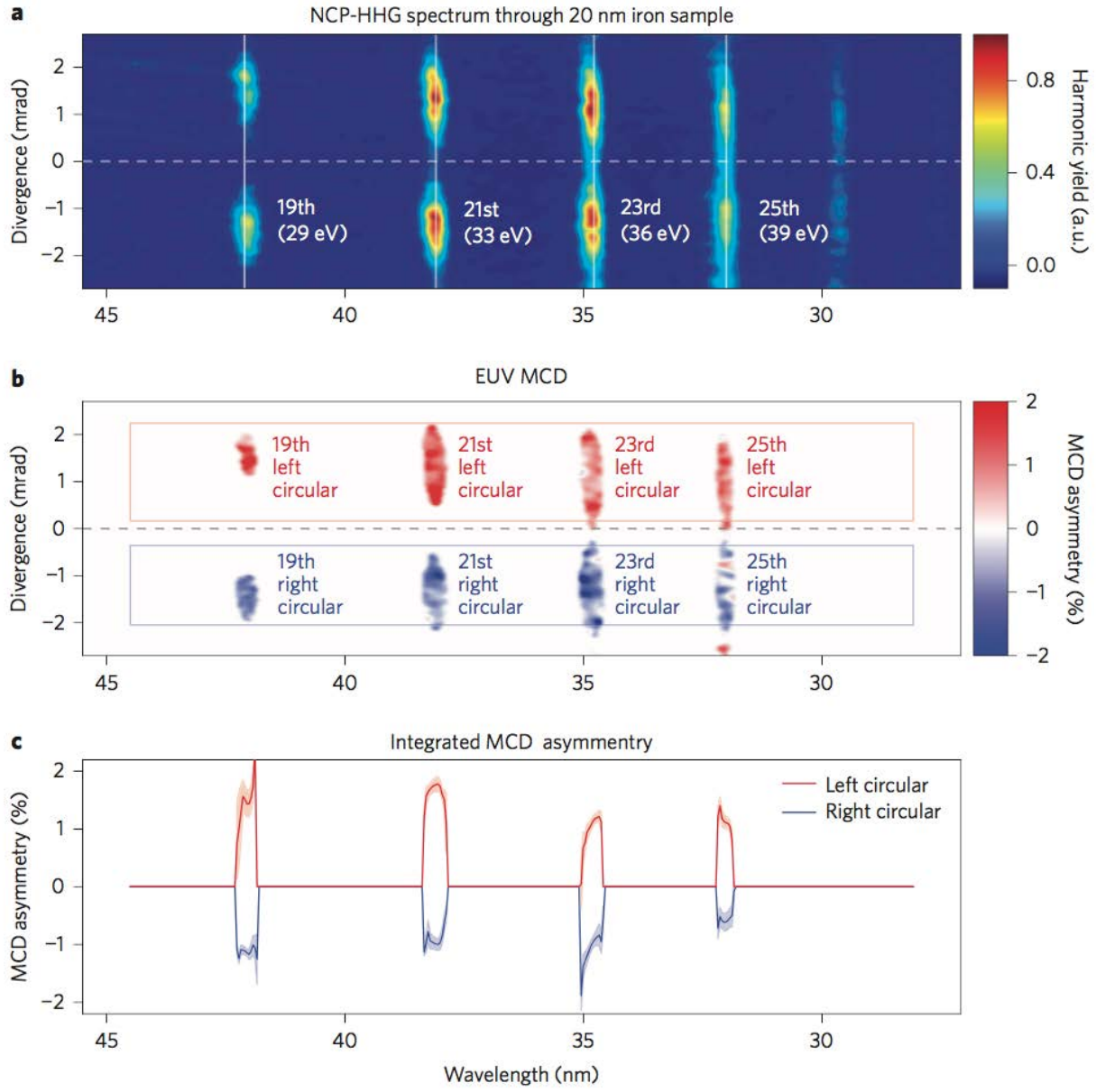

Figure 3.4: **EUV MCD of an iron film.** (a) Spectrum of circularly polarized harmonics generated from 800 nm beams focused in argon and transmitted through a 20-nm-thick iron sample at 45° incidence. (b) MCD asymmetry between opposing magnetization states in the iron sample. As expect, LCP harmonics (red) display opposite dichroism to RCP harmonics (blue). (c) Integrated MCD asymmetry and 95% confidence interval demonstrate that the dichroism is antisymmetric for the LCP and RCP polarizations and is in good quantitative agreement with the predicted magneto-optical contrast based on the available synchrotron data. Figure from [48].

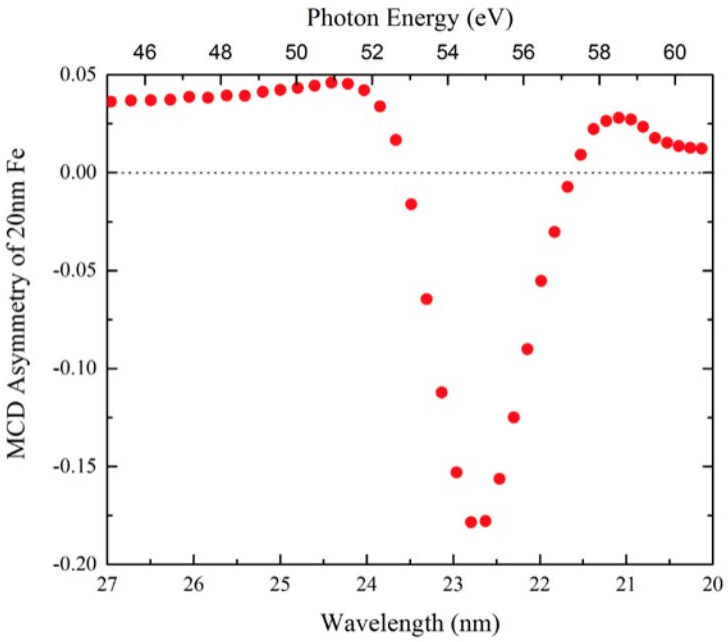

Figure 3.5: **Predicted MCD contrast for a 20 nm iron sample at** 45°**.** In this study we probed the iron sample in the range of 29 eV to 39 eV, which is not explicitly covered by the available data and this graph. However, the MCD asymmetry is approximately 3.5% at 45 eV and slowly decreasing. Thus, the MCD asymmetry of approximately 1.5% seen experimentally at 33 eV is consistent with an extrapolation of this synchrotron-derived data [127]. Figure from [48].

Simulations also provide clear insight into the temporal structure of the EUV emission. When all the harmonics are angularly separated (Fig. 3.6a), the EUV beams emerge as single long pulses (Fig. 3.6b), with a temporal duration somewhat shorter than that of the driving laser (that is, a several-femtosecond pulse). When the harmonics are angularly overlapped, the standard attosecond pulse train is generated, which consists of numerous attosecond bursts (Fig. 3.3e). However, with few-cycle driving pulses, angularly dispersed super-continuum harmonics are generated (Fig. 3.6c). In the time domain, this manifests as an isolated attosecond pulse of circularly polarized EUV light (Fig. 3.6d). Though previous theoretical works have proposed the generation of isolated circularly polarized attosecond pulses using exotic conditions, such as very intense terahertz fields [176], to our knowledge, the NCP-HHG method is the first experimentally realized method that is capable of producing isolated attosecond pulses with pure-circular polarization. This exciting capability

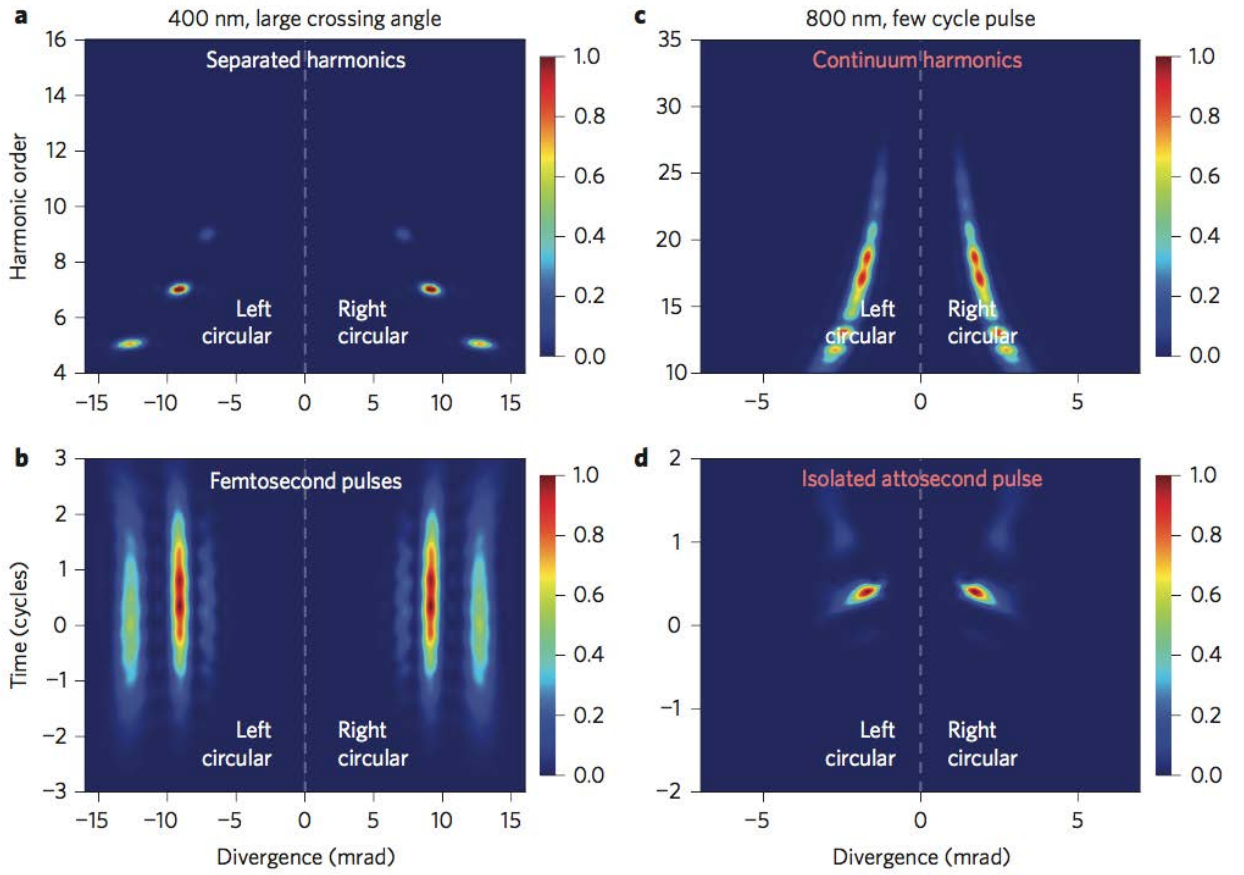

Figure 3.6: **Numerical simulations reveal additional capabilities of the NCP-HHG method.** (a) When driven by 4.3-cycle 400 nm pulses at a large (64 mrad) crossing angle, angularly separated harmonics are produced, obviating the need for a spectrometer. (b) In the time domain, each of these harmonics manifests as an angularly separated pulse with a timescale similar to the driving laser. (c) When driven with 1.1-cycle 800 nm pulses (32 mrad crossing angle), supercontinuum harmonics are produced. (d) In the time domain, the EUV emission manifests as two isolated attosecond pulses, on LCP and one RCP. Color scales are in linear arbitrary units. Each panel is normalized separately. Figure from [48].

has been further theoretically explored [177] and recently experimentally demonstrated [49, 178], thereby enabling the use of NCP-HHG to study chiral dynamics on femtosecond and attosecond timescales.

Note that it should be possible to produce elliptically polarized isolated attosecond pulses through the collinear two-color counter-rotating HHG scheme, albeit with reduced flux as compared to the typical case of linearly polarized attosecond bursts generated in that modality [47].

3.3.3 Circularly Polarized Noncollinear HHG Conclusions

Looking forward, the NCP-HHG method is poised to enable breakthrough probes of ultrafast dynamics. When driven with few-cycle pulses, simulations indicate that the NCP-HHG method will produce two circularly polarized isolated attosecond pulses, one propagating to the left and one to the right. This geometry naturally lends itself to an attosecond pumpattosecond probe experiment, which could be implemented using a single split-mirror focusing optic to adjust the temporal delay. Because the NCP-HHG method can eliminate the need for all other optics, gratings and filters, both the EUV intensity at the sample and the EUV flux at the detector could reach levels unprecedented in attosecond pumpattosecond probe experiments, potentially transforming these formidable experiments into commonplace techniques for probing the fastest processes in materials, molecules and atoms. Similarly, for imaging studies, refocusing the two beams of opposite helicity with a single optic will allow for new control over illumination, proving either separated right and left circular polarization, or a textured linear polarization reproducing the rotating polarization pattern of the source. Furthermore, recent work has shown that high-intensity circularly polarized EUV pulses can be used to generate attosecond magnetic field pulses [179].

Here, we have demonstrated NCP-HHG for the first time, and have shown that this method generates bright circularly polarized EUV beams of both left and right helicity simultaneously. Owing to selection rules, the two helicities are angularly isolated, and each harmonic order is emitted at a different angle, allowing the HHG process itself to serve as a spectrometer. Conveniently, the EUV light is well separated from the intense driving-laser beams. Using this new light source, we performed an EUV MCD measurement that confirmed the circular polarization of the EUV light and demonstrated that the flux and stability of the source are sufficient for real-world studies of femtosecond magnetic dynamics. Importantly, we demonstrated that the single-atom physics of the NCP-HHG process is identical to that of single-beam linearly polarized HHG, indicating that the NCP-HHG method can be extended to produce circularly polarized harmonics in the soft x-ray region by using mid-infrared driving lasers [96, 120], produce high-flux EUV sources using

ultraviolet driving lasers [110], and generate isolated attosecond pulses using few-cycle driving lasers [100].

3.4 Phase Matching in Noncollinear High-Harmonic Generation

Due to the angular separation between the driving laser beams, phase matching in noncollinear HHG [51, 166] is fundamentally different from either single-beam or collinear HHG [5, 36–38, 43, 105] and presents both new challenges and new opportunities. Previous investigations of noncollinear HHG have shown that phase matching effects can determine the angle of preferential harmonic emission and used this angular dependence to infer the difference in the magnitude of the harmonic and driving laser wavevectors [51]. Here, we experimentally and theoretically investigate the macroscopic physics of phase-matched noncollinear HHG at high pressures. First, we experimentally demonstrate phase matching of noncollinear HHG at ionization levels above critical ionization for the first time - which is normally the maximum ionization fraction at which full phase matching is possible in HHG. This capability is important because phase matching above critical ionization makes it possible to use higher driving laser intensities to produce bright higher-energy harmonics through the extension of the phase matched cutoff for a given wavelength driving laser. Second, we broadly explore the role of pressure in phase matching noncollinear HHG and show that the high pressures necessary to phase match noncollinear HHG mitigate the shortened interaction length in this geometry so that in many situations the flux can be identical to that produced in traditional HHG. Third, we extend the production of bright noncollinear highly elliptically polarized harmonics to photon energies of 90 eV, nearly doubling those obtained in previous studies [48]. Finally, we demonstrate the angular separation of high-harmonic orders due to the noncollinear geometry of the generation process, removing the need for a spectrometer and therefore avoiding the associated losses.

As discussed in the Introduction to this chapter (Section 3.1), when the driving lasers are linearly polarized there is no restriction on the number of photons from each beam contributing to the HHG process, as long as the total number of photons involved is odd to conserve parity [42].

This allows for many different channels of both high-order-sum-frequency generation (HOSFG, Fig. 3.7b) and high-order-difference-frequency generation (HODFG, Fig. 3.7c). If we recall the expression for the angle of harmonic emission, $\tan\theta_q = \Delta m \tan\theta_1/q$, where Δm is the difference in the number of photons absorbed from each beam, HOSFG corresponds to $|\Delta m| < q$ and HODFG corresponds to $|\Delta m| > q$. Therefore, high-harmonic photons created through an HOSFG process will be emitted at smaller angles than the driving laser separation (inside the two beams) and HODFG is emitted at larger angles than the driving laser separation (outside the two beams).

This angular dependence in the harmonic emission fundamentally changes the relationship between the phase velocity of the harmonics and the phase velocity of the driving laser. This change is important because the production of bright high-harmonic beams requires phase matched frequency upconversion. Phase matching is achieved when there is no wave vector mismatch between the driving lasers and the emitted harmonics ($\Delta\vec{k} = 0$), such that harmonics generated at different spatial locations add coherently. In a collinear geometry, a scalar comparison of the wavevectors is sufficient (Fig. 3.7d). However, in a noncollinear geometry we must consider the *projection* of the driving laser wavevectors along the direction of the harmonic emission due to the angular differences between them (Fig. 3.7e-f) [48, 51, 180–182]. This projection results in a modified phase-matching equation:

$$\Delta k = m_A k_A \cos(\theta_1 - \theta_q) + m_B k_B \cos(\theta_1 + \theta_q) - k_q, \tag{3.2}$$

where k_q is the wavevector of the emitted harmonic radiation, k_A and k_B are the driving laser wavevectors, and m_A and m_B are the number of photons absorbed from each beam respectively. Here, each wavevector includes the frequency-dependent bound- and free-electron contributions to the refractive index of the medium ($n_{neutral}$ and n_{plasma} respectively). While the refractive index of the medium for the harmonic light is close to one ($k_q \approx 2\pi/\lambda$), the refractive index at the driving laser frequency is increased in the presence of bound electrons and decreased in the presence of free electrons [5, 36], i.e. $n_{neutral} > 1$ and $n_{plasma} < 1$. Additionally, as the crossing angle θ_1 is increased, the noncollinear projection provides an increasing geometry-dependent phase mismatch

that is negative for HOSFG and positive for HODFG (Fig. 3.7b,c). Therefore, phase matching must be accomplished by balancing this large noncollinear phase mismatch with the correspondingly large pressure dependent contributions to the refractive index from the bound or free electrons.

The bound- and free-electron contributions to the refractive index are of opposite sign, and both scale linearly with the pressure in the interaction region, while their relative magnitude is determined by the ionization fraction (η). The ionization fraction at which the bound- and free-electron dispersions are equal is known as the critical ionization level ($\eta_c \approx 0.5\%$ for He with 800 nm) [5, 36]; here the phase mismatch due to the electrons bound in neutral atoms exactly cancels that of the free-electron plasma. Typically, critical ionization places an upper limit on the laser intensities that can be used to drive HHG because at ionization levels about η_c, the free-electron contribution to the index dominates, resulting in a driving laser phase velocity much greater than the speed of light [183, 184]. Exceptions to this rule include quasi phase matching [185] or UV-driven HHG, where bright HHG beams can be produced through effective phase matching in multiply-ionized plasmas [110].

In noncollinear HHG, phase matching requires a balance between the pressure dependent bound- and free-electron dispersions and the geometry-dependent phase mismatch from the noncollinear projection. Here, the geometry-dependent vacuum phase mismatch has different consequences for HOSFG and HODFG. In HOSFG a large (positive) neutral contribution is required to balance the negative phase mismatch from the noncollinear projection (Fig. 3.7h). Conversely, in HODFG a large (negative) plasma contribution is needed to balance the positive phase mismatch induced by the noncollinear projection (Fig. 3.7i). Note that regardless of the specific conditions, the noncollinear phase mismatch varies as the cosine of the angular separation between the emitted harmonics and the driving lasers, which behaves quadratic in the small angle approximation [51].

The effect of this noncollinear phase mismatch on the experimental conditions necessary for HHG, i.e. the pressure (P) and ionization fraction (η), can be calculated rigorously by considering the constituent components of the driving laser wavevectors, $k = k_{vacuum} + k_{neutral} + k_{plasma} + ...$ Because each of the wavevectors can be broken into individual components the noncollinear phase

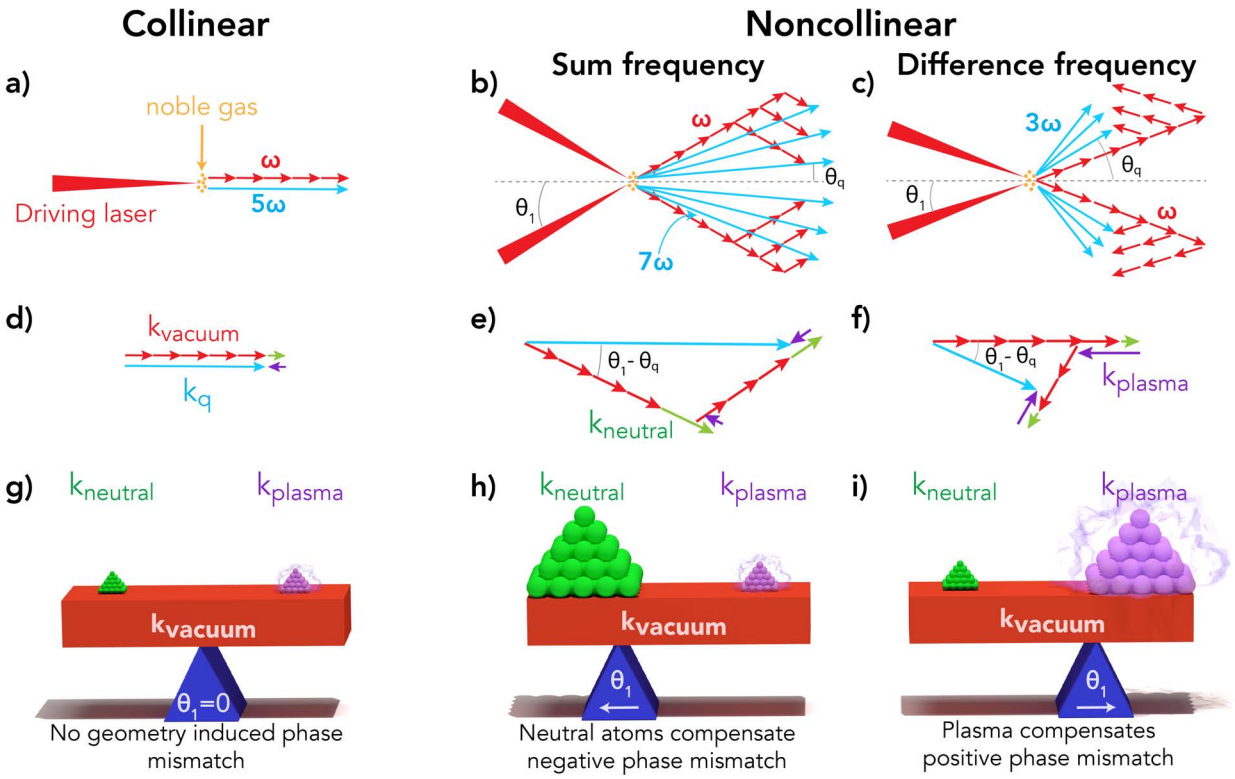

Figure 3.7: **Macroscopic physics of collinear and noncollinear HHG.** In collinear HHG, the driving laser and emitted harmonics propagate in the same direction (a), so that there is no angle induced phase mismatch between the vacuum wavevectors (d) and the neutral and plasma contributions to the phase mismatch can primarily balance each other to phase match the process (g). Conversely, in noncollinear HHG, two intense femtosecond lasers are overlapped in a gas jet at an angle $2\theta_1$. High-harmonic beams are emitted at angles θ_q, which are determined by conservation of energy and momentum. For high-order-sum-frequency mixing (HOSFG), the harmonic beams are emitted at smaller angles than the driving lasers (b), while for high-order-difference-frequency mixing (HODFG), the harmonic beams are emitted at larger angles (c). The difference in propagation direction introduces an angle-dependent contribution to the phase mismatch that is negative for HOSFG (e) and positive for HODFG (f). This phase mismatch must be balanced by either a large neutral contribution in HOSFG (h) or a large plasma contribution in HODFG (i). Figure from [167].

mismatch can also be broken into pressure independent (vacuum phase mismatch) and pressure dependent ($k_{neutral} + k_{plasma}$) portions. The pressure independent portion is given by

$$\Delta k_{vac} = m_A \frac{2\pi}{\lambda_A} \cos(\theta_1 - \theta_q) + m_B \frac{2\pi}{\lambda_B} \cos(\theta_1 + \theta_q) - \frac{2\pi}{\lambda_q}, \tag{3.3}$$

where λ_A and λ_B are the wavelengths of the driving lasers and λ_q is the harmonic wavelength (Fig. 3.8a). This projection gives a $(\theta_1 \pm \theta_q)^2$ dependence in the small angle approximation. The remaining portion of the wavevector mismatch is linearly dependent on pressure, so that the pressure at which $\Delta k = 0$ (Fig. 3.8b) will scale according to the pressure independent phase mismatch, with a θ_q^2 dependence (since θ_1 is fixed here). Different ionization fractions will require a different absolute phase matching pressure but will maintain the same functional form of the angular dependence (Fig. 3.8b).

There are additional terms that modify the driving laser wavevector, such as the Gouy phase and the atomic dipole terms that were not discussed above. However, these terms are independent of the pressure and ionization fraction and are small compared to the effect of the noncollinear angle on the vacuum wavevectors ($\sim 10^3$ m^{-1} vs $\sim 10^4$ m^{-1}). In general, the phase mismatch introduced by the noncollinear geometry dominates because it corresponds to a projection of the full vacuum wavevectors, which are large ($\sim 10^6$ m^{-1}). Consequently, even a small angle will have a large effect on the phase-matching conditions. Including the effect of the Gouy phase and atomic dipole terms in this analysis provides an additional pressure independent phase mismatch that is essentially angularly independent (because it's so much smaller than the vacuum phase mismatch). Therefore, these terms will uniformly increase or decrease the noncollinear phase mismatch by some amount but leave the angular dependence unchanged. Consequently, the phase matching pressures would be slightly shifted but the quadratic dependence on θ_q remains.

3.4.1 Experimental Measurements of Phase Matching in a Noncollinear Geometry

To experimentally investigate the angular dependence on phase matching in a noncollinear geometry we measure the high-harmonic flux as a function of gas pressure in the generation region

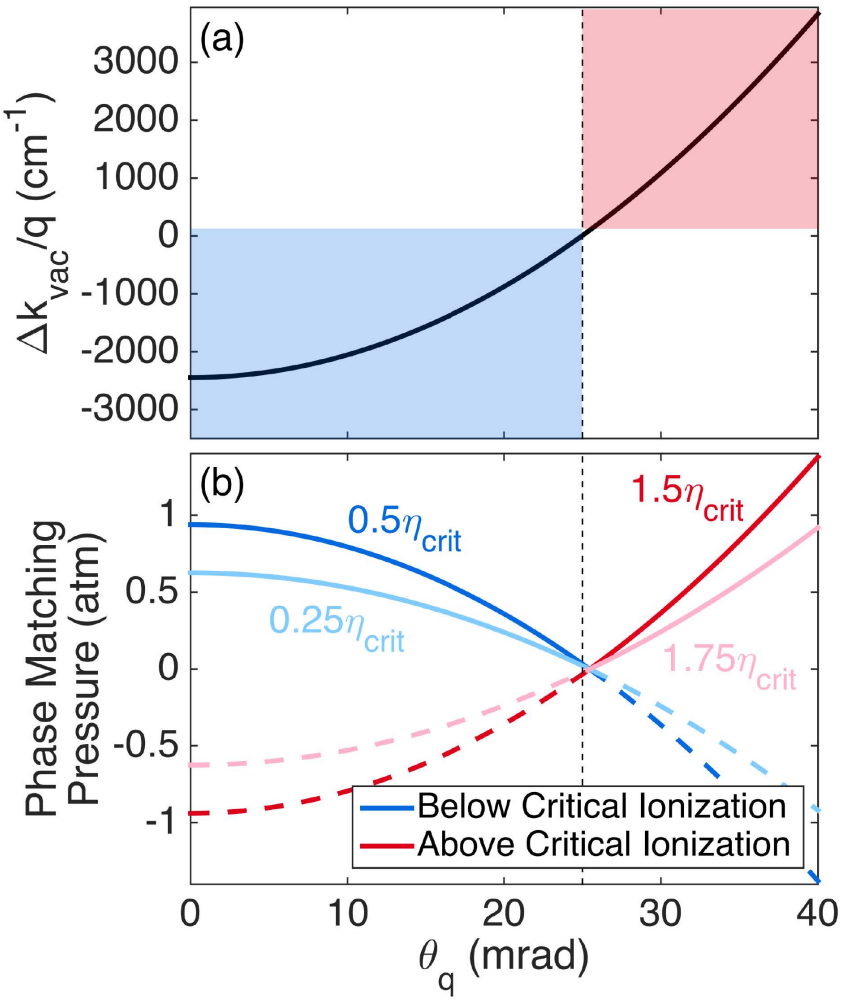

Figure 3.8: **Theoretical angular dependence of the phase matching of noncollinear HHG** in xenon with a driving laser angular separation with half-angle $\theta_1 = 25$ mrad (vertical dashed line). (a) The wave vector mismatch as a function of harmonic emission angle is negative for HOSFG and positive for HODFG. (b) Pressure tuning is used to balance the geometry-dependent phase mismatch, resulting in phase-matching pressures that increase with increasing angular separation from the driving laser. The sign of the pressure-dependent phase matching term is dependent on the ionization fraction of the medium, so HOSFG is phase matched below critical ionization (blue) because the positive pressure-dependent terms balance the negative noncollinear phase mismatch (blue region in (a)). Conversely, HODFG is phase matched above critical ionization (red), where the negative pressure-dependent terms balance a positive noncollinear phase mismatch (red region in(a)). Different experimental conditions (light and dark curves) change the absolute scaling of the phase-matching pressure but the angular dependence maintains the functional form of the wavevector mismatch. Dashed lines indicate regions where phase matching is experimentally unachievable because the required pressure are negative. Figure from [167].

(either Xe or Ar, see Appendix B). We generate noncollinear HHG by overlapping two focused 790-nm pulses (45 fs) in a 100-μm-diameter gas jet with an adjustable angle between them. The harmonic flux is maximized at the pressure that fully phase matches the HHG process (see Appendix B) [36, 37]. We probe this phase-matching pressure using linearly polarized driving lasers, taking advantage of the many high-harmonic beams emitted at many different angles simultaneously (Fig. 3.9a) through both HOSFG and HODFG. Additionally, we investigate phase matching both above and below critical ionization ($\eta \approx 4\eta_c$ and either $0.25\eta_c$ or $0.99\eta_c$ respectively), where these two distinctly different regimes exhibit different angular dependencies of the phase matching pressure (Fig. 3.9b).

Below critical ionization, the phase mismatch due to the neutral and plasma dispersion is positive and increases with increasing pressure. Consequently, increasingly high pressures can compensate the negative phase mismatch due to the noncollinear projection in HOSFG. This results in higher phase matching pressures for larger angular separations between the emitted harmonics and the driving laser beams (Fig. 3.9b, blue curve). Therefore, this increase in phase-matching pressure is especially important for larger angular separation between the driving lasers and circularly polarized noncollinear HHG. Although challenging to achieve, high gas pressures increase the number of emitters, which produces brighter harmonic emission (up to absorption limited lengths [36, 37]). Therefore, the high pressures required for phase matching noncollinear HOSFG help to counter the decrease in harmonic flux arising from the shortened interaction length as compared to the length attainable in single-beam or collinear HHG.

Above critical ionization, the phase mismatch due to the neutral and plasma dispersion is negative. In this case, higher pressures provide a more negative phase mismatch, which compensates the positive noncollinear phase mismatch in HODFG (Fig. 3.9b, red curve). Therefore, the observation of increasing phase-matching pressures for HODFG with increasing angular separation from the driving lasers is a clear signature of phase matching above critical ionization.

To provide further evidence of HODFG phase matching above critical ionization we perform numerical simulations of HHG including propagation using a method based on the electromagnetic

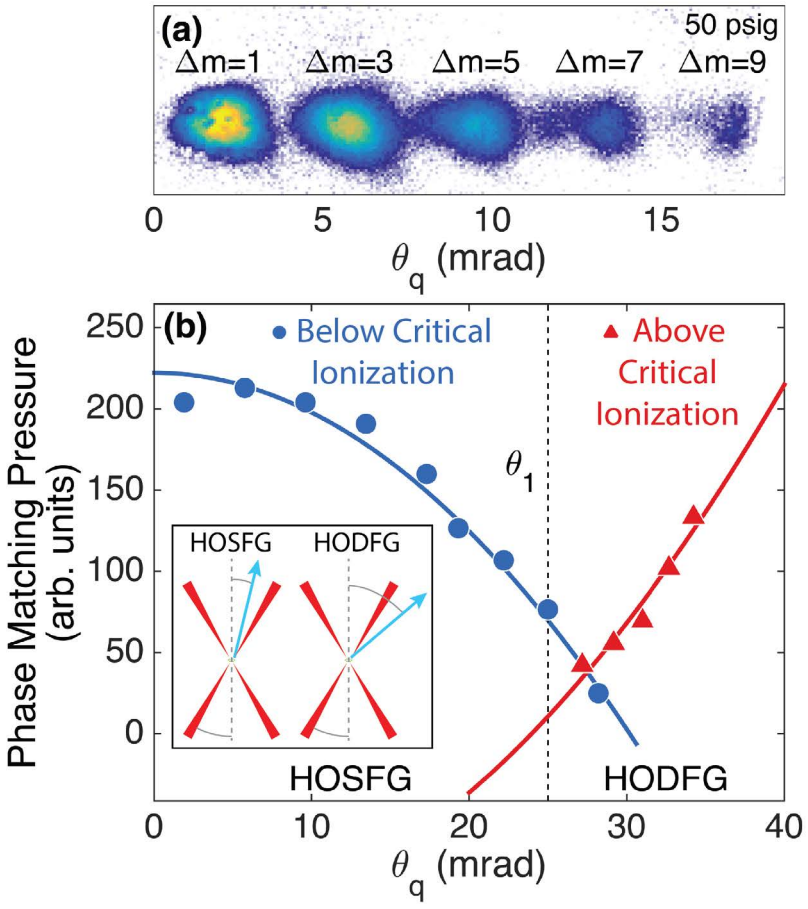

Figure 3.9: **Experimental phase-matching pressure measurements.** (a) Raw camera image showing HHG beams emitted into several different angles, θ_q, due to the absorption of different numbers of photons from each driving beam (Δm). We monitor the flux in each HHG emission angle as a function of the gas jet backing pressure to measure the angular dependence of the phase-matching pressure. (b) Phase-matching pressure as a function of harmonic-emission angle measured both above and below critical ionization; the angle of the driving laser, θ_1, as shown in the inset, is indicated by the vertical-dashed line. The noncollinear geometry results in a negative phase mismatch for HOSFG and a positive phase mismatch for HODFG, which increases in magnitude with increasing angular separation from the fundamental driving laser. Below critical ionization (blue circles, Xe, $\eta \approx 0.25\eta_c$ and $0.99\eta_c$), HOSFG requires higher pressures to compensate this geometric factor and HODFG requires lower pressures. The increase in phase matching pressure is more pronounced for harmonics with larger angular separation from the driving laser. Conversely, the opposite behavior is seen above critical ionization (red triangles, Ar, $\eta \approx 4\eta_c$). The solid lines are the result of fitting the data to the expected θ_q^2, dependence of the phase matching pressure. The experimental data points are measured at three different experimental conditions (see Appendix B). Figure from [167].

field propagator [186]. In these simulations, as in the experiment, two linearly polarized beams are crossed at an angle ($\theta_1 = 25$ mrad) to drive high-harmonic generation, producing high harmonics that are angularly dispersed (Fig. 3.10a). Comparing the simulated HHG yield at different pressures allows us to numerically investigate the role of phase matching in a noncollinear geometry. If the HHG process is equally well phase matched at all pressures then the harmonic intensity will scale as the pressure squared; deviations from that scaling indicate more or less efficient phase matching. The driving laser pulses are modeled so the ionization fraction in the interaction region is above critical ionization ($\eta = 2\eta_c$) at the peak of the pulse. Consequently, the pressure scaled harmonic yield for HOSFG decreases with increasing pressure. Conversely, the pressure scaled harmonic yield for HODFG either remains unchanged (one photon of DFG) or increases (two photons of DFG) for increasing pressures, indicating that HODFG is well phase matched above critical ionization and HOSFG is not (Fig. 3.10b) The ability to phase match above critical ionization provides the opportunity to drive the HHG process with more pulse energy than is possible for single-beam of collinear HHG, producing higher energy harmonics.

3.4.2 Circularly Polarized Noncollinear HHG Above 90 eV

Now that we have verified our model of phase matching in a noncollinear geometry, we can apply thet understanding to produce noncollinear highly elliptically polarized high harmonics. In HHG with circularly polarized counter-rotating driving lasers the conservation of spin angular momentum limits the difference in the number of photons absorbed from each beam to $\Delta m = \pm 1$. Therefore, the suppression of any HHG channels corresponding to higher values of Δm indicates that the remaining HHG emission is either circularly or highly elliptically polarized [45]. We produce highly elliptically polarized high harmonics up to 90 eV (Fig. 3.11), which is almost double the photon energies previously obtained using this technique [48]. We achieve these photon energies by modifying our experimental chamber to accommodate higher gas flow rates that result from increasing the pressure in the generation region and by using helium as the HHG medium. In single-beam HHG, higher-energy harmonics are produced by increasing the ionization potential of

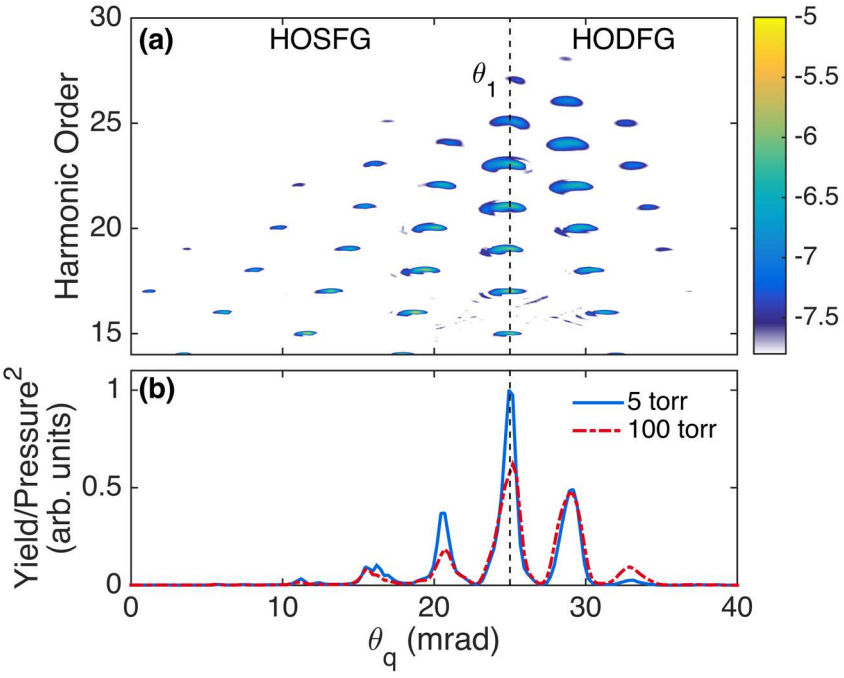

Figure 3.10: **Numerical simulations of noncollinear high-harmonic generation above critical ionization** ($\eta = 2\eta_c$) in an argon gas jet. (a) Harmonics are emitted into many different angles corresponding to both HOSFG and HODFG. Note the presence of even harmonic orders because this simulation uses a 790 nm and a 395 nm driving beam; here harmonic order is denoted with respect to the 790 nm beam. The harmonic intensity is shown on a log scale. (b) The integrated harmonic yield as a function of harmonic emission angle is dependent on the pressure. If the phase matching efficiency is unchanged then the yield will scale as the pressure squared, therefore differences in the pressure-normalized yield are due to phase matching. Comparison of low (solid blue) and high (dashed red) pressure shoes that HOSFG is not well phase matched above critical ionization but HODFG is. Here, the lines correspond to integrating the 21st harmonic order and above. Figure from [167].

the HHG medium or increasing the wavelength of the driving laser [5, 14, 36, 110, 187]. However, both of these approaches require increasingly high phase-matching pressures. In the noncollinear geometry, these effects are compounded by the geometry-dependent phase mismatch because the production of circularly polarized harmonics with counter-rotating driving lasers is an HOSFG process. Here, only HOSFG processes (with $\Delta m = \pm 1$) are possible because HODFG process would result in photons with a large and therefore forbidden spin angular momentum. Consequently, to favor HOSFG, the ionization fraction was maintained below the critical ionization level. As demonstrated here, the challenge of phase matching high energy circularly polarized noncollinear

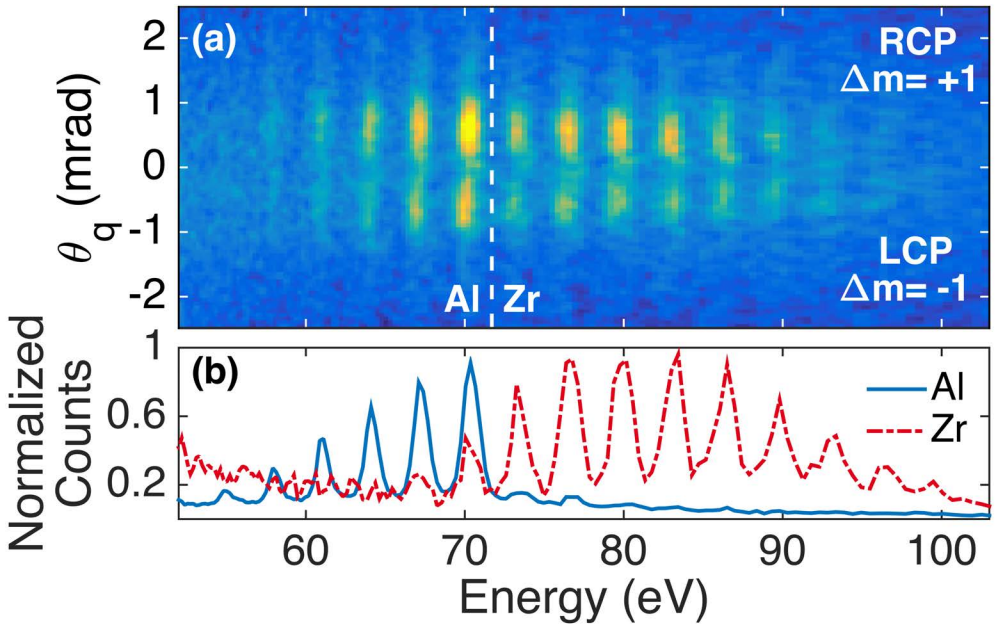

Figure 3.11: **Circularly polarized noncollinear HHG in excess of 90 eV.** (a) The angularly resolved spectrum obtained through noncollinear HHG in helium with circularly polarized driving lasers shows two circularly polarized harmonic beams with right and left circular polarization, respectively, at positive and negative divergence angles. (b) The angularly integrated spectrum shows high-order harmonics that extend to energies above 90 eV. An aluminum (Al) filter is used to isolate the low-energy portion of the spectrum (blue solid line) and a zirconium (Zr) filter is used to isolate the high-energy portion (red dashed line). Figure from [167].

HHG can be overcome with a full understanding of the phase-matching conditions in this geometry.

The high-energy harmonics from He (Fig. 3.11) are generated with usable flux ($\sim 10^6$ photons/sec/harmonic above the aluminum edge at ~70 eV [167]). We note that this flux is an order of magnitude lower than the flux that has been attained in high energy collinear circularly polarized HHG ($\sim 5 \times 10^7$ photons/sec/harmonic [45]). This difference is due to the difficulty in implementing very high pressures in the gas jet geometry required for noncollinear HHG and therefore the difficulty in achieving the maximum absorption limited HHG flux. Therefore, in the future, further increasing the gas pressure could result in even brighter harmonics because of a favorable phase matching pressure scaling, which mitigates the decrease in interaction length due to the finite overlap region between the two beams. This can be understood by considering the crossing angle dependence of the pressure-length-product – in the small angle approximation the length of the

overlap region between the two beams decreases linearly as θ_1 is increased but the phase matching pressure increases quadratically with θ_1. Consequently, the phase matched pressure-length-product actually increases linearly with increasing noncollinear crossing angle. In the case where the flux is limited by the length of the interaction region, for example by the extent of the gas jet, we would expect the flux generated by a noncollinear geometry to exceed that obtained in the collinear geometry. In the case where significant reabsorption of the harmonic light takes phase, as in the commonly encountered absorption limited regime, noncollinear and collinear HHG should produce identical flux. However, we emphasize that the pressure required for phase matching noncollinear HHG increases dramatically with angle, as well as with the wavelength of the driving laser and the ionization potential of the gas species, quickly reaching many atmospheres. Moreover, to avoid reabsorption of the harmonic light, the pressure must quickly transition to high vacuum, presenting a formidable design challenge.

3.4.3 Angular Separation of High Harmonics Without a Spectrometer

Finally, we use our understanding of noncollinear phase matching to achieve spatial separation between different high-harmonic orders without the use of spectrometer. This spatial separation is possible in a noncollinear geometry because the angle at which harmonics are emitted, θ_q, depends on the harmonic order. Separating the harmonic orders in the far field requires that the difference in θ_q between adjacent harmonic orders be larger than the divergence of the high harmonics. Previously we showed the separation of low-order harmonics in circularly polarized noncollinear HHG (3rd and 5th, see Appendix A). Here, we extend this technique to demonstrate a clear spatial separation of higher harmonic orders (13th and 15th) in the far field (Fig. 3.12a). We do so with linearly polarized noncollinear HHG, which allows for the use of a larger Δm to increase the angular spread between adjacent harmonic orders (see Eq. 3.1).

As we increase the pressure in the interaction region harmonics emitted with larger angular separation from the driving lasers, and therefore with smaller θ_q, are preferentially phase matched (Fig. 3.12b-c). Therefore, we can use pressure tuning to favor harmonic emission at a particular

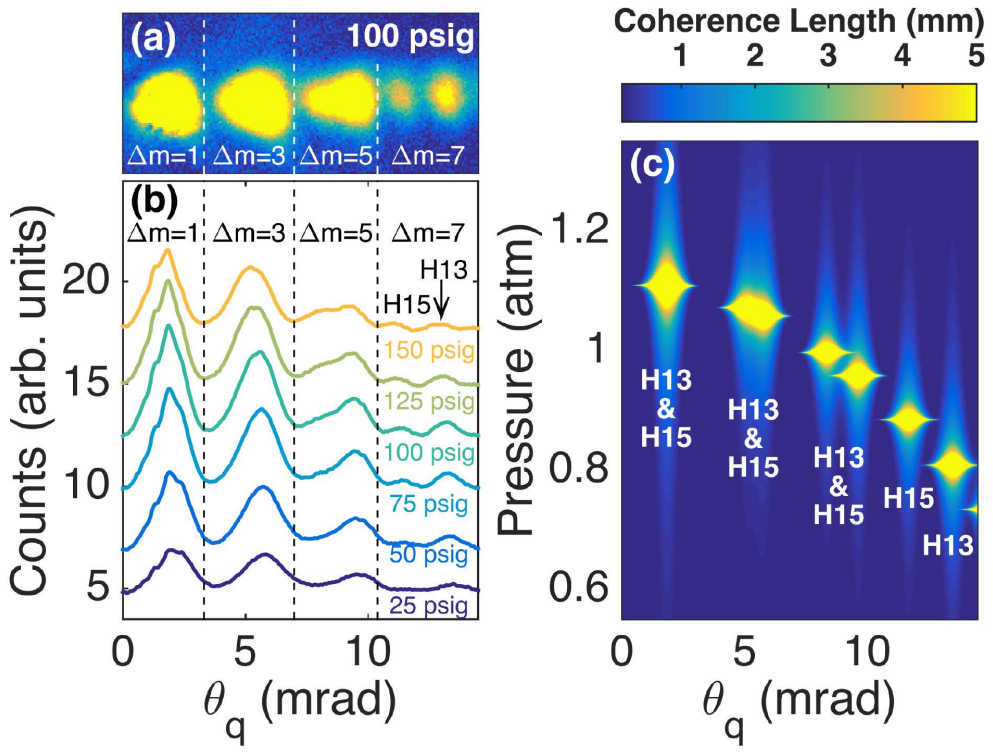

Figure 3.12: **Angular separation of high-harmonic orders without a spectrometer.** (a) At higher pressures, the raw camera image clearly shows two spatially separated peaks on the right hand side, corresponding to the 13th and 15th harmonic orders produced through HOSFG with $\Delta m = 7$. (b) Spatial distribution of harmonic flux with increasing gas-jet backing pressure, vertically displaced for clarity. The peak that grows in between the main $\Delta m = 5$ and 7 peaks corresponds to the 15th harmonic order, which is spatially separated from the 13th harmonic order. (c) Spatial separation of high-harmonic orders in the far field is only possible if the difference in the emission angle of adjacent harmonic orders is larger than the divergence of the harmonics themselves. The theoretical coherence length of harmonic emission as a function of pressure and θ_1 shows pressures where this can be achieved and bright well-separated emission of the 13th and 15th harmonic orders is attained. Figure from [167].

angle corresponding to bright harmonic emission of the 13th and 15th harmonic orders, produced through HOSFG with $\Delta m = 7$. At these harmonic emission angles the 13th and 15th harmonic orders are well separated, demonstrating the spatial separation of high-harmonic orders in the far field without a spectrometer. In this case the laser intensity is chosen so that very little of the next harmonic order is produced. If the 17th harmonic order was present it could not be similarly separated without increasing either Δm or the angle between the fundamental driving beams.

Consequently, this technique can only be applied to achieve complete angular separation without a spectrometer in a situation where a small number of harmonic orders are produced, but in general provides an easily tunable spatially varying energy distribution.

3.4.4 Phase Matching in Noncollinear HHG Conclusions

In summary, noncollinear HHG is an emerging technique that can be used to produce angularly separated circularly polarized high harmonics, generate isolated attosecond bursts, and separate high-harmonic orders from both each other and the fundamental driving lasers. However, to fully harness HHG in a noncollinear geometry, a complete understanding of the phase matching is necessary. We showed that phase matching HOSFG requires increasingly high pressures in the interaction region, which has important experimental consequences for the production of high-energy circularly polarized high harmonics. These increased phase matching pressures are technically challenging to achieve but offset the decrease in flux due to the shortened interaction region in a noncollinear geometry. Additionally, we demonstrated phase matching above critical ionization using HODFG, which enables higher driving laser intensities to produce higher energy harmonics than are attainable in single-beam HHG. Next, we used our understanding of phase matching in this noncollinear geometry to produce noncollinear highly elliptically polarized high harmonics in excess of 90 eV, extending the energy range over which this technique is useful for studying circular dichroism. Finally, we demonstrated angular separation of high-harmonic orders without the use of a spectrometer, which is experimentally advantageous because EUV optics are difficult to fabricate and can exhibit high loss. Further experiments may extend noncollinear HHG to produce noncollinear circularly polarized harmonics at even higher energies and use bright (i.e. phase matched) circularly polarized isolated attosecond bursts [49, 178] to investigate dichroism on the fastest timescales.

3.5 Conclusions and Outlook

Noncollinear HHG is a promising geometry, which employs the use of two angularly separated driving beams to provide additional control over and degrees of freedom in the HHG process. Excitingly, this geometry enables the generation of circularly polarized high harmonics that are angularly separated into energetically identical RCP and LCP beams. Additionally, the macroscopic physics of noncollinear HHG is modified such that HODFG requires ionization levels above critical ionization to phase match. There are a number of exciting extensions of this work that can be explored, which include extending NCP-HHG to longer wavelength driving lasers, applying NCP-HHG to study dichroism, and producing bright HHG beams at keV photon energies with Ti:Sapphire lasers via noncollinear HODFG.

Additionally, NCP-HHG may provide a solution for an outstanding issue that is predicted to arise when generating HHG with driving laser wavelengths far in the IR ($\sim$10 μm) – the Lorentz force. Recall that in NCP-HHG the combination of two circularly polarized driving lasers produces a linearly-polarized rotating polarization grating in the region of overlap. However, this stated linearity is actually an approximation. If the two circularly polarized lasers were combined collinearly, then the resultant field would be perfectly linearly polarized everywhere. When instead the two beams are combined noncollinearly the polarization planes of the two beams are not exactly the same and there is an incomplete cancellation of the electric field, which results in a small amount of ellipticity remaining in the direction along the centerline between the two beams. During the HHG process, as the electron is accelerating in the laser field, this ellipticity will therefore push the electron in that direction along the centerline between the two beams. This deflection of the electron trajectory can cause the electron to "miss" the parent atom and therefore decreases the probability of recombination and the HHG yield [188].

While this may sound like a bad thing, it is actually potentially advantageous because it can counter another well known deflection of the electron trajectory – the deflection due to the Lorentz force ($\vec{F} = \vec{v}/c \times \vec{B}$) [189–191]. Typically the Lorentz force is vanishingly small in HHG because

the magnetic field component of the laser field is much smaller than the electric field component. However, when the driving laser wavelength gets sufficiently long, the electron is accelerated to velocities large enough that the Lorentz force can be significant. The Lorentz force always acts in the direction of propagation of the laser and deflects the electron in that forward direction so that it can quench recombination. This effect therefore hinders the scaling of HHG to longer wavelength driving lasers and the associated production of higher energy harmonic photons.

Interestingly, NCP-HHG presents itself as a scheme to mitigate the detrimental effects of the Lorentz force at long wavelengths [188] because the deflection of the electron due to the ellipticity along the centerline acts along the same axis as the Lorentz force. However, while the Lorentz force always pushes the electron in the forward direction, the direction that the ellipticity pushes the electron flips every half cycle of the driving laser field. Therefore, once per cycle, these two effects should cancel out, enabling efficient recombination. The main signature of this effect, besides efficient HHG at longer wavelengths, is the appearance of even harmonic orders because of the symmetry breaking resulting in harmonic emission every cycle (instead of every half cycle, which results in only odd harmonic orders). Theoretical simulations indicate that these even harmonics should be observable at relatively modest wavelengths (1.6 μm) and noncollinear crossing angles (70 mrad) [188].

Another exciting application of NCP-HHG is as a light source for dichroism studies. NCP-HHG is an ideal source because energetically identical beams of RCP and LCP are produced. Therefore, dichroism can still be easily investigated in situations where the handedness of the sample cannot be flipped, by instead flipping the helicity of the light. Finally, the benefits of the noncollinear phase mismatch need to be further developed. While we did successfully demonstrate phase matching of noncollinear HHG above critical ionization we did not produce dramatically higher energies than attainable with single-beam HHG. Therefore, more work must be done to push this technique to it's full potential.

Chapter 4

High Harmonics with Spatially Varying Ellipticity

This chapter is adapted, with permission, from:

- Jennifer L. Ellis, Kevin M. Dorney, Daniel D. Hickstein, Nathan J. Brooks, Christian Gentry, Carlos Hernandez-Garcia, Dmitriy Zusin, Justin M. Shaw, Quynh L. Nguyen, Christopher A. Mancuso, G. S. Matthijs Jansen, Stefan Witte, Henry C. Kapteyn, and Margaret M. Murnane. High harmonics with spatially varying ellipticity. *Optica*, In press. Copyright 2018 Optical Society of America

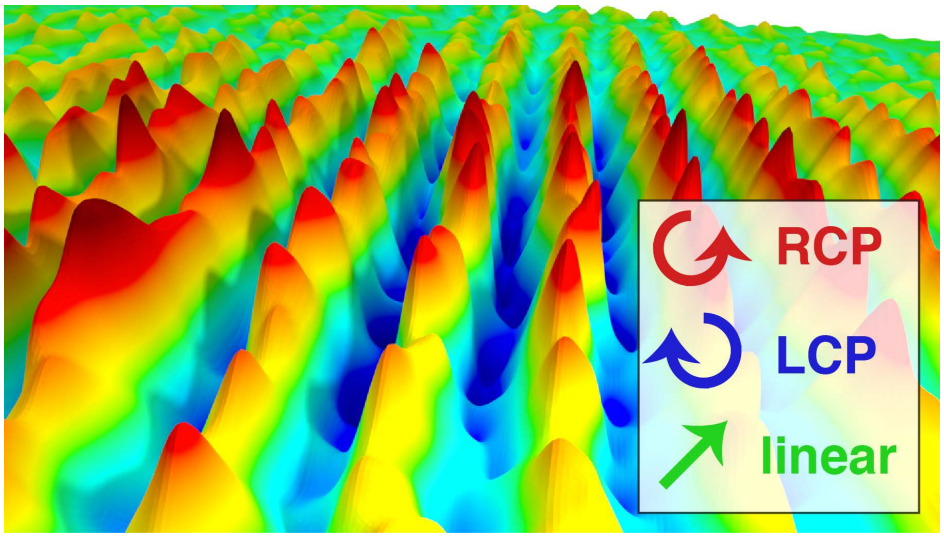

Figure 4.1: **Illustration of the spatial polarization distribution produced through the superposition of two spatially separated and orthogonally polarized high-harmonic beams, resulting in a spatially varying ellipticity.**

4.1 Abstract

We present a new method to produce ultrashort pulses of circularly polarized extreme ultraviolet (EUV) light. We combine two orthogonally polarized high-harmonic sources to produce a far-field beam with a uniform intensity distribution but with a spatially varying ellipticity – ranging from linearly to fully circularly polarized. This spatially varying ellipticity was characterized using EUV magnetic circular dichroism, which demonstrates that a high degree of circularity is achieved, reaching almost 100% near the magnetic M-edge of cobalt. The spatial modulation of the polarization facilitates measurements of circular dichroism, enabling us to measure spectrally resolved magnetic circular dichroism without the use of an EUV spectrometer, thereby avoiding the associated losses in both flux and spatial resolution, which could enable hyperspectral imaging of chiral systems. Through numerical simulations, we also show the generality of this scheme, which can be applied with both the discrete harmonic orders generated by many-cycle pulses, or the high-harmonic supercontinua generated by few-cycle driving laser pulses. Therefore, this technique provides a promising route for the production of bright isolated attosecond pulses with circular polarization that can probe ultrafast spin dynamics in materials.

4.2 Introduction

High-harmonic generation (HHG) is an extreme nonlinear optical process, in which an intense femtosecond laser pulse is coherently upconverted to produce ultrashort pulses of extreme ultraviolet (EUV) and soft x-ray light [3–5]. As a unique tabletop source of ultrafast and spatially and temporally coherent beams at short wavelengths, HHG enables novel probes of atoms, molecules, and materials at their natural spatial and temporal scales. Recent advances include the use of ultrafast photoelectron spectroscopies to uncover the fastest femtosecond-to-attosecond charge dynamics known to date in molecules, nanoparticles, and materials [24, 28, 29, 192–194] and the first sub-wavelength imaging at few-nm wavelengths [8]. Traditionally, HHG is driven by a single linearly polarized laser, which results in linearly polarized high harmonics [34, 40, 195].

However, novel combinations of two differently polarized driving lasers can produce bright circularly polarized high harmonics [42–45, 48, 114, 115]. This polarization control in HHG has made it possible to study nanoscale dynamics in magnetic, molecular, and other spin-dependent systems [43, 45, 46, 196–199].

Here, we present a new method to produce circularly polarized EUV light, which generates a high-harmonic beam with spatially varying ellipticity (SVE-HHG) through the coherent superposition of two spatially separated and orthogonally linearly polarized high-harmonic sources. In close analogy to a Young's double-slit experiment [200], two spatially separated high-harmonic sources diverge to overlap in the far field (Fig. 4.2). If the polarization vectors of the independent HHG sources are parallel, as in the typical Young's experiment, the far-field distribution exhibits intensity interference resulting in the classic fringe pattern [201]. However, if these two sources have orthogonal linear polarizations, then there are no interference fringes in the intensity. Instead, there is a phase interference that results in a spatially varying ellipticity [202–204]. Therefore, in the far field there is a uniform intensity profile but the polarization in the transverse plane varies from linear, to elliptical, to purely circular polarization (Fig. 4.2). We note that this scheme was previously proposed for HHG in Zerne *et al.* [201] but to our knowledge has not been demonstrated to date.

SVE-HHG is an interesting and advantageous geometry for several reasons. First, both driving lasers are linearly polarized and independently drive the HHG process – so that both the single-atom and macroscopic physics of the HHG process are identical to that of traditional single-beam HHG. This makes SVE-HHG the first method to produce circularly polarized harmonics with the same cutoff photon energy and photon flux as linearly polarized HHG. Furthermore, when there are several harmonic orders present, the far-field polarization distribution is the coherent superposition of the spatially varying ellipticity of each individual harmonic order. Therefore, for samples that are sensitive to the polarization, a high-harmonic spectrum can be obtained via Fourier transformation of the spatial polarization pattern along the direction of the ellipticity variations. We experimentally demonstrate that this ability provides for energy-resolved measurements of circular

dichroism without the use of a spectrometer, thus avoiding the associated losses and enabling spatially resolved spectroscopy of chiral systems. Finally, we show through numerical simulations that this scheme is general and can be applied to either discrete harmonic orders, driven by multi-cycle pulses, or high-harmonic supercontinua, driven by few-cycle laser pulses. Therefore, SVE-HHG presents an exciting route for the production of isolated attosecond pulses with circular polarization, enabling the study of the fastest known spin dynamics in magnetic materials, which can occur on femtosecond-to-attosecond timescales [28].

While other HHG approaches, such as the collinear or noncollinear mixing of counter-rotating beams, can also produce isolated attosecond bursts of circularly polarized EUV light [47, 49, 177], there are significant challenges for extending those techniques to the mid-infrared. Mid-infrared driven HHG is advantageous because the harmonics are produced with higher photon energies and naturally emerge as isolated attosecond bursts [99, 101]. However, noncollinear HHG is hampered by a finite interaction length and the need for high gas pressures to achieve reasonable conversion efficiencies [51, 167], both of which decrease the achievable flux. Collinear bi-chromatic HHG, on the other hand, suffers from polarization degradation and eventual photon energy limits due to the spectral overlap of oppositely polarized adjacent harmonic orders [45, 93]. In contrast, SVE-HHG can be applied with the same high conversion efficiency as single-beam HHG at any wavelength and in any geometry (gas jet, gas cell, waveguide, etc.). This makes mid-infrared driven SVE-HHG a promising route for producing bright beams of circularly polarized isolated attosecond pulses in the soft x-ray region.

4.3 Experiment

To experimentally implement this technique, we use a common-path interferometer to split the driving laser (KM Labs Wyvern HE, 800 nm, 45 fs, 1 kHz, 8 mJ) into two orthogonally polarized beams, which are then focused into a gas jet to drive two independent HHG sources (Fig. 4.2). The common-path interferometer consists of a birefringent plate (α-BBO), with its extraordinary axis oriented vertically, and a pair of birefringent wedges (α-BBO, wedge angle=100 mrad), with

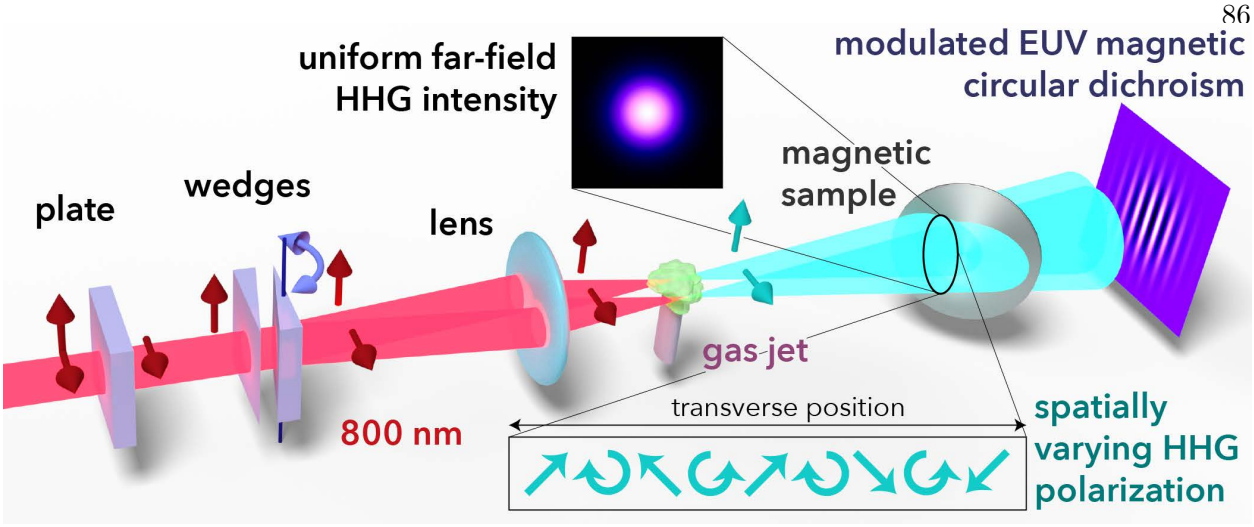

Figure 4.2: **Experimental setup to produce a high-harmonic beam with spatially varying ellipticity.** A common-path interferometer creates two orthogonally polarized and angularly separated beams, which are focused to two spatially separated focal spots for driving the high-harmonic generation (HHG) process in a neon gas jet. The interferometer consists of a birefringent plate and a pair of birefringent wedges (α-BBO), which split an incoming pulse into two orthogonally polarized and angularly separated pulses. The degree of angular separation is controlled by the rotation of the second wedge about the vertical axis. A lens then focuses the two orthogonally polarized beams into a gas jet and maps the angular separation into a spatial separation at the focus (exaggerated for clarity). The spatially separated focal spots each independently drive the HHG process yielding two orthogonally polarized HHG beams, which diverge to overlap in the far field and thereby produce a far-field distribution with a spatially varying ellipticity (SVE-HHG). This ellipticity distribution is measured using the extreme ultraviolet magnetic circular dichroism (EUV MCD) response of a cobalt thin film. The fundamental is blocked with an aluminum filter (not shown) to isolate the EUV light before the magnetic sample. Figure from [205].

their extraordinary axes oriented horizontally [206–208]. First, the birefringent plate splits the incident fundamental beam into a time-delayed and orthogonally polarized pulse pair. Following the delay plate, the beams encounter the first wedge such that one of the beams is polarized along the extraordinary axis while the other beam is polarized along the ordinary axis, which introduces an angular separation between the two orthogonally polarized beams. The second wedge compensates most of the angular separation induced by the first wedge; however, small rotations of the second wedge about the vertical axis leave a controllable amount of angular separation between the two orthogonally polarized beams. Additionally, since the extraordinary axis of the delay pate is orthogonal to those of the wedges, the time delay between the two fundamental pulses can be

precisely compensated by the degree of insertion of the second wedge. Finally, a focusing lens (f = 25 cm, waist ∼40 μm) is positioned after the interferometer such that the angular separation between the two beams (∼0.2 mrad) is mapped to a spatial separation (∼100 μm) at the focus (i.e., the second wedge is at the back focal plane of the lens). Each linearly poalrized beam independently drives the HHG process in a neon gas jet, producing two spatially separated and orthogonally polarized HHG sources (Fig. 4.2). These two high-harmonic beams diverge and overlap in the far field, thereby producing a sinusoidally spatially varying ellipticity.

4.4 Characterization of the Far-Field Polarization

We confirm the spatially varying ellipticity of the SVE-HHG scheme through EUV magnetic circular dichroism (EUV MCD), in which the magnetic state of a material is probed by the dichroic absorption of circularly polarized light (Fig. 4.2) [124]. The helicity dependent absorption of light by magnetic materials varies linearly with the degree of circularity of the illumination field, i.e. with the ratio of the Stokes parameters, S_3/S_0 [125, 126]. Therefore, EUV MCD provides a rigorous characterization of the polarization state of this source. We perform EUV MCD measurements on a 20-nm-thick cobalt film, which is supported in 200 nm of aluminum. An electromagnet magnetizes the cobalt in the plane of the thin film, which is oriented at 45° with respect to the direction of propagation of the harmonic beam. This geometry results in a reasonable projection of the in-plane magnetization vector along the spin-angular momentum vector of the incident light. We compare the transmitted EUV intensity for opposite magnetizations of the film ($I_{+,-}$), and quantify the dichroism signal via the magnetic asymmetry, $A = (I_+ - I_-)/(I_+ + I_-)$ [125]. Placing a curved grating (Hitachi 001-0266) after the magnetic sample spectrally resolves the harmonics in one dimension while preserving spatial resolution in the dimension of the polarization modulations, thereby enabling the measurement of the spatially resolved magnetic asymmetry for each harmonic order individually.

While the transmitted intensity does not directly show any interference due to the orthogonal polarization of the two harmonic sources (Fig. 4.3a), the spatially varying ellipticity is revealed

upon subtraction of the transmitted intensity for the two opposite magnetizations of the cobalt film (Fig. 4.3b). This polarization grating manifests as a sinusoidal variation in the magnetic asymmetry spatially along the beam profile, which is visible in several harmonic orders. Since the film is uniformly magnetized, this variation in the asymmetry is due to the spatially varying ellipticity of the high-harmonic light, where zero asymmetry indicates linear polarization and positive or negative asymmetry corresponds to either right- or left-circular polarization, depending on the sign of the MCD response of the material. Therefore, the amplitude of the sinusoidal variation in the magnetic asymmetry is directly related to the maximum ellipticity present in the high-harmonic polarization distribution (Fig. 4.3b inset). Additionally, the relative phase of the sinusoidally varying asymmetry between harmonic orders indicates the relative sign of the EUV MCD (see Appendix C).

Comparison with literature values for the magnetic asymmetry of cobalt films [127] indicates that the degree of circularity attained is high (Fig. 4.3c), approaching 100 % near the magnetic M-edge of cobalt (see Appendix C). While there are some discrepancies in the measured asymmetry at the harmonic orders below the M-edge, it is possible that these disagreements are due to differences in sample preparation, which can modify the magneto-optical constant. These small modifications would have larger ramifications away from the M-edge, where the MCD effect is small. To confirm these results, we repeated the measurement with an unmagnetized sample and observed no modulations in the asymmetry, indicating that these sinusoidal variations are indeed due to EUV MCD in the cobalt film, thus confirming the spatially varying ellipticity of the high harmonics. We note that reflection off the grating does have polarization dependence, so that after the grating the circularity of the harmonics is diminished. However, the magnetic sample is upstream from the grating so this does not affect the MCD measurement. This polarization dependence can impart a fringe structure on the reflected harmonics depending on the orientation of the polarization of the linearly polarized regions, which is useful for alignment purposes but is minimized when taking MCD measurements (by rotating the linearly polarized regions to be an equal mixture of s- and p-polarization).

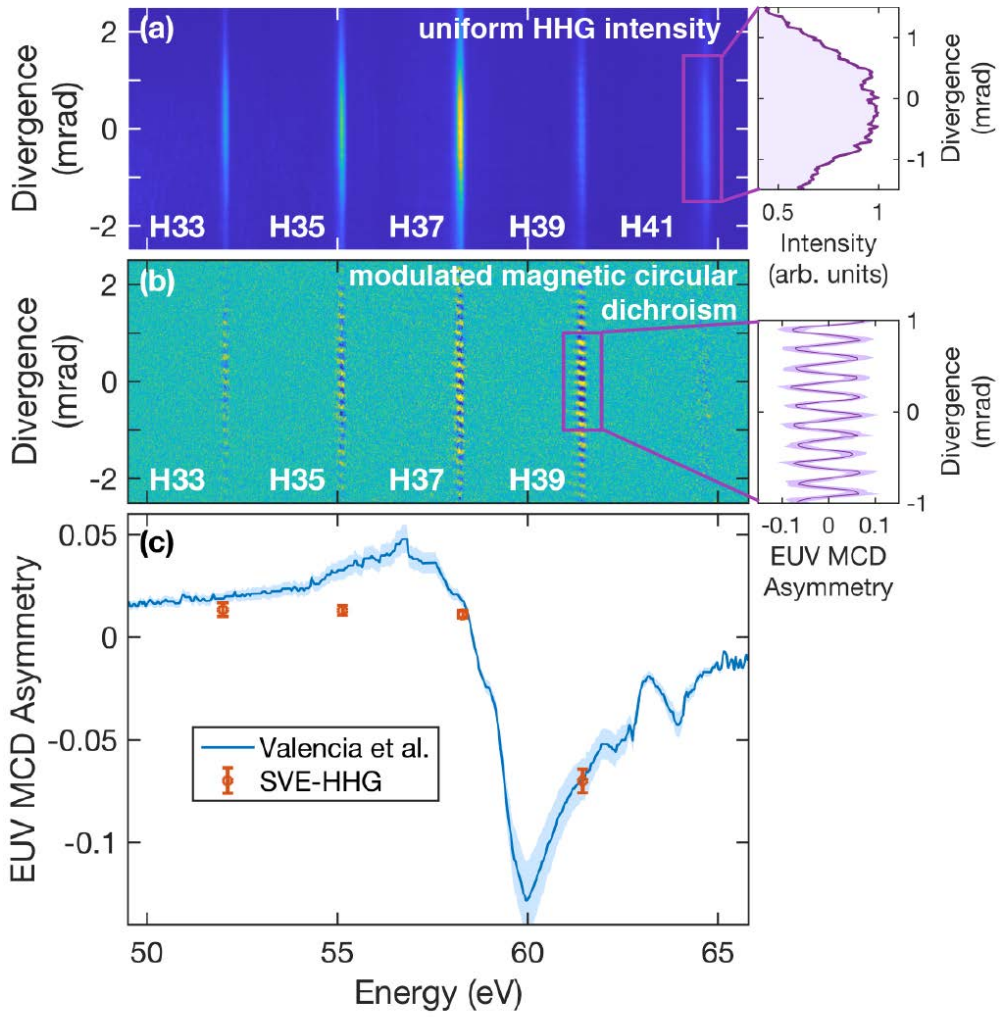

Figure 4.3: **The spatially varying ellipticity in SVE-HHG is characterized via EUV magnetic circular dichroism (EUV MCD).** (a) Spectrally resolved intensity of harmonics transmitted through a uniformly magnetized, 20-nm-thick cobalt thin film. The spatial intensity profile of each harmonic order is uniform. (b) Subtraction of the harmonic intensity transmitted through the cobalt thin film with two opposite magnetizations shows a sinusoidal spatial variation vertically along each harmonic profile. This is due to the differential absorption in MCD, which reveals the spatially varying ellipticity across the high-harmonic beam profile. (c) The amplitude of our measured EUV MCD asymmetry (red circles) is compared with literature values for the magnetic asymmetry expected from a 20-nm-thick cobalt film [127] (blue lines with errors represented by shaded region) to determine the maximum ellipticity present in the far-field polarization distribution. The close agreement with previous measurements indicates a high degree of circularity. The errors on the SVE-HHG data points represent the statistical errors in the fitting procedure and therefore do not capture any systematic effects. We estimate that the systematic errors present are smaller than the statistical ones shown here. Figure from [205].

4.5 Spatially Resolved Magnetic Spectroscopy

After characterizing the spatially varying ellipticity and high degree of circularity obtained with SVE-HHG, we investigated this scheme's applicability for spatially resolved dichroic spectroscopy. Spatially-resolved spectroscopy is possible in SVE-HHG because the far-field polarization pattern is a coherent superposition of the sinusoidal ellipticity variation of each harmonic order present, the spatial frequency of which depends on the harmonic wavelength. Consequently, a Fourier transform of the spatially varying dichroism signal recovers the harmonic spectrum without the need for dispersive optics [209], thereby avoiding the associated losses in both flux and spatial resolution.

To demonstrate this unique capability, we measure the fully spatially-resolved EUV MCD response of the same cobalt thin film, simply by propagating the harmonic beam directly from the sample to the CCD without using a grating (Fig. 4.4a). Again, the magnetic asymmetry shows clear spatial variations (Fig. 4.4b), which, in this case, are the result of the coherent superposition of the sinusoidal ellipticity variations of the four harmonic orders contributing to the MCD signal (Fig. 4.3b). A Fourier transform of the magnetic asymmetry along the plane of ellipticity variation recovers the high-harmonic spectrum transmitted through the sample, multiplied by the energy-dependent magnetic asymmetry (Fig. 4.4c, see Appendix C). Therefore, by independently measuring the spectral weights of the individual harmonic orders transmitted through the sample, we can extract the energy-dependent EUV MCD asymmetry. This measurement is in excellent agreement with the MCD values obtained using a spectrometer to spectrally disperse the harmonic orders (Fig. 4.4d).

In this work, we measured the spectral weights of the transmitted harmonic orders using a grating. We only measured the spectral region near the cobalt M-edge instead of the entire high-harmonic spectrum, so that only the relative EUV MCD response between harmonic orders could be calculated. However, measuring the entire transmitted spectrum does enable the recovery of the absolute MCD response (see Appendix C). An alternative to using a grating to measure the

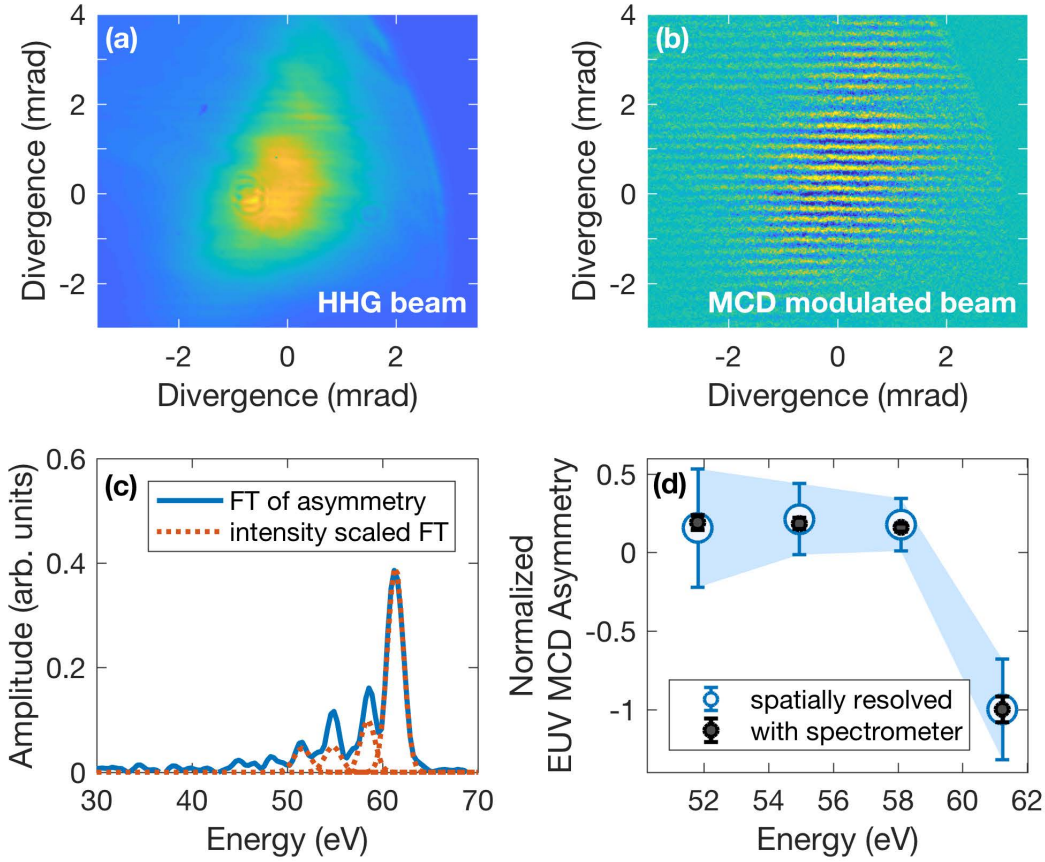

Figure 4.4: **Energy resolved EUV MCD without the use of a spectrometer.** (a) Intensity profile of the high-harmonic beam transmitted through a thin cobalt film (20 nm). (b) Subtraction of the transmission through the two opposite magnetizations shows the coherent superposition of the spatially varying ellipticity of several harmonic orders contributing to the MCD signal. (c) A Fourier transform (FT) of the spatially varying EUV MCD asymmetry recovers the transmitted harmonic spectrum multiplied by the energy-dependent dichroic response of the material (solid blue). Therefore, scaling by the transmitted spectral weights of the individual harmonic orders isolates the material's dichroic response (dotted red). (d) The relative EUV MCD asymmetry obtained using a spatial FT to separate the spectral content (blue) is in excellent agreement with the values obtained by spectrally dispersing hte harmonic orders with a spectrometer (black), indicating that this scheme recovers the spectrally resolved MCD response of magnetic materials without the need for a grating. The blue shaded region indicates the standard deviation in the FT-recovered MCD asymmetry. Figure from [205].

transmitted HHG spectrum is to instead characterize the harmonics by making the polarization of the two focal spots parallel, which results in an intensity interference that similarly contains the spectral weights.

4.6 Numerical Simulations

We further support these experimental characterizations with theoretical simulations of SVE-HHG including propagation [186] (see Appendix C for details). In the simulations, as in the experiment, two independent, orthogonally polarized focal spots (800 nm, 10.6 fs pulse duration) drive the HHG process in neon gas, and the single-atom response is propagated to the far-field, where the beams overlap. The resulting polarization distribution exhibits a sinusoidal spatial variation in the degree of circularity for each harmonic order, which can be seen by isolating the projection of the polarization distribution into pure right-circular polarization (Fig. 4.5a). The projection along left-circular polarization is identical except spatially phase shifted by π.

After confirming that SVE-HHG does indeed produce a spatially varying ellipticity that reaches pure circular polarization, we performed similar simulations with near-single-cycle pulses (2.9 fs, Fig. 4.5b). Here a quasi-supercontinuum is generated instead of individual harmonic orders, but the unique polarization properties of this source are maintained. This makes SVE-HHG a promising route to produce bright isolated attosecond pulses with circular polarization (Fig. 4.5c, see Appendix C). While it is potentially possible to make circularly polarized isolated attosecond pulses via either collinear [47] or noncollinear [49, 177] mixing of two counter-rotating driving lasers, these methods suffer from a decrease in flux due to either single-atom or macroscopic effects. Fortunately, in SVE-HHG the HHG process itself is identical to single-beam HHG so that the attainable flues and cutoff photon energies are just as high as in traditional single-beam HHG. Additionally, since the SVE-HHG supercontinuum still exhibits a clear sinusoidal polarization modulation at every energy, a spatial Fourier transform will still be able to recover the spectral content. Therefore, SVE-HHG can be extended to HHG supercontinua to measure spatially resolved EUV MCD with more energy resolution than attainable with spectrally isolated high harmonics. In

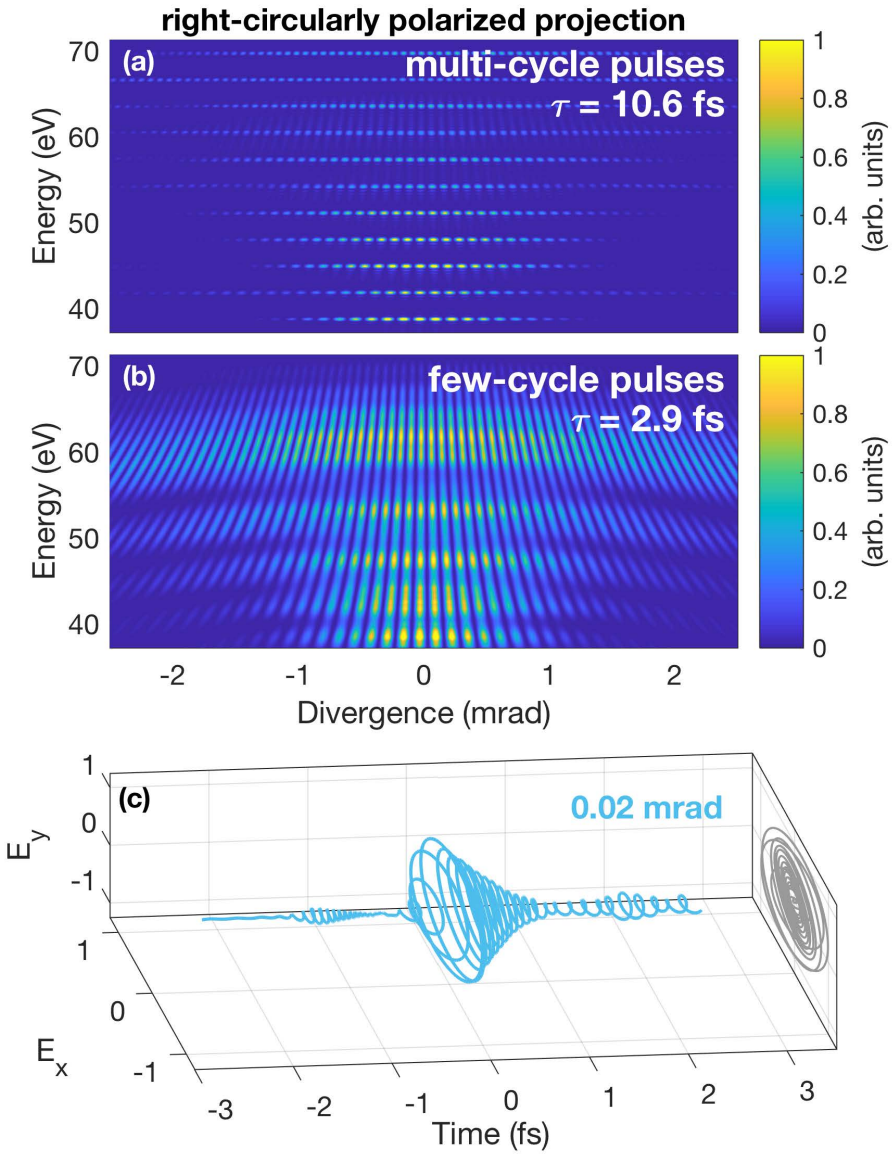

Figure 4.5: **Numerical simulations of SVE-HHG visualized by taking the projection of the far-field polarization distribution along pure right-circular polarization.** (a) For multi-cycle pulses, the HHG emission is spectrally resolved into well-separated harmonic orders, which each exhibit a polarization modulation with a spatial frequency that depends on the harmonic order. (b) For near-single-cycle pulses, an HHG supercontinuum is produced. However, every energy still exhibits sinusoidally varying ellipticity with a well-defined spatial frequency that increases with increasing photon energy. (c) This HHG supercontinuum corresponds to an isolated attosecond pulse in the time domain, which is either circularly, elliptically, or linearly polarized depending on divergence angle (+/- 0.02 mrad for circular, see Appendix C). Figure from [205].

the supercontinuum case, the energy resolution is limited only by the geometry of both the source and sample and the subsequent energy resolution obtained by the spatial Fourier transform. In the present work, we achieved an experimental energy resolution of ∼1.3 eV, which was adequate to distinguish the well separated high-harmonic orders (∼3 eV separation). This energy resolution can be increased by both moving the focal spots farther apart to increase the fringe density and increasing the angular range over which light is detected. Through these numerical simulations we have demonstrated good agreement between the true spectrum and the spectrum obtained via spatial Fourier transform. However, we find small discrepancies between the two due to the nonuniform intensity distribution across the Gaussian focal spots and the resulting transverse phase matching conditions [210, 211]. These discrepancies could therefore be mitigated by using flat-top beams to drive the HHG process (see Appendix C).

4.7 Conclusions and Outlook

In conclusion, we experimentally and theoretically demonstrate that two spatially separated and orthogonal linearly polarized harmonic sources can be combined to produce a high-harmonic beam with sinusoidally spatially varying ellipticity in the far field. We found that this polarization distribution exhibits regions with a high degree of circularity, thereby making SVE-HHG a useful technique for studying circular dichroism in the EUV. Additionally, numerical simulations show that SVE-HHG is compatible with short-pulse driving lasers, enabling the production of isolated attosecond pulses with circular polarization to probe the fastest chiral processes known to date [28]. Indeed, SVE-HHG is a promising route for producing circularly polarized isolated attosecond pulses with mid-infrared driven HHG, since it does not suffer from the unfavorable scalings that hinder the extension of other methods of circularly polarized HHG into the mid-infrared. Furthermore, we have shown that SVE-HHG enables spatially resolved spectroscopy of dichroic samples. This capability arises because energy resolution can be recovered through the spatial variation in the ellipticity of the source itself without the use of a spectrometer, thereby obtaining spectral resolution without sacrificing spatial resolution.

Looking forward, an exciting extension of this technique is to combine it with Fourier transform spectroscopy by controlling the time delay between the two high-harmonic sources [99, 206, 212–215]. In that case, the energy resolution achievable would be limited by the range in time that is scanned instead of the source and sample geometry, enabling higher energy resolution than can feasibly be obtained with the current scheme. This increase in energy resolution via Fourier transform spectroscopy is especially useful in combination with short-pulse driving lasers to easily exploit the energetically dense supercontinuum spectrum. Additionally, controlling the time delay between the two sources is advantageous because it entails EUV MCD measurements through changing the local helicity of the light, instead of flipping the magnetization state of the sample. This capability enables the study of dichroism in samples that are not uniformly magnetized, such as magnetic domains and grain boundaries, or high coercivity samples that cannot be magnetized along an external magnetic field. Finally, we note that when the time delay is scanned SVE-HHG is, in principle, compatible with coherent diffractive imaging techniques, enabling nanoscale hyperspectral magnetic imaging.

Chapter 5

Photoelectron Spectroscopy of Charge Transfer from Quantum Dots

This chapter is adapted, with permission, from:

- Jennifer L. Ellis, Daniel D. Hickstein, Kyle J. Schnitzenbaumer, Molly B. Wilker, Brett B. Palm, Jose L. Jimenez, Gordana Dukovic, Henry C. Kapteyn, Margaret M. Murnane, and Wei Xiong. Solvents Effects on Charge Transfer from Quantum Dots. *J. Am. Chem. Soc.*, **137** (11), 3759–3762 (2015). DOI:10.1021/jacs.5b00463.

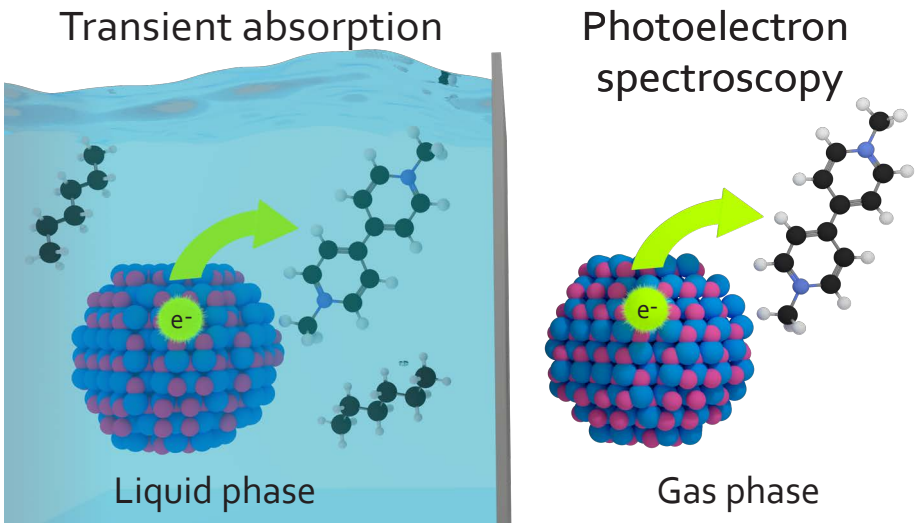

Figure 5.1: **Illustration of the comparison of quantum dot charge transfer processes occurring in both liquid phase and in vacuum.** Figure from [138].

5.1 Abstract

To predict and understand the performance of nanodevices in different environments, the influence of the solvent must be explicitly understood. In this Chapter, this important but largely unexplored question is addressed through a comparison of quantum dot charge transfer processes occurring in both liquid phase and in vacuum. By comparing solution phase transient absorption spectroscopy and gas-phase photoelectron spectroscopy, we show that hexane (a common nonpolar solvent for quantum dots) has negligible influence on charge transfer dynamics. Our experimental results, which are supported by insights from theory, indicate that the reorganization energy of nonpolar solvents plays a minimal role in the energy landscape of charge transfer in quantum dot devices. Thus, this study demonstrates that measurements conducted in nonpolar solvents can indeed provide insight into nanodevice performance in a wide variety of environments.

5.2 Introduction

To design efficient devices using nanoscale components (nanodevices), the charge transfer pathways between nanostructures must be understood in a predictive way. Numerous studies have used time-resolved spectroscopy techniques to determine the rate-limiting steps in charge transfer between individual components in nanodevices [53–57, 62, 216, 217]. These studies are typically conducted using liquid phase samples, and the effect of the local solvent environment on the charge transfer process has proven difficult to investigate [55, 58]. Understanding the influence of the solvent is important since nanodevices are often synthesized and tested in one environment, but ultimately deployed in a different environment. For example, colloidal semiconductor quantum dots (QDs) are typically prepared and characterized in organic solvents, but often attached to surfaces as films in photovoltaics [218]. Solvent molecules can alter the charge transfer process by perturbing the dielectric layer, or through the dynamic configuration rearrangements (electronic and conformational) of the solvent molecules at the nanomaterial surface during a charge transfer process [55]. Therefore, rational design and characterization of nanomaterials requires that we understand

solvent effects. In this Chapter, using a combination of novel experiments and theoretical insights, we show that charge transfer dynamics measurements conducted in nonpolar solvents are indeed relevant for understanding nanodevices operating in air or vacuum.

Prior investigations utilized liquid phase transient absorption spectroscopy (TA), and showed that polar solvents can significantly alter the charge transfer rate [219]. However, to dissolve nanoparticles into solvents with different polarities, it is typically necessary to alter the ligand coverage or swap ligands entirely, thereby convolving solvent effects with ligand effects. This makes it difficult to isolate the effect of the solvent alone.

In this Chapter, we overcome this technical challenge by utilizing a velocity map imaging spectrometer [130, 220] coupled with a nanoparticle aerosol source [79, 141, 221]. This allows us to perform a time-resolved photoelectron spectroscopy experiment (PES, Fig. 5.2a) on isolated nanoparticles in vacuum. To eliminate complications arising from the use of different ligands, we implement gas phase PES on QDs with identical ligand coverage as in solution phase. Here, we unambiguously characterize the influence of a commonly used nonpolar solvent (hexane) on charge transfer by comparing PES data with solution phase TA measurements conducted on the same QD sample. Specifically, we compare gas-phase PES and solution-phase TA measurements of the charge transfer rate between CdSe QDs and methyl viologen (MV^{2+}) cations (Fig. 5.2) to characterize the influence of the solvent (hexane) on this process. We selected the CdSe-MV complex for these studies because it is a well characterized system that exhibits fast and efficient charge transfer [54, 217, 222–224]. Furthermore, hexane is frequently used as a solvent for the synthesis and characterization of QDs. Thus, it is important to determine whether hexane influences charge transfer between the QD and the electron acceptor.

5.3 Preparing the QD Charge Transfer System

To prepare the charge-transfer system, we adsorbed MV dye (Sigma-Aldrich) to octadecylamine-capped CdSe QDs with a diameter of 2.3 nm (NN-Labs). We added methanol dropwise to 12 mg of MV powder until the powder was completely dissolved, and then added this to a 0.01 mg/mL

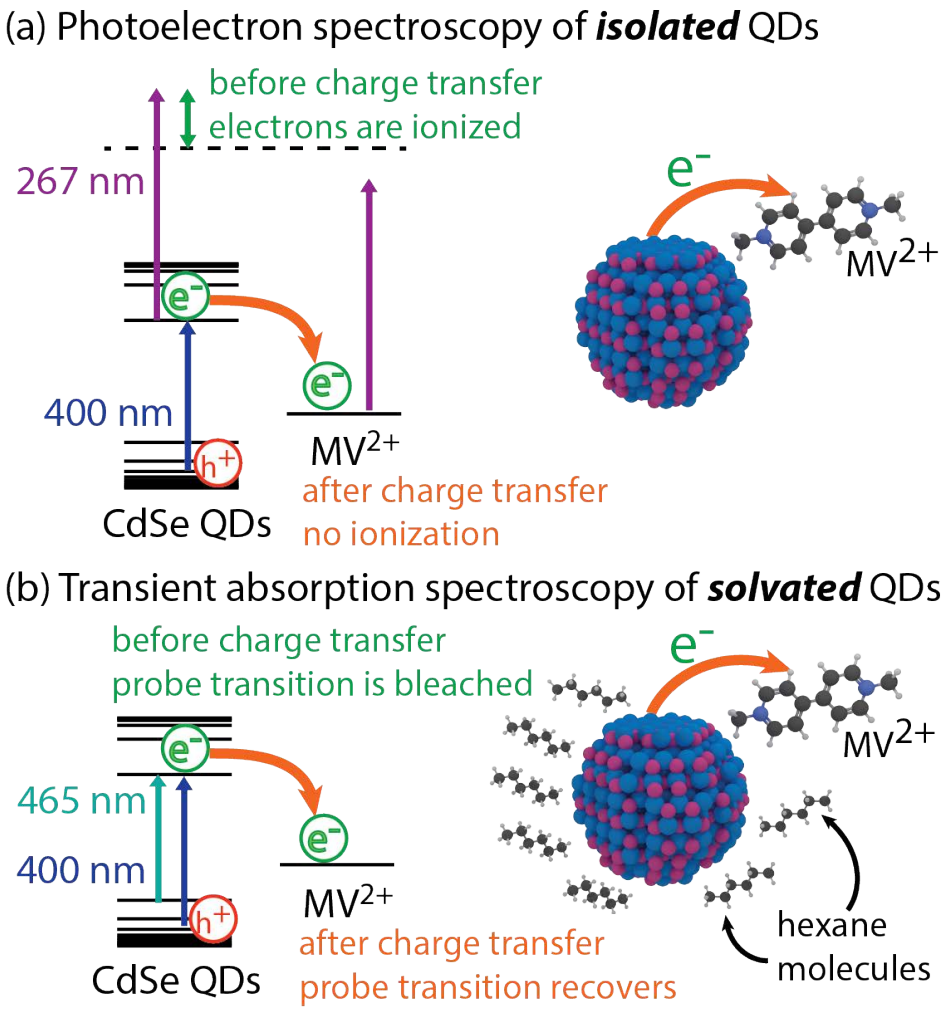

Figure 5.2: **Experimental schemes for measuring solution-free and solvated quantum dot charge transfer reactions.** (a) Photoelectron spectroscopy (PES) detects electrons to follow charge transfer dynamics in *solvent-free* quantum dots (QDs – ligands are present, but not depicted here). A 400 nm pump pulse excites electrons, and before (or without) charge transfer, they can be ionized by a delayed 267 nm probe pulse. Once transferred to methyl viologen (MV), the probe photon energy is insufficient to ionize the electron. (b) The transient absorption (TA) measurements follows the same dynamics by observing a time-dependent absorption change in *solvated* QDs. Here, before (or without) charge transfer, the probe transition is bleached, due to the presence of the excited electron, resulting in a decrease in absorption. By comparing PES and TA, we can isolate the effect of the solvent (hexane) on charge transfer. Figure from [138].

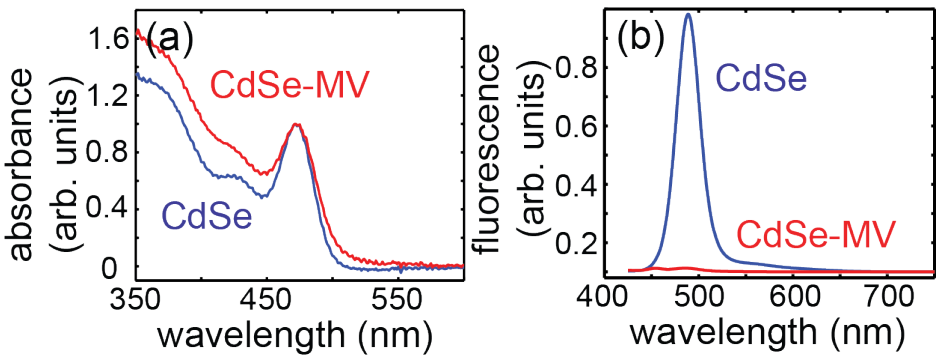

Figure 5.3: **Static characterization of the CdSe-MV complex.** (a) The similarity of the UV-visible absorption spectra of CdSe and the CdSe-MV in solution reveals that the addition of MV does not alter the quantum confinement of the CdSe QDs. (b) The quench in the fluorescence spectra upon addition of MV indicates that electrons excited in the CdSe transfer to MV. Figure from [138].

solution of QDs in hexane. This concentration corresponds to ∼100 MV molecules per QD in solution. We also prepared a control sample, consisting of CdSe QDs also diluted to 0.01 mg/mL in hexane, but otherwise used as received. We then used UV-visible absorption and fluorescence spectroscopies to characterize the static spectral features of CdSe QDs and CdSe-MV complexes. The absorption spectra of both samples show a peak at 480 nm (Fig. 5.3a) that corresponds to the $1S(e) - 1S_{3/2}(h)$ transition. The CdSe-MV spectrum shows slightly broadened peaks, which is likely due to the excitonic coupling of the 1S(e) exciton state to the LUMO level of MV [225]. The fact that all of the peaks are preserved demonstrates that adding MV to the CdSe does not significantly influence quantum confinement in the QD. The quenching of the CdSe fluorescence peak upon the addition of MV (Fig. 5.3b) indicates that the MV molecules successfully attach to the QD surfaces and that excited electrons in the CdSe QDs migrate to the MV faster than the rate of radiative decay [217, 222, 224].

5.4 Experimental Details

We used a nanoparticle aerosol source coupled ot a velocity map imaging spectrometer [79, 141, 221] to perform PES on QDs. A hexane solution containing the QDs is aerosolized using

a compressed gas atomizer (TSI). The atomizer creates micron sized droplets of solution, which dry as they travel through a gas line, leaving behind ∼100 nm sized clusters of nanoparticles suspended in the gas phase. The nanoparticle aerosol beam is collimated to a width of ∼500 μm by an aerodynamic lens [146] (Aerodyne) and injected into the first vacuum chamber before passing through a skimmer into the differentially pumped VMI chamber, which is maintained below ∼5 × 10^{-6} torr.

The QDs are excited by a 400 nm pump pulse (40 fs) and the resulting dynamics are followed via subsequent photoionization by a delayed 267 nm probe pulse (40 fs). Both pulses originate from a 1 kHz Ti:sapphire amplifier (KMLabs) centered at 800 nm, and are up-converted to the second and third harmonic in BBO crystals. The time delay between the two pulses is controlled using a mechanical delay stage (Thorlabs). To improve the signal-to-noise ratio, the VMI was operated in spatial imaging mode [135, 136], and therefore provided a measure of total photoelectron yield but without energy resolution. Charge transfer between the CdSe QDs and attached MV molecules manifests as a decay in the total photoelectron yield. This decay is observed because an electron occupying the LUMO of MV is bound by 4.95 eV and therefore cannot be photoionized by the 4.65 eV probe pulse (Fig. 5.2a).

The pressure in the VMI chamber is ∼10^{-6} torr so, based on a simple Langmuir relation, only about 10^{-6} layers of hexane molecules can cover the surface of the QDs in equilibrium [226]. Hexane is a rather volatile liquid and only weakly interacts with the organic ligands covering the QDs since they are both nonpolar. Therefore, the equilibrium surface coverage should be quickly reached before the QDs arrive at the interaction region so that PES probes the QD charge transfer processes in a hexane-free environment.

The experimental setup used for TA measurements have been described previously [57]. Samples were measured in 2 mm quartz cuvettes with constant stirring under 405 nm excitation. To probe the role of solvents in a charge transfer reaction we performed PES and TA spectroscopy on the same samples, of both CdSe and the CdSe-MV complex. However, to acquire adequate signal in both experiments different concentrations needed to be used. After the PES experiment,

a portion of the remaining solution was concentrated (up to 10x) immediately before use in the TA measurement. Samples were concetrated by evaporating the hexane solvent under vacuum and then redispersing the sample in hexane to reach the desired concentration. We confimed that TA measurements of samples of different concentrations display similar kinetics (see [138] Supporting Information), demonstrating the validity of comparing the solution phase TA and gas-phase PES experiments.

5.5 Solvated v.s. Solution-Free Charge Transfer

Before addressing the effect of solvent molecules on charge transfer processes, we first verified that PES can indeed be used to track excited state dynamics, through comparison with TA measurements of electron dynamics occurring within CdSe QDs. In the PES experiment, the 400 nm pump pulse excites electrons primarily to the 1S(e) level (leaving a deeper hole in the valance band, based on the assignment of features in UV-visible absorption spectra [64, 148, 158, 227]), while a time delayed 267 nm probe pulse ionizes the excited electron (Fig. 5.2a). Therefore, immediately after the creation of 1S electrons, the photoelectron signal is enhanced. The decay of the photoelectron signal reflects the decay of the 1S population. In the TA experiment, we monitor the dynamics of the bleach of the $1S(e) - 1S_{3/2}(h)$ transition (Fig. 5.2b), which also probes the population of electrons in the 1S state [227, 228]. Therefore, both the TA and the PES measurements probe the 1S electron population. In both experiments, the fluence of the 400 nm pump pulse is selected so that an electron is excited in less than 10% of QDs in the interaction region, to minimize the effects from multiple excitons in a single quantum dot.

The difference between the two measurements is the presence (TA) or absence (PES) of surrounding solvent molecules. In the absence of charge transfer (i.e., no MV attached), we expect identical results from TA and PES, because the solvent should not strongly affect the dynamics that take place inside of the QD. Indeed, we do observe good agreement between the TA and PES measurements (Fig. 5.4a) demonstrating that PES has the ability to follow exciton dynamics. Both measurements of CdSe QDs (Fig. 5.4a) show a fast rise at $t = 0$, followed by a small initial

decay and a long plateau. To quantify these dynamics, they were fit with a double exponential decay convoluted with the instrument response-function (IRF). The slow component is beyond the temporal range of the delay stage, which is consistent with the few nanosecond radiative lifetime of the 1S electron [151]. The small fast component results from the small fraction of electrons that undergo faster decay. While the presence or absence of solvent molecules could have an effect on carrier trapping at surface states [229–232], we do not observe such effects. This is indication that the CdSe QD surface is well passivated and that the ligand coverage (i.e., passivation) is identical for the two measurements. We note that the difference between the two measurements at $t < 0$ results from the fact that the 267 nm pulse used in the PES experiment excites hot electrons, which can then be ionized by the 400 nm pulse. Thus, the TA experiment and the PES experiment probe different processes in the $t < 0$ regime. In this Chapter, we focus only on the band edge electron dynamics ($t >= 0$), where TA and PES can be directly compared.

Having verified that PES can track charge dynamics in CdSe QDs, we can now apply it to study charge transfer in the CdSe-MV complex. In this case, we see a faster decay of the PES signal (Fig. 5.4b) and, therefore, the 1S electron population, due to electron transfer to the MV LUMO. The TA measurements conducted on the same sample also detect faster decay in the 1S electron population when MV is adsorbed, seen as the faster recovery of the bleach of the $1S(e) - 1S_{3/2}(h)$ transition. We fit the CdSe-MV kinetics using a triple exponential decay convoluted with the IRF, fixing two of the time constants with the values determined in the absence of MV. The newly extracted time constant (τ_3) is indicative of an electron transfer rate of 220 ± 70 fs (TA) and 100 ± 150 fs (PES) (Fig. 5.4b), which are in agreement with previous studies in organic solvents [217, 222]. The charge transfer rates obtained in both measurements are the same within the fitting error (one standard deviation). This indicates that the presence of hexane has a negligible effect on the charge transfer process. We note that these recovered τ_3 values are very close to the time scale of the instrument response functions of the TA and PES experiments, leading to the large errors seen in the fit values.

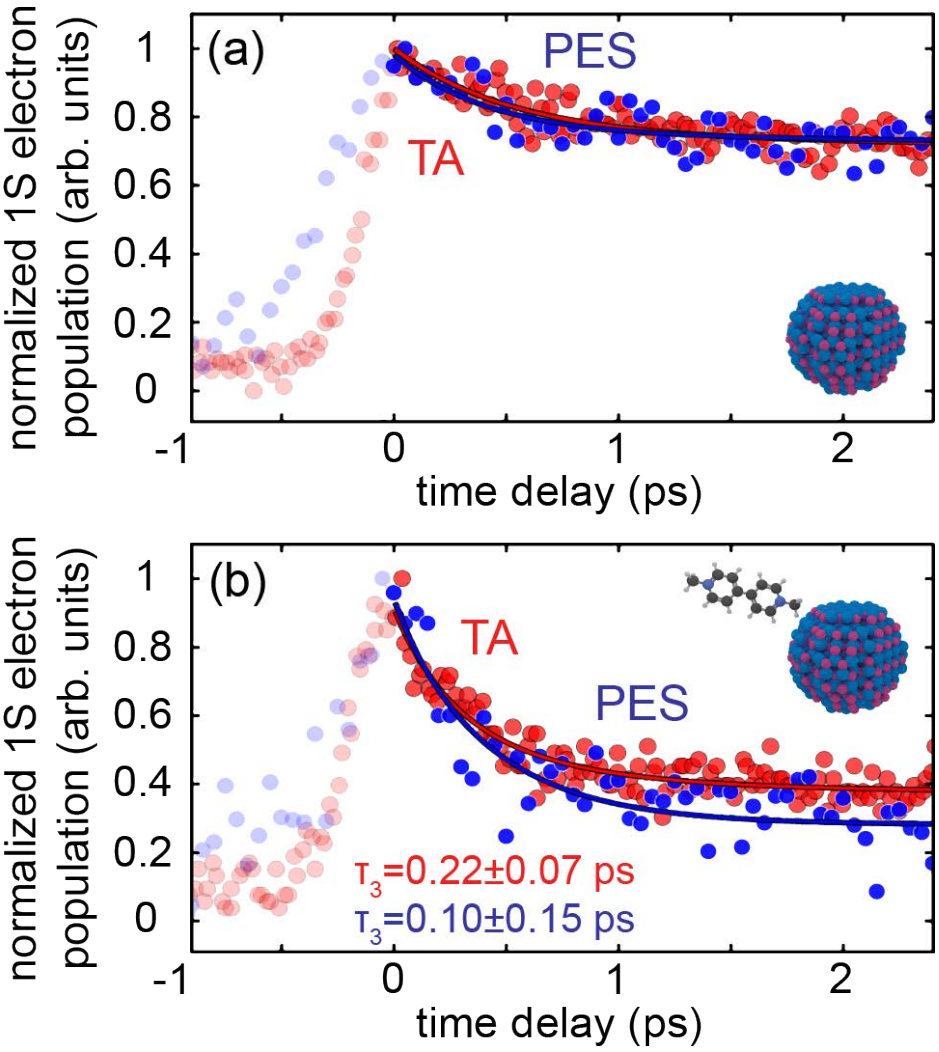

Figure 5.4: **Comparison of solvated and solution-free dynamics in CdSe and CdSe-MV complexes.** (a) In the absence of MV^{2+}, the 1S electron population only decays slightly on a few picosecond time scale. (b) When MV is attached to the QDs, a ∼100 fs decay is seen, indicating charge transfer from the QD to the MV. There is no significant difference between the decay rates obtained from the TA and PES experiments, indicating that the hexane solvent molecules have a minimal effect on the charge transfer process. Figure from [138].

5.6 Solvent Electronic Polarization Model

The negligible influence of the hexane solvent molecules can be understood through the solvent electronic polarization model developed by Kim and Hynes [233–237]. In this model, solvent molecules contribute to the charge transfer reorganization energy through both the electronic polarization and the orientational polarization. Since hexane is nonpolar, reorientation of the molecules does not alter the electron distribution. Therefore, the orientational contribution vanishes. Alternatively, the solvent molecules can influence the charge transfer by the redistribution of their electron populations. The electronic contribution will only be significant when the charge transfer reaction is fast compared to the solvent electronic polarization rate. This can be characterized by the ratio between the rates of charge transfer and solvent electronic polarization, $\rho = 2\beta/(\hbar\omega)$, where β is the electronic coupling factor and ω is the electronic transition frequency of the solvent [235]. We estimated β using the broadening [225] of the absorption spectra of the QDs upon the MV adsorption (Fig. 5.3a), which is approximately 0.05 eV. Since hexane does not absorb in the visible region, its electronic transition energy, $\hbar\omega$, is > 3 eV [235, 237]. Therefore, $\rho < 0.02$, which means that the solvent electronic polarization is rapid compared to the charge transfer process (nonadiabatic). As a result, neither the electronic nor the orientational polarization of hexane contributes significantly to the reogranization energy, and consequently, one would not expect solvent reorganization to have a large influence on the charge migration dynamics of the CdSe-MV complex. Furthermore, from this analysis we predict that the influence on QD charge transfer of *any* nonpolar transparent solvent should be minimal, as long as the charge transfer process is slower than a few femtoseconds, which is true for most charge-transfer processes. This is not necessarily the case for polar solvents, where the orientational reorganization energy can affect the charge transfer process, so that dynamic solvent effects must be considered [238, 239].

5.7 Conclusions and Outlook

In conclusion, we investigated the influence of the solvent on charge transfer between quantum dots and methyl viologen by comparing dynamics measured using solvent-free two-photon photoelectron spectroscopy with those measured by solution-phase transient absorption spectroscopy. We first verified that photoelectron spectroscopy is a viable method of measuring excited electron dynamics in quantum dots. After this verification, we applied this technique to study a charge transfer reaction. The good agreement in the charge transfer dynamics obtained by solvent-free and solution phase spectroscopies indicates that common nonpolar organic solvents, such as hexane, have a negligible influence on the charge transfer process between quantum dots and electron acceptor molecules. We explain this observation using theoretical insights that have not previously been applied to nanocrystals. Our results indicate that kinetic data measured by transient absorption spectroscopy, under nonpolar solvent environments, can be used to infer nanodevice behavior in air or vacuum. In the future, this approach can also be used to investigate polar solvents, to gain a general picture of the solvent effects on charge transfer on the nanoscale. This knowledge will provide another tunable parameter to manipulate the charge motion in nanodevices.

Chapter 6

Extreme Ultraviolet Photoelectron Spectroscopy as a Probe of Material Properties and Dynamics

This chapter is adapted, with permission, from:

- Jennifer L. Ellis, Daniel D. Hickstein, Wei Xiong, Franklin Dollar, Brett B. Palm, K. Ellen Keister, Kevin M. Dorney, Chengyuan Ding, Tingting Fan, Molly B. Wilker, Kyle J. Schnitzenbaumer, Gordana Dukovic, Jose L. Jimenez, Henry C. Kapteyn, and Margaret M. Murnane. Materials Properties and Solvated Electron Dynamics of Isolated Nanoparticles and Nanodroplets Probed with Ultrafast Extreme Ultraviolet Beams. *J. Phys. Chem. Lett.*, **7** (4), 609–615 (2016). DOI:10.1021/acs.jpclett.5b02772.

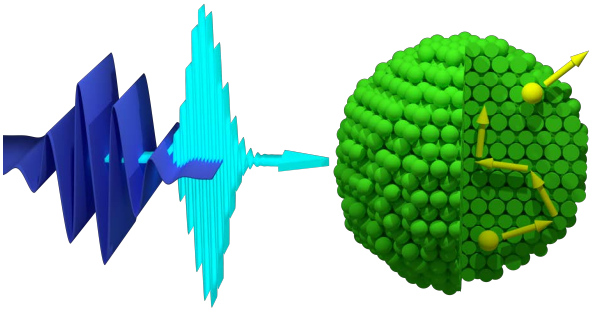

Figure 6.1: **Illustration of EUV light, produced through HHG with near-UV driving lasers, exciting hot electrons inside of a nanoparticle.** Figure from [240].

6.1 Abstract

In this chapter, I present ultrafast photoemission measurements of isolated nanoparticles in vacuum using extreme ultraviolet (EUV) light produced through high-harmonic generation. Surface-selective static EUV photoemission measurements were performed on nanoparticles with a wide array of compositions, ranging from ionic crystals to nanodroplets of organic material. We find that the total photoelectron yield varies greatly with nanoparticle composition and provides insight into material properties such as the electron mean free path and effective mass. Additionally, we conduct time-resolved photoelectron yield measurements of isolated oleylamine nanodroplets, observing that EUV photons can create solvated electrons in liquid nanodroplets. Using photoemission from a time-delayed 790-nm pulse, we observed that a solvated electron is produced in an excited state and subsequently relaxes to its ground state with a lifetime of 151 ± 31 fs. This work demonstrates that femtosecond EUV photoemission is a versatile surface sensitive probe of the properties and ultrafast dynamics of isolated nanoparticles.

6.2 Introduction

Nanoparticles exhibit a surface-area-to-volume ratio many orders of magnitude higher than bulk materials, allowing them to serve as powerful catalysts for chemical reactions, both in the laboratory [241–243] and as atmospheric aerosols [244–246]. Such surface-catalyzed chemical reactions often involve molecular motions that take place on femtosecond and picosecond time scales [247–250], with associated electronic dynamics that can occur on attosecond time scales. To capture and understand these dynamics, new experimental techniques are needed to probe the surfaces of nanoparticles on femtosecond-to-attosecond time scales. Furthermore, theoretical models of nanoparticle surface dynamics are best validated with measurements performed in the absence of solvents or surface-deposition effects, creating a demand for measurements of completely isolated (gas phase) nanoparticles on ultrafast time scales.

Photoemission following extreme ultraviolet (EUV) illumination is a well established and

robust technique for probing the electronic structure of atoms, molecules, and the surfaces of bulk materials [81, 251–253]. EUV photoemission is intrinsically surface sensitive because the excited electrons have mean free paths (MFPs) of only a few nanometers [80, 254]. Consequently, only electrons from the several outermost atomic layers can escape a material and reach the detector. Thus, EUV photoemission could serve as an ideal probe of nanoparticle surfaces, provided that the nanoparticles are larger than a few MFPs and can be isolated in an ultrahigh vacuum chamber [156, 255–257]. Although time-resolved EUV photoemission studies have been conducted on large isolated helium clusters [258, 259], the ultrafast surface dynamics of isolated nanoparticles have been largely unexplored to date. Photoemission studies of isolated nanoparticles face the challenges of generating high-flux tabletop sources of ultrashort EUV pulses and preparing a high-density beam of nanoparticles in vacuum.

In this chapter, we overcome both of these challenges and present the first experimental study of the properties and dynamics of fully isolated nanoparticles of varying composition using ultrashort pulses of EUV light. This breakthrough is accomplished through the combination of high-harmonic generation (HHG) to produce ultrashort pulses of EUV light, a velocity-map-imaging (VMI) photoelectron spectrometer to provide high electron-collection efficiency, and an aerodynamic lens for introducing collimated beams of nanoparticles into vacuum. We present two demonstrations of how this technique can provide new insights into nanosystems. First, we demonstrate that EUV photoelectron yields can provide a surface-specific probe of nanoparticle properties. Specifically, we measure the static EUV photoelectron yield from ∼100 nm diameter nanoparticles with a wide variety of compositions – ranging from organic materials to ionic crystals – and find that the photoelectron yield changes by more than an order of magnitude depending on the composition of the nanoparticles. We attribute this difference in photoelectron yield to varying electron MFPs and interfacial scattering (electron effective mass) in different nanoparticle systems. Second, we conduct time-resolved photoemission measurements of isolated nanoparticles using EUV light, finding that the absorption of EUV photons can create excited-state solvated electrons in oleylamine nanodroplets.

6.3 Experimental Details

This study was enabled through the combination of capabilities from atmospheric science (aerodynamic lens), physical chemistry (VMI photoelectron spectrometer), and extreme nonlinear optical science (HHG EUV source), as depicted in Fig. 6.2. We utilize a compressed gas atomizer (TSI, model 3076) to produce an aerosol of nanoparticles, which is then introduced into the vacuum chamber via an aerodynamic lens [146] (Aerodyne), resulting in a collimated beam of isolated nanoparticles streaming through vacuum. The atomizer is extremely versatile and can produce nanoparticles with a wide range of compositions, including ionic crystals, organic liquids, and clusters of chemically synthesized nanoparticles [79, 138, 141, 156, 221]. A beam of EUV photons produced through HHG is gently focused onto the nanoparticle beam. We use the majority of the output of a Ti:sapphire regenerative amplifier (8 mJ, 790 nm) to produce the second harmonic (1.5 mJ, 395 nm) in a beta-barium borate crystal (β-BBO, 200 μm thickness), which is coupled into an argon-filled waveguide to drive HHG emission. The use of shorter-wavelength driving lasers for HHG achieves higher conversion efficiencies than traditional 790 nm driven HHG, producing more output EUV photons and concentrating that flux into a single narrowband harmonic (at 22 eV), instead of producing a spectral comb of many high-harmonic orders [122, 260]. This single-bright harmonic makes 2ω driven HHG an ideal tool for photoemission, providing bright ultrafast-pulses of spectrally narrow EUV light on the tabletop.

The photoelectrons ejected from the nanoparticles are detected by a VMI photoelectron spectrometer, which consists of three parallel-plate electrodes in the Eppink-Parker geometry [130, 131, 220]. We operated the VMI in spatial imaging mode [135, 136, 138], which allows us to measure the total photoelectron yield from the nanoparticles separate from the electrons from the ionization of the background gas [135, 136, 138]. This is especially advantageous in this case because the number of photoelectrons generated from the nanoparticles is small compared to the number of electrons resulting from ionization of the background gas. This difference in electron yield results from the extreme surface sensitivity of EUV photoemission. The photon MFP ($\sim$10–20 nm) is

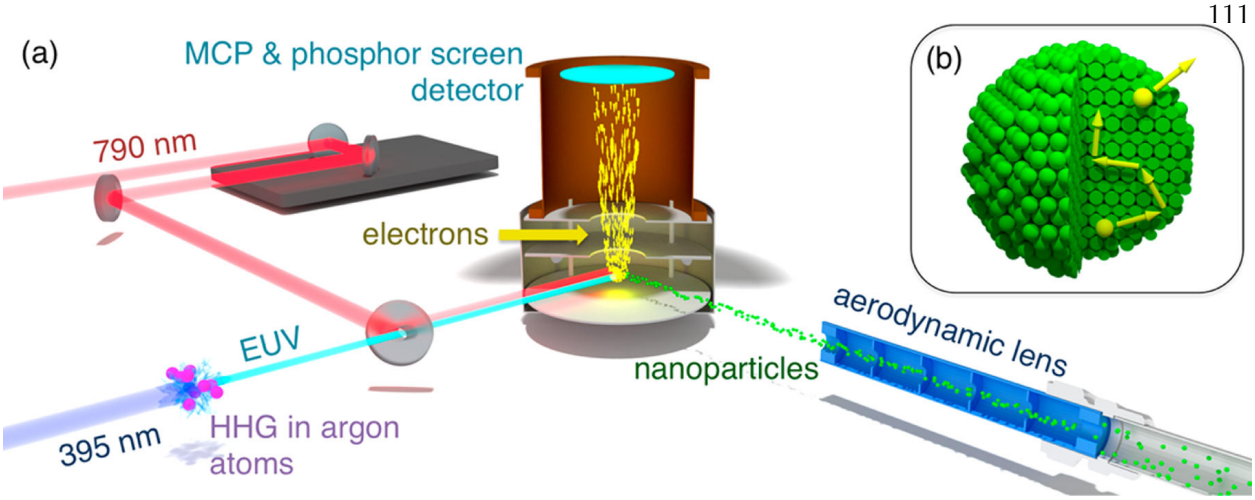

Figure 6.2: **Experimental scheme for EUV photoemission from isolated nanoparticles.** (a) A nanoparticle aerosol passes through an aerodynamic lens, which forms a collimated beam of nanoparticles while leaving the carrier gas divergent. The isolated nanoparticles then enter the differentially pumped photoemission chamber, where they are ionized by femtosecond EUV pulses produced through HHG. Electrodes guide the photoelectrons toward a microchannel-plate–phosphor-screen detector, which is imaged with a CCD camera (not shown). (b) EUV light is absorbed throughout the nanoparticle, creating hot electrons (yellow). However, because of short electron mean free paths (MFPs), only electrons excited near the surface can escape the nanoparticle. In liquid nanodroplets, the excited electrons that remain inside the nanoparticle become highly excited solvated electrons. Figure from [240].

much larger than the electron MFP (∼1 nm), so that only a small fraction of photons absorbed by the nanoparticle lead to detectable photoelectrons. Conversely, every photon absorbed by the background gas produces a photoelectron. Fortunately, since the nanoparticle beam is tightly collimated, while the background gas fills the entire vacuum chamber, the electrons generated from the particle beam are easily distinguished from those originating from the background gas via the spatial imaging mode of the VMI.

Because of the surface sensitivity of EUV photoemission [261–263], we avoided chemically synthesized nanoparticles, which must be passivated with surface ligands to remain suspended in solution [141]. Instead, nanoparticles with bare surfaces can be produced through the aerosolization process itself, simply by using solutes that completely dissolve into a solvent without the use if ligands, for example, dissolving table salt (NaCl) into water [141, 156, 221]. The atomizer produces an aerosol of droplets from a solution, which dry to produce nanoparticles of solute. the size of the

nanoparticles produced therefore is determined by the concentration of the solute and the initial droplet size distribution, which is influenced primarily by the solvent. We produced nanoparticle aerosols from an array of different compounds, including organic compounds and ionic crystals, using three different solvents (hexane, water, and acetone). We measured the distribution of particle sizes in each case, finding the average diameter to be constant to within a factor of 1.4 for particles originating from the same solvent. Across all of the nanoparticle aerosols investigated, the average particle diameter ranged from 65 to 150 nm (Fig. 6.3,a-c).

6.4 Photoelectron Yield as a Measure of Material's Properties

The static photoelectron yields upon EUV irradiation show dramatic material-dependent differences (Fig. 6.3d), which cannot be accounted for by the variation in the nanoparticle size distributions (i.e., total available volume or total available surface area available for photoemission, see Appendix D). Even within a given solvent, where the nanoparticle diameter distributions are nearly identical, there is large variation in the photoelectron yield.

To understand the origin of the observed variations in photoelectron yield, we can consider the specifics of the photoemission process. Photoemission can be described in terms of a three-step model, where each step contributes to the probability of electron emission and therefore the final photoelectron yield [71, 78, 81]. First, a photon is absorbed and a hot electron is created within the nanoparticle. In this experiment, the probability for creating a hot electron is proportional to the material absorption at 22 eV, since any photon that is absorbed must create a hot electron. Second, the hot electron travels through the material with a probability of scattering that is given by the electron MFP in that material. Third, the eelctron impinges upon the nanoparticle surface, where the electron can escape into the vacuum or reflect back into the nanoparticle. The probability to escape depends on the geometry of the nanoparticle and the electron effective mass. In the specific case that the nanoparticle size is much greater than the electron MFP, the escape probability is largely independent of geometry. Differences in the material absorption at 22 eV (see Appendix D) do not account for the observed variations in photoelectron yield, demonstrating that considering

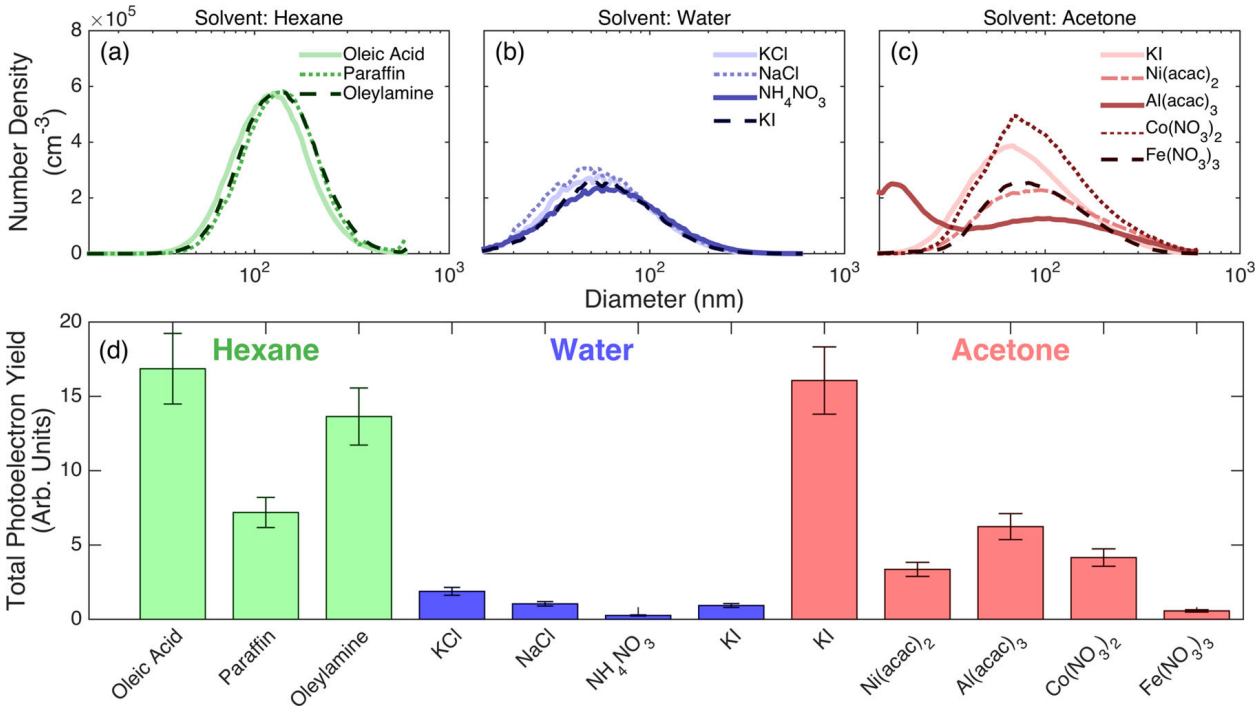

Figure 6.3: **Size distributions of isolated nanoparticles measured with a scanning mobility particle sizer and total photoelectron yield measured using 22 eV high harmonics.** Nanoparticles are produced through compressed gas atomization and originate from solutions of (a) hexane, (b) water, and (c) acetone. Although differences in the atomization process lead to variation in nanoparticle size distribution between the three solvents, within a given solvent, the distributions are quite similar. (d) The differences in photoelectron yield between various compounds are a result of different material properties, which result in different electron MFPs and different probabilities for the electron to transmit through the surface. acac = acetylacetonate ($C_5H_7O_2$). Figure from [240].

only the first step in the three-step model of photoemission is not sufficient to explain the experimental observations. The remaining differences in photoelectron yield must therefore be related to electron transport and scattering at the interface, making this technique a sensitive probe of the associated materials properties, namely, the electron MFP and effective mass.

Additionally, the surface sensitivity of EUV photoemission is illustrated by the large difference in photoelectron yield between KI nanoparticles produced from solvation in acetone versus water. Despite the similarity in the particle size distributions from the two solvents (Fig. 6.3b,c), the photoelectron yield from KI nanoparticles produced in water is 20 times lower than from KI nanoparticles produced using acetone as the solvent. Because this difference in photoelectron yield cannot be explained by the variations in the nanoparticle size distributions, it must be due to a difference in the nanoparticle surfaces. The vapor pressure of water is more than an order-of-magnitude lower than acetone [264], so it is quite likely that, although the acetone evaporates completely, several monolayers of water remain on the nanoparticle surface. This thickness of water is on the same order-of-magnitude as the attinuation length of electrons in water [265] and could account for the dramatic decrease in the photoelectron yield. Alternatively, the morphology or surface roughness of the KI nanoparticles produced through the atomization process could vary depending on the solvent of origin, changing the available surface area for photoemission. In either case, this demonstrates that EUV photoemission is an effective probe of the chemical environments and the surfaces of nanoparticles.

6.5 Solvated Electron Dynamics

Having investigated the surface sensitivity of EUV photoemission from nanoparticles, we further demonstrate that this technique can probe femtosecond dynamics in nanoparticles. We performed EUV-pump–near-IR-probe spectroscopy on oleylamine ($C_{18}H_{35}NH_2$) nanodroplets, monitoring the total photoelectron yield as a function of the time delay between 790 nm and EUV pulses. We find a pronounced enhancement in the yield when the pulses are overlapped in time, a significant decay on the femtosecond time scale (151 ± 31 fs, Fig. 6.4a), and then a long-lived

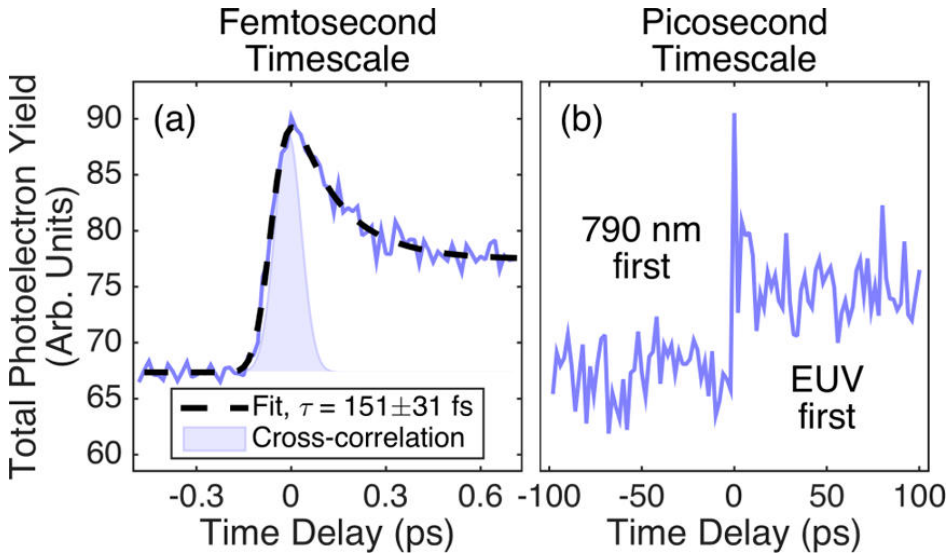

Figure 6.4: **Photoelectron yield from oleylamine nanodroplets as a function of time delay between a 790 nm pulse and a 22 eV EUV pulse.** Negative time delays have nonzero photoelectron yield because there are static signals from both the pump and the probe included here, photoelectros originating from the probe alone are due to multiphoton ionization from the nanodroplets. (a) On femtosecond time scales, the electron yield is enhanced when the pulses are overlapped and drops exponentially to an equilibrium value with a time constant of 151 ± 31 fs. This decay corresponds to the time scale for excited solvated electron states to relax to their ground state. (b) When the EUV pulse precedes the 790 nm pulse, the photoelectron yield is enhanced (lifetime ≫ 100 ps), indicating that electrons in the nanodroplet have been excited into a long-lived solvated-electron ground state by the EUV irradiation, which makes subsequent ionization by the 790 nm pulse more probable. Figure from [240].

enhancement of the yield when the EUV pulse precedes the 790 nm pulse (≫ 100 ps, Fig. 6.4b). We observe no such dynamics or enhancement in photoelectron yield when instead the 790 nm pulse precedes the EUV pulse.

These dynamics likely result from the formation of excited solvated electrons in the oleylamine nanodroplet and their subsequent relaxation to their ground state. Solvated electrons were first observed in ammonia in 1908 [266] and have recently attracted much attention because of their high reactivity [267–270], for example, their role in dissociated electron-transfer reactions. Since their discovery in ammonia, they have been observed in many different liquids, including water, alcohols, and acetonitrile [84, 85, 271, 272]. Solvated electrons are typically created after electrons have been promoted into the conduction band of a liquid [84, 273, 274]. When an EUV photon ionizes a

molecule within a nanodroplet, a high-energy electron is produced, which typically cannot directly escape the droplet. Instead, it scatters within the droplet, relaxing through the conduction band until the electron becomes solvated by the surrounding oleylamine [275, 276]. Solvated electrons are relatively loosely bound, with typical ground-state binding energies ranging from about −3.3 eV (water) [84, 271] to −1.5 eV (ammonia) [276] relative to the vacuum. Therefore, solvated electrons are much more easily ionized by the 790 nm (1.57 eV) pulse than electrons that are still in the ground state of oleylamine molecules, leading to an enhancement in the photoelectron yield when the 790 nm pulse arrives after an EUV pulse. The long persistence of this enhancement is in agreement with previously observed lifetimes of solvated electrons [271, 277]. Furthermore, the initial 151 ± 31 fs decay is consistent with previous measurements of the time scale for excited-solvated electrons to be created and decay to the ground 1s state in ammonia [276, 278].

The greater photoelectron yields observed when 790 nm pulses ionize excited states of the solvated electron can be understood through two separate mechanisms. One explanation is that the excited states are more delocalized than the ground state, leading to a larger photoionization cross section. Another possibility is that the binding energy of the ground-state solvated electron in oleylamine is greater than 1.57 eV. In that case, two 790 nm photons are required to ionize a ground-state solvated electron, while only one is necessary for excited states, resulting in a greater probability of photoionization from the excited state. We observe no measurable dynamics when the 790 nm pulse precedes the EUV pulse because 22 eV photons can easily ionize unexcited oleylamine in a single photon process, making it relatively insensitive to any prior excitation of the nanodroplet caused by the 790 nm pulse.

6.6 Conclusions and Outlook

In this chapter, I presented measurements of isolated nanoparticles using EUV light from a tabletop high-harmonic-generation source. We found that the EUV light is a sensitive probe of the nanoparticle surface and that the total photoelectron yield from the nanoparticles is strongly dependent on the material properties, namely the electron MFP and effective mass. Although

these total photoelectron-yield measurements cannot distinguish the contributions of the second and third steps in the three-step model of photoemission, measuring the change in photoelectron yield with nanoparticle size could be used to deconvolve them, which has been explored in detail in Goldmann, *et al.* [279]. Therefore, this technique provides an exciting new opportunity to directly measure material properties like electron MFPs and effective masses for a wide array of materials that cannot readily be studied with other techniques. For example, traditional bulk photoemission measurements can only really be done on conductive samples without suffering from space-charge issues. However, the flowing nanoparticle source employed here mitigates any charging effects. The capability to measure these material properties for a wide array of unocnventional materials can greatly enhance our understanding of the behavior of hot electrons in materials, including solvated electrons in nanodroplets [280–282].

We also demonstrated a pump–probe measurement of the femtosecond electron dynamics that occur after a nanodroplet is irradiated by high-flux femtosecond pulses of EUV light, which create excited-state solvated electrons within the nanodroplet. These solvated electrons can be probed by subsequent ionization by a near-IR pulse, revealing that the solvated electrons are created in an excited state and then relax to their ground state within 151 ± 31 fs. They remain as ground-state solvated electrons for $\gg 100$ ps, producing a long-lived enhancement in the photoelectron yield.

Here, the spatial imaging mode of the VMI spectrometer was used to obtain a higher signal-to-noise ratio; however, future studies (at higher laser repetition rates) may obtain fully energy and angularly resolved photoelectron distributions, providing further insight into nanoparticle surface dynamics. This technique can scale readily to smaller nanostructures, higher photon energies, and attosecond pulse durations, paving the way for a convenient tabletop probe of ultrafast dynamics of nanoparticles and their surfaces. Driving the HHG process with 790 nm or longer wavelengths produces higher energy photons and attosecond pulse trains or even isolated attosecond bursts [96, 99]. Higher-energy probe photons provide access to core levels of the atoms within nanoparticles, providing elemental and chemical specificity. Additionally, the energy dependence of electron MFPs can be exploited by tuning the EUV photon energy to tune the depth into the nanoparticle that

photoemission probes. Furthermore, methods of generating bright circularly polarized EUV light through novel HHG techniques [42–44, 48, 283] will allow the study of chiral and magnetic nanoparticles. Therefore, future improvements ot the apparatus may provide a breakthrough method for understanding the femtosecond and attosecond dynamics of nanoparticle surfaces.

Chapter 7

Conclusions and Outlook

This thesis is concerned with the development and application of extreme ultraviolet light sources, specifically with the goal of using novel spectroscopies to gain insight into nanoscale phenomena. As such, there are several exciting extensions of this work that I hope will be successfully implemented by subsequent generations of graduate students in the Kapteyn-Murnane group. First, the novel HHG geometries presented here are promising developments towards harnessing HHG as a probe of the chiral properties of nanomaterials:

- NCP-HHG generates two angularly separated beams that are nominally identical, except that one is RCP and the other is LCP. Therefore, this geometry provides a straight forward route to probe a sample with both helicities of light and thereby isolate any circular dichroism. Experimentally, one must simply image the HHG generation region to the sample of interest and alternatively block either the LCP or the RCP beam.[1] While this is not quite as simple as rotating a quarter wave plate, as in visible dichroism studies, it is pretty darn close. Indeed, NCP-HHG seems like the ideal tool to combine with the VMI and nanoparticle aerosol source to study chiral effects in nanoparticles via photoelectron circular dichroism.

- SVE-HHG combines two high-harmonic sources to produce a high-harmonic beam with spatially varying ellipticity. At any given spatial location, the precise helicity/ellipticity

[1] Note that allowing both of the beams to hit the sample simultaneously will reproduce the rotating polarization grating responsible for the generation of NCP-HHG light. While it is not immediately clear to me when or how this would be useful, it is an interesting situation to consider.

depends on the relative time delay between the two high-harmonic sources. Therefore, scanning the time delay enables one to apply Fourier transform spectroscopy, and thereby measure the *spectrally* resolved chiral response of the material without any dispersive optics. This capability means that spectral resolution is gained without sacrificing spatial resolution, thereby enabling hyperspectral chiral imaging. Combining this light source with coherent diffractive imaging techniques will give insight into a myriad of nanostructured chiral phenomena, such as magnetic domains, grain boundaries in materials, or nanoscale magnetic devices.

I am excited by the prospect of future students successfully applying these HHG schemes as probes of nanoscale structure and dynamics. Continuing on with this idea of combining multiple driving lasers or multiple harmonic sources, it is also intriguing to imagine the new and clever HHG geometries yet to be developed, which will hopefully give even greater control over the HHG process and tailor the emitted harmonic light in useful and exciting ways.

Additionally, to move forward with HHG as a probe of gas-phase nanoparticles we must first circumvent the contamination issue that arises due to the surface sensitivity of EUV photoemission and the realities of how pure or how clean solvents can be. An exciting route forward, which is currently being investigated in the Kapteyn-Murnane group, is the the use of a Haberland-type nanoparticle source [284] instead of the compressed gas atomizer employed in this thesis. The Haberland-type source is a completely in-vacuum nanoparticle generation technique that uses DC magnetron sputtering coupled with a gas-aggregation zone to produce nanoparticles from bulk material. As such, it is a fairly versatile source in that nanoparticles can be produced from essentially any material that can be DC sputtered. Additionally, these nanoparticles are exceedingly pure and their size distribution is somewhat tunable over the range from ∼2–20 nm (unfortunately, the particles are not monodisperse and instead have ∼20% size variation).

Excitingly, we have successfully coupled one of these Haberland-type nanoparticle sources (the NanoGen50 from Mantis Deposition, Fig. 7.1a) to our VMI spectrometer. Initial investigations

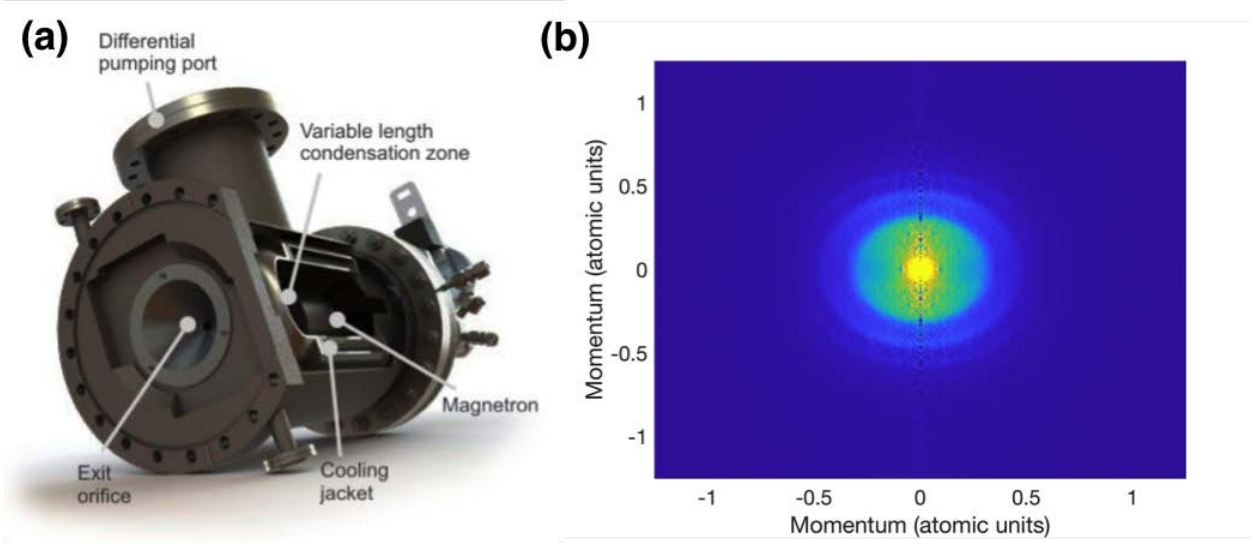

Figure 7.1: **Haberland-type nanoparticle source for the in-vacuum production of nanoparticles with completely clean surfaces.** (a) Artist rendering of the nanoparticle source, which is the NanoGen50 from Mantis Deposition. Figure from Mantis Deposition. (b) Photoelectron angular distribution from copper nanoparticles probed with 800 nm light. The vertical line at zero momentum is an artifact from the reconstruction of the 3D momentum distribution from the measured 2D projection.

using visible lasers demonstrated that this nanoparticle source has enough long-term stability for photoelectron spectroscopy measurements and enabled us to observe strong-field effects in metal nanoparticles (for example above threshold ionization [285, 286], Fig. 7.1b). While it has so far proved challenging to detect these nanoparticles with high harmonics, I am optimistic that the technical barriers can be overcome, thereby paving the way for exciting ultrafast EUV spectroscopy characterizations of both metallic and semiconductor nanparticles. In any case, this unique source of nanoparticles should enable access to a myriad of interesting physics and I am very eager to watch where this project goes in the future.

References

[1] R. A. Potyrailo, R. K. Bonam, J. G. Hartley, T. A. Starkey, P. Vukusic, M. Vasudev, T. Bunning, R. R. Naik, Z. Tang, M. A. Palacios, M. Larsen, L. A. Le Tarte, J. C. Grande, S. Zhong, and T. Deng. Towards outperforming conventional sensor arrays with fabricated individual photonic vapour sensors inspired by Morpho butterflies. *Nature Communications*, 6 (1), **2015**, p. 7959. DOI: 10.1038/ncomms8959 (cited on page 2).

[2] C. Chen. Attosecond Light Pulses and Attosecond Electron Dynamics Probed using Angle-Resolved Photoelectron Spectroscopy. PhD thesis. University of Colorado, 2017 (cited on page 3).

[3] A. McPherson, G. Gibson, H. Jara, U. Johann, T. S. Luk, I. A. McIntyre, K. Boyer, and C. K. Rhodes. Studies of multiphoton production of vacuum-ultraviolet radiation in the rare gases. *Journal of the Optical Society of America B*, 4 (4), **1987**, p. 595. DOI: 10.1364/JOSAB.4.000595 (cited on pages 3, 4, 83).

[4] M Ferray, A L'Huillier, X. F. Li, L. A. Lompre, G Mainfray, and C Manus. Multiple-harmonic conversion of 1064 nm radiation in rare gases. *Journal of Physics B: Atomic, Molecular and Optical Physics*, 21 (3), **1988**, pp. L31–L35. DOI: 10.1088/0953-4075/21/3/001 (cited on pages 3, 4, 83).

[5] A. Rundquist, C. G. Durfee, Z. Chang, C. Herne, S. Backus, M. M. Murnane, and H. C. Kapteyn. Phase-matched generation of coherent soft x-rays. *Science*, 280, **1998**, pp. 1412–1415. DOI: 10.1126/science.280.5368.1412 (cited on pages 3, 5, 17, 19, 66–68, 75, 83).

[6] R. A. Bartels, A. Paul, H. Green, H. C. Kapteyn, M. M. Murnane, S. Backus, I. P. Christov, Y. Liu, D. Attwood, and C. Jacobsen. Generation of spatially coherent light at extreme ultraviolet wavelengths. *Science*, 297 (5580), **2002**, pp. 376–378. DOI: 10.1126/science.1071718 (cited on page 3).

[7] C. L. Porter, M. Tanksalvala, M. Gerrity, G. Miley, X. Zhang, C. Bevis, E. Shanblatt, R. Karl, M. M. Murnane, D. E. Adams, and H. C. Kapteyn. General-purpose, wide field-of-view reflection imaging with a tabletop 13nm light source. *Optica*, 4 (12), **2017**, p. 1552. DOI: 10.1364/OPTICA.4.001552 (cited on page 3).

[8] D. F. Gardner, M. Tanksalvala, E. R. Shanblatt, X. Zhang, B. R. Galloway, C. L. Porter, R. Karl Jr, C. Bevis, D. E. Adams, H. C. Kapteyn, M. M. Murnane, and G. F. Mancini. Subwavelength coherent imaging of periodic samples using a 13.5nm tabletop high-harmonic light source. *Nature Photonics*, 11 (4), **2017**, pp. 259–263. DOI: 10.1038/nphoton.2017.33 (cited on pages 3, 83).

[9] E. R. Shanblatt, C. L. Porter, D. F. Gardner, G. F. Mancini, R. M. Karl, M. D. Tanksalvala, C. S. Bevis, V. H. Vartanian, H. C. Kapteyn, D. E. Adams, and M. M. Murnane. Quantitative Chemically Specific Coherent Diffractive Imaging of Reactions at Buried Interfaces with Few Nanometer Precision. *Nano Letters*, 16 (9), **2016**, pp. 5444–5450. DOI: 10.1021/acs.nanolett.6b01864 (cited on page 3).

[10] M. D. Seaberg, B. Zhang, D. F. Gardner, E. R. Shanblatt, M. M. Murnane, H. C. Kapteyn, and D. E. Adams. Tabletop nanometer extreme ultraviolet imaging in an extended reflection mode using coherent Fresnel ptychography. *Optica*, 1 (1), **2014**, p. 39. DOI: 10.1364/OPTICA.1.000039 (cited on page 3).

[11] B. Henke, E. Gullikson, and J. Davis. X-Ray Interactions: Photoabsorption, Scattering, Transmission, and Reflection at E = 50-30,000 eV, Z = 1-92. *Atomic Data and Nuclear Data Tables*, 54 (2), **1993**, pp. 181–342. DOI: 10.1006/adnd.1993.1013 (cited on pages 3, 34, 35, 183).

[12] C. Spielmann, N. H. Burnett, S. Sartania, R. Koppitsch, M. Schnürer, C. Kan, M. Lenzner, P. Wobrauschek, and F. Krausz. Generation of Coherent X-rays in the Water Window Using 5-Femtosecond Laser Pulses. *Science*, 278 (5338), **1997**, pp. 661–664. DOI: 10.1126/science.278.5338.661 (cited on page 3).

[13] E. Seres, J. Seres, and C. Spielmann. X-ray absorption spectroscopy in the keV range with laser generated high harmonic radiation. *Applied Physics Letters*, 89 (18), **2006**, p. 181919. DOI: 10.1063/1.2364126 (cited on page 3).

[14] T. Popmintchev, M.-C. Chen, D. Popmintchev, P. Arpin, S. Brown, S. Alisauskas, G. Andriukaitis, T. Balciunas, O. D. Mücke, A. Pugzlys, A. Baltuska, B. Shim, S. E. Schrauth, A. Gaeta, C. Hernández-García, L. Plaja, A. Becker, A. Jaron-Becker, M. M. Murnane, and H. C. Kapteyn. Bright coherent ultrahigh harmonics in the keV x-ray regime from mid-infrared femtosecond lasers. *Science*, 336 (6086), **2012**, pp. 1287–91. DOI: 10.1126/science.1218497 (cited on pages 3–5, 16, 20, 75).

[15] S. Mathias, C. La-O-Vorakiat, P. Grychtol, P. Granitzka, E. Turgut, J. M. Shaw, R. Adam, H. T. Nembach, M. E. Siemens, S. Eich, C. M. Schneider, T. J. Silva, M. Aeschlimann, M. M. Murnane, and H. C. Kapteyn. Probing the timescale of the exchange interaction in a ferromagnetic alloy. *PNAS*, 109 (13), **2012**, pp. 4792–7. DOI: 10.1073/pnas.1201371109 (cited on page 3).

[16] J. Vura-Weis, C.-M. Jiang, C. Liu, H. Gao, J. M. Lucas, F. M. F. de Groot, P. Yang, A. P. Alivisatos, and S. R. Leone. Femtosecond M2,3 -Edge Spectroscopy of Transition-Metal Oxides: Photoinduced Oxidation State Change in α-Fe2O3. *The Journal of Physical Chemistry Letters*, 4 (21), **2013**, pp. 3667–3671. DOI: 10.1021/jz401997d (cited on page 3).

[17] T. Gaumnitz, A. Jain, Y. Pertot, M. Huppert, I. Jordan, F. Ardana-Lamas, and H. J. Wörner. Streaking of 43-attosecond soft-X-ray pulses generated by a passively CEP-stable mid-infrared driver. *Optics Express*, 25 (22), **2017**, p. 27506. DOI: 10.1364/OE.25.027506 (cited on pages 3, 5).

[18] I. J. Sola, E. Mével, L. Elouga, E. Constant, V. Strelkov, L. Poletto, P. Villoresi, E. Benedetti, J.-P. Caumes, S. Stagira, C. Vozzi, G. Sansone, and M. Nisoli. Controlling attosecond electron dynamics by phase-stabilized polarization gating. *Nature Physics*, 2 (5), **2006**, pp. 319–322. DOI: 10.1038/nphys281 (cited on pages 3, 23).

[19] G. Sansone, E. Benedetti, F. Calegar, C. Vozzi, L. Avaldi, R. Flammini, L. Polett, P. Villoresi, C. Altucci, R. Velotta, S. Stagira, S. De Silvestri, and M. Nisoli. Isolated Single-Cycle Attosecond Pulses. *Science*, 314 (5798), **2006**, pp. 443–446. DOI: 10.1126/science.1132838 (cited on pages 3, 5).

[20] E. Goulielmakis, M. Schultze, M. Hofstetter, V. S. Yakovlev, J. Gagnon, M. Uiberacker, A. L. Aquila, E. M. Gullikson, D. T. Attwood, R. Kienberger, F. Krausz, and U. Kleineberg. Single-Cycle Nonlinear Optics. *Science*, 320 (5883), **2008**, pp. 1614–1617. DOI: 10.1126/science.1157846 (cited on pages 3, 5, 179).

[21] H. Mashiko, S. Gilbertson, C. Li, S. D. Khan, M. M. Shakya, E. Moon, and Z. Chang. Double Optical Gating of High-Order Harmonic Generation with Carrier-Envelope Phase Stabilized Lasers. *Physical Review Letters*, 100 (10), **2008**, p. 103906. DOI: 10.1103/PhysRevLett.100.103906 (cited on pages 3, 23).

[22] F. Silva, S. M. Teichmann, S. L. Cousin, M. Hemmer, and J. Biegert. Spatiotemporal isolation of attosecond soft X-ray pulses in the water window. *Nature Communications*, 6, **2015**, p. 6611. DOI: 10.1038/ncomms7611 (cited on pages 3, 16).

[23] J. Li, X. Ren, Y. Yin, K. Zhao, A. Chew, Y. Cheng, E. Cunningham, Y. Wang, S. Hu, Y. Wu, M. Chini, and Z. Chang. 53-attosecond X-ray pulses reach the carbon K-edge. *Nature Communications*, 8 (1), **2017**, p. 186. DOI: 10.1038/s41467-017-00321-0 (cited on pages 3, 5).

[24] M Schultze, M Fiess, N Karpowicz, J Gagnon, M Korbman, M Hofstetter, S Neppl, A. L. Cavalieri, Y Komninos, T. Mercouris, C. A. Nicolaides, R Pazourek, S Nagele, J Feist, J Burgdörfer, A. M. Azzeer, R Ernstorfer, R Kienberger, U Kleineberg, E Goulielmakis, F

Krausz, and V. S. Yakovlev. Delay in photoemission. *Science*, 328 (5986), **2010**, pp. 1658–62. DOI: 10.1126/science.1189401 (cited on pages 3, 10, 83).

[25] K. Klünder, J. M. Dahlström, M. Gisselbrecht, T. Fordell, M. Swoboda, D. Guénot, P. Johnsson, J. Caillat, J. Mauritsson, A. Maquet, R. Taïeb, and A. L'Huillier. Probing Single-Photon Ionization on the Attosecond Time Scale. *Physical Review Letters*, 106 (14), **2011**, p. 143002. DOI: 10.1103/PhysRevLett.106.143002 (cited on page 3).

[26] S Nagele, R Pazourek, J Feist, K Doblhoff-Dier, C Lemell, K Tkési, and J Burgdörfer. Time-resolved photoemission by attosecond streaking: extraction of time information. *Journal of Physics B: Atomic, Molecular and Optical Physics*, 44 (8), **2011**, p. 081001. DOI: 10.1088/0953-4075/44/8/081001 (cited on page 3).

[27] M. Sabbar, S. Heuser, R. Boge, M. Lucchini, T. Carette, E. Lindroth, L. Gallmann, C. Cirelli, and U. Keller. Resonance Effects in Photoemission Time Delays. *Physical Review Letters*, 115 (13), **2015**, p. 133001. DOI: 10.1103/PhysRevLett.115.133001 (cited on page 3).

[28] C. Chen, Z. Tao, A. Carr, P. Matyba, T. Szilvási, S. Emmerich, M. Piecuch, M. Keller, D. Zusin, S. Eich, M. Rollinger, W. You, S. Mathias, U. Thumm, M. Mavrikakis, M. Aeschlimann, P. M. Oppeneer, H. Kapteyn, and M. Murnane. Distinguishing attosecond electron-electron scattering and screening in transition metals. *PNAS*, 114 (27), **2017**, E5300–E5307. DOI: 10.1073/pnas.1706466114 (cited on pages 3, 83, 85, 94).

[29] Z. Tao, C. Chen, T. Szilvási, M. Keller, M. Mavrikakis, H. Kapteyn, and M. Murnane. Direct time-domain observation of attosecond final-state lifetimes in photoemission from solids. *Science*, 353 (6294), **2016**, pp. 62–7. DOI: 10.1126/science.aaf6793 (cited on pages 4, 83).

[30] B. W. J. McNeil and N. R. Thompson. X-ray free-electron lasers. *Nature Photonics*, 4 (12), **2010**, pp. 814–821. DOI: 10.1038/nphoton.2010.239 (cited on page 4).

[31] R. W. Schoenlein, S. Chattopadhyay, H. H. W. Chong, T. E. Glover, P. A. Heimann, C. V. Shank, A. A. Zholents, and M. S. Zolotorev. Generation of femtosecond pulses of synchrotron

radiation. *Science*, 287 (5461), **2000**, pp. 2237–40. DOI: 10.1126/SCIENCE.287.5461.2237 (cited on page 4).

[32] M. Y. Kuchiev. Atomic antenna. *JETP Lett.*, 45 (7), **1987**, pp. 404–406 (cited on page 5).

[33] J. L. Krause, K. J. Schafer, and K. C. Kulander. High-order harmonic generation from atoms and ions in the high intensity regime. *Physical Review Letters*, 68 (24), **1992**, pp. 3535–3538. DOI: 10.1103/PhysRevLett.68.3535 (cited on pages 5, 12).

[34] P. B. Corkum. Plasma perspective on strong field multiphoton ionization. *Physical Review Letters*, 71 (13), **1993**, pp. 1994–1997. DOI: 10.1103/PhysRevLett.71.1994 (cited on pages 5, 12, 83).

[35] M. Lewenstein, P. Balcou, M. Y. Ivanov, A. L'Huillier, and P. B. Corkum. Theory of high-harmonic generation by low-frequency laser fields. *Physical Review A*, 49 (3), **1994**, pp. 2117–2132. DOI: 10.1103/PhysRevA.49.2117 (cited on pages 5, 16, 21).

[36] C. G. Durfee, A. R. Rundquist, S. Backus, C. Herne, M. M. Murnane, and H. C. Kapteyn. Phase matching of high-order harmonics in hollow waveguides. *Phys. Rev. Lett.*, 83 (11), **1999**, p. 2187. DOI: 10.1103/PhysRevLett.83.2187 (cited on pages 5, 17, 19, 66–68, 72, 75, 171).

[37] E. Constant, D. Garzella, P. Breger, E. Mével, C. Dorrer, C. Le Blanc, F. Salin, and P. Agostini. Optimizing high harmonic generation in absorbing gases: Model and experiment. *Physical Review Letters*, 82 (8), **1999**, pp. 1668–1671. DOI: 10.1103/PhysRevLett.82.1668 (cited on pages 5, 17, 22, 23, 66, 72, 171).

[38] M. Schnürer, Z. Cheng, M. Hentschel, G. Tempea, P. Kálmán, T. Brabec, and F. Krausz. Absorption-limited generation of coherent ultrashort soft-x-ray pulses. *Physical Review Letters*, 83 (4), **1999**, pp. 722–725. DOI: 10.1103/PhysRevLett.83.722 (cited on pages 5, 66).

[39] K. Zhao, Q. Zhang, M. Chini, Y. Wu, X. Wang, and Z. Chang. Tailoring a 67 attosecond pulse through advantageous phase-mismatch. *Optics Letters*, 37 (18), **2012**, p. 3891. DOI: 10.1364/OL.37.003891 (cited on pages 5, 16).

[40] K. S. Budil, P. Salières, A. L'Huillier, T. Ditmire, and M. D. Perry. Influence of ellipticity on harmonic generation. *Physical Review A*, 48 (5), **1993**, R3437–R3440. DOI: 10.1103/PhysRevA.48.R3437 (cited on pages 5, 23, 83).

[41] P. Antoine, A. L'Huillier, M. Lewenstein, P. Salières, and B. Carré. Theory of high-order harmonic generation by an elliptically polarized laser field. *Physical Review A*, 53 (3), **1996**, pp. 1725–1745. DOI: 10.1103/PhysRevA.53.1725 (cited on page 5).

[42] A. Fleischer, O. Kfir, T. Diskin, P. Sidorenko, and O. Cohen. Spin angular momentum and tunable polarization in high-harmonic generation. *Nature Photon.*, 8 (7), **2014**, pp. 543–549. DOI: 10.1038/nphoton.2014.108 (cited on pages 5, 23, 36, 66, 84, 118, 167).

[43] O. Kfir, P. Grychtol, E. Turgut, R. Knut, D. Zusin, D. Popmintchev, T. Popmintchev, H. Nembach, J. M. Shaw, A. Fleischer, H. Kapteyn, M. Murnane, and O. Cohen. Generation of bright phase-matched circularly-polarized extreme ultraviolet high harmonics. *Nature Photonics*, 9 (2), **2014**, pp. 99–105. DOI: 10.1038/nphoton.2014.293 (cited on pages 5, 23, 25, 26, 36, 66, 84, 118, 167).

[44] G. Lambert, B. Vodungbo, J. Gautier, B. Mahieu, V. Malka, S. Sebban, P. Zeitoun, J. Luning, J. Perron, A. Andreev, S. Stremoukhov, F. Ardana-Lamas, A. Dax, C. P. Hauri, A. Sardinha, and M. Fajardo. Towards enabling femtosecond helicity-dependent spectroscopy with high-harmonic sources. *Nature Communications*, 6, **2015**, p. 6167. DOI: 10.1038/ncomms7167 (cited on pages 5, 24, 84, 118).

[45] T. Fan, P. Grychtol, R. Knut, C. Hernández-García, D. D. Hickstein, D. Zusin, C. Gentry, F. J. Dollar, C. A. Mancuso, C. W. Hogle, O. Kfir, D. Legut, K. Carva, J. L. Ellis, K. M. Dorney, C. Chen, O. G. Shpyrko, E. E. Fullerton, O. Cohen, P. M. Oppeneer, D. B. Milošević, A. Becker, A. A. Jaroń-Becker, T. Popmintchev, M. M. Murnane, and H. C. Kapteyn. Bright

circularly polarized soft x-ray high harmonics for x-ray magnetic circular dichroism. *PNAS*, 112 (46), **2015**, pp. 14206–14211. DOI: 10.1073/pnas.1519666112 (cited on pages 5, 26, 27, 74, 76, 84, 85).

[46] A. Ferré, C. Handschin, M. Dumergue, F. Burgy, A. Comby, D. Descamps, B. Fabre, G. A. Garcia, R. Géneaux, L. Merceron, E. Mével, L. Nahon, S. Petit, B. Pons, D. Staedter, S. Weber, T. Ruchon, V. Blanchet, and Y. Mairesse. A table-top ultrashort light source in the extreme ultraviolet for circular dichroism experiments. *Nature Photonics*, 9 (2), **2015**, pp. 93–98. DOI: 10.1038/nphoton.2014.314 (cited on pages 5, 23, 36, 84).

[47] K. M. Dorney, J. L. Ellis, C. Hernández-García, D. D. Hickstein, C. A. Mancuso, N. Brooks, T. Fan, G. Fan, D. Zusin, C. Gentry, P. Grychtol, H. C. Kapteyn, and M. M. Murnane. Helicity-Selective Enhancement and Polarization Control of Attosecond High Harmonic Waveforms Driven by Bichromatic Circularly Polarized Laser Fields. *Physical Review Letters*, 119 (6), **2017**, p. 063201. DOI: 10.1103/PhysRevLett.119.063201 (cited on pages 5, 26, 64, 85, 92).

[48] D. Hickstein, F. Dollar, P. Grychtol, J. Ellis, R. Knut, C. Hernandez-Garcia, D. Zusin, C. Gentry, J. Shaw, T. Fan, K. Dorney, A. Becker, A. Jaron-Becker, H. Kapteyn, M. Murnane, and C. Durfee. Non-collinear generation of angularly isolated circularly polarized high harmonics. *Nature Photonics*, 9 (11), **2015**, pp. 743–750. DOI: 10.1038/nphoton.2015.181 (cited on pages 5, 55, 57, 60, 62–64, 66, 67, 74, 84, 118, 165, 166, 168, 171).

[49] P.-C. Huang, C.-H. Lu, C. Hernández-García, R.-T. Huang, P.-S. Wu, D. D. Hickstein, D. A. Thrasher, J. Ellis, A. H. Kung, S.-D. Yang, A. Jaron-Becker, A. Becker, H. Kapteyn, M. M. Murnane, C. Durfee, and M.-C. Chen. Isolated, circularly polarized, attosecond pulse generation. In: **Conference on Lasers and Electro-Optics**. Washington, D.C.: OSA, 2016, JTh4A.7. DOI: 10.1364/CLEO_AT.2016.JTh4A.7 (cited on pages 5, 64, 79, 85, 92).

[50] A. V. Birulin, V. T. Platonenko, and V. V. Strelkov. High-order harmonic generation in colliding beams. *Quantum Electronics*, 26 (5), **1996**, pp. 377–378. DOI: 10.1070/QE1996v026n05ABEH000676 (cited on pages 5, 55).

[51] C. M. Heyl, P. Rudawski, F. Brizuela, S. N. Bengtsson, J. Mauritsson, and A. L'Huillier. Macroscopic effects in noncollinear high-order harmonic generation. *Physical Review Letters*, 112 (14), **2014**, p. 143902. DOI: 10.1103/PhysRevLett.112.143902 (cited on pages 5, 55, 66–68, 85).

[52] C. M. Heyl, S. N. Bengtsson, S Carlström, J Mauritsson, C. L. Arnold, and A L'Huillier. Noncollinear optical gating. *N. J. Phys*, 16 (10), **2014**, p. 052001. DOI: 10.1088/1367-2630/16/10/109501 (cited on pages 5, 55).

[53] M. B. Wilker, K. J. Schnitzenbaumer, and G. Dukovic. Recent Progress in Photocatalysis Mediated by Colloidal II-VI Nanocrystals. *Israel Journal of Chemistry*, 52 (11-12), **2012**, pp. 1002–1015. DOI: 10.1002/ijch.201200073 (cited on pages 8, 97).

[54] L. Dworak, V. V. Matylitsky, V. V. Breus, M. Braun, T. Basche, and J. Wachtveitl. Ultrafast Charge Separation at the CdSe/CdS Core/Shell Quantum Dot/Methylviologen Interface: Implications for Nanocrystal Solar Cells. *The Journal of Physical Chemistry C*, 115 (10), **2011**, pp. 3949–3955. DOI: 10.1021/jp111574w (cited on pages 8, 97, 98).

[55] B.-R. Hyun, A. C. Bartnik, J.-K. Lee, H. Imoto, L. Sun, J. J. Choi, Y. Chujo, T. Hanrath, C. K. Ober, and F. W. Wise. Role of Solvent Dielectric Properties on Charge Transfer from PbS Nanocrystals to Molecules. *Nano Letters*, 10 (1), **2010**, pp. 318–323. DOI: 10.1021/nl903623n (cited on pages 8, 97).

[56] E. Hendry, M. Koeberg, F. Wang, H. Zhang, C. de Mello Donegá, D. Vanmaekelbergh, and M. Bonn. Direct Observation of Electron-to-Hole Energy Transfer in CdSe Quantum Dots. *Physical Review Letters*, 96 (5), **2006**, p. 057408. DOI: 10.1103/PhysRevLett.96.057408 (cited on pages 8, 97).

[57] H.-W. Tseng, M. B. Wilker, N. H. Damrauer, and G. Dukovic. Charge Transfer Dynamics between Photoexcited CdS Nanorods and Mononuclear Ru Water-Oxidation Catalysts. *Journal of the American Chemical Society*, 135 (9), **2013**, pp. 3383–3386. DOI: 10.1021/ja400178g (cited on pages 8, 97, 101).

[58] X. Ai, R. Jin, C. Ge, J. Wang, Y. Zou, X. Zhou, and X. Xiao. Femtosecond investigation of charge carrier dynamics in CdSe nanocluster films. *Journal of Chemical Physics*, 106, **1997**, p. 3387. DOI: 10.1063/1.473087 (cited on pages 8, 97).

[59] B. O. Dabbousi, M. G. Bawendi, O. Onitsuka, and M. F. Rubner. Electroluminescence from CdSe quantumdot/polymer composites. *Applied Physics Letters*, 66 (11), **1995**, pp. 1316–1318. DOI: 10.1063/1.113227 (cited on page 8).

[60] J. Lee, V. C. Sundar, J. R. Heine, M. G. Bawendi, and K. F. Jensen. Full Color Emission from II-VI Semiconductor Quantum Dot-Polymer Composites. *Advanced Materials*, 12 (15), **2000**, pp. 1102–1105. DOI: 10.1002/1521-4095(200008)12:15<1102::AID-ADMA1102>3.0.CO;2-J (cited on page 8).

[61] L. Bakueva, S. Musikhin, M. A. Hines, T.-W. F. Chang, M. Tzolov, G. D. Scholes, and E. H. Sargent. Size-tunable infrared (10001600 nm) electroluminescence from PbS quantum-dot nanocrystals in a semiconducting polymer. *Applied Physics Letters*, 82 (17), **2003**, pp. 2895–2897. DOI: 10.1063/1.1570940 (cited on page 8).

[62] L. Miaja-Avila, J. R. Tritsch, A. Wolcott, W.-L. Chan, C. A. Nelson, and X.-Y. Zhu. Direct Mapping of Hot-Electron Relaxation and Multiplication Dynamics in PbSe Quantum Dots. *Nano Letters*, 12 (3), **2012**, pp. 1588–1591. DOI: 10.1021/nl204489a (cited on pages 8, 47, 97).

[63] Z. Xie, T. Z. Markus, G. Gotesman, Z. Deutsch, D. Oron, and R. Naaman. How Isolated Are the Electronic States of the Core in Core/Shell Nanoparticles? *ACS Nano*, 5 (2), **2011**, pp. 863–869. DOI: 10.1021/nn102002x (cited on pages 8, 47).

[64] P. Sippel, W. Albrecht, D. Mitoraj, R. Eichberger, T. Hannappel, and D. Vanmaekelbergh. Two-Photon Photoemission Study of Competing Auger and Surface-Mediated Relaxation of Hot Electrons in CdSe Quantum Dot Solids. *Nano Letters*, 13 (4), **2013**, pp. 1655–1661. DOI: 10.1021/nl400113t (cited on pages 8, 51, 102).

[65] N. M. Gabor, Z. Zhong, K. Bosnick, J. Park, P. L. McEuen, A. J. Nozik, and M. C. Beard. Extremely Efficient Multiple Electron-Hole Pair Generation in Carbon Nanotube Photodiodes. *Science*, 325 (5946), **2009**, pp. 1367–1371. DOI: 10.1126/science.1176112 (cited on page 8).

[66] S. A. McDonald, G. Konstantatos, S. Zhang, P. W. Cyr, E. J. D. Klem, L. Levina, and E. H. Sargent. Solution-processed PbS quantum dot infrared photodetectors and photovoltaics. *Nature Materials*, 4 (2), **2005**, pp. 138–142. DOI: 10.1038/nmat1299 (cited on page 8).

[67] V. Wood, M. J. Panzer, J. Chen, M. S. Bradley, J. E. Halpert, M. G. Bawendi, and V. Bulovic. Inkjet-Printed Quantum Dot-Polymer Composites for Full-Color AC-Driven Displays. *Advanced Materials*, 21 (21), **2009**, pp. 2151–2155. DOI: 10.1002/adma.200803256 (cited on page 8).

[68] K. R. Choudhury, Y. Sahoo, T. Y. Ohulchanskyy, and P. N. Prasad. Efficient photoconductive devices at infrared wavelengths using quantum dot-polymer nanocomposites. *Applied Physics Letters*, 87 (7), **2005**, p. 073110. DOI: 10.1063/1.2011768 (cited on page 8).

[69] J. M. Caruge, J. E. Halpert, V. Wood, V. Bulović, and M. G. Bawendi. Colloidal quantum-dot light-emitting diodes with metal-oxide charge transport layers. *Nature Photonics*, 2 (4), **2008**, pp. 247–250. DOI: 10.1038/nphoton.2008.34 (cited on page 8).

[70] A. Henglein. Photochemistry of Colloidal Cadmium Sulfide. 2. Effects of Adsorbed Methyl Viologen and of Colloidal Platinum. *J. Phys. Chem*, 86, **1982**, pp. 301–305 (cited on page 8).

[71] L. Spanhel, M. Haase, H. Weller, and A. Henglein. Photochemistry of colloidal semiconductors. 20. Surface modification and stability of strong luminescing CdS particles. *Journal of*

the American Chemical Society, 109 (19), **1987**, pp. 5649–5655. DOI: 10.1021/ja00253a015 (cited on pages 8, 112).

[72] W. G. J. H. M. van Sark, P. L. T. M. Frederix, D. J. van den Heuvel, H. C. Gerritsen, A. A. Bol, J. N. J. van Lingen, C. de Mello Donegá, and A. Meijerink. Photooxidation and Photobleaching of Single CdSe/ZnS Quantum Dots Probed by Room-Temperature Time-Resolved Spectroscopy. *Journal of Physical Chemistry B*, 105 (35), **2001**, pp. 8281–8284. DOI: 10.1021/JP012018H (cited on page 8).

[73] G. Nair, L.-Y. Chang, S. M. Geyer, and M. G. Bawendi. Perspective on the Prospects of a Carrier Multiplication Nanocrystal Solar Cell. *Nano Letters*, 11 (5), **2011**, pp. 2145–2151. DOI: 10.1021/nl200798x (cited on page 8).

[74] H. Borchert, D. V. Talapin, C. McGinley, S. Adam, A. Lobo, A. R. B. de Castro, T. Möller, and H. Weller. High resolution photoemission study of CdSe and CdSe/ZnS core-shell nanocrystals. *The Journal of Chemical Physics*, 119 (3), **2003**, pp. 1800–1807. DOI: 10.1063/1.1580096 (cited on page 8).

[75] L. R. Moore, M. A. Lysaght, J. S. Parker, H. W. van der Hart, and K. T. Taylor. Time delay between photoemission from the 2p and 2s subshells of neon. *Physical Review A*, 84 (6), **2011**, p. 061404. DOI: 10.1103/PhysRevA.84.061404 (cited on page 10).

[76] D. Guénot, K. Klünder, C. L. Arnold, D. Kroon, J. M. Dahlström, M. Miranda, T. Fordell, M. Gisselbrecht, P. Johnsson, J. Mauritsson, E. Lindroth, A. Maquet, R. Taïeb, A. L'Huillier, and A. S. Kheifets. Photoemission-time-delay measurements and calculations close to the 3s-ionization-cross-section minimum in Ar. *Physical Review A*, 85 (5), **2012**, p. 053424. DOI: 10.1103/PhysRevA.85.053424 (cited on page 10).

[77] S. Heuser, Á. Jiménez Galán, C. Cirelli, C. Marante, M. Sabbar, R. Boge, M. Lucchini, L. Gallmann, I. Ivanov, A. S. Kheifets, J. M. Dahlström, E. Lindroth, L. Argenti, F. Martín, and U. Keller. Angular dependence of photoemission time delay in helium. *Physical Review A*, 94 (6), **2016**, p. 063409. DOI: 10.1103/PhysRevA.94.063409 (cited on page 10).

[78] S. Hüfner. **Photoelectron Spectroscopy: Principles and Applications**. 3rd. Berlin, Heidelberg, New York: Springer-Verlag, 2003, pp. 349–357 (cited on pages 10, 11, 112).

[79] W. Xiong, D. D. Hickstein, K. J. Schnitzenbaumer, J. L. Ellis, B. B. Palm, K. E. Keister, C. Ding, L. Miaja-Avila, G. Dukovic, J. L. Jimenez, M. M. Murnane, and H. C. Kapteyn. Photoelectron Spectroscopy of CdSe Nanocrystals in the Gas Phase: A Direct Measure of the Evanescent Electron Wave Function of Quantum Dots. *Nano Letters*, 13 (6), **2013**, pp. 2924–2930. DOI: 10.1021/nl401309z (cited on pages 10, 45, 48–52, 98, 100, 110).

[80] M. P. Seah and W. A. Dench. Quantitative Electron Spectroscopy of Surfaces: A Standard Data Base for Electron Inelastic Mean Free Paths in Solids. *Surface and Interface Analysis*, 1 (1), **1979**, pp. 2–11 (cited on pages 11, 109).

[81] A. Damascelli. Probing the Electronic Structure of Complex Systems by ARPES. *Physica Scripta*, 2004 (T109), **2004**, pp. 61–74. DOI: 10.1238/Physica.Topical.109a00061 (cited on pages 11, 109, 112).

[82] B. Winter. Liquid microjet for photoelectron spectroscopy. *Nuclear Instruments and Methods in Physics Research Section A: Accelerators, Spectrometers, Detectors and Associated Equipment*, 601 (1-2), **2009**, pp. 139–150. DOI: 10.1016/J.NIMA.2008.12.108 (cited on page 11).

[83] A. T. Shreve, T. A. Yen, and D. M. Neumark. Photoelectron spectroscopy of hydrated electrons. *Chemical Physics Letters*, 493 (4-6), **2010**, pp. 216–219. DOI: 10.1016/J.CPLETT.2010.05.059 (cited on page 11).

[84] K. R. Siefermann, Y. Liu, E. Lugovoy, O. Link, M. Faubel, U. Buck, B. Winter, and B. Abel. Binding energies, lifetimes and implications of bulk and interface solvated electrons in water. *Nature Chemistry*, 2 (4), **2010**, pp. 274–9. DOI: 10.1038/nchem.580 (cited on pages 11, 115, 116).

[85] A. T. Shreve, M. H. Elkins, and D. M. Neumark. Photoelectron spectroscopy of solvated electrons in alcohol and acetonitrile microjets. *Chemical Science*, 4 (4), **2013**, pp. 1633–1639. DOI: 10.1039/c3sc22063j (cited on pages 11, 115).

[86] C. H Keitel, P. L Knight, and K Burnett. Relativistic High-Harmonic Generation. *Europhysics Letters*, 24 (7), **1993**, pp. 539–544. DOI: 10.1209/0295-5075/24/7/006 (cited on page 12).

[87] B. Dromey, M. Zepf, A. Gopal, K. Lancaster, M. S. Wei, K. Krushelnick, M. Tatarakis, N. Vakakis, S. Moustaizis, R. Kodama, M. Tampo, C. Stoeckl, R. Clarke, H. Habara, D. Neely, S. Karsch, and P. Norreys. High harmonic generation in the relativistic limit. *Nature Physics*, 2 (7), **2006**, pp. 456–459. DOI: 10.1038/nphys338 (cited on page 12).

[88] S. Ghimire, A. D. DiChiara, E. Sistrunk, P. Agostini, L. F. DiMauro, and D. A. Reis. Observation of high-order harmonic generation in a bulk crystal. *Nature Physics*, 7 (2), **2011**, pp. 138–141. DOI: 10.1038/nphys1847 (cited on page 12).

[89] G. Vampa, T. J. Hammond, N. Thiré, B. E. Schmidt, F. Légaré, C. R. McDonald, T. Brabec, and P. B. Corkum. Linking high harmonics from gases and solids. *Nature*, 522 (7557), **2015**, pp. 462–464. DOI: 10.1038/nature14517 (cited on page 12).

[90] T. T. Luu, M. Garg, S. Y. Kruchinin, A. Moulet, M. T. Hassan, and E. Goulielmakis. Extreme ultraviolet high-harmonic spectroscopy of solids. *Nature*, 521 (7553), **2015**, pp. 498–502. DOI: 10.1038/nature14456 (cited on page 12).

[91] T. Popmintchev. Tunable Ultrafast Coherent Light in the Soft and Hard X-ray Regions of the Spectrum: Phase Matching of Extreme High-Order Harmonic Generation. PhD thesis. University of Colorado, Boulder, 2009 (cited on pages 12, 17, 20, 22).

[92] B. R. Galloway. High-Order Harmonic Generation Driven by Mid-Infrared Laser Light. PhD thesis. University of Colorado, Boulder, 2017 (cited on pages 12, 15).

[93] T. Fan. Bright Linearly and Circularly Polarized Extreme Ultraviolet and Soft X-Ray High Harmonics for Absorption Spectroscopy. PhD thesis. University of Colorado Boulder, 2017 (cited on pages 12, 27, 85).

[94] L. V. Keldysh. Ionization in the Field of a Strong Electromagnetic Wave. *Soviet Physics JETP*, 20 (5), **1964**, pp. 1307–1314 (cited on page 13).

[95] M. V. Ammosov, N. B. Delone, and V. P. Krainov. Tunnel ionization of complex atoms and atomic ions in an alternating electromagnetic field. *Soviet Physics JETP*, 64 (6), **1986**, pp. 1191–1194 (cited on page 13).

[96] T. Popmintchev, M.-C. Chen, P. Arpin, M. M. Murnane, and H. C. Kapteyn. The attosecond nonlinear optics of bright coherent X-ray generation. *Nature Photonics*, 4 (12), **2010**, pp. 822–832. DOI: 10.1038/nphoton.2010.256 (cited on pages 13, 65, 117, 166).

[97] S. T. Cundiff and J. Ye. Colloquium: Femtosecond optical frequency combs. *Reviews of Modern Physics*, 75 (1), **2003**, pp. 325–342. DOI: 10.1103/RevModPhys.75.325 (cited on page 14).

[98] S. A. Diddams. The evolving optical frequency comb. *Journal of the Optical Society of America B*, 27 (11), **2010**, B51. DOI: 10.1364/JOSAB.27.000B51 (cited on page 14).

[99] M.-C. Chen, C. Mancuso, C. Hernández-García, F. Dollar, B. Galloway, D. Popmintchev, P.-C. Huang, B. Walker, L. Plaja, A. A. Jaroń-Becker, A. Becker, M. M. Murnane, H. C. Kapteyn, and T. Popmintchev. Generation of bright isolated attosecond soft X-ray pulses driven by multicycle midinfrared lasers. *PNAS*, 111 (23), **2014**, E2361–7. DOI: 10.1073/pnas.1407421111 (cited on pages 16, 85, 95, 117).

[100] F. Ferrari, F. Calegari, M. Lucchini, C. Vozzi, S. Stagira, G. Sansone, and M. Nisoli. High-energy isolated attosecond pulses generated by above-saturation few-cycle fields. *Nature Photonics*, 4 (12), **2010**, pp. 875–879. DOI: 10.1038/nphoton.2010.250 (cited on pages 16, 66).

[101] S. M. Teichmann, F. Silva, S. L. Cousin, M. Hemmer, and J. Biegert. 0.5-keV Soft X-ray attosecond continua. *Nature Communications*, 7, **2016**, p. 11493. DOI: 10.1038/ncomms11493 (cited on pages 16, 85).

[102] A. Paul, E. Gibson, X. Zhang, A. Lytle, T. Popmintchev, X. Zhou, M. Murnane, I. Christov, and H. Kapteyn. Phase-Matching Techniques for Coherent Soft X-Ray Generation. *IEEE Journal of Quantum Electronics*, 42 (1), **2006**, pp. 14–26. DOI: 10.1109/JQE.2005.859914 (cited on pages 17, 21).

[103] M.-C. Chen, P. Arpin, T. Popmintchev, M. Gerrity, B. Zhang, M. Seaberg, D. Popmintchev, M. M. Murnane, and H. C. Kapteyn. Bright, Coherent, Ultrafast Soft X-Ray Harmonics Spanning the Water Window from a Tabletop Light Source. *Physical Review Letters*, 105 (17), **2010**, p. 173901. DOI: 10.1103/PhysRevLett.105.173901 (cited on page 17).

[104] T. Popmintchev, M.-C. Chen, A. Bahabad, M. Gerrity, P. Sidorenko, O. Cohen, I. P. Christov, M. M. Murnane, and H. C. Kapteyn. Phase matching of high harmonic generation in the soft and hard X-ray regions of the spectrum. *PNAS*, 106 (26), **2009**, pp. 10516–21. DOI: 10.1073/pnas.0903748106 (cited on pages 17, 18).

[105] E. J. Takahashi, T. Kanai, K. L. Ishikawa, Y. Nabekawa, and K. Midorikawa. Coherent water window X ray by phase-matched high-order harmonic generation in neutral media. *Physical Review Letters*, 101 (25), **2008**, p. 253901. DOI: 10.1103/PhysRevLett.101.253901 (cited on pages 17, 66).

[106] B. K. Dinh. Phase-Matched High Order Harmonic Generation and Applications. PhD thesis. Swinburne University of Technology, 2012 (cited on page 20).

[107] L. G. Gouy. Sur une propriete nouvelle des ondes lumineuses. *C. R. Acad. Sci. Paris*, 110, **1890**, p. 1251 (cited on page 20).

[108] S. Feng and H. G. Winful. Physical origin of the Gouy phase shift. *Optics Letters*, 26 (8), **2001**, p. 485. DOI: 10.1364/OL.26.000485 (cited on page 20).

[109] E. A. J. Marcatili and R. A. Schmeltzer. Hollow Metallic and Dielectric Waveguides for Long Distance Optical Transmission and Lasers. *Bell System Technical Journal*, 43 (4), **1964**, pp. 1783–1809. DOI: 10.1002/j.1538-7305.1964.tb04108.x (cited on page 21).

[110] D. Popmintchev, C. Hernández-García, F. Dollar, C. Mancuso, J. A. Pérez-Hernández, M.-C. Chen, A. Hankla, X. Gao, B. Shim, A. L. Gaeta, M. Tarazkar, D. A. Romanov, R. J. Levis, J. A. Gaffney, M. Foord, S. B. Libby, A. Jaron-Becker, A. Becker, L. Plaja, M. M. Murnane, H. C. Kapteyn, and T. Popmintchev. Ultraviolet surprise: Efficient soft x-ray high-harmonic generation in multiply ionized plasmas. *Science*, 350 (6265), **2015**, pp. 1225–31. DOI: 10.1126/science.aac9755 (cited on pages 22, 66, 68, 75).

[111] D. Oron, Y. Silberberg, N. Dudovich, and D. M. Villeneuve. Efficient polarization gating of high-order harmonic generation by polarization-shaped ultrashort pulses. *Physical Review A*, 72 (6), **2005**, p. 063816. DOI: 10.1103/PhysRevA.72.063816 (cited on page 23).

[112] S. Long, W. Becker, and J. K. McIver. Model calculations of polarization-dependent two-color high-harmonic generation. *Physical Review A*, 52 (3), **1995**, pp. 2262–2278. DOI: 10.1103/PhysRevA.52.2262 (cited on pages 23, 167).

[113] D. B. Milošević, W. Becker, and R. Kopold. Generation of circularly polarized high-order harmonics by two-color coplanar field mixing. *Physical Review A*, 61 (6), **2000**, p. 063403. DOI: 10.1103/PhysRevA.61.063403 (cited on pages 23, 167).

[114] D. B. Milošević and W. Becker. Attosecond pulse trains with unusual nonlinear polarization. *Physical Review A*, 62 (1), **2000**, p. 011403. DOI: 10.1103/PhysRevA.62.011403 (cited on pages 23, 84).

[115] H. Eichmann, A. Egbert, S. Nolte, C. Momma, B. Wellegehausen, W. Becker, S. Long, and J. K. McIver. Polarization-dependent high-order two-color mixing. *Physical Review A*, 51 (5), **1995**, R3414–R3417. DOI: 10.1103/PhysRevA.51.R3414 (cited on pages 23, 84, 167).

[116] P. F. Moulton. Spectroscopic and laser characteristics of Ti:Al2O3. *Journal of the Optical Society of America B*, 3 (1), **1986**, p. 125. DOI: 10.1364/JOSAB.3.000125 (cited on pages 29, 31).

[117] S. Backus, C. G. Durfee III, M. M. Murnane, and H. C. Kapteyn. High power ultrafast lasers. *Review of Scientific Instruments*, 69 (3), **1998**, pp. 1207–1223 (cited on pages 29, 31).

[118] D. E. Spence, P. N. Kean, and W. Sibbett. 60-fsec pulse generation from a self-mode-locked Ti:sapphire laser. *Optics Letters*, 16 (1), **1991**, p. 42. DOI: 10.1364/OL.16.000042 (cited on page 30).

[119] D. Strickland and G. Mourou. Compression of Amplified Chirped Optical Pulses. *Optics Communications*, 55 (6), **1985**, pp. 447–449. DOI: 10.1016/0030-4018(85)90151-8 (cited on page 30).

[120] C. Ding, W. Xiong, T. Fan, D. D. Hickstein, T. Popmintchev, X. Zhang, M. Walls, M. M. Murnane, and H. C. Kapteyn. High flux coherent super-continuum soft X-ray source driven by a single-stage, 10mJ, Ti:sapphire amplifier-pumped OPA. *Optics Express*, 22 (5), **2014**, p. 6194. DOI: 10.1364/OE.22.006194 (cited on pages 31, 65).

[121] C. Ding. Bright Coherent Ultrafast Tabletop Light Sources Development and the Application on EUV to Soft X-Ray Absorption Spectroscopy. PhD thesis. University of Colorado, 2014 (cited on page 31).

[122] S. Eich, A. Stange, A. Carr, J. Urbancic, T. Popmintchev, M. Wiesenmayer, K. Jansen, A. Ruffing, S. Jakobs, T. Rohwer, S. Hellmann, C. Chen, P. Matyba, L. Kipp, K. Rossnagel, M. Bauer, M. Murnane, H. Kapteyn, S. Mathias, and M. Aeschlimann. Time- and angle-resolved photoemission spectroscopy with optimized high-harmonic pulses using frequency-doubled Ti:Sapphire lasers. *Journal of Electron Spectroscopy and Related Phenomena*, 195, **2014**, pp. 231–236. DOI: 10.1016/j.elspec.2014.04.013 (cited on pages 34, 110).

[123] K. Rabinovitch, L. R. Canfield, and R. P. Madden. A Method for Measuring Polarization in the Vacuum Ultraviolet. *Applied Optics*, 4 (8), **1965**, p. 1005. DOI: 10.1364/AO.4.001005 (cited on page 36).

[124] P. J. Stephens. Magnetic Circular Dichroism. *Annual Review of Physical Chemistry*, 25 (1), **1974**, pp. 201–232. DOI: 10.1146/annurev.pc.25.100174.001221 (cited on pages 36, 87).

[125] P. M. Oppeneer. "Handbook of magnetic materials. Volume 13". In: ed. by K. H. J. Buschow. Elsevier, 2001, pp. 229–422 (cited on pages 36, 87, 176).

[126] J. Stohr and H. C. Siegmann. **Magnetism**. Solid-Stat. Berlin, Heidelberg: Springer, 2006 (cited on pages 36, 87).

[127] S Valencia, A Gaupp, W Gudat, H.-C. Mertins, P. M. Oppeneer, D Abramsohn, and C. M. Schneider. Faraday rotation spectra at shallow core levels: 3p edges of Fe, Co, and Ni. *New Journal of Physics*, 8 (10), **2006**, pp. 254–254. DOI: 10.1088/1367-2630/8/10/254 (cited on pages 37, 61, 63, 88, 89, 174).

[128] D. W. Chandler and P. L. Houston. Twodimensional imaging of stateselected photodissociation products detected by multiphoton ionization. *The Journal of Chemical Physics*, 87 (2), **1987**, pp. 1445–1447. DOI: 10.1063/1.453276 (cited on page 38).

[129] W. C. Wiley and I. H. McLaren. Time-of-Flight Mass Spectrometer with Improved Resolution. *Review of Scientific Instruments*, 26 (12), **1955**, pp. 1150–1157. DOI: 10.1063/1.1715212 (cited on page 38).

[130] A. T. J. B. Eppink and D. H. Parker. Velocity map imaging of ions and electrons using electrostatic lenses: Application in photoelectron and photofragment ion imaging of molecular oxygen. *Review of Scientific Instruments*, 68, **1997**, p. 3477. DOI: 10.1063/1.1148310 (cited on pages 38, 39, 98, 110).

[131] D. H. Parker and A. T. J. B. Eppink. Photoelectron and photofragment velocity map imaging of state-selected molecular oxygen dissociation/ionization dynamics. *Journal of Chemical Physics*, 107 (7), **1997**, p. 2357. DOI: 10.1063/1.474624 (cited on pages 38, 110).

[132] V. Dribinski, A. Ossadtchi, V. A. Mandelshtam, and H. Reisler. Reconstruction of Abel-transformable images: The Gaussian basis-set expansion Abel transform method. *Review of Scientific Instruments*, 73 (7), **2002**, pp. 2634–2642. DOI: 10.1063/1.1482156 (cited on pages 40, 50).

[133] M. J. J. Vrakking. An iterative procedure for the inversion of two-dimensional ion/photoelectron imaging experiments. *Review of Scientific Instruments*, 72 (11), **2001**, pp. 4084–4089. DOI: 10.1063/1.1406923 (cited on page 40).

[134] G. M. Roberts, J. L. Nixon, J. Lecointre, E. Wrede, and J. R. R. Verlet. Toward real-time charged-particle image reconstruction using polar onion-peeling. *Review of Scientific Instruments*, 80 (5), **2009**, p. 053104. DOI: 10.1063/1.3126527 (cited on page 40).

[135] P Johnsson, A Rouzée, W Siu, Y Huismans, F Lépine, T Marchenko, S Düsterer, F Tavella, N Stojanovic, H Redlin, A Azima, and M. J. J. Vrakking. Characterization of a two-color pump-probe setup at FLASH using a velocity map imaging spectrometer. *Optics Lett.*, 35 (24), **2010**, pp. 4163–5. DOI: 10.1364/OL.35.004163 (cited on pages 40, 101, 110).

[136] M. Stei, J. von Vangerow, R. Otto, A. H. Kelkar, E. Carrascosa, T. Best, and R. Wester. High resolution spatial map imaging of a gaseous target. *J. Chem. Phys.*, 138 (21), **2013**, p. 214201. DOI: 10.1063/1.4807482 (cited on pages 40, 101, 110).

[137] D. D. Hickstein. Photoelectron and photoion spectroscopy of atoms, nanoparticles, and nanoplasmas irradiated with strong femtosecond laser fields. PhD thesis. University of Colorado, Boulder, 2014 (cited on page 41).

[138] J. L. Ellis, D. D. Hickstein, K. J. Schnitzenbaumer, M. B. Wilker, B. B. Palm, J. L. Jimenez, G. Dukovic, H. C. Kapteyn, M. M. Murnane, and W. Xiong. Solvents Effects on Charge

Transfer from Quantum Dots. *Journal of the American Chemical Society*, 137 (11), **2015**, pp. 3759–3762. DOI: 10.1021/jacs.5b00463 (cited on pages 41, 96, 99, 100, 102, 104, 110).

[139] K. R. May. The collison nebulizer: Description, performance and application. *Journal of Aerosol Science*, 4 (3), **1973**, pp. 235–238. DOI: 10.1016/0021-8502(73)90006-2 (cited on page 42).

[140] J. W. Fleming, B. A. Williams, R. S. Sheinson, W. Yang, and R. J. Kee. Water mist fire suppression research: Laboratory studies. In: **2nd National Research Institute Fire and Disaster Symposium**. 2002 (cited on page 42).

[141] D. D. Hickstein, F. Dollar, J. L. Ellis, K. J. Schnitzenbaumer, K. E. Keister, G. M. Petrov, C. Ding, B. B. Palm, J. A. Gaffney, M. E. Foord, S. B. Libby, G. Dukovic, J. L. Jimenez, H. C. Kapteyn, M. M. Murnane, and W. Xiong. Mapping Nanoscale Absorption of Femtosecond Laser Pulses Using Plasma Explosion Imaging. *ACS Nano*, 8 (9), **2014**, pp. 8810–8818. DOI: 10.1021/nn503199v (cited on pages 44, 98, 100, 110, 111).

[142] P. F. DeCarlo, J. G. Slowik, D. R. Worsnop, P. Davidovits, and J. L. Jimenez. Particle Morphology and Density Characterization by Combined Mobility and Aerodynamic Diameter Measurements. Part 1: Theory. *Aerosol Science and Technology*, 38 (12), **2004**, pp. 1185–1205. DOI: 10.1080/027868290903907 (cited on pages 44, 45, 182, 183).

[143] P. Liu, P. J. Ziemann, D. B. Kittelson, and P. H. McMurry. Generating Particle Beams of Controlled Dimensions and Divergence: I. Theory of Particle Motion in Aerodynamic Lenses and Nozzle Expansions. *Aerosol Science and Technology*, 22 (3), **1995**, pp. 293–313. DOI: 10.1080/02786829408959748 (cited on page 45).

[144] P. Liu, P. J. Ziemann, D. B. Kittelson, and P. H. McMurry. Generating Particle Beams of Controlled Dimensions and Divergence: II. Experimental Evaluation of Particle Motion in Aerodynamic Lenses and Nozzle Expansions. *Aerosol Science and Technology*, 22 (3), **1995**, pp. 314–324. DOI: 10.1080/02786829408959749 (cited on page 45).

[145] X. Wang, A. Gidwani, S. L. Girshick, and P. H. McMurry. Aerodynamic Focusing of Nanoparticles: II. Numerical Simulation of Particle Motion Through Aerodynamic Lenses. *Aerosol Science and Technology*, 39 (7), **2005**, pp. 624–636. DOI: 10.1080/02786820500181950 (cited on page 45).

[146] P. S. K. Liu, R. Deng, K. A. Smith, L. R. Williams, J. T. Jayne, M. R. Canagaratna, K. Moore, T. B. Onasch, D. R. Worsnop, and T. Deshler. Transmission Efficiency of an Aerodynamic Focusing Lens System: Comparison of Model Calculations and Laboratory Measurements for the Aerodyne Aerosol Mass Spectrometer. *Aerosol Science and Technology*, 41 (8), **2007**, pp. 721–733. DOI: 10.1080/02786820701422278 (cited on pages 45, 101, 110, 183).

[147] H. Zhu, N. Song, and T. Lian. Controlling Charge Separation and Recombination Rates in CdSe/ZnS Type I CoreShell Quantum Dots by Shell Thicknesses. *Journal of the American Chemical Society*, 132 (42), **2010**, pp. 15038–15045. DOI: 10.1021/ja106710m (cited on page 47).

[148] S. L. Sewall, R. R. Cooney, K. E. H. Anderson, E. A. Dias, and P. Kambhampati. State-to-state exciton dynamics in semiconductor quantum dots. *Physical Review B*, 74 (23), **2006**, p. 235328. DOI: 10.1103/PhysRevB.74.235328 (cited on pages 47, 50, 102).

[149] B. Cho, W. K. Peters, R. J. Hill, T. L. Courtney, and D. M. Jonas. Bulklike Hot Carrier Dynamics in Lead Sulfide Quantum Dots. *Nano Letters*, 10 (7), **2010**, pp. 2498–2505. DOI: 10.1021/nl1010349 (cited on page 47).

[150] R. D. Schaller, J. M. Pietryga, S. V. Goupalov, M. A. Petruska, S. A. Ivanov, and V. I. Klimov. Breaking the Phonon Bottleneck in Semiconductor Nanocrystals via Multiphonon Emission Induced by Intrinsic Nonadiabatic Interactions. *Physical Review Letters*, 95 (19), **2005**, p. 196401. DOI: 10.1103/PhysRevLett.95.196401 (cited on page 47).

[151] V. I. Klimov, D. W. McBranch, C. A. Leatherdale, and M. G. Bawendi. Electron and hole relaxation pathways in semiconductor quantum dots. *Physical Review B*, 60 (19), **1999**, pp. 13740–13749. DOI: 10.1103/PhysRevB.60.13740 (cited on pages 47, 51, 103).

[152] F. Gesuele, M. Y. Sfeir, W.-K. Koh, C. B. Murray, T. F. Heinz, and C. W. Wong. Ultrafast Supercontinuum Spectroscopy of Carrier Multiplication and Biexcitonic Effects in Excited States of PbS Quantum Dots. *Nano Letters*, 12 (6), **2012**, pp. 2658–2664. DOI: 10.1021/nl2021224 (cited on page 47).

[153] P. Kambhampati. Unraveling the Structure and Dynamics of Excitons in Semiconductor Quantum Dots. *Accounts of Chemical Research*, 44 (1), **2011**, pp. 1–13. DOI: 10.1021/ar1000428 (cited on page 47).

[154] M. Pelton, G. Smith, N. F. Scherer, and R. A. Marcus. Evidence for a diffusion-controlled mechanism for fluorescence blinking of colloidal quantum dots. *PNAS*, 104 (36), **2007**, pp. 14249–54. DOI: 10.1073/pnas.0706164104 (cited on page 47).

[155] C. Galland, Y. Ghosh, A. Steinbrück, J. A. Hollingsworth, H. Htoon, and V. I. Klimov. Lifetime blinking in nonblinking nanocrystal quantum dots. *Nature Communications*, 3, **2012**, p. 908. DOI: 10.1038/ncomms1916 (cited on page 47).

[156] K. R. Wilson, S. Zou, J. Shu, E. Rühl, S. R. Leone, G. C. Schatz, and M. Ahmed. Size-Dependent Angular Distributions of Low-Energy Photoelectrons Emitted from NaCl Nanoparticles. *Nano Letters*, 7 (7), **2007**, pp. 2014–2019. DOI: 10.1021/nl070834g (cited on pages 48, 109–111).

[157] S. Zherebtsov, T. Fennel, J. Plenge, E. Antonsson, I. Znakovskaya, A. Wirth, O. Herrwerth, F. Süßmann, C. Peltz, I. Ahmad, S. A. Trushin, V. Pervak, S. Karsch, M. J. J. Vrakking, B. Langer, C. Graf, M. I. Stockman, F. Krausz, E. Rühl, and M. F. Kling. Controlled near-field enhanced electron acceleration from dielectric nanospheres with intense few-cycle laser fields. *Nature Physics*, 7 (8), **2011**, pp. 656–662. DOI: 10.1038/nphys1983 (cited on page 48).

[158] D. J. Norris and M. G. Bawendi. Measurement and assignment of the size-dependent optical spectrum in CdSe quantum dots. *Physical Review B*, 53 (24), **1996**, pp. 16338–16346. DOI: 10.1103/PhysRevB.53.16338 (cited on pages 50, 102).

[159] D. Schooss, A. Mews, A. Eychmüller, and H. Weller. Quantum-dot quantum well CdS/HgS/CdS: Theory and experiment. *Physical Review B*, 49 (24), **1994**, pp. 17072–17078. DOI: 10.1103/PhysRevB.49.17072 (cited on page 51).

[160] S. Kim, B. Fisher, H.-J. Eisler, and M. Bawendi. Type-II Quantum Dots: CdTe/CdSe(Core/Shell) and CdSe/ZnTe(Core/Shell) Heterostructures. *Journal of the American Chemical Society*, 125 (38), **2003**, pp. 11466–11467. DOI: 10.1021/JA0361749 (cited on page 51).

[161] B. O. Dabbousi, J. Rodriguez-Viejo, F. V. Mikulec, J. R. Heine, H. Mattoussi, R. Ober, K. F. Jensen, and M. G. Bawendi. (CdSe)ZnS CoreShell Quantum Dots: Synthesis and Characterization of a Size Series of Highly Luminescent Nanocrystallites. *The Journal of Physical Chemistry B*, 101 (46), **1997**, pp. 9463–9475. DOI: 10.1021/jp971091y (cited on page 51).

[162] C. N. Berglund and W. E. Spicer. Photoemission Studies of Copper and Silver: Theory. *Physical Review*, 136 (4A), **1964**, A1030–A1044. DOI: 10.1103/PhysRev.136.A1030 (cited on page 52).

[163] L. Miaja-Avila, J. Yin, S. Backus, G. Saathoff, M. Aeschlimann, M. M. Murnane, and H. C. Kapteyn. Ultrafast studies of electronic processes at surfaces using the laser-assisted photoelectric effect with long-wavelength dressing light. *Physical Review A*, 79 (3), **2009**, p. 030901. DOI: 10.1103/PhysRevA.79.030901 (cited on page 52).

[164] S. V. Fomichev, P. Breger, B. Carré, P. Agostini, and D. F. Zaretsky. Non-collinear high-harmonic generation. *Laser Physics*, 12 (2), **2002**, pp. 383–388 (cited on page 55).

[165] M. Negro, M. Devetta, D. Faccialá, A. Ciriolo, F. Calegari, F. Frassetto, L. Poletto, V. Tosa, C. Vozzi, and S. Stagira. Non-collinear high-order harmonic generation by three interfering

laser beams. *Optics Express*, 22 (24), **2014**, p. 29778. DOI: 10.1364/OE.22.029778 (cited on page 55).

[166] R. Rajeev, J. Hellwagner, A. Schumacher, I. Jordan, M. Huppert, A. Tehlar, B. R. Niraghatam, D. Baykusheva, N. Lin, A. von Conta, and H. J. Wörner. In situ frequency gating and beam splitting of vacuum- and extreme-ultraviolet pulses. *Light: Science & Applications*, 5 (11), **2016**, e16170. DOI: 10.1038/lsa.2016.170 (cited on pages 55, 66).

[167] J. L. Ellis, K. M. Dorney, C. G. Durfee, C. Hernández-García, F. Dollar, C. A. Mancuso, T. Fan, D. Zusin, C. Gentry, P. Grychtol, H. C. Kapteyn, M. M. Murnane, and D. D. Hickstein. Phase matching of noncollinear sum and difference frequency high harmonic generation above and below the critical ionization level. *Optics Express*, 25 (9), **2017**, p. 10126. DOI: 10.1364/OE.25.010126 (cited on pages 55, 69, 71, 73, 75, 76, 78, 85, 170, 172).

[168] M Louisy, C. L. Arnold, M Miranda, E. W. Larsen, S. N. Bengtsson, D Kroon, M Kotur, D Guénot, L Rading, P Rudawski, F Brizuela, F Campi, B Kim, A Jarnac, A Houard, J Mauritsson, P Johnsson, A L'Huillier, and C. M. Heyl. Gating attosecond pulses in a noncollinear geometry. *Optica*, 2 (6), **2015**, pp. 563–566. DOI: 10.1364/OPTICA.2.000563 (cited on page 55).

[169] J. B. Bertrand, H. J. Wörner, H.-C. Bandulet, É. Bisson, M. Spanner, J.-C. Kieffer, D. M. Villeneuve, and P. B. Corkum. Ultrahigh-order wave mixing in noncollinear high harmonic generation. *Phys. Rev. Lett.*, 106 (2), **2011**, p. 023001. DOI: 10.1103/PhysRevLett.106.023001 (cited on pages 55, 169).

[170] A. Ozawa, A. Vernaleken, W. Schneider, I. Gotlibovych, T. Udem, and T. W. Hänsch. Noncollinear high harmonic generation: a promising outcoupling method for cavity-assisted XUV generation. *Optics Express*, 16 (9), **2008**, p. 6233 (cited on page 55).

[171] J. Wu and H. Zeng. Cavity-enhanced noncollinear high-harmonic generation for extreme ultraviolet frequency combs. *Optics Letters*, 32 (22), **2007**, p. 3315. DOI: 10.1364/OL.32.003315 (cited on page 55).

[172] K. D. Moll, R. J. Jones, and J. Ye. Output coupling methods for cavity-based high-harmonic generation. *Optics Express*, 14 (18), **2006**, p. 8189. DOI: 10.1364/OE.14.008189 (cited on page 55).

[173] K. T. Kim, C. Zhang, A. D. Shiner, S. E. Kirkwood, E. Frumker, G. Gariepy, A. Naumov, D. M. Villeneuve, and P. B. Corkum. Manipulation of quantum paths for space-time characterization of attosecond pulses. *Nature Physics*, 9 (3), **2013**, pp. 159–163. DOI: 10.1038/nphys2525 (cited on page 55).

[174] C. Boeglin, E. Beaurepaire, V. Halté, V. López-Flores, C. Stamm, N. Pontius, H. A. Dürr, and J.-Y. Bigot. Distinguishing the ultrafast dynamics of spin and orbital moments in solids. *Nature*, 465 (7297), **2010**, pp. 458–461. DOI: 10.1038/nature09070 (cited on page 59).

[175] H. Hochst, D. Zhao, and D. L. Huber. M2,3 magnetic circular dichroism (MCD) measurements of Fe, Co and Ni using a newly developed quadruple reflection phase shifter. *Surface Science*, 352-354, **1996**, pp. 998–1002. DOI: 10.1016/0039-6028(95)01315-6 (cited on page 61).

[176] K.-J. Yuan and A. D. Bandrauk. Single Circularly Polarized Attosecond Pulse Generation by Intense Few Cycle Elliptically Polarized Laser Pulses and Terahertz Fields from Molecular Media. *Physical Review Letters*, 110 (2), **2013**, p. 023003. DOI: 10.1103/PhysRevLett.110.023003 (cited on page 63).

[177] C. Hernández-García, C. G. Durfee, D. D. Hickstein, T. Popmintchev, A. Meier, M. M. Murnane, H. C. Kapteyn, I. J. Sola, A. Jaron-Becker, and A. Becker. Schemes for generation of isolated attosecond pulses of pure circular polarization. *Physical Review A*, 93 (4), **2016**, p. 043855. DOI: 10.1103/PhysRevA.93.043855 (cited on pages 64, 85, 92).

[178] P.-C. Huang, J.-T. Huang, P.-Y. Huang, C.-H. Lu, C. Hernandez-Garcia, A. H. Kung, S.-D. Yang, M.-C. Chen, S.-D. Yang, and M.-C. Chen. Polarization Control of Isolated Attosecond Pulses. In: **Conference on Lasers and Electro-Optics**. Washington, D.C.: OSA, 2017, JTh5B.9. DOI: 10.1364/CLEO_AT.2017.JTh5B.9 (cited on pages 64, 79).

[179] K.-J. Yuan and A. D. Bandrauk. Attosecond-magnetic-field-pulse generation by coherent circular molecular electron wave packets. *Physical Review A*, 91 (4), **2015**, p. 042509. DOI: 10.1103/PhysRevA.91.042509 (cited on page 65).

[180] A. Averchi, D. Faccio, R. Berlasso, M. Kolesik, J. V. Moloney, A. Couairon, and P. Di Trapani. Phase matching with pulsed Bessel beams for high-order harmonic generation. *Physical Review A*, 77 (2), **2008**, p. 021802 (cited on page 67).

[181] J. L. Silva, H. M. Crespo, and R. Weigand. Generation of high-energy vacuum UV femtosecond pulses by multiple-beam cascaded four-wave mixing in a transparent solid. *Applied Optics*, 50 (14), **2011**, pp. 1968–1973 (cited on page 67).

[182] V Vaicaitis, V Jarutis, K Steponkevicius, and S Algirdas. Noncollinear six-wave mixing of femtosecond laser pulses in air. *Phys. Rev. A*, 87 (6), **2013**, p. 063825 (cited on page 67).

[183] P. L. Shkolnikov, A. E. Kaplan, and A. Lago. Phase matching for large-scale frequency upconversion in plasma. *Optics Letters*, 18 (20), **1993**, p. 1700. DOI: 10.1364/OL.18.001700 (cited on page 68).

[184] O. Cohen, T. Popmintchev, D. M. Gaudiosi, M. M. Murnane, and H. C. Kapteyn. Unified microscopic-macroscopic formulation of high-order difference-frequency mixing in plasmas. *Physical Review Letters*, 98 (4), **2007**, p. 043903. DOI: 10.1103/PhysRevLett.98.043903 (cited on page 68).

[185] X. Zhang, A. L. Lytle, T. Popmintchev, X. Zhou, H. C. Kapteyn, M. M. Murnane, and O. Cohen. Quasi-phase-matching and quantum-path control of high-harmonic generation using counterpropagating light. *Nature Physics*, 3 (4), **2007**, pp. 270–275. DOI: 10.1038/nphys541 (cited on page 68).

[186] C. Hernández-García, J. A. Pérez-Hernández, J. Ramos, E. C. Jarque, L. Roso, and L. Plaja. High-order harmonic propagation in gases within the discrete dipole approximation. *Physical Review A*, 82 (3), **2010**, p. 033432. DOI: 10.1103/PhysRevA.82.033432 (cited on pages 74, 92, 178).

[187] X. Zhang, A. R. Libertun, A. Paul, E. Gagnon, S. Backus, I. P. Christov, M. M. Murnane, H. C. Kapteyn, R. A. Bartels, Y. Liu, and D. T. Attwood. Highly coherent light at 13 nm generated by use of quasi-phase-matched high-harmonic generation. *Optics Letters*, 29 (12), **2004**, p. 1357. DOI: 10.1364/OL.29.001357 (cited on page 75).

[188] E. Pisanty, D. D. Hickstein, B. R. Galloway, C. G. Durfee, H. C. Kapteyn, M. M. Murnane, and M. Ivanov. High harmonic interferometry of the Lorentz force in strong mid-infrared laser fields, **2016**. arXiv: 1606.01931 (cited on pages 80, 81).

[189] H. R. Reiss. Dipole-approximation magnetic fields in strong laser beams. *Physical Review A*, 63 (1), **2000**, p. 013409. DOI: 10.1103/PhysRevA.63.013409 (cited on page 80).

[190] M. W. Walser, C. H. Keitel, A. Scrinzi, and T. Brabec. High Harmonic Generation Beyond the Electric Dipole Approximation. *Physical Review Letters*, 85 (24), **2000**, pp. 5082–5085. DOI: 10.1103/PhysRevLett.85.5082 (cited on page 80).

[191] A. S. Emelina, M. Y. Emelin, and M. Y. Ryabikin. On the possibility of the generation of high harmonics with photon energies greater than 10 keV upon interaction of intense mid-IR radiation with neutral gases. *Quantum Electronics*, 44 (5), **2014**, pp. 470–477. DOI: 10.1070/QE2014v044n05ABEH015436 (cited on page 80).

[192] M. Huppert, I. Jordan, D. Baykusheva, A. von Conta, and H. J. Wörner. Attosecond Delays in Molecular Photoionization. *Physical Review Letters*, 117 (9), **2016**, p. 093001. DOI: 10.1103/PhysRevLett.117.093001 (cited on page 83).

[193] F. Süßmann and M. F. Kling. Attosecond nanoplasmonic streaking of localized fields near metal nanospheres. *Physical Review B*, 84 (12), **2011**, p. 121406. DOI: 10.1103/PhysRevB.84.121406 (cited on page 83).

[194] L. Seiffert, Q. Liu, S. Zherebtsov, A. Trabattoni, P. Rupp, M. C. Castrovilli, M. Galli, F. Süßmann, K. Wintersperger, J. Stierle, G. Sansone, L. Poletto, F. Frassetto, I. Halfpap, V. Mondes, C. Graf, E. Rühl, F. Krausz, M. Nisoli, T. Fennel, F. Calegari, and M. Kling.

Attosecond chronoscopy of electron scattering in dielectric nanoparticles. *Nature Physics*, 13 (8), **2017**, pp. 766–770. DOI: 10.1038/nphys4129 (cited on page 83).

[195] P. Dietrich, N. H. Burnett, M. Ivanov, and P. B. Corkum. High-harmonic generation and correlated two-electron multiphoton ionization with elliptically polarized light. *Physical Review A*, 50 (5), **1994**, R3585–R3588. DOI: 10.1103/PhysRevA.50.R3585 (cited on page 83).

[196] N. Böwering, T. Lischke, B. Schmidtke, N. Müller, T. Khalil, and U. Heinzmann. Asymmetry in Photoelectron Emission from Chiral Molecules Induced by Circularly Polarized Light. *Physical Review Letters*, 86 (7), **2001**, pp. 1187–1190. DOI: 10.1103/PhysRevLett.86.1187 (cited on page 84).

[197] F. Gaie-Levrel, G. A. Garcia, M. Schwell, and L. Nahon. VUV state-selected photoionization of thermally-desorbed biomolecules by coupling an aerosol source to an imaging photoelectron/photoion coincidence spectrometer: case of the amino acids tryptophan and phenylalanine. *Physical Chemistry Chemical Physics*, 13 (15), **2011**, p. 7024. DOI: 10.1039/c0cp02798g (cited on page 84).

[198] S. Beaulieu, A. Comby, B. Fabre, D. Descamps, A. Ferré, G. Garcia, R. Géneaux, F. Légaré, L. Nahon, S. Petit, T. Ruchon, B. Pons, V. Blanchet, and Y. Mairesse. Probing ultrafast dynamics of chiral molecules using time-resolved photoelectron circular dichroism. *Faraday Discussions*, 194 (0), **2016**, pp. 325–348. DOI: 10.1039/C6FD00113K (cited on page 84).

[199] E. Beaurepaire, J.-C. Merle, A. Daunois, and J.-Y. Bigot. Ultrafast Spin Dynamics in Ferromagnetic Nickel. *Physical Review Letters*, 76 (22), **1996**, pp. 4250–4253. DOI: 10.1103/PhysRevLett.76.4250 (cited on page 84).

[200] T. Young. The Bakerian Lecture: On the Theory of Light and Colours. *Philosophical Transactions of the Royal Society of London*, 92 (0), **1802**, pp. 12–48. DOI: 10.1098/rstl.1802.0004 (cited on page 84).

[201] R. Zerne, C. Altucci, M. Bellini, M. B. Gaarde, T. W. Hänsch, A. L'Huillier, C. Lyngå, and C.-G. Wahlström. Phase-Locked High-Order Harmonic Sources. *Physical Review Letters*, 79 (6), **1997**, pp. 1006–1009. DOI: 10.1103/PhysRevLett.79.1006 (cited on page 84).

[202] W. R. Mellen. Interference of Linearly Polarized Light with Perpendicular Polarizations. *American Journal of Physics*, 30 (10), **1962**, pp. 772–772. DOI: 10.1119/1.1941786 (cited on page 84).

[203] R. Hanau. Interference of Linearly Polarized Light with Perpendicular Polarizations. *American Journal of Physics*, 31 (4), **1963**, pp. 303–304. DOI: 10.1119/1.1969459 (cited on page 84).

[204] E. Collett. Mathematical Formulation of the Interference Laws of Fresnel and Arago. *American Journal of Physics*, 39 (12), **1971**, pp. 1483–1495. DOI: 10.1119/1.1976702 (cited on page 84).

[205] J. L. Ellis, K. M. Dorney, D. D. Hickstein, N. J. Brooks, C. Gentry, C. Hernandez-Garcia, G. S. M. Jansen, S. Witte, H. C. Kapteyn, and M. M. Murnane. High harmonics with spatially varying ellipticity. *Optica*, In press, **2018** (cited on pages 86, 89, 91, 93, 174, 175, 180, 181).

[206] G. S. M. Jansen, D. Rudolf, L. Freisem, K. S. E. Eikema, and S. Witte. Spatially resolved Fourier transform spectroscopy in the extreme ultraviolet. *Optica*, 3 (10), **2016**, p. 1122. DOI: 10.1364/OPTICA.3.001122 (cited on pages 86, 95).

[207] D. Brida, C. Manzoni, and G. Cerullo. Phase-locked pulses for two-dimensional spectroscopy by a birefringent delay line. *Optics Letters*, 37 (15), **2012**, p. 3027. DOI: 10.1364/OL.37.003027 (cited on page 86).

[208] A. Oriana, J. Réhault, F. Preda, D. Polli, and G. Cerullo. Scanning Fourier transform spectrometer in the visible range based on birefringent wedges. *Journal of the Optical Society of America A*, 33 (7), **2016**, p. 1415. DOI: 10.1364/JOSAA.33.001415 (cited on page 86).

[209] M. J. Padgett and A. R. Harvey. A static Fouriertransform spectrometer based on Wollaston prisms. *Review of Scientific Instruments*, 66 (4), **1995**, pp. 2807–2811. DOI: 10.1063/1.1145559 (cited on page 90).

[210] C. Hernández-García, I. J. Sola, and L. Plaja. Signature of the transversal coherence length in high-order harmonic generation. *Physical Review A*, 88 (4), **2013**, p. 043848. DOI: 10.1103/PhysRevA.88.043848 (cited on pages 94, 181).

[211] F. Catoire, A. Ferré, O. Hort, A. Dubrouil, L. Quintard, D. Descamps, S. Petit, F. Burgy, E. Mével, Y. Mairesse, and E. Constant. Complex structure of spatially resolved high-order-harmonic spectra. *Physical Review A*, 94 (6), **2016**, p. 063401. DOI: 10.1103/PhysRevA.94.063401 (cited on pages 94, 181).

[212] M. Kovačev, S. V. Fomichev, E. Priori, Y. Mairesse, H. Merdji, P. Monchicourt, P. Breger, J. Norin, A. Persson, A. L'Huillier, C.-G. Wahlström, B. Carré, and P. Salières. Extreme Ultraviolet Fourier-Transform Spectroscopy with High Order Harmonics. *Physical Review Letters*, 95 (22), **2005**, p. 223903. DOI: 10.1103/PhysRevLett.95.223903 (cited on page 95).

[213] S. Witte, V. T. Tenner, D. W. Noom, and K. S. Eikema. Lensless diffractive imaging with ultra-broadband table-top sources: from infrared to extreme-ultraviolet wavelengths. *Light: Science & Applications*, 3 (3), **2014**, e163. DOI: 10.1038/lsa.2014.44 (cited on pages 95, 165).

[214] Y. Meng, C. Zhang, C. Marceau, A. Y. Naumov, P. B. Corkum, and D. M. Villeneuve. Octave-spanning hyperspectral coherent diffractive imaging in the extreme ultraviolet range. *Optics Express*, 23 (22), **2015**, p. 28960. DOI: 10.1364/OE.23.028960 (cited on page 95).

[215] Y. Nabekawa, T. Shimizu, Y. Furukawa, E. J. Takahashi, and K. Midorikawa. Interferometry of Attosecond Pulse Trains in the Extreme Ultraviolet Wavelength Region. *Physical Review Letters*, 102 (21), **2009**, p. 213904. DOI: 10.1103/PhysRevLett.102.213904 (cited on page 95).

[216] K. E. Knowles, M. D. Peterson, M. R. McPhail, and E. A. Weiss. Exciton Dissociation within Quantum DotOrganic Complexes: Mechanisms, Use as a Probe of Interfacial Structure, and Applications. *The Journal of Physical Chemistry C*, 117 (20), **2013**, pp. 10229–10243. DOI: 10.1021/jp400699h (cited on page 97).

[217] H. Zhu, N. Song, W. Rodríguez-Córdoba, and T. Lian. Wave Function Engineering for Efficient Extraction of up to Nineteen Electrons from One CdSe/CdS Quasi-Type II Quantum Dot. *Journal of the American Chemical Society*, 134 (9), **2012**, pp. 4250–4257. DOI: 10.1021/ja210312s (cited on pages 97, 98, 100, 103).

[218] P. V. Kamat, K. Tvrdy, D. R. Baker, and J. G. Radich. Beyond Photovoltaics: Semiconductor Nanoarchitectures for Liquid-Junction Solar Cells. *Chemical Reviews*, 110 (11), **2010**, pp. 6664–6688. DOI: 10.1021/cr100243p (cited on page 97).

[219] B.-R. Hyun, Y.-W. Zhong, A. C. Bartnik, L. Sun, H. D. Abruna, F. W. Wise, J. D. Goodreau, J. R. Matthews, T. M. Leslie, and N. F. Borrelli. Electron Injection from Colloidal PbS Quantum Dots into Titanium Dioxide Nanoparticles. *ACS Nano*, 2 (11), **2008**, pp. 2206–2212. DOI: 10.1021/nn800336b (cited on page 98).

[220] D. D. Hickstein, P. Ranitovic, S. Witte, X.-M. Tong, Y. Huismans, P. Arpin, X. Zhou, K. E. Keister, C. W. Hogle, B. Zhang, C. Ding, P. Johnsson, N. Toshima, M. J. J. Vrakking, M. M. Murnane, and H. C. Kapteyn. Direct Visualization of Laser-Driven Electron Multiple Scattering and Tunneling Distance in Strong-Field Ionization. *Physical Review Letters*, 109 (7), **2012**, p. 073004. DOI: 10.1103/PhysRevLett.109.073004 (cited on pages 98, 110).

[221] D. D. Hickstein, F. Dollar, J. A. Gaffney, M. E. Foord, G. M. Petrov, B. B. Palm, K. E. Keister, J. L. Ellis, C. Ding, S. B. Libby, J. L. Jimenez, H. C. Kapteyn, M. M. Murnane, and W. Xiong. Observation and Control of Shock Waves in Individual Nanoplasmas. *Physical Review Letters*, 112 (11), **2014**, p. 115004. DOI: 10.1103/PhysRevLett.112.115004 (cited on pages 98, 100, 110, 111).

[222] V. V. Matylitsky, L. Dworak, V. V. Breus, T. Basche, and J. Wachtveitl. Ultrafast Charge Separation in Multiexcited CdSe Quantum Dots Mediated by Adsorbed Electron Acceptors. *Journal of the American Chemical Society*, 131 (7), **2009**, pp. 2424–2425. DOI: 10.1021/ja808084y (cited on pages 98, 100, 103).

[223] M. Tagliazucchi, D. B. Tice, C. M. Sweeney, A. J. Morris-Cohen, and E. A. Weiss. Ligand-Controlled Rates of Photoinduced Electron Transfer in Hybrid CdSe Nanocrystal/Poly(viologen) Films. *ACS Nano*, 5 (12), **2011**, pp. 9907–9917. DOI: 10.1021/nn203683s (cited on page 98).

[224] C. Harris and P. V. Kamat. Photocatalysis with CdSe Nanoparticles in Confined Media: Mapping Charge Transfer Events in the Subpicosecond to Second Timescales. *ACS Nano*, 3 (3), **2009**, pp. 682–690. DOI: 10.1021/nn800848y (cited on pages 98, 100).

[225] C. D. Lindstrom and X.-Y. Zhu. Photoinduced Electron Transfer at MoleculeMetal Interfaces. 106 (10), **2006**, pp. 4281–4300. DOI: 10.1021/CR0501689 (cited on pages 100, 105).

[226] S. M. Wetterer, D. J. Lavrich, T. Cummings, S. L. Bernasek, and G. Scoles. Energetics and Kinetics of the Physisorption of Hydrocarbons on Au(111). 102 (46), **1998**, pp. 9266–9275. DOI: 10.1021/JP982338+ (cited on page 101).

[227] V. I. Klimov. Spectral and Dynamical Properties of Multiexcitons in Semiconductor Nanocrystals. *Annual Review of Physical Chemistry*, 58 (1), **2007**, pp. 635–673. DOI: 10.1146/annurev.physchem.58.032806.104537 (cited on page 102).

[228] S. Banerjee, S. Maity, and A. Datta. Enhanced Trapping Efficiency in Acid-Treated Silica Nanostructures. *The Journal of Physical Chemistry C*, 115 (46), **2011**, pp. 22804–22809. DOI: 10.1021/jp2068039 (cited on page 102).

[229] M. Jones, S. S. Lo, and G. D. Scholes. Quantitative modeling of the role of surface traps in CdSe/CdS/ZnS nanocrystal photoluminescence decay dynamics. *PNAS*, 106 (9), **2009**, p. 3011. DOI: 10.1073/pnas.0809316106 (cited on page 103).

[230] P Kambhampati. On the kinetics and thermodynamics of excitons at the surface of semiconductor nanocrystals: Are there surface excitons? *Chemical Physics*, 446, **2015**, pp. 92–107. DOI: 10.1016/J.CHEMPHYS.2014.11.008 (cited on page 103).

[231] M. M. Krause, J. Mooney, and P. Kambhampati. Chemical and Thermodynamic Control of the Surface of Semiconductor Nanocrystals for Designer White Light Emitters. *ACS Nano*, 7 (7), **2013**, pp. 5922–5929. DOI: 10.1021/nn401383t (cited on page 103).

[232] J. Mooney, M. M. Krause, J. I. Saari, and P. Kambhampati. Challenge to the deep-trap model of the surface in semiconductor nanocrystals. *Physical Review B*, 87 (8), **2013**, p. 081201. DOI: 10.1103/PhysRevB.87.081201 (cited on page 103).

[233] H. J. Kim and J. T. Hynes. Equilibrium and nonequilibrium solvation and solute electronic structure. I. Formulation. *The Journal of Chemical Physics*, 93 (7), **1990**, pp. 5194–5210. DOI: 10.1063/1.459665 (cited on page 105).

[234] H. J. Kim and J. T. Hynes. Equilibrium and nonequilibrium solvation and solute electronic structure. II. Strong coupling limit. *The Journal of Chemical Physics*, 93 (7), **1990**, pp. 5211–5223. DOI: 10.1063/1.459666 (cited on page 105).

[235] H. J. Kim and J. T. Hynes. Equilibrium and nonequilibrium solvation and solute electronic structure. III. Quantum theory. *The Journal of Chemical Physics*, 96 (7), **1992**, pp. 5088–5110. DOI: 10.1063/1.462752 (cited on page 105).

[236] H. J. Kim and J. T. Hynes. Role of solvent electronic polarization in electron-transfer processes. *The Journal of Physical Chemistry*, 94 (7), **1990**, pp. 2736–2740. DOI: 10.1021/j100370a004 (cited on page 105).

[237] J. T. Hynes, K. J. Hyung, J. R. Mathis, and J. J. i. Timoneda. Solute electronic structure and solvation in chemical reactions in solution. *Journal of Molecular Liquids*, 57, **1993**, pp. 53–73. DOI: 10.1016/0167-7322(93)80047-Y (cited on page 105).

[238] M. Maroncelli, J. MacInnis, and G. R. Fleming. Polar Solvent Dynamics and Electron-Transfer Reactions. *Science*, 243, **1989**, pp. 1674–1681. DOI: 10.2307/1703477 (cited on page 105).

[239] P. F. Barbara, G. C. Walker, and T. P. Smith. Vibrational Modes and the Dynamic Solvent Effect in Electron and Proton Transfer. *Science*, 256, **1992**, pp. 975–981. DOI: 10.2307/2877116 (cited on page 105).

[240] J. L. Ellis, D. D. Hickstein, W. Xiong, F. Dollar, B. B. Palm, K. E. Keister, K. M. Dorney, C. Ding, T. Fan, M. B. Wilker, K. J. Schnitzenbaumer, G. Dukovic, J. L. Jimenez, H. C. Kapteyn, and M. M. Murnane. Materials Properties and Solvated Electron Dynamics of Isolated Nanoparticles and Nanodroplets Probed with Ultrafast Extreme Ultraviolet Beams. *The Journal of Physical Chemistry Letters*, 7 (4), **2016**, pp. 609–615. DOI: 10.1021/acs.jpclett.5b02772 (cited on pages 107, 111, 113, 115, 184, 186).

[241] T. Mitsudome, A. Noujima, T. Mizugaki, K. Jitsukawa, and K. Kaneda. Efficient Aerobic Oxidation of Alcohols using a Hydrotalcite-Supported Gold Nanoparticle Catalyst. *Advanced Synthesis & Catalysis*, 351 (11-12), **2009**, pp. 1890–1896. DOI: 10.1002/adsc.200900239 (cited on page 108).

[242] Y. Lou, M. M. Maye, L. Han, J. Luo, and C.-J. Zhong. Gold-platinum alloy nanoparticle assembly as catalyst for methanol electrooxidation. *Chemical Communications*, **2001**, pp. 473–474. DOI: 10.1039/b008669j (cited on page 108).

[243] P. Waszczuk, T. M. Barnard, C. Rice, R. I. Masel, and A. Wieckowski. A nanoparticle catalyst with superior activity for electrooxidation of formic acid. *Electrochemistry Communications*, 4 (7), **2002**, pp. 599–603. DOI: 10.1016/S1388-2481(02)00386-7 (cited on page 108).

[244] I. Riipinen, T. Yli-Juuti, J. R. Pierce, T. Petäjä, D. R. Worsnop, M. Kulmala, and N. M. Donahue. The contribution of organics to atmospheric nanoparticle growth. *Nature Geoscience*, 5 (7), **2012**, pp. 453–458. DOI: 10.1038/ngeo1499 (cited on page 108).

[245] L. H. van Poppel, H. Friedrich, J. Spinsby, S. H. Chung, J. H. Seinfeld, and P. R. Buseck. Electron tomography of nanoparticle clusters: Implications for atmospheric lifetimes and radiative forcing of soot. *Geophysical Research Letters*, 32 (24), **2005**, p. L24811. DOI: 10.1029/2005GL024461 (cited on page 108).

[246] J. N. Smith, M. J. Dunn, T. M. VanReken, K. Iida, M. R. Stolzenburg, P. H. McMurry, and L. G. Huey. Chemical composition of atmospheric nanoparticles formed from nucleation in Tecamac, Mexico: Evidence for an important role for organic species in nanoparticle growth. *Geophysical Research Letters*, 35 (4), **2008**, p. L04808. DOI: 10.1029/2007GL032523 (cited on page 108).

[247] E. T. J. Nibbering and T. Elsaesser. Ultrafast Vibrational Dynamics of Hydrogen Bonds in the Condensed Phase. *Chemical Reviews*, 104 (4), **2004**, pp. 1887–1914. DOI: 10.1021/CR020694P (cited on page 108).

[248] A. Douhal, S. K. Kim, and A. H. Zewail. Femtosecond molecular dynamics of tautomerization in model base pairs. *Nature*, 378 (6554), **1995**, pp. 260–263. DOI: 10.1038/378260a0 (cited on page 108).

[249] S. Takeuchi and T. Tahara. Femtosecond absorption study of photodissociation of diphenylcyclopropenone in solution: Reaction dynamics and coherent nuclear motion. *The Journal of Chemical Physics*, 120 (10), **2004**, pp. 4768–4776. DOI: 10.1063/1.1645778 (cited on page 108).

[250] Q. Wang, R. W. Schoenlein, L. A. Peteanu, R. A. Mathies, and C. V. Shank. Vibrationally coherent photochemistry in the femtosecond primary event of vision. *Science*, 266 (5184), **1994**, pp. 422–424. DOI: 10.1126/science.7939680 (cited on page 108).

[251] H. Petek and S. Ogawa. Femtosecond time-resolved two-photon photoemission studies of electron dynamics in metals. *Progress in Surface Science*, 56 (4), **1997**, pp. 239–310. DOI: 10.1016/S0079-6816(98)00002-1 (cited on page 109).

[252] R Haight. Electron dynamics at surfaces. *Surface Science Reports*, 21 (8), **1995**, pp. 275–325. DOI: 10.1016/0167-5729(95)00002-X (cited on page 109).

[253] S. Mathias, A. Ruffing, F. Deicke, M. Wiesenmayer, M. Aeschlimann, and M. Bauer. Band structure dependence of hot-electron lifetimes in a Pb/Cu(111) quantum-well system. *Physical Review B*, 81 (15), **2010**, p. 155429. DOI: 10.1103/PhysRevB.81.155429 (cited on page 109).

[254] C. Powell. The quest for universal curves to describe the surface sensitivity of electron spectroscopies. *Journal of Electron Spectroscopy and Related Phenomena*, 47, **1988**, pp. 197–214. DOI: 10.1016/0368-2048(88)85012-6 (cited on page 109).

[255] J. Shu, K. R. Wilson, M. Ahmed, and S. R. Leone. Coupling a versatile aerosol apparatus to a synchrotron: Vacuum ultraviolet light scattering, photoelectron imaging, and fragment free mass spectrometry. *Review of Scientific Instruments*, 77 (4), **2006**, p. 043106. DOI: 10.1063/1.2194474 (cited on page 109).

[256] K. R. Wilson, M. Jimenez-Cruz, C. Nicolas, L. Belau, S. R. Leone, and M. Ahmed. Thermal Vaporization of Biological Nanoparticles: Fragment-Free Vacuum Ultraviolet Photoionization Mass Spectra of Tryptophan, Phenylalanine-Glycine-Glycine, and β-Carotene. *Journal of Physical Chemistry A*, 110 (6), **2006**, pp. 2106–2113. DOI: 10.1021/JP0543734 (cited on page 109).

[257] J. Shu, K. R. Wilson, M. Ahmed, S. R. Leone, C. Graf, and E. Rühl. Elastic light scattering from nanoparticles by monochromatic vacuum-ultraviolet radiation. *The Journal of Chemical Physics*, 124 (3), **2006**, p. 034707. DOI: 10.1063/1.2159485 (cited on page 109).

[258] O. Kornilov, C. C. Wang, O. Bunermann, A. T. Healy, M. Leonard, C. Peng, S. R. Leone, D. M. Neumark, and O. Gessner. Ultrafast Dynamics in Helium Nanodroplets Probed by Femtosecond Time-Resolved EUV Photoelectron Imaging. *The Journal of Physical Chemistry A*, 114 (3), **2010**, pp. 1437–1445. DOI: 10.1021/jp907312t (cited on page 109).

[259] O. Bünermann, O. Kornilov, D. J. Haxton, S. R. Leone, D. M. Neumark, and O. Gessner. Ultrafast probing of ejection dynamics of Rydberg atoms and molecular fragments from electronically excited helium nanodroplets. *The Journal of Chemical Physics*, 137 (21), **2012**, p. 214302. DOI: 10.1063/1.4768422 (cited on page 109).

[260] H. Wang, Y. Xu, S. Ulonska, J. S. Robinson, P. Ranitovic, and R. A. Kaindl. Bright high-repetition-rate source of narrowband extreme-ultraviolet harmonics beyond 22 eV. *Nature Communications*, 6, **2015**, p. 7459. DOI: 10.1038/ncomms8459 (cited on page 110).

[261] B. Winter, R. Weber, I. V. Hertel, M. Faubel, P. Jungwirth, E. C. Brown, and S. E. Bradforth. Electron binding energies of aqueous alkali and halide ions: EUV photoelectron spectroscopy of liquid solutions and combined ab initio and molecular dynamics calculations. *Journal of the American Chemical Society*, 127 (19), **2005**, pp. 7203–14. DOI: 10.1021/ja0429081 (cited on page 111).

[262] M. Bauer. Femtosecond ultraviolet photoelectron spectroscopy of ultra-fast surface processes. *Journal of Physics D: Applied Physics*, 38 (16), **2005**, R253–R267. DOI: 10.1088/0022-3727/38/16/R01 (cited on page 111).

[263] P Siffalovic, M Drescher, and U Heinzmann. Femtosecond time-resolved core-level photoelectron spectroscopy tracking surface photovoltage transients on p GaAs. *Europhysics Letters*, 60 (6), **2002**, pp. 924–930. DOI: 10.1209/epl/i2002-00306-3 (cited on page 111).

[264] W. M. Haynes. **CRC Handbook of Chemistry and Physics**. 96th. Boca Raton: CRC Press, 2015, p. 2677 (cited on page 114).

[265] Y.-I. Suzuki, K. Nishizawa, N. Kurahashi, and T. Suzuki. Effective attenuation length of an electron in liquid water between 10 and 600 eV. *Physical Review E*, 90 (1), **2014**, p. 010302. DOI: 10.1103/PhysRevE.90.010302 (cited on page 114).

[266] C. A. Kraus. Solutions of Metals in Non-Metallic Solvents; IV. 1 Material Effects Accompanying the Passage of an Electrical Current through Solutions of Metals in Liquid Ammonia.

Migration Experiments. *Journal of the American Chemical Society*, 30 (9), **1908**, pp. 1323–1344. DOI: 10.1021/ja01951a001 (cited on page 115).

[267] J. Simons. How Do Low-Energy (0.12 eV) Electrons Cause DNA-Strand Breaks? *Accounts of Chemical Research*, 39 (10), **2006**, pp. 772–779. DOI: 10.1021/ar0680769 (cited on page 115).

[268] C.-R. Wang, J. Nguyen, and Q.-B. Lu. Bond Breaks of Nucleotides by Dissociative Electron Transfer of Nonequilibrium Prehydrated Electrons: A New Molecular Mechanism for Reductive DNA Damage. *Journal of the American Chemical Society*, 131 (32), **2009**, pp. 11320–11322. DOI: 10.1021/ja902675g (cited on page 115).

[269] F. Arnold. Solvated electrons in the upper atmosphere. *Nature*, 294 (5843), **1981**, pp. 732–733. DOI: 10.1038/294732a0 (cited on page 115).

[270] C. D. Jonah, D. M. Bartels, and A. C. Chernovitz. Primary processes in the radiation chemistry of water. *International Journal of Radiation Applications and Instrumentation. Part C. Radiation Physics and Chemistry*, 34 (1), **1989**, pp. 145–156. DOI: 10.1016/1359-0197(89)90019-2 (cited on page 115).

[271] Y.-i. Yamamoto, Y.-I. Suzuki, G. Tomasello, T. Horio, S. Karashima, R. Mitríc, and T. Suzuki. Time- and Angle-Resolved Photoemission Spectroscopy of Hydrated Electrons Near a Liquid Water Surface. *Physical Review Letters*, 112 (18), **2014**, p. 187603. DOI: 10.1103/PhysRevLett.112.187603 (cited on pages 115, 116).

[272] O. T. Ehrler and D. M. Neumark. Dynamics of Electron Solvation in Molecular Clusters. *Accounts of Chemical Research*, 42 (6), **2009**, pp. 769–777. DOI: 10.1021/ar800263z (cited on page 115).

[273] C. G. Elles, A. E. Jailaubekov, R. A. Crowell, and S. E. Bradforth. Excitation-energy dependence of the mechanism for two-photon ionization of liquid H(2)O and D(2)O from 8.3 to 12.4 eV. *The Journal of Chemical Physics*, 125 (4), **2006**, p. 44515. DOI: 10.1063/1.2217738 (cited on page 115).

[274] R Laenen, T Roth, and A Laubereau. Novel precursors of solvated electrons in water: evidence for a charge transfer process. *Physical Review Letters*, 85 (1), **2000**, pp. 50–3. DOI: 10.1103/PhysRevLett.85.50 (cited on page 115).

[275] J. Savolainen, F. Uhlig, S. Ahmed, P. Hamm, and P. Jungwirth. Direct observation of the collapse of the delocalized excess electron in water. *Nature Chemistry*, 6 (8), **2014**, pp. 697–701. DOI: 10.1038/nchem.1995 (cited on page 116).

[276] P. Vöhringer. Ultrafast Dynamics of Electrons in Ammonia. *Annual Review of Physical Chemistry*, 66 (1), **2015**, pp. 97–118. DOI: 10.1146/annurev-physchem-040214-121228 (cited on page 116).

[277] F. Buchner, A. Lübcke, N. Heine, and T. Schultz. Time-resolved photoelectron spectroscopy of liquids. *The Review of Scientific Instruments*, 81 (11), **2010**, p. 113107. DOI: 10.1063/1.3499240 (cited on page 116).

[278] J. Lindner, A.-N. Unterreiner, and P. Vöhringer. Femtosecond Relaxation Dynamics of Solvated Electrons in Liquid Ammonia. *ChemPhysChem*, 7 (2), **2006**, pp. 363–369. DOI: 10.1002/cphc.200500467 (cited on page 116).

[279] M. Goldmann, J. Miguel-Sánchez, A. H. C. West, B. L. Yoder, and R. Signorell. Electron mean free path from angle-dependent photoelectron spectroscopy of aerosol particles. *The Journal of Chemical Physics*, 142 (22), **2015**, p. 224304. DOI: 10.1063/1.4922307 (cited on page 117).

[280] G. H. Lee, S. T. Arnold, J. G. Eaton, H. W. Sarkas, K. H. Bowen, C. Ludewigt, and H. Haberland. Negative ion photoelectron spectroscopy of solvated electron cluster anions, (H2O) n- and (NH3) n-. *Zeitschrift fur Physik D Atoms, Molecules and Clusters*, 20 (1-4), **1991**, pp. 9–12. DOI: 10.1007/BF01543925 (cited on page 117).

[281] J. C. Alfano, P. K. Walhout, Y. Kimura, and P. F. Barbara. Ultrafast transient-absorption spectroscopy of the aqueous solvated electron. *The Journal of Chemical Physics*, 98 (7), **1993**, p. 5996. DOI: 10.1063/1.464839 (cited on page 117).

[282] M. H. Elkins, H. L. Williams, A. T. Shreve, and D. M. Neumark. Relaxation mechanism of the hydrated electron. *Science*, 342 (6165), **2013**, pp. 1496–9. DOI: 10.1126/science.1246291 (cited on page 117).

[283] C. A. Mancuso, D. D. Hickstein, P. Grychtol, R. Knut, O. Kfir, X.-M. Tong, F. Dollar, D. Zusin, M. Gopalakrishnan, C. Gentry, E. Turgut, J. L. Ellis, M.-C. Chen, A. Fleischer, O. Cohen, H. C. Kapteyn, and M. M. Murnane. Strong-field ionization with two-color circularly polarized laser fields. *Physical Review A*, 91 (3), **2015**, p. 031402. DOI: 10.1103/PhysRevA.91.031402 (cited on page 118).

[284] H. Haberland, M. Karrais, M. Mall, and Y. Thurner. Thin films from energetic cluster impact: A feasibility study. *Journal of Vacuum Science & Technology A: Vacuum, Surfaces, and Films*, 10 (5), **1992**, pp. 3266–3271. DOI: 10.1116/1.577853 (cited on page 120).

[285] P. Agostini, F. Fabre, G. Mainfray, G. Petite, and N. K. Rahman. Free-Free Transitions Following Six-Photon Ionization of Xenon Atoms. *Physical Review Letters*, 42 (17), **1979**, pp. 1127–1130. DOI: 10.1103/PhysRevLett.42.1127 (cited on page 121).

[286] J. Eberly, J. Javanainen, and K. Rzażewski. Above-threshold ionization. *Physics Reports*, 204 (5), **1991**, pp. 331–383. DOI: 10.1016/0370-1573(91)90131-5 (cited on page 121).

[287] B. Zhang, D. F. Gardner, M. H. Seaberg, E. R. Shanblatt, C. L. Porter, R. Karl, C. A. Mancuso, H. C. Kapteyn, M. M. Murnane, and D. E. Adams. Ptychographic hyperspectral spectromicroscopy with an extreme ultraviolet high harmonic comb. *Optics Express*, 24 (16), **2016**, p. 18745. DOI: 10.1364/OE.24.018745 (cited on page 165).

[288] Y. Meng, C. Zhang, C. Marceau, A. Y. Naumov, P. B. Corkum, and D. M. Villeneuve. Interferometric time delay correction for Fourier transform spectroscopy in the extreme ultraviolet. *Journal of Modern Optics*, 63 (17), **2016**, pp. 1661–1667. DOI: 10.1080/09500340.2016.1165872 (cited on page 174).

[289] C Hernández-García, T Popmintchev, M. M. Murnane, H. C. Kapteyn, L Plaja, A Becker, and A Jaron-Becker. Group velocity matching in high-order harmonic generation driven by

mid-infrared lasers. *New Journal of Physics*, 18 (7), **2016**, p. 073031. DOI: 10.1088/1367-2630/18/7/073031 (cited on page 178).

[290] I. P. Christov, M. M. Murnane, and H. C. Kapteyn. High-Harmonic Generation of Attosecond Pulses in the Single-Cycle Regime. *Physical Review Letters*, 78 (7), **1997**, pp. 1251–1254. DOI: 10.1103/PhysRevLett.78.1251 (cited on page 179).

[291] C. Hernández-García and L. Plaja. Resolving multiple rescatterings in high-order-harmonic generation. *Physical Review A*, 93 (2), **2016**, p. 023402. DOI: 10.1103/PhysRevA.93.023402 (cited on page 181).

Appendix A

Noncollinear HHG with Different Wavelength Driving Lasers

This chapter is adapted, with permission, from:

- Daniel D. Hickstein, Franklin J. Dollar, Patrik Grychtol, Jennifer L. Ellis, Ronny Knut, Carlos Hernandez-Garcia, Dmitriy Zusin, Christian Gentry, Justin M. Shaw, Tingting Fan, Kevin M. Dorney, Andreas Becker, Agnieszka Jaron-Becker, Henry C. Kapteyn, Margaret M. Murnane, and Charles G. Durfee. Non-collinear generation of angularly isolated circularly polarized high harmonics. *Nature Photonics*, **9**, 743–750 (2015).
  DOI:10.1038/nphoton.2015.181

A.1 400 nm Driven NCP-HHG

We also generated circularly polarized high harmonics with the noncollinear mixing of two 400 nm lasers with counter-rotating circular polarization (Fig. A.1). As expected, the photon energies produced with 400 nm lasers were lower than for 800 nm, but the photon flux is high, reaching 2×10^8 photons per pulse. When argon was used as the HHG medium (Fig. A.1a,b), a single harmonic (22 eV) was observed (lower energy harmonics are blocked by the 200 nm Al filter). The isolation of a single harmonic makes this source attractive for applications such as coherent diffractive imaging and photoelectron spectroscopy that require a bright monochromatic light source. When neon is used as the generation medium (Fig. A.1c,d), additional harmonics are observed at higher photon energies, mirroring the behavior of single-beam HHG. The large energy

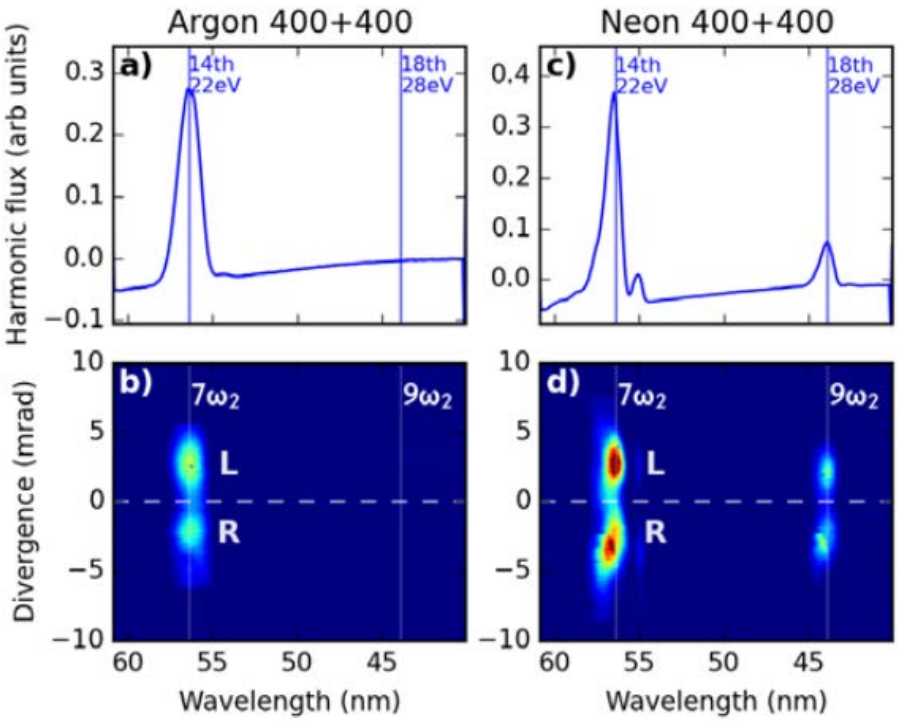

Figure A.1: **NCP-HHG with two 400 nm beams** (a) and (b) Mixing of 400 + 400 nm light in argon produces a single harmonic at 22 eV (lower harmonics are blocked by an aluminum filter), which is ideally suited for applications that require a high-flux monochromatic source, such as photoelectron spectroscopy or nanoscale imaging. (c) and (d) The higher ionization potential of neon allows additional well-separated (6 eV) harmonics to be produced, providing a convenient source for multi-wavelength imaging techniques. Figure from [48].

separation between these harmonics may prove useful for multicolor nanoscale imaging techniques [213, 287].

A.2 267 nm Driven NCP-HHG

When 267 nm beams were used to drive the NCP-HHG process, angularly separated beams were generated. The NCP-HHG method is capable of producing angularly separated harmonics across a wide range of driving laser wavelengths. However, the lower phase-matching pressures and larger separation angles of UV-driven NCP-HHG mean that full angular separation of the harmonics is easiest to experimentally achieve using driving lasers in the UV spectral region. Using two 267 nm driving laser beams in argon gas, we demonstrate that NCP-HHG generates four

separate beams (Fig. A.2b), corresponding to the left and right circularly polarized harmonics at 14 eV and 23.4 eV (3rd and 5th harmonic of 267 nm, which correspond to the 9th and 15th harmonic of the fundamental 800 nm field). By using an Al filter, we block the 3rd harmonic and transmit only the 5th harmonic (Fig. A.2a), confirming these spectral assignments. To our knowledge, this is the first demonstration of a HHG process that naturally separates different harmonic orders. With sufficient pressure, angularly separated harmonics can be produced using longer wavelength driving lasers, allowing for spectroscopy experiments without the need for a spectrometer.

Due to favorable conversion efficiency scaling of HHG at shorter wavelength driving lasers [96], very little pulse energy is required for NCP-HHG using 267 nm driving lasers. For example, the bright harmonics shown in Fig. A.2 were generated using only 15 μJ in each beam.

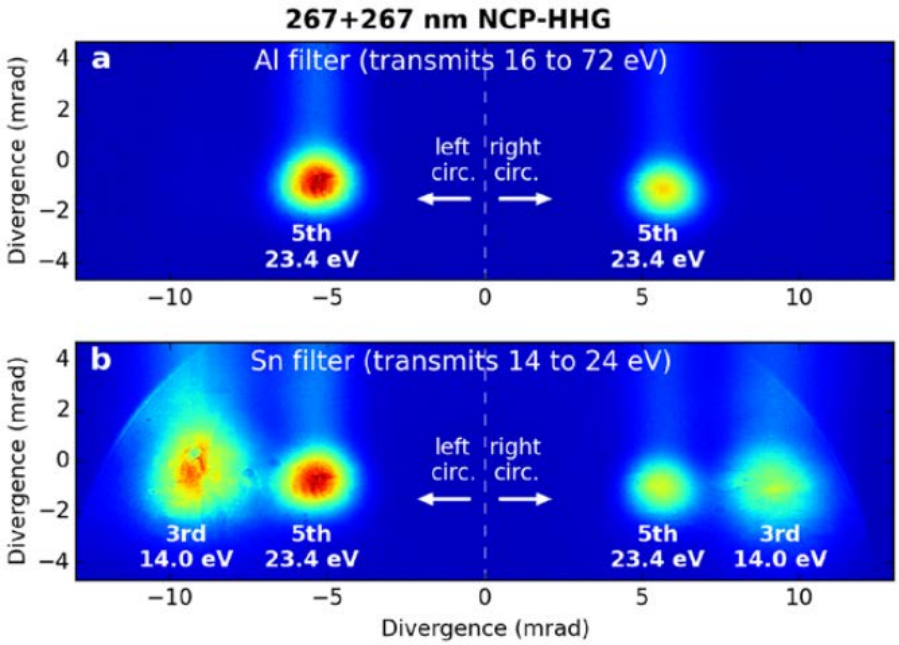

Figure A.2: **Angularly separated harmonics using NCP-HHG driven by UV beams.** (a) When a 200 nm Al filter is placed between the HHG region and the camera, only two beams are seen, which correspond to the left and right circularly polarized beams if the 5th harmonic of 267 nm (15th harmonic of the fundamental) at 23.4 eV. (b) When a tin (Sn) filter is used, the 3rd harmonic (9th harmonic of the fundamental, 14 eV) is also transmitted. The 3rd harmonic is angularly separated from the 5th harmonic and 4 distinct beams are seen at the camera. Figure from [48].

A.3 Two Color Driven NCP-HHG

The circularly polarized noncollinear HHG process is not limited to mixing two beams of the same frequency. We demonstrated this by generating circularly polarized harmonics by mixing 400 nm and 800 nm beams in argon (Fig. A.3). The angle-integrated spectrum (Fig. A.3a) of the EUV emission exhibits the familiar "left, right, missing" pattern seen in collinear circularly polarized HHG, where the left circular harmonics are separated in frequency from the right circular harmonics, and every third harmonic is suppressed [42, 43, 112, 113, 115]. Furthermore, the angle-resolved spectrum (Fig. A.3b) reveals that the left circularly polarized harmonics are emitted in one direction, and the right circular harmonics in the opposite direction. Moreover, in contrast to noncollinear mixing at the same frequency, where the harmonics are grouped around the centerline of the pump beams, the harmonics generated from the mixing of 400 nm and 800 nm beams are displaced towards the direction of the 400 nm output beam because of momentum conservation.

The noncollinear mixing of different frequencies can be explained using similar conservation of momentum arguments as when mixing at the same frequency. For the mixing of n_1 photons of the fundamental with n_2 photons of the second harmonic, the effective harmonic order relative to the fundamental is $q = n_1 + 2n_2$, and conservation of spin angular momentum requires $|n_1 - n_2| = 1$. This restricts the allowed mixing orders:

$$\text{for } n_2 = n_1 + 1,\ q = 3n_1 + 2;$$

$$\text{for } n_2 = n_1 - 1,\ q = 3n_1 - 2;$$

$$\text{and } n_2 = n_1 \text{ is forbidden.}$$

The relationship between the harmonic signal angle θ_q and the input angle θ_0 relative to the bisecting line is somewhat more complicated than we found earlier in the degenerate mixing case: $\tan\theta_q = (\frac{n_1 - 2n_2}{q})\tan\theta_0$. For $n_2 = n_1 \pm 1$, $\tan\theta_q = -(\frac{q \pm 4}{3q})\tan\theta_0$. Taking the limit of high harmonic order, we see that the harmonics are again divided into left and right circularly polarized directions, centered on an angle $-\tan\theta_0/3$, which is displaced away from the bisecting line towards the direction of the second harmonic beam. The same principles of conservation of spin angular

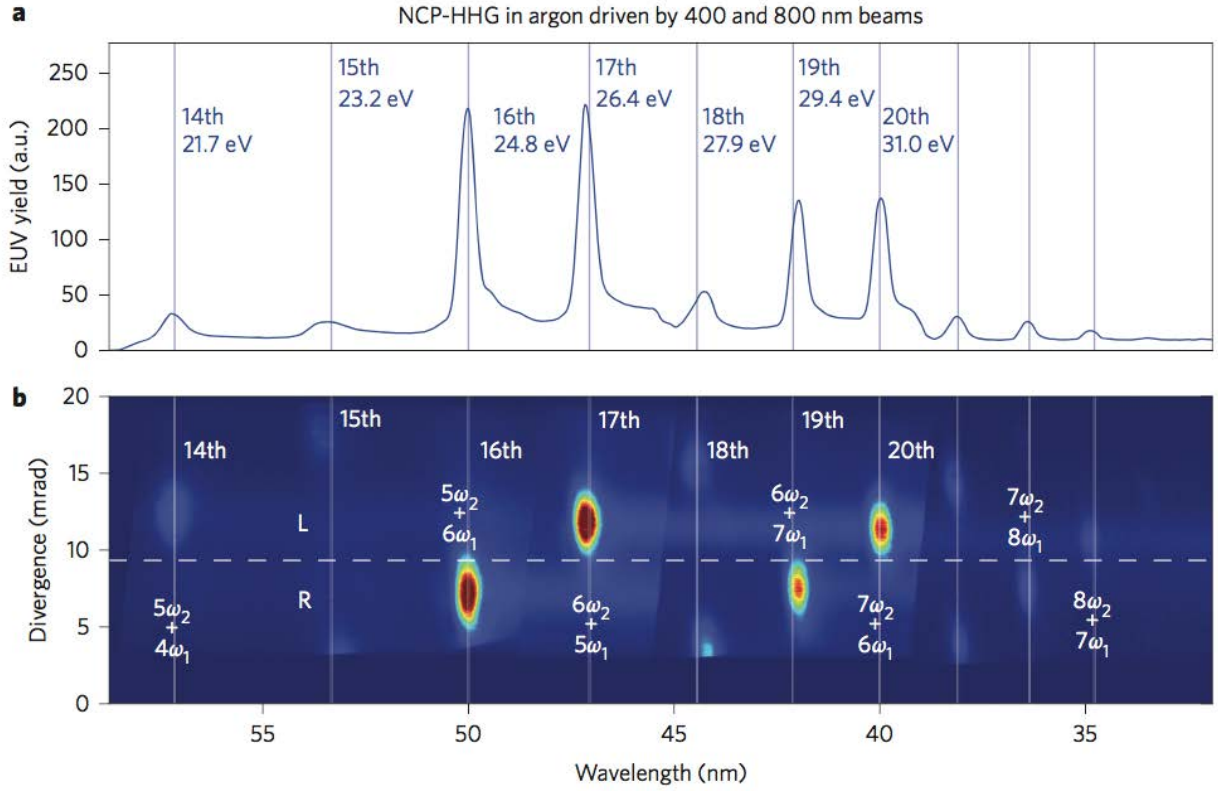

Figure A.3: **NCP-HHG driven by different frequency driving lasers (400 nm and 800 nm).** (a) The angle-integrated harmonic spectrum reveals the "left, right, missing" pattern seen in collinear circularly polarized HHG. a.u., arbitrary units. (b) In contrast to collinear generation, noncollinear HHG generates one helicity in one direction and the opposite helicity in the other direction. The low intensity peaks at the 15th, 18th, and 21st harmonic orders are a result of the slight ellipticity of the driving laser beams. Figure from [48].

momentum and linear momentum can be used to find the output angles for any mixing frequencies.

The wave mixing picture can be extended to the $\omega + 2\omega$ case as well: when the relative $\omega/2\omega$ phase varies, the orientation of the bursts of linearly polarized attosecond pulses rotates in a manner similar to the rotation of the linear polarization shown in Fig. 3.2. The result is a rotating polarization grating that behaves identically to the $\omega + \omega$ case, producing two beams of opposite-helicity circularly polarized light.

Appendix B

Experimental Details for Noncollinear Phase-Matching Measurements

This chapter is adapted, with permission, from:

- Jennifer L. Ellis, Kevin M. Dorney, Charles G. Durfee, Carlos Hernandez-Garcia, Franklin Dollar, Christopher A. Mancuso, Tingting Fan, Dmitriy Zusin, Christian Gentry, Patrik Grychtol, Henry C. Kapteyn, Margaret M. Murnane, and Daniel D. Hickstein. Phase matching of noncollinear sum and difference frequency high harmonic generation above and below the critical ionization level. *Optics Express*, **25**, 10126–10144 (2017). DOI:10.1364/OE.25.010126

B.1 Absolute Phase-Matching Pressures at Different Experimental Conditions

Practically, it is not possible to map out the entire angular dependence of the phase-matching pressure using a single set of experimental conditions. Obviously, both above and below critical ionization cannot be probed simultaneously. However, even when exploring the phase-matching pressure below critical ionization the harmonic emission at all HOSFG angles could not be measured at the same experimental conditions. This is because the harmonic emission angle that is statistically the most probable depends on the intensity ratio between the two driving beams [169]. When the two driving lasers are the same intensity harmonics are predominately emitted equally between the two lasers and therefore at small angles ($\theta_q \sim 0$). However, when one beam is more intense harmonics are preferentially emitted at angles near the more intense driving laser ($\theta_q \sim \theta_1$).

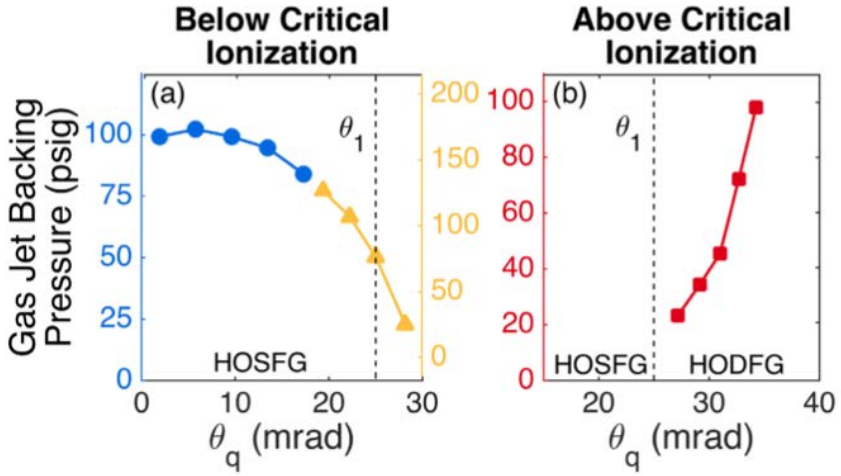

(c)	Gas	λ_1, λ_2 (nm)	$\sim I_1 / I_2$	$\sim I_{tot}$ (W / cm^2)	$\sim \eta / \eta_{crit}$
Blue Circles	Xe	790, 790	1	7×10^{13}	0.25
Yellow Triangles	Xe	790, 790	10	9×10^{13}	0.99
Red Squares	Ar	395, 790	10	3×10^{14}	4

Figure B.1: **Experimentally observed dependence of the phase-matching pressure on the emission angle.** This data was collected at three different experimental conditions to fully explore the angular dependence of the phase matching pressure. (a) Two different experimental conditions were necessary below critical ionization to optimize harmonic emission at either small (blue circles) or large (yellow triangles) angles. (b) A single set of experimental parameters was used above critical ionization (red squares). (c) The relevant experimental parameters, where intensities are estimated from Gaussian beam optics. Figure from [167].

Therefore, we used three different experimental conditions to map out the phase-matching pressure at a wide range of harmonic emission angles, as well as above and below critical ionization. These different experimental conditions result in different absolute phase matching pressures (Fig. B.1). However, regardless of the specific conditions the phase matching pressure goes as θ_q^2. Therefore, the experimental pressures in Fig. 3.9 were scaled to emphasize the universal behavior of the phase mismatch.

B.2 Angularly Resolved Scaling of the Harmonic Yield with Gas Jet Pressure

To obtain the angularly dependent phase matching pressures (Fig. 3.9 and Fig. B.1) we measure the angularly resolved harmonic yield as a function of the gas jet backing pressure with linearly polarized driving lasers. Without a spectrometer in place, we observe a series of harmonic beamlets on the camera, which correspond to the absorption of different numbers of photons from each driving laser (Fig. B.2a). We note that because the angle of harmonic emission depends on the harmonic order, the fact that we see a series of discrete beamlets means that there are not very many harmonic orders present. When there are many harmonic orders present these beamlets merge and assignments can no longer be made without also spectrally dispersing the harmonics.

We record a series of these angularly resolved images at several different gas jet backing pressures. This allows us to find the phase-matching pressure at many different harmonic angles simultaneously by observing the harmonic yield in each beamlet as a function of pressure (Fig. B.2b-f). For each harmonic beamlet, there is a pressure at which the harmonic yield in that beamlet is maximized. This optimal pressure is due to phase matching effects [36, 37] and therefore has an angular dependence due to the angularly varying phase mismatch that arises in a noncollinear geometry.

We obtained the θ_q axis by considering the number of photons absorbed from each beam and enforcing conservation of linear momentum (Eq. 3.1), which has been previously shown to accurately predict the angles of harmonic emission in a noncollinear geometry [48]. For the conditions shown in Fig. B.2a (blue circles in Fig. B.1a) we observed primarily the 13th harmonic order with a small contribution from the 15th harmonic order. As a check, we used the θ_q axis obtained from Eq. 3.1 and the known pixel size of the CCD camera (Andor, DO420-BN) to calculate the distance from the gas jet to the camera to ensure that this procedure gives a physically reasonable result.

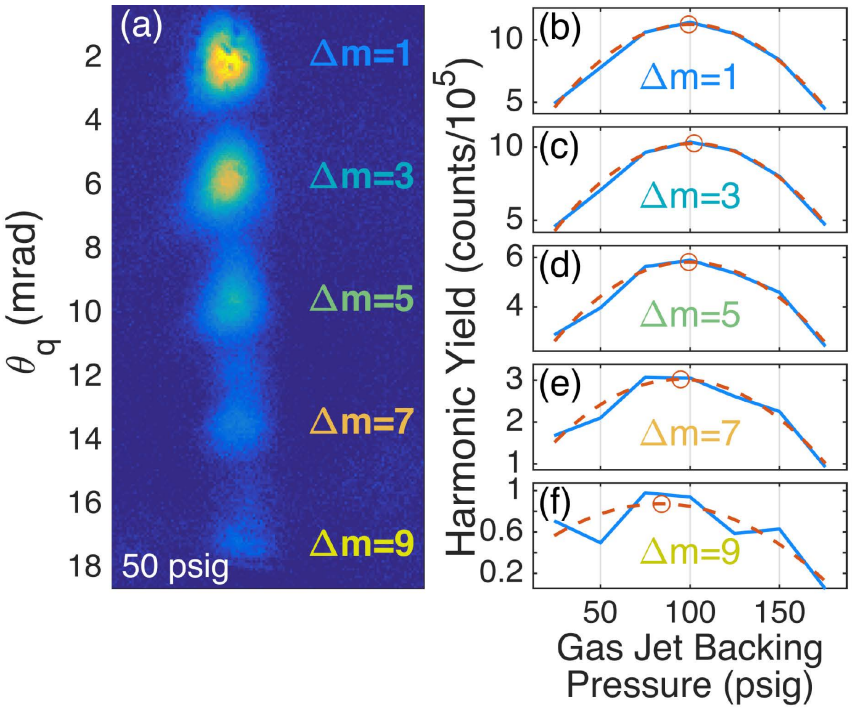

Figure B.2: **Angularly resolved pressure dependence of harmonic yield.** (a) The raw camera image shows several high-harmonic beamlets emitted into different angles, which correspond to absorption of different numbers of photons from each driving laser beam ($\Delta m = 1, 3, ...9$). (b-f) The yield in each high-harmonic beamlet in (a) is measured as a function of the gas jet backing pressure (solid blue lines) to find the optimal pressure as a function of the harmonic emission angle. As the pressure is increased the harmonic yield will increase until the pressure at which the phase matching is optimized (i.e. the phase-matching pressure). After this point, further increasing the pressure causes the harmonic yield to decrease. The phase matching pressure found for each harmonic beamlet is marked with a red circle. The dashed red lines are quadratic fits to the yield as a function of pressure. Figure from [167].

Appendix C

Additional Details for Harmonics with Spatially Varying Ellipticity

This chapter is adapted, with permission, from:

- Jennifer L. Ellis, Kevin M. Dorney, Daniel D. Hickstein, Nathan J. Brooks, Christian Gentry, Carlos Hernandez-Garcia, Dmitriy Zusin, Justin M. Shaw, Quynh L. Nguyen, Christopher A. Mancuso, G. S. Matthijs Jansen, Stefan Witte, Henry C. Kapteyn, and Margaret M. Murnane. High harmonics with spatially varying ellipticity. *In submission.*

C.1 Determining the Sign of Magnetic Circular Dichroism

While it is straightforward to determine the amplitude of the sinusoidally varying magnetic asymmetry and therefore the magnitude of the EUV MCD, it is slightly more involved to determine the sign. This is because regions of both right- (RCP) and left- (LCP) circular polarization are present, which manifests as regions of both positive and negative magnetic asymmetry. It is therefore not immediately clear if the asymmetry is negative at a given spatial location because of the sign of the MCD or due to the helicity of the light. The most straightforward way to disentangle these two effects would be to first characterize the spatially varying ellipticity of the light before measuring an unknown sample. However, even if no prior characterization is done, it is possible to identify the *relative* sign of the asymmetry for different energies by comparing the phase of the spatially varying asymmetry. This determination is possible because a sign change in the EUV MCD results in a π-phase shift (i.e., a flip in sign of the amplitude) in the measured spatially varying asymmetry.

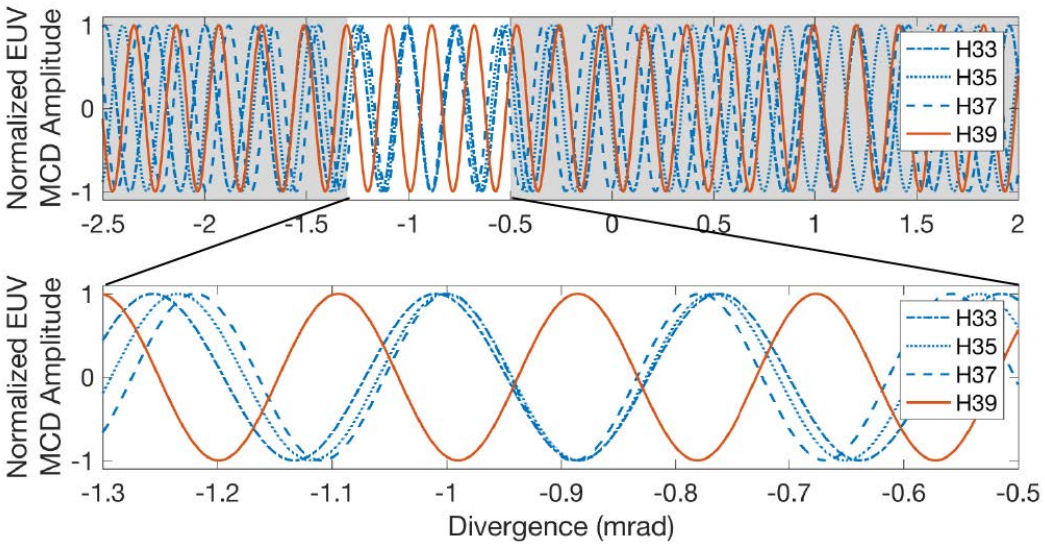

Figure C.1: **Normalized EUV MCD amplitude as a function of divergence angle.** The spatially varying asymmetry of H39 is π out of phase as compared to the other harmonic orders present, which is due to the opposite sign of the EUV MCD asymmetry for H39 compared to H33-H37. Figure from [205].

For the cobalt sample studied here, there is a change in sign in the energy dependent magnetic asymmetry going through the M-edge (Fig. 4.3c). Comparing the normalized sinusoidally varying asymmetry (Fig. C.1) of harmonic orders above (H39) and below (H33-H37) the M-edge clearly shows a π-phase shift that is due to this difference in sign of the EUV MCD effect. Note that the "zero" (where the different frequency sine waves for the different harmonic orders line up) is slightly shifted to a divergence angle of -0.94 mrad. This shift is because of a small time delay between the two harmonic sources [288].

C.2 Degree of Circularity Obtained

Comparison of our measured EUV MCD asymmetry (Fig. 4.3) with literature values for the expected magnetic asymmetry for 20 nm of cobalt [127] enables us to characterize the degree of circularity attained in SVE-HHG for each harmonic order. In SVE-HHG, the ellipticity varies sinusoidally, such that the amplitude of the sinusoidal variations in the measured magnetic asymmetry indicates the maximum ellipticity present in the spatial polarization distribution. To characterize

this maximally attained degree of circularity, we preformed a weighted fit of sinusoidal functions to the spatially varying asymmetry. We computed the value and errors of the asymmetry as a function of divergence angle, for the weighted fit, by taking the mean and the standard deviation of the asymmetry across each harmonic in energy out to an intensity threshold of 25 % for each harmonic order (Fig. C.2).

The weighted nonlinear-least-squares fit recovers an amplitude and associated error (95 % confidence interval) for the sinusoidally varying asymmetry for each harmonic order. Comparison of this amplitude to the expected magnetic asymmetry gives the maximal degree of circularity present in the SVE, $S_3/S_0 = A_{measured}/A_{literature}$ (Table C.1). The weighted average of the degree of circularity for all four harmonic orders observed gives a total circularity of $S_3/S_0 = 0.85 \pm 0.09$. However, the degree of circularity recovered near the magnetic M-edge, where the MCD effect is

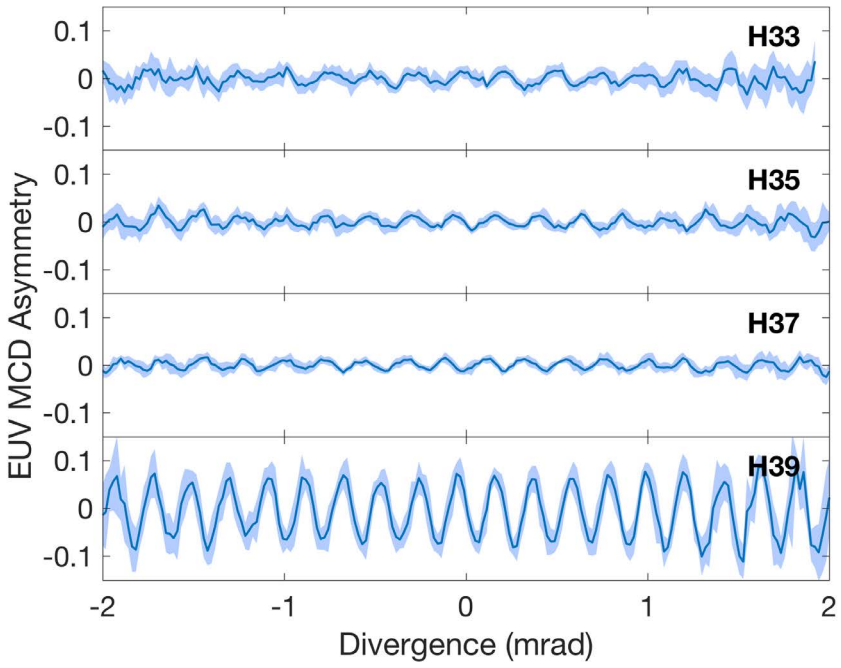

Figure C.2: **Lineouts along the divergence plane of the EUV MCD asymmetry of spectrally dispersed high harmonics.** Each harmonic shows a sinusoidal variation in the magnetic asymmetry with an amplitude that corresponds to the magnitude of the EUV MCD effect observed in the maximally circularly polarized spatial locations. The shaded blue area represents the standard deviation across the width of each harmonic in energy. Figure from [205].

strong, approaches 100 %. We note that variations in sample preparation procedures could lead to small modifications in the magneto-optical constant. Because the magneto-optical constant is small far from the edge, such modifications could change its value substantially at those photon energies, thus leading to large differences in the observed MCD away from the edge where the MCD effect is weak.

	H33	H35	H37	H39
$A_{measured}$ (%)	1.3 ± 0.3	1.3 ± 0.2	1.1 ± 0.1	-0.7 ± 0.6
$A_{literature}$ (%)	1.9 ± 0.3	3.3 ± 0.5	1.8 ± 0.3	-6.9 ± 1.0
$\mathbf{S_3/S_0}$	$\mathbf{0.71 \pm 0.17}$	$\mathbf{0.40 \pm 0.08}$	$\mathbf{0.63 \pm 0.10}$	$\mathbf{1.01 \pm 0.08}$

Table C.1: **Degree of circularity for each harmonic order present.** Obtained by comparison of the amplitude of the spatially varying asymmetry measured with SVE-HHG to literature values for the asymmetry of 20 nm cobalt.

C.3 Determination of the Energetically Resolved EUV MCD Asymmetry from a Fourier Transform of the Spatially Varying Asymmetry in SVE-HHG

Typically EUV MCD is measured in an energetically resolved way, such that the MCD of every energy present can be considered individually. In this case, the magnetic asymmetry for perfectly circularly polarized light is simply $A = (I_{up} - I_{down})/(I_{up} + I_{down}) = \tanh(2k\Delta\beta L)$, where k is the k-vector of the light, $\Delta\beta$ is the energy-dependent magneto-optical constant of the material, and L is the path length through the material [125]. However, when many energies are overlapping on the detector and the polarization deviates from perfect circularity the situation is slightly more complicated. Therefore, we must relate the asymmetry that we measure in SVE-HHG, $A^m = (I_{up} - I_{down})/(I_{up} + I_{down})$, to the literature values, $A = \tanh(2k\Delta\beta L)$.

For perfectly RCP light of a single energy, $I_{up} = I_0 e^{2k\Delta\beta L}$ and $I_{down} = I_0 e^{-2k\Delta\beta L}$. Extending these expressions to the case of arbitrary polarization gives $I_{up} = I_R e^{2k\Delta\beta L} + I_L e^{-2k\Delta\beta L}$ and $I_{down} = I_R e^{-2k\Delta\beta L} + I_L e^{2k\Delta\beta L}$, where I_R (I_L) is the component of the polarization that is RCP

(LCP). Finally, if the presence of several harmonic orders is included then

$$I_{up} = \Sigma_i I_{R,i} e^{2k_i \Delta\beta_i L} + I_{L,i} e^{-2k_i \Delta\beta_i L}$$
$$I_{down} = \Sigma_i I_{R,i} e^{-2k_i \Delta\beta_i L} + I_{L,i} e^{2k_i \Delta\beta_i L}, \tag{C.1}$$

where the sum over i is a sum over harmonic orders and each harmonic order has its own associated k and $\Delta\beta$. Using these expressions for I_{up} and I_{down} gives a measured magnetic asymmetry of,

$$A^m = \frac{\Sigma_i (I_{R,i} - I_{L,i})(e^{2k_i \Delta\beta_i L} - e^{-2k_i \Delta\beta_i L})}{\Sigma_i (I_{R,i} + I_{L,i})(e^{2k_i \Delta\beta_i L} + e^{-2k_i \Delta\beta_i L})}. \tag{C.2}$$

This expression is still completely general, but at this point we can start making simplifications based on knowledge of the light source. Specifically, we include the spatially varying ellipticity by considering the spatial form of the degree of circularity, $S_3/S_0 = (I_R - I_L)/(I_R + I_L) = \epsilon \sin(k_\theta \theta)$, where $\epsilon = |S_3/S_0|_{max}$. Additionally, since there is no intensity interference and therefore no spatially varying intensity, at every given spatial location the sum $I_{R,i} + I_{L,i}$ is simply the total intensity in that harmonic order, I_i. Note that these assertions also assume that there is no randomly polarized light present. Substituting this into the numerator of Eq. C.2 gives an expression for the measured spatially varying asymmetry,

$$A^m = \frac{\Sigma_i \epsilon \sin(k_{\theta,i}\theta) I_i (e^{2k_i \Delta\beta_i L} - e^{-2k_i \Delta\beta_i L})}{\Sigma_i I_i (e^{2k_i \Delta\beta_i L} + e^{-2k_i \Delta\beta_i L})}. \tag{C.3}$$

This spatially varying asymmetry is precisely the asymmetry that we measure in SVE-HHG, which is the superposition of the sinusoidally varying asymmetry for each harmonic order present. Therefore, a spatial Fourier transform (FT) can isolate the amplitude of each individual sinusoidal contribution, so that

$$A_i^m = \frac{\epsilon I_i (e^{2k_i \Delta\beta_i L} - e^{-2k_i \Delta\beta_i L})}{\Sigma_i I_i (e^{2k_i \Delta\beta_i L} + e^{-2k_i \Delta\beta_i L})} = \frac{\epsilon I_i \sinh(2k_i \Delta\beta_i L)}{\Sigma_i I_i \cosh(2k_i \Delta\beta_i L)} \tag{C.4}$$

While this expression is still exact, it is not very useful in it's present form and cannot be simplified any further. Fortunately, in typical EUV MCD experiments the small angle approximation ($2k_i \Delta\beta_i L \ll 1$) is perfectly valid. For example, for the maximum MCD asymmetry present in

our experiment $A = \tanh(2k_i\Delta\beta_i L) = 0.07$, which deviates from the small angle approximation by $< 1\%$. Therefore, we can approximate cosh ≈ 1 and sinh $\approx$ tanh so that

$$A_i^m = \frac{\epsilon I_i \tanh(2k_i\Delta\beta_i L)}{\Sigma_i I_i} = \epsilon A_i(I_i/I_{tot}). \tag{C.5}$$

Therefore, the amplitude of the sinusoidally varying asymmetry at a given energy that is recovered from a spatial FT in SVE-HHG is simply what is measured in the energetically dispersed case (ϵA_i) scaled by the fractional spectral weight of that energy (I_i/I_{tot}). This result means that if the spectral weights are known then the fundamental MCD properties of the material can be determined via spatial FT, and therefore energy resolved measurements can be obtained without a grating.

C.4 Simulation Details

We have performed theoretical simulations to gain further insight into SVE-HHG. We employ an HHG method [186] that combines the fully-quantum single-atom HHG response (through the Strong Field Approximation) with macroscopic propagation through the use of the electromagnetic field propagator. Here, the harmonics emitted at each atom position within the target are propagated towards the detector, where the far-field HHG profile is calculated. We assume the harmonic radiation to propagate with the vacuum phase velocity, which is a reasonable assumption for the high-order harmonics observed experimentally. Propagation effects in the fundamental field, such as the production of free charges, the refractive index of the neutrals, the group velocity walk-off [289], as well as absorption in the propagation of the harmonics, are taken into account. Note that although we account for the time-dependent nonlinear phase shifts in the driving fields, nonlinear spatial effects are not taken into account.

In the simulations presented in this work, we have considered two different driving laser pulses, so called multi-cycle and few-cycle pulse drivers, both of them with a central wavelength of 800 nm and peak intensity of 3×10^{14} W/cm^2. The few-cycle pulse envelope is modeled with a sin^2 function of 2.6 fs pulse duration at full-width-half-maximum of the intensity. The carrier-

envelope-phase is chosen to optimize the generation of a single attosecond pulse. The multi-cycle pulse envelope is modeled with a trapezoidal function with two cycles of linear turn-on, four cycles of constant amplitude (10.6 fs), and two cycles of linear turn-off.

The two orthogonally polarized driving beams of the SVE-HHG scheme are modeled as Gaussian beams, with a beam waist of 30 μm at the focus. The two Gaussian focal spots are separated by 500 μm. The neon gas jet, flowing along the perpendicular direction to the beam propagation is modeled as a Gaussian distribution of 100 μm at full width half maximum, and with a peak density of 5 torr.

Numerical simulations also enable us to analyze the temporal behavior of the harmonics produced through SVE-HHG (Fig. C.3). As expected from single-beam HHG, when multi-cycle pulses are used to drive the HHG process attosecond pulse trains are produced (Fig. C.3, left column). However, near single-cycle driving pulses can instead produce isolated attosecond pulses [20, 290] (Fig. C.3, right column). In SVE-HHG the polarization of these pulses varies as a function of divergence angle. The far-field emission detected on-axis (Fig. C.3c,f) consists of linearly polarized attosecond pulses. As the divergence angle increases, the emission moves from linear to elliptical pulses, so that at particular angles ($\pm$ 0.02 mrad) the harmonic emission consists of circularly polarized attosecond pulses (Fig. C.3b,e). Due to the different polarization distributions of the harmonic orders (Fig. C.3a,d), for larger emission angles the pulses resulting from the whole bandwidth do not exhibit a pure polarization state.

We can also use simulations to inform the spectral resolution practically attainable through SVE-HHG (Fig. C.4). Here we preform an FT analysis of the far-field polarization distribution from the numerical simulations (Fig. 4.5). In this case, we can use an FT of the spatially varying ellipticity to recover the spectrum for comparison with the true spectrum (i.e. the spectrum that would be measured with a spectrometer). We find that when Gaussian focal spots are used to drive the HHG process the spatial FT does a good job of recovering the true spectrum (Fig. C.4a,c), however there are some small deviations between the two. Interestingly, when only two point-source emitters (also separated by 500 μm) are considered, the FT recovers the true spectrum

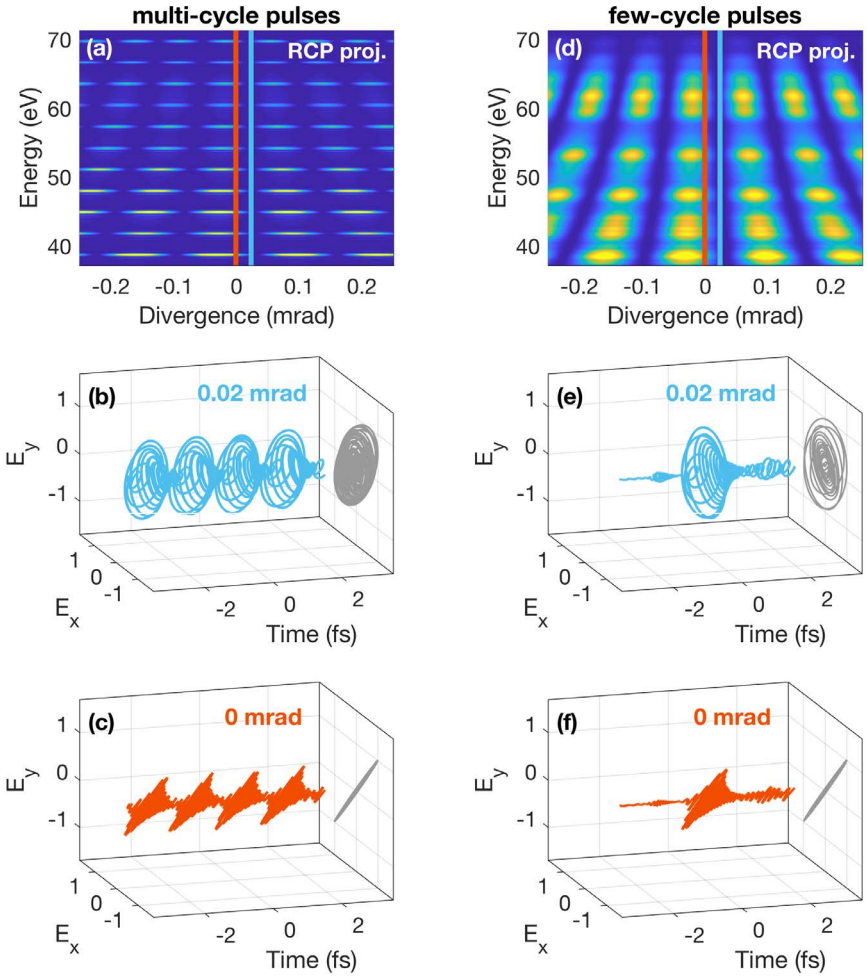

Figure C.3: **Numerical simulations of the temporal characteristics of high harmonics emitted from SVE-HHG.** (a) When multi-cycle driving pulses are used the resulting spectrum consists of discrete harmonics, corresponding to attosecond pulse trains. The individual pulses within these pulse trains are either circularly (b) or linearly (c) polarized depending on the divergence angle. (d) Alternatively, when near single-cycle driving pulses are used a supercontinuum spectrum is produced, corresponding to isolated attosecond pulses in the time domain. Depending on the divergence angle, these isolated attosecond pulses can be either circularly (e) or linearly (f) polarized. Panels (a) and (d) show the projection of the far-field polarization distribution along pure right-circular polarization (RCP). The vertical lines denote the angles corresponding to the circularly (blue) and linearly (red) polarized temporal plots shown in the panels below. Figure from [205].

nearly perfectly (Fig. C.4b,d). This indicates that the discrepancies between the FT-recovered spectrum and the true spectrum in the Gaussian-focal-spot case stem from the nonuniform intensity distribution across the two Gaussian sources. This nonuniform intensity results in transverse phase matching [210, 211, 291] conditions that are responsible for the slight deviations between the true spectrum and the FT-recovered spectrum. Therefore, increased accuracy can be attained in SVE-HHG by employing flat-top beams with a uniform intensity distribution at the focus, similar to the two-emitter case.

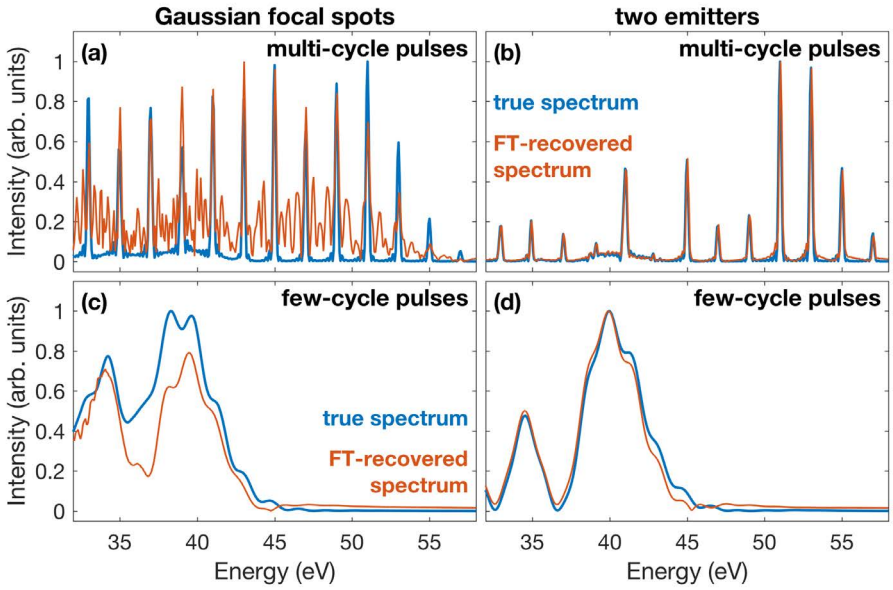

Figure C.4: **Spectral analysis of numerical simulations of SVE-HHG.** (a), (c) When Gaussian focal spots are used to drive the HHG process there are some small discrepancies between the spectrum recovered through FT of the spatially varying polarization (red) and the true spectrum (blue). (b), (d) When only two emitters are considered the FT analysis (red) recovers the true spectrum (blue) nearly perfectly. Figure from [205].

Appendix D

Nanoparticle Size Distribution Details

This chapter is adapted, with permission, from:

- Jennifer L. Ellis, Daniel D. Hickstein, Wei Xiong, Franklin Dollar, Brett B. Palm, K. Ellen Keister, Kevin M. Dorney, Chengyuan Ding, Tingting Fan, Molly B. Wilker, Kyle J. Schnitzenbaumer, Gordana Dukovic, Jose L. Jimenez, Henry C. Kapteyn, and Margaret M. Murnane. Materials Properties and Solvated Electron Dynamics of Isolated Nanoparticles and Nanodroplets Probed with Ultrafast Extreme Ultraviolet Beams. *J. Phys. Chem. Lett.*, **7** (4), 609–615 (2016). DOI:10.1021/acs.jpclett.5b02772

D.1 Nanoparticle Size Distributions

We used a scanning mobility particle sizer (SMPS) to characterize the aerosols produced from the compressed gas atomizer. The SMPS system consists of an electrostatic classifier (TSI, Model 3080L) and a condensation particle counter (TSI, Model 3010). The electrostatic classifier selects nanoparticles in an aerosol based on their mobility diameter and the condensation particle counter determines the number density of nanoparticles at that diameter. For spherical particles, the mobility diameter is equal to the physical diameter. However, in general the mobility diameter is larger than the volume-equivalent diameter (the diameter resulting from melting the material into a sphere while keeping the same material density) [142]. Salts such as KI typically produce

nonspherical particles, and thus there may be additional differences in mass between the different particle compositions than implied by the differences in mobility distribution.

The measured size distributions for the aerosols investigated in this study are shown in Fig. D.1. However, it is the aerodynamic diameter, rather than the mobility diameter, that determines the transmission of nanoparticles through the aerodynamic lens. The aerodynamic diameter is different from the mobility diameter by a factor of density, meaning that denser particles behave like larger particles when transmitting through the aerodynamic lens. Aerodynamic diameter also depends on particle shape, with nonspherical particles appearing smaller than spherical particles of the same mass [142]. To estimate the density effect of the differences in the nanoparticle size distributions on the variations in photoelectron yield, we approximate the transmission of the aerodynamic lens as a rectangle function, where particles with aerodynamic diameters in the range of $70-700$ nm are completely transmitted and any particle outside of that range is not transmitted [146]. The same range of aerodynamic diameter corresponds to different ranges of mobility diameter for the different nanoparticle densities investigated (dashed-vertical lines in Fig. D.1).

D.2 Photoelectron Yield Adjusted for Concentrations and Material Absorption

To understand the variations in the measured total photoelectron yield (Fig. D.2, lighter bars), we considered the material absorption at 22 eV, which accounts for the first step in the three-step model of photoemission. To do so, we utilized the Center for X-Ray Optics (CXRO) database [11] to determine the photon mean-free-path (MFP) for all of the materials considered here. We note that the CXRO database only includes the individual atomic contributions to absorption, and therefore does not include any orbital mixing effects.

The first step in the three-step-model is the creation of a hot electron through the absorption of a high-energy photon. Integrating Beer's Law absorption over a sphere gives the total absorption

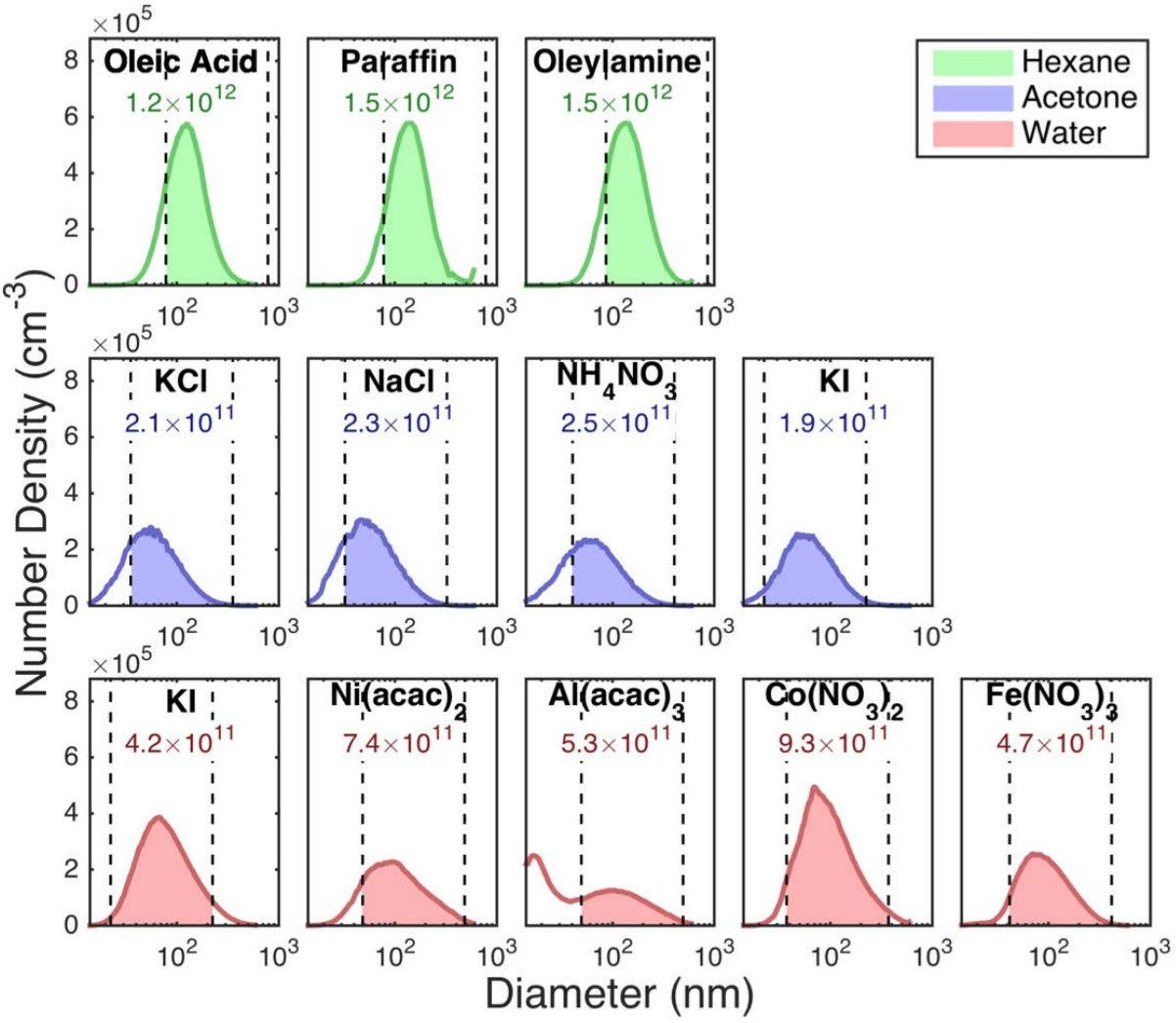

Figure D.1: **Nanoparticle size distributions obtained from scanning mobility particle sizer measurements.** The distributions are arranged according to the solvent they originated from: the top row is hexane (green), the middle row is water (blue), and the bottom row is acetone (red). The vertical-dashed lines indicate, for each material, the range of diameters that will transmit through the aerodynamic lens. The distributions are labeled with the total amount of nanoparticle surface area (nm^2/cm^3) delivered into the experimental chamber, which is similar to within an order of magnitude between the different materials. Figure from [240].

by spherical nanoparticles as a function of nanoparticle radius (R) and photon MFP (l),

$$A = 1 - \iint \frac{r\,dr\,d\theta}{\pi R^2} e^{-\frac{2\sqrt{R^2-r^2}}{l}} = 1 - \frac{1}{2}(\frac{l}{R})^2[1 - e^{-\frac{2R}{l}}(1 + 2\frac{R}{l})].$$

Dividing by this absorption fraction adjusts for the first step in the three-step-model (Fig. D.2, middle bars). If the differences in photoelectron yield were dominated by differences in EUV absorption throughout the particle, this correction would remove the variations. However, all of the nanoparticles studied here are large enough that most of the incident EUV light is absorbed ($A \sim 1$), so there is very little variation in the total absorption with composition. The small differences in EUV absorption that do occur are not sufficient to account for the differences in photoelectron yield between different nanoparticles. Therefore, simply considering the total EUV absorption does not account for the measured variation in the total photoelectron yield, meaning that the second and third steps in the three-step-model must dominate the yield.

A more sophisticated correction for material absorption can be made with the knowledge that the electron MFPs of ∼10 eV electrons are typically short (∼1 nm), so that only photons absorbed in the outermost portion of the nanoparticle can escape. Therefore, nanoparticles with higher absorption will absorb more photons in the outer layer, which will be more likely to produce photoelectrons. This effect is approximated by dividing the measured photoelectron yield by the relative absorption of a thin layer (1 nm) of material with the same surface area as the nanoparticle (Fig. D.2, darker bars). Although this correction more accurately represents the effect of different EUV absorption lengths between the different nanoparticle compositions, it still does not account for the variations in measured total photoelectron yield. Therefore, we conclude that differences in EUV absorption are not sufficient to explain the experimentally observed differences in photoelectron yield.

Since the first step of the three-step model is not sufficient to explain the differences in photoelectron yield between compounds, the cause of this difference must be the second (transmission of electrons through the material) or third (transmission of electrons through the surface of the particle) step. Thus, our EUV photoemission experiment is providing insight into the materials

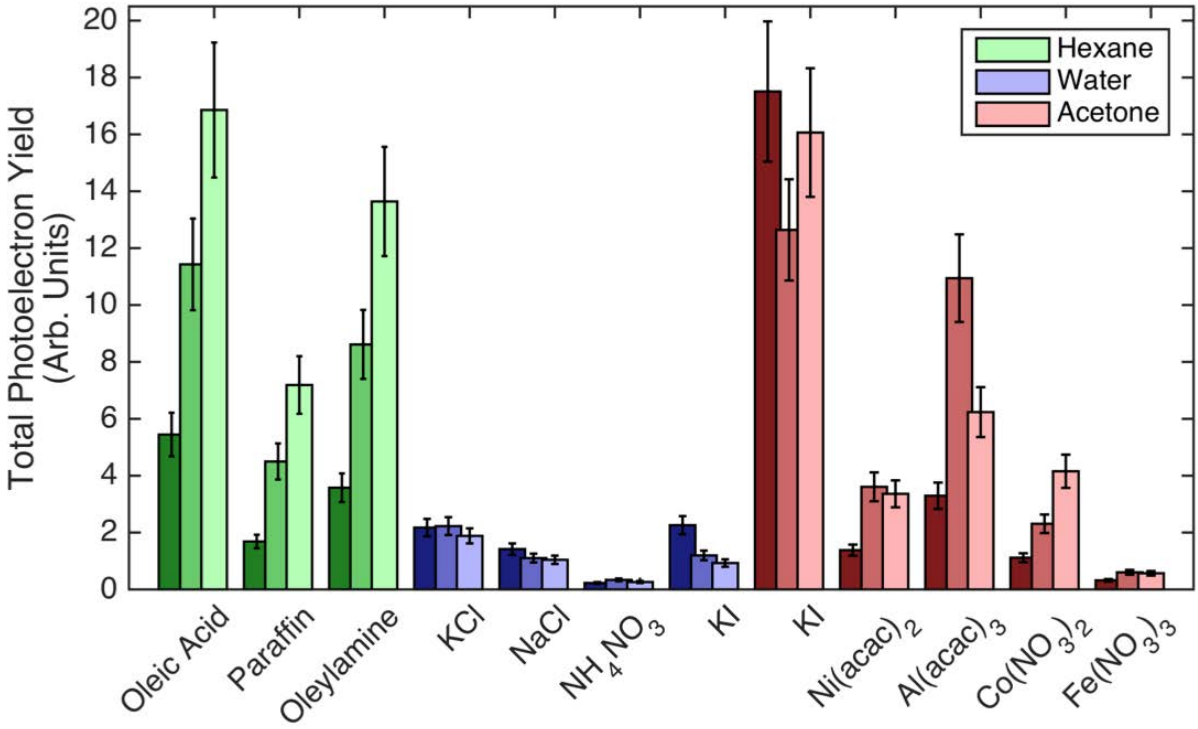

Figure D.2: **Scaled total photoelectron yield from various nanoparticles of differing size and composition, ionized with 22 eV light.** The lightest bars correspond to the measured photoelectron yield. The middle bars show the photoelectron yield adjusted for the total absorption of 22 eV light throughout the nanoparticle (divided by 2 to show simultaneously). The darkest bars correspond to the photoelectron yield adjusted for nanoparticle absorption in the outermost 1 nm of the particle (divided by 75 to show simultaneously). acac = acetylacetonate ($C_5H_7O_2$). Figure from [240].

properties of nanocrystals, namely the electron MFP and effective mass. In the future, measuring the photoelectron yield as a function of particle size will allow deconvolution of these two effects and therefore provide a method for determining these material properties.